Sede Amministrativa: Università degli Studi di Padova

Dipartimento di Scienze Chimiche

_____

CORSO DI DOTTORATO DI RICERCA IN SCIENCE AND ENGINEERRING OF MATERIALS AND NANOSTRUCTURES

CICLO XXXIV

Colloidal Plexcitonic Materials:
Design and dynamics

Coordinatore: Ch.mo Prof. Giovanni Mattei

Supervisore: Ch.ma Prof. Elisabetta Collini

Co-Supervisore: Ch.mo Prof. Fabrizio Mancin

Dottorando: Nicola Peruffo

To Chiara

J'ai des amis à découvrir et

beaucoup de choses à connaître.

Antoine de Saint-Exupéry (1943), The little prince.

Abstract

The light-matter coupling has been studied during the previous and the present centuries because of the plethora of different phenomena achievable depending on the coupling strength. The knowledge of the mechanisms ruling this coupling, and the dynamics of the involved states could find applications in photonics, solar cells, in the whole emerging panorama of the quantum technologies and, overall, wherever it becomes relevant to control the energy flux either temporally and spatially, even at the nanometric scale.

Among the systems exploited to generate hybrid light-matter states, the class of Colloidal Plexcitonic Materials (CPMs) is defined as the assembly of coupled colloidal plasmonic nanoparticles and organic dyes. CPMs are cheap, easy to characterize, and their synthesis is easy to scale up. However, to date, only a limited number of studies have been devoted to the investigation of the optimization of their properties and their dynamics in different coupling regimes.

With this Thesis, I want to bring my contribution to both these aspects. For this reason, I analysed the design of these materials either by cataloguing and interpreting the existing literature, and by preparing two new families of CPMs. The study of the dynamics was thus focussed on these families, sifted with the state-of-the-art ultrafast electronic spectroscopy techniques.

Overall, the knowledge gained studying the design properties and the dynamics of these systems revealed that, first, these two aspects are strongly correlated, and second, that these materials are highly versatile. Indeed, their design has been found to play a central role in the light-matter strength of interaction and coupling. Moreover, again with the fine tuning of these materials, it was possible to modulate their relaxation mechanisms: their lifetimes could be increased up to two orders of magnitude and, mostly, their quantum nature can be engineered.

Abstract (italiano)

L'interazione fra luce e materia, studiata ormai quasi da un secolo, può generare differenti fenomeni a seconda della forza dell'accoppiamento di queste due entità. La conoscenza dei meccanismi che la regolano e delle dinamiche degli stati energetici coinvolti ne potrebbe permettere l'applicazione in ambito fotovoltaico, in fotonica, nell'intero panorama emergente delle tecnologie quantistiche e, più in generale, laddove sia importante controllare il flusso dell'energia sia temporalmente che spazialmente, anche a livello nanometrico.

Una classe di sistemi in cui è possibile generare stati elettronici ibridi luce-materia è quella dei nanomateriali pleccitonici colloidali, ottenuti attraverso l'assemblaggio di nanoparticelle plasmoniche e fluorofori organici in forma aggregata o meno. Questi materiali sono economici, facilmente caratterizzabili e la loro sintesi scalabile semplicemente. Tuttavia, il loro studio ad oggi risulta limitato sia nell'ottimizzazione del loro design che nella razionalizzazione delle dinamiche in differenti regimi di accoppiamento.

Con questa tesi di dottorato voglio portare il mio contributo in entrambi gli ambiti. Ho analizzato il design di questi materiali sia attraverso un lavoro di catalogazione e interpretazione della letteratura esistente, sia attraverso la preparazione di due famiglie di nuovi materiali pleccitonici. Lo studio della dinamica si concentra proprio su tali famiglie di materiali, sondate con tecniche di spettroscopia elettronica ultraveloce all'avanguardia.

Nel complesso, attraverso la correlazione fra le conoscenze ottenute in questi due ambiti, mai d'altro canto totalmente scindibili, ho dimostrato la versatilità di questi materiali. L'interazione fra luce e materia è, infatti, regolata profondamente dal design dei nanosistemi, che ne influenza fortemente il regime di accoppiamento. Inoltre, sempre attraverso il design di questi materiali, è stato possibile modulare i meccanismi di rilassamento, in particolare rallentandone i tempi caratteristici fino a due ordini di grandezza, e, soprattutto, ingegnerizzando la loro natura quantistica.

x

List of abbreviations

K_a	Association constant
BNS	Gold "big" TMAOt-nanospheres
CAS	Coherent decay-Associated Spectra
CE	Condition of Existence of polaritons
CIT-NU	Citrate-capped nanourchin
CL	Capping Layer
CPM	Colloidal Plexcitonic Materials
CPM-D	CPM deposited onto a solid substrate
CPM-S	CPM dispersed in solution
DAS	Decay-Associated Spectra
DLS	Dynamic Light Scattering
ESA	Excited State Absorption
FROG	Frequency Resolved Optical Gating
FT	Fourier Transform
FWHM	Full Width Half Maximum
GSB	Ground State Bleaching
LO	Local Oscillator
LP	Lower Polariton
NP	Nanoparticle
NS	Nanosphere
NSA	Aggregated nanospheres
NU	Nanourchin

PAP	Particle Area per Porphyrin
PL	Photoluminescence
PPP	Porphyrins-Per-Particle
QEs	Quantum Emitters
SC	Strong Coupling
SE	Stimulated Emission
SERS	Surface-enhanced Raman scattering
SNSs	Gold "small" TMAOt-nanospheres
SOt-NUs	SOt-capped NUs
SPWV	Smoothed-Pseudo-Wigner-Ville
TA	Transient Absorption
TCSPC	Time-Correlated Single Photon Counting
TEM	Transmission Electronic Microscopy
TGA	Thermogravimetric analysis
TMAOt-NUs	TMAOt-capped nanourchins
UP	Upper Polariton
2DES	Two-Dimensional Electronic Spectroscopy

Table of contents

Introduction

The photophysical properties of the matter can drastically change when its states couple with the states of light. Light-matter interaction has been studied for almost a century, and numerous phenomena originating from this interaction have been revealed.[1-5] Depending on the coupling strength, indeed, one may run into the enhancement of the relaxation rate of the excited states of the matter,[6] the interference between light and matter states,[7] or the generation of new hybrid states called polaritons.[8,9] Polaritons can even present coherent dynamics if peculiar conditions are satisfied.[10] Just because of the massive amount of possible phenomena, the materials involved in the light-matter coupling have been indicated as promising in numerous technological fields such as solar cells,[11] low threshold lasers and parametric amplifier production,[12] sensing,[13] imaging,[14] quantum technologies,[15] and others. The study and the engineering of the structure-to-properties relationships in these materials are thus of crucial importance for the realisation of a new generation of smart functional devices.

In this framework, colloidal plexcitonic materials (CPMs) are fascinating systems.[16,17] They are prepared assembling plasmonic nanoparticles and molecules or aggregates of molecules. Coupling strengths in different regimes can be achieved acting on the nanosystems' design; moreover, they are cheap, and easy to prepare, characterize and scale-up.[18] Despite these promising prerogatives, the fundamental aspects of their design, as well as the knowledge of their dynamics in different coupling regimes and, mostly, the understanding of the relationships that exist between structure and dynamics are scarce.

In this PhD thesis, this topic is faced both from a supramolecular perspective, to characterize the assembly of CPMs and their design, and from a spectroscopical point of view, to study the dynamics of plexcitons in different coupling regimes.

The Thesis is organized as follows: Part I introduces the plexcitonic colloidal materials within a historical framework and describing their possible applications. Furthermore, the different phenomena observed in the different coupling regimes will be explained in a solid theoretical frame. In Part II, I will report the protocols for assembling the colloidal plexcitonic materials and the techniques used for their characterization. The dynamical optical properties have been studied mainly using pump and probe and 2-dimensional electronic (2DES) spectroscopies; therefore, the theoretical background and the experimental setups used for these techniques will be furtherly described.

In Part III, all the experimental results and their discussion are reported. Here I described the preparation of two families of plexcitonic materials. The first one is composed of nanospheres and porphyrins and presents two sets of plexcitonic resonances: chapter 11 sifts the experimental conditions to selectively activate them, while chapter 12 broadens the horizons rationalizing the nanospheres templating effects on the porphyrin spatial organisation. Finally, in chapter 13 the dynamics of this family of plexcitonic materials will be analysed with the pump and probe technique. The second family of plexcitonic materials has been prepared by starting from gold nanourchins as plasmonic substrates and several aggregating and non-aggregating dyes. Chapter 14 is focussed on the design of these nanohybrids and in the following chapters 15 and 16 the ultrafast dynamics of the most promising materials in different coupling regimes have been characterized by 2DES.

Lastly, part IV includes a thorough review of the plexcitonic materials already proposed in the literature. This review work has been crucial to extract meaningful information about the plexcitonic materials design.

I Fundamentals of plexcitonics

In this section, the essential concepts about plexcitonics will be discussed. First, I will explain in an intuitive way the light-matter coupling phenomenon. Then, I will give an overview of the historical development of this field and of its main features and potential applications. Successively, the three main regimes of coupling - namely weak, intermediate, and strong - will be described, focussing on the last two, which are the regimes in which plexcitons can be typically observed. Recent efforts on studying plexcitonic dynamics conclude this section.

1.   Light-matter coupling: an intuitive picture

The physicochemical properties of a molecule strongly depend on the environment that it experiences. In particular, these properties can significantly change when the molecular transitions are in resonance with the enhanced electromagnetic field of interacting radiations.[19] Such enhancement of the electromagnetic field can be produced in different ways. For instance, optical cavities enhance the electromagnetic field of those wavelengths that correspond to their cavity modes.[20] This also happens for plasmonic materials, exactly at the wavelengths of their plasmons, which are light-matter dressed states where the electrons oscillate coherently.[21,22] When the resonance between molecular transitions and enhanced radiations occurs, a light-matter coupling is established. This coupling can occur at the single molecule level, with collections of individual molecules (simultaneously) or with aggregates of molecules. Moreover, other quantum objects can also couple with light, such as quantum dots or carbon nanotubes, as reviewed in the next chapter. In general, molecules, aggregates or inorganic excitonic materials coupled with light states are called "Quantum Emitters" (QEs), while the materials that enhance the field of the light are called "cavities".[8,12] In the light-matter coupling jargon, the electronical excited states of the QEs are called "excitons".

Depending on the coupling strength, different regimes and phenomena can occur. For example, in the case of weak coupling, the cavity acts by increasing the density of states of the molecule. This phenomenon, also known as Purcell effect,[5,6,23] in suitable conditions can give rise to higher photoluminescence quantum yield and faster radiative times.

As the coupling strength increases, the coupling regime becomes intermediate. In this case, the electromagnetic field of the cavity interferes destructively with the one of the QEs, generating a dip in the absorption spectrum in correspondence of the QE resonance. This phenomenon, called "Fano interference"[24,25] or "induced transparency", has been found in several situations where a broad distribution of states interferes with a narrow one – in our case, the cavity modes and the molecular transitions, respectively.[7] Fano interferences and Purcell effect are sometimes referred to as weak coupling phenomena, in contrast with the strong coupling described below. However, in this thesis, I will explicitly distinguish between weak and intermediate coupling regimes.

The Strong Coupling (SC) occurs when the dissipation rates of the QE and the cavity get slower than the energy transfer.[8] In this case, their back-and-forth energy exchange, i.e., the coherence, results in the formation of a new quasiparticle called polariton, associated with two new hybrid

light-matter states, called upper and lower polaritons (UP and LP, respectively).[8,9] The frequency splitting of these states is called Rabi splitting Ω_R and it corresponds to the frequency of the energy exchange.[9,10] The definition of the coupling regimes will be critically analysed in chapter 4.

In this thesis, I will focus on a class of light-matter coupled systems, called colloidal plexciton materials, which have the peculiarity to be hosted onto plasmonic nanoparticles synthesised by wet chemistry. Their coupling ranges from the intermediate to the strong regime.

2. Light-matter coupling: a historical point of view

In 1946 E. M. Purcell was the first scientist to hypothesise that the spontaneous emission rate of quantum emitters at radio frequencies could be enhanced by several orders of magnitude if coupled to a suitable cavity.[5] Later, in the late '60, Drexhage first observed experimentally an increase of the emission rate from a layer of dye molecules at nanometer-scale distances from metal films.[26] However, the Purcell effect raised more and more attention after the observation of the surface-enhanced Raman scattering (SERS), a decade later.[27,28]

More or less in the same years, Ugo Fano proposed a theory capable to explain the asymmetric and sharp atomic absorption lines of the Rydberg atom observed by Beutler.[29] In this theory, the asymmetries were a direct consequence of the interference between two processes: the direct ionization of a deep inner-shell electron of the hydrogen atom and the autoionization of two excited electrons followed by the Auger effect. The first paper with the derivation of the line shape expression was published in 1935,[1] during his postdoctoral fellowship in the group of Enrico Fermi. Later, in 1961, he published a much more elaborated work that became one of the most important publications in the physics of the 20th century.[24] Fano's theory can indeed explain numerous experimental results in different fields, ranging from plasmonics[30] to energy transfer[11] and plexcitonics.[16,31] Lately, the investigation of the boundaries between intermediate and strong coupling revealed a grey area challenging the characterization efforts, as further explained in section 4.4.

Theoretical models of SC were developed between 1950 and 1970 by Dicke, Tavis, Jaynes and Cummings.[2–4] The first experimental results arrived only later, in the '80s, among which in 1983 the Haroche's group reported the strong coupling of a collection of Rydberg atoms with a millimetric wave cavity.[32] The important progresses of micro and nanotechnologies in the '90s allowed relevant advances in the field of solid-state nanofabrication, reducing the size of the cavities at the micrometre scale (microcavities) and allowing the preparations of quantum wells.

In this scenario, both inorganic and organic QEs were used. In 1990 the first polariton material formed by an inorganic excitonic part placed within a GaAs quantum wells was reported.[33] However, in this case the coupling strength was low because the excitons in this kind of materials are of the Wannier-Mott type, with a large Bohr radius which induces a low saturation density; furthermore, the electron-hole pairs are typically weakly bound and easily ionize when not kept at very low temperatures.[20,34-36] On the contrary, excitons in organic materials are of the Frenkel type: they have high dipole moments, can reach a high density of molecules and their carriers are more strongly bounded, making them better candidates for light-matter coupling.[37,38] The first examples using organic QEs also appeared in the '80s,[39] with some examples of very high Rabi splitting, until 800 meV[40] or far more.[19] In the class of the organic excitonic materials, J-aggregates are among the most used because of their strong transition dipole moments and narrow bands.[41]

Plexitonics is a parallel line of research where a plasmonic material, such as a plasmonic surface or a plasmonic nanoparticle, plays the role of the cavity in the light-matter coupling. As for the classical cavities, the first works about plexitonic materials made with plasmonic surfaces were published in the '80s.[42-44] Generally speaking, plasmonic surfaces have higher dissipation rates than microcavities.[6,23] Indeed, the plasmonic modes are polaritonic states too, expressed as collective oscillation of electrons, which then dephase and relax within 5-10 fs to generate hot electrons[45-47]. For this reason, the SC with plasmonic cavities should be hampered, but this is widely compensated the small volumes in which the plasmonic resonances, orders of magnitude lower than optical cavities.[23] Hence, the coupling strength between the plasmonic and the excitonic moieties can be considerably high. Furthermore, the broad absorption spectrum of the plasmon, due to the fast damping of the plasmon itself, makes easier the coupling with the dye's transitions. These materials comprehend either intermediate and strong coupled samples because it is not always easy to discriminate between these regimes (section 4.4). Usually, Fano resonances in plexitonic materials are called "Fano plexitons".[11,31]

The first paper on plexitonic materials prepared using suspensions of nanoparticles – i.e. colloidal plexitonic materials – appeared only in 2001, twenty years after the first reports using plasmonic materials.[48] Still, this class of plexitons is particularly interesting because of its good scalability, low costs and easiness of characterization with standard morphological techniques.

Since 2015, polaritonic materials prepared with inorganic excitonic materials started again to attract a strong interest because of the use of new nano-confined materials like carbon nanotubes, graphene and quantum dots.[8,12] Transition Metal Dichalcogenides represent another

interesting class of materials,[8] some of which can act both as cavity and excitonic system when confined in peculiar nanostructures.[49]

Another emerging research line is the study of cavities smaller than the plasmonic suraface. The configuration realized by nanoparticle-dye-mirror (or plasmonic surface) allows to confine the electromagnetic field of the light in the so-called "hotspot" region, i.e., the small space between the nanoparticle and the mirror.[50,51] Here, the electromagnetic field and, consequently, the coupling are greatly enhanced.

3.   Properties and applications of light-matter coupled materials

The intrinsic coherence of plexcitonic and, in general, polaritonic states have been gaining more and more attention in the field of quantum technologies. For instance, a polaritonic quantum computer has been theoretically predicted[15] and some entanglement experiments have been performed with a coupled collection of Rydberg atoms.[52]

In the emerging field of nanophotonics, plasmonic nanoparticles have been used as cavities to enhance the energy transfer among coupled quantum dots[53] and dyes[54] tuned to be donors and acceptors. Moreover, since polaritons belong to the larger family of bosons, they can present macroscopical quantum phenomena such as superfluidity,[55,56] superconductivity,[19,55] and the Bose-Einstein Condensation.[57,58] In particular, Bose-Einstein Condensation is achieved when all the polaritonic quasiparticles are in the same state simultaneously. The photons leakage in these systems, also observed at room temperature, generates lasing (almost) without threshold.[57] For this reason, polaritonic materials raise a high interest even as materials for lasers and parametric amplifiers.[59]

Furthermore, the polaritonic low effective mass reduces the interactions with the surrounding molecular vibrations and should enhance the fluorescence emission intensity. Based on this principle, some polaritonic Organic Light-Emitting Diodes with low voltage were produced.[60] However, their quantum yield is typically below 1%, as also reported in other works.[61,62]

Promising results were achieved with solar cells exploiting Fano plexcitons. Indeed, plasmonic materials are excellent light absorbers, but they cannot efficiently transfer energy, unless they are coupled with dyes, as Nan *et al.* demonstrated.[11]

Some pioneering works showed that plexciton materials could act as sensors for gas, just looking at variations in the Rabi splitting in the presence of an analyte species.[13] Some others reported

applications in the field of imaging, both *in vitro* and *in vivo*.[14,63] Since these measurements rely on the scattering spectrum of the samples, they have the great advantage of overcoming the typical blinking and bleaching of the dyes molecules and the signal does not have to be discriminated from an intense background noise.

As discussed in chapter 1, the cavity in which the dye molecules are set can be seen as an environment that strongly modifies their optical properties, but not only. In fact, the strong light-matter coupling can change the kinetics and the products of a reaction by modifying the energy levels of the involved molecules, as it was demonstrated for a photochromic molecule by Hutchison *et al*.[40] Also, when the molecular vibrations are coupled with these new electronic states, they can be enhanced, similarly to what happens with the SERS effect. This effect will be further discussed later in chapter 16.

These examples expand the horizon of the light-matter coupling research work, demonstrating how much matter properties can be changed and controlled when coupled with light.

4. Theoretical description

This chapter will discuss the theoretical concepts used to define weak, intermediate, and strong coupling regimes, including the Purcell effect, the Fano interferences, and the formation of new polaritonic states. Moreover, the transition from intermediate to strong coupling will be analysed in detail, both from the theorical and the experimental point of view. This will allow better comprehension and discrimination of the two regimes.

4.1 Weak coupling: the Purcell effect

A key concept in the description of the light-matter coupling is the matrix element of the coupling Hamiltonian W_{int}, which, in the Jaynes-Cummings formalism, can be written as:[6]

$$W_{int} = \mu \cdot E_C(r_{QE}) = \hbar g \tag{4.1}$$

where μ is the transition dipole moment of a two-level QE system and $E_C(r_{QE})$ is the electric field of the cavity mode at the QE position. The coupling constant of the interaction, g, also called coupling strength, is proportional to the frequency of the energy transfer between the cavity and the QE.

The quantities k and γ are defined as the decay rate of the cavity in the absence of the QE and of the QE in absence of the cavity, respectively. Even if a more formal treatment will be given later, we can now phenomenologically state that when $k > g$, the lifetime of the cavity is faster

than the coupling strength, so the photon escapes from the cavity before being reabsorbed by the QEs: this is the case of the weak coupling. In this scenario, the Purcell effect takes place, enhancing the emission rate of the QEs. This can be formally demonstrated using the Fermi Golden Rule, whose requirements are well satisfied since the cavity is spectrally much broader than the QE:[6]

$$\gamma_C = \frac{2\pi}{\hbar^2} |W_{if}|^2 D(w),$$ (4.2)

where γ_C is the decay rate of the emitters in the presence of the cavity and $D(w) = 2/\pi k$ is the density of states in resonance, assuming that the cavity mode has a Lorentzian profile with width k. Rewriting equation (4.2) by using equation (4.1) and normalizing by γ, we obtain the Purcell factor P_F:

$$P_F = \frac{\gamma_C}{\gamma} = \frac{4g^2}{k\gamma}.$$ (4.3)

Assuming that all the decay rates but the cavity mode are the same with or without the cavity, then, simply, the total decay rate Γ is:

$$\Gamma = \gamma + \gamma_C = \gamma(1 + P_F)$$ (4.4)

which explains the faster radiative emission of the QE in a cavity.

4.2   Intermediate coupling: Fano interferences

The destructive interference occurring between the level of the QEs and the cavity mode, already defined as Fano interference, can be generalised as the interference between a discrete level and a continuum of states. This phenomenon was first explained by Ugo Fano, that predicted the shape of the scattering cross-section σ in these peculiar conditions:[24,25]

$$\sigma = \frac{(\varepsilon + q)^2}{\varepsilon^2 + 1},$$ (4.5)

where q is a phenomenological shape parameter, ε is the reduced energy defined as $2(E - E_o)/\gamma$, and E_o is the energy of the discrete energy level. This equation has a minimum ($\sigma = 0$) at $\varepsilon = -q$ and a maximum ($\sigma = 1 + q^2$) at $\varepsilon = 1/q$. E_o lies between the maximum and the minimum of the asymmetric profile. When $q \to -\infty$, the resonance frequency of the discrete level coincides with the maximum of σ and the line shape is the typical Lorentzian that describes the inhomogeneous broadening of a QE (figure 4.1, black line). When $q = 1$ (figure 4.1, blue line), E_0 is located exactly at half the distance between the minimum and maximum, resulting in an asymmetric profile. Finally, when $q = 0$, the resonance frequency coincides with the minimum and the Fano resonance shows a symmetrical dip (figure 4.1, red line).
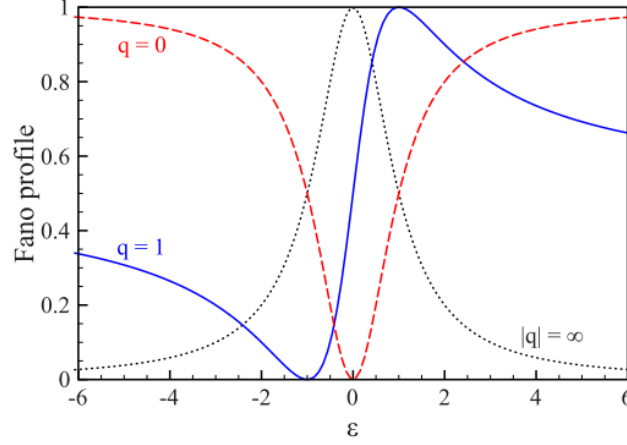
Figure 4.1. Normalized Fano profiles for various values of the asymmetry parameter q. Reprinted from ref.[25]

4.3   Strong coupling: new plexcitonic states arise

In the full quantum mechanical approach, the light-matter interaction can be described as the interplay between a two-level QE system and a quantized field of a cavity.[2-4,9] The QE has an excited state $|e>$, a ground state $|g>$, and a resonance at energy $\hbar\omega_{QE}$; the quantized field, instead, can be expressed with the operator $E_C(r_{QE}) = \xi(a^+ + a^-)$, with a^+ and a^- the creation and annihilation operators of the electromagnetic mode, respectively.[64] We also consider only one mode for the photon energy $\hbar\omega_C$. The Hamiltonian describing the complete coupled system is composed of the unperturbed Hamiltonians of the QE and the cavity and the interaction Hamiltonian: $H = H_C + H_{QE} + H_{int}$. H_{int}, in the rotating wave approximation, can be described with the Jaynes-Cummings Hamiltonian:[4,65]

$$H = \hbar\omega_C a^+ a^- + \hbar\omega_{QE}|e><e| + \hbar g(|g><e|a^+ + |e><g|a^-).$$ (4.6)

Depending on the number n of photons in the cavity, the interaction Hamiltonian couples the states $|g, n+1>$ and $|e, n>$ (in the other cases the eigenvalues of H_{int} are nulls). However, for what concerns the discussion in this thesis, the phenomena observed can be explained considering $n \approx 0$, which means that before the arrival of a second photon, the excited QE has (almost) completely relaxed to the ground state. In this case, neglecting for the moment the losses, the eigenfrequencies are:[65]

$$\omega_\pm = \frac{\omega_C + \omega_{QE}}{2} \pm \sqrt{\frac{\delta^2}{4} + g^2},$$ (4.7)

where $\delta = \omega_C - \omega_{QE}$ is a new parameter called "detuning". In figure 4.2, the new eigenenergies are plotted as a function of δ. The more δ is reduced, the more ω_+ and ω_- move away from the energies of the uncoupled systems. The energy difference between the new eigenstates at zero detuning is called Rabi splitting, Ω_R and is equal to twice the coupling strength g.
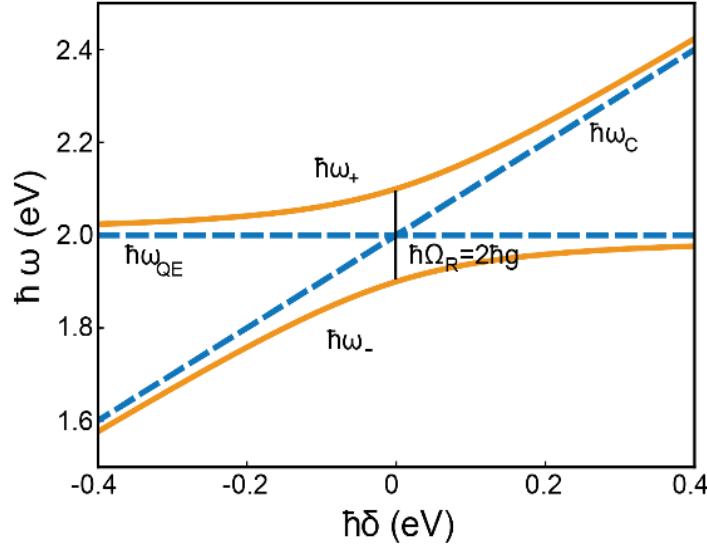
Figure 4.2. Eigenenergies $\hbar\omega_+$ and $\hbar\omega_-$ of the coupled system plotted as a function of the detuning (orange lines). The blue dotted lines represent the energies of the uncoupled cavity and QE.[66]

One might ask why, if we supposed $n \approx 0$, the coupling is still different from zero. This is because the vacuum fluctuations of the electric field are non-vanishing since their expectation value depends on the squared electric field:

$$< 0|E^2|0 >=< 0|\xi(a^+ + a^-)^2|0 >= |\xi|^2. \tag{4.8}$$

This parameter is also called the *vacuum electric field*.[9] We also know that the vacuum energy is restricted to a specific volume V, also called "effective volume", and that the total energy within this value is $\hbar\omega_C/2$. Assuming that both electric and magnetic fields contribute equally to the energy, this means that:[67]

$$\varepsilon\varepsilon_0|\xi|^2 V = \frac{\hbar\omega_C}{2}. \tag{4.9}$$

By introducing equation (4.9) in equation (4.1), we obtain:

$$\hbar g = \mu\xi = \mu\sqrt{\frac{\hbar\omega_C}{2\varepsilon\varepsilon_0 V}}. \tag{4.10}$$

This expression formally explains why plasmonic materials, despite their huge losses, can often generate Rabi splittings in the same order of magnitude or stronger than traditional optical cavities. The plasmonic effective volume, indeed, is orders of magnitude smaller than the optical cavities one.[6,23] However, the effective volume described as such, does not keep into account the plasmonic losses, which cannot be neglected. For this reason, it is recognized that this definition is not completely accurate and nowadays there is still an open and vibrant debate about possible more reliable definitions.[6]

The eigenstates derived from equation (4.6) are:

$$|+> = sin\,(\theta_0)|g,1> + cos\,(\theta_0)\,|e,0>; \tag{4.11a}$$

$$|-> = cos\,(\theta_0)|g,1> - sin\,(\theta_0)\,|e,0>; \tag{4.11b}$$

corresponding to ω_+ and ω_-, respectively.[64] In equations (4.11) we define:

$$sin\,(\theta_0) \;=\; \frac{2g}{\sqrt{(R_0 - \delta)^2 + 4g^2}}; \tag{4.12a}$$

$$cos\,(\theta_0) \;=\; \frac{R_0 - \delta}{\sqrt{(R_0 - \delta)^2 + 4g^2}}; \tag{4.12b}$$

$$R_0 = \sqrt{\delta^2 + 4g^2}. \tag{4.12c}$$

In the special case of $\delta = 0$, it is verified that:

$$|+> = \frac{1}{\sqrt{2}}(|g,1> + |e,0>); \tag{4.13a}$$

$$|-> = \frac{1}{\sqrt{2}}(|g,1> - |e,0>). \tag{4.13b}$$

Since the excitation is distributed equally among the parts, it is no more possible to treat the cavity and the QE independently, and |+> and |−> become new states with new properties. The time evolution for such system is given by:[9]

$$|\Psi(t)> = cos\left(\frac{\Omega_R t}{2}\right)\Big|g,1> - isin\left(\frac{\Omega_R t}{2}\right)\Big|e,0>. \tag{4.14}$$

This allows calculating directly the probability $P_e(t)$ to find the QE in the excited state $|e>$, and the probability $P_g(t)$ to find the photon in the cavity:

$$P_e \;=\; |<e,0|\Psi(t)>|^2 = \frac{1 + cos\,(\Omega_R t)}{2}\;; \tag{4.15a}$$

$$P_g = |<g,1|\Psi(t)>|^2 = \frac{1 - cos\,(\Omega_R t)}{2}. \tag{4.15b}$$

From these results, plotted in figure 4.3, it is clear that the cavity and the QE exchange the photon (coherence) with a frequency that is exactly the Rabi splitting frequency.
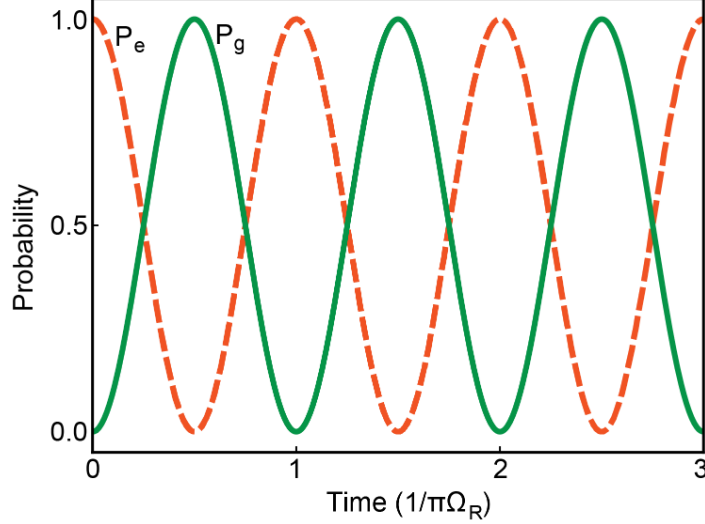
Figure 4.3. Occupancy probabilities P_e and P_g as a function of time. Reprinted from ref.[66]

However, the losses of the QE and especially the ones of the plasmonic cavity have to be considered. We then introduce complex frequency to account for them:

$$\omega'_C = \omega_C - ik; \tag{4.16a}$$

$$\omega'_{QE} = \omega_{QE} - i\gamma. \tag{4.16b}$$

Introducing equations (4.16) in equation (4.6), the complex eigenfrequencies $\omega_\pm$ of the diagonalized non-Hermitian Hamiltonian are:[8]

$$\omega'_\pm = \frac{\omega_C + \omega_{QE}}{2} - \frac{i}{2}(\gamma + k) + \frac{1}{2}\sqrt{4g^2 + (\delta - i(\gamma - k))^2}. \tag{4.17}$$

From this equation we calculate the Rabi splitting in the condition of zero detuning:

$$\Omega_R = R[\omega'_+] - R[\omega'_-] = \sqrt{4g^2 - (\gamma - k)^2}. \tag{4.18}$$

This result is rather different than what was previously stated: Ω_R is no more equal to $2g$ when losses are kept into account. These losses also concur to the dephasing of the coherence, for which equations (4.15a-b) can be rewritten by adding an extra exponential decay which damps the energy exchange until the probability reaches zero (or one if the photon is absorbed).

Finally, the light-matter coupling can occur not only at the single QE level, but also when many QEs are coupled to the same cavity. Actually, this is the most common experimental case since the effective volume of the cavities, even the smallest ones (for instance, the nanogaps previously presented) are large enough to host more than one QE. Moreover, the nanofabrication of plexcitonic samples is not yet refined enough to couple a single QE to each cavity.[23] In this framework, the Hamiltonian must be generalized to consider all the possible interactions among N QEs and the cavity. The Dicke or Tavis-Cummings Hamiltonian is thus defined:[2,4,68]

$$H = \hbar\omega_C a^+ a^- + \sum_{s=1}^{N} \hbar\omega_{QE} |e>_s < e|_s + \sum_{s=1}^{N} \hbar g (|g>_s < e|_s a^+ + |e>_s < g|_s a^-),$$

(4.19)

where $|g>_s$ and $|e>_s$ are the ground and the excited states of the s-th emitters. In the case of a few excitations in the system, this Hamiltonian can be simplified considering all the s-th emitters as a single giant oscillator with b^+ and b^- its creation and annihilation operators:

$$H = \hbar\omega_C a^+ a^- + \hbar\omega_{QE} b^+ b^- + \hbar g (b^- a^+ + b^+ a^-).$$

(4.20)

Considering again the simplest situation when $n \approx 0$, among the new $N + 1$ eigenstates, two of them are bright and, in the case of zero losses, the corresponding eigenfrequencies are:[69]

$$\omega_{\pm} = \frac{\omega_C + \omega_{QE}}{2} \pm \sqrt{\frac{\delta^2}{4} + N g_s^2},$$

(4.21)

where g_s is the coupling strength of the single QE. The other $N - 1$ eigenstates are dark states (figure 4.4b). Equation (4.21) is similar to (4.7), but the total coupling strength g is now increased by a factor $\sqrt{N}$, implying that the excitation is shared among the cavity and the whole N coupled QEs. In this situation, the overall coupling strength strongly depends on N. Moreover, the losses of the QEs and the cavity can be made explicit in equation (4.21), resulting in expressions equivalent to equations (4.17) and (4.18), where now $g = \sqrt{N} g_s$.
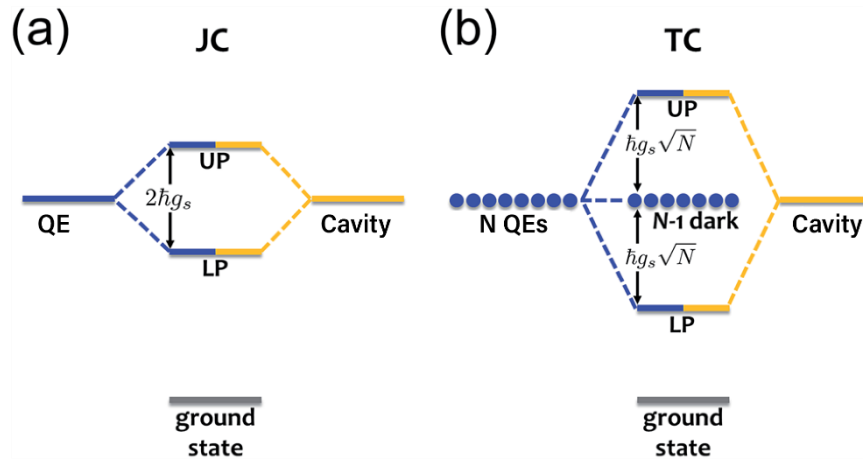
Figure 4.4. Comparison between a) Jaynes-Cumming (JC) and b) Tavis-Cumming or Dicke (TC) models. While JC model considers the coupling between a single QE and the cavity mode, TC includes N QEs states.

4.4 The fine line between Intermediate and Strong Coupling regimes

Weak coupling does not strongly modify the cavity and QE properties because it only enhances and speeds up the emission, while the energy levels of the different moieties remain the same. This situation is rather easy to identify from the other cases in which the coupling is stronger. Fano interferences and polaritons states, indeed, are generated when significant interactions between the QEs and the cavity are established, which significantly change the physicochemical properties of the system. Both phenomena are manifested with very similar features in the experimental extinction spectra of the coupled systems, i.e., the appearance of the dip in the spectrum at the frequency of the uncoupled QE. For this reason, their discrimination is rather challenging.

Theoretically speaking, the problem can be solved by studying the condition of existence of the polaritons (CE) and the SC conditions.[9,10] CE considers that the square root element of the equation for the new eigenfrequencies $\omega_\pm$ (equation 4.17) must be positive. In case of zero detuning, it turns out that:

$$|2g| > |k - \gamma|. \tag{4.22}$$

This condition is necessary but not sufficient because the new states need to be resolved one from the other. This happens when:

$$\Omega_R^2 > \frac{\gamma^2 + k^2}{2}, \tag{4.23}$$

which is the so-called SC condition. When this condition is fulfilled, QE(s) and cavity exchange coherently the energy. Considering these two conditions, the samples that do not satisfy

equation (4.22), and still present a minimum at the QE transition frequency, are in the intermediate regime. The samples that instead fulfil equation (23) possess true coherent polaritonic states. Several papers investigated the "grey area" at the boundaries of the two regimes, studying samples that satisfy equation (4.22) but not equation (4.23): it has been reported that the transition from intermediate to strong coupling is progressive.[7,70,71] Moreover, Stete *et al.* demonstrated that the typical plexcitonic splitting can occur even before the strong coupling regime is established because the vacuum fluctuations can saturate the QE optical transition.[72]

The difficulties in the experimental characterization contribute to the complexity of this scenario. The extinction spectrum cannot be fully helpful in the deep understanding of the nature of light-matter coupling. Also, in the scattering and extinction spectra, the weight of the QE and the cavity contributions is unbalanced towards the cavity.[73] Thus, pure absorption spectra have been proposed as a more reliable starting point to calculate Ω_R. However, the determination of the absorption cross-sections of single nanostructures is challenging and requires specialized techniques.[7] For this reason, only 2 over 100 papers about colloidal plexcitonic materials report their pure absorption spectra (for further information about these materials, see part IV). The study of the polaritonic luminescence is more often reported (see for instance ref.[54,74-77]). It has been demonstrated that for strongly coupled samples the luminescence spectrum presents two peaks, while in the intermediate regime, only one peak is measured at the minimum of the dip (figure 4.5).[7] However, the quantum yield of polaritons is typically very low, below 1%, and not all the samples are luminescent.[7,78]

In the most recent years, 2-Dimensional Electronic Spectroscopy (2DES) emerged as a particularly powerful tool to verify the presence of strong coupling and characterize the relaxation mechanisms in these challenging samples, including the possible presence of coherent dynamic phenomena (see part II).[79]
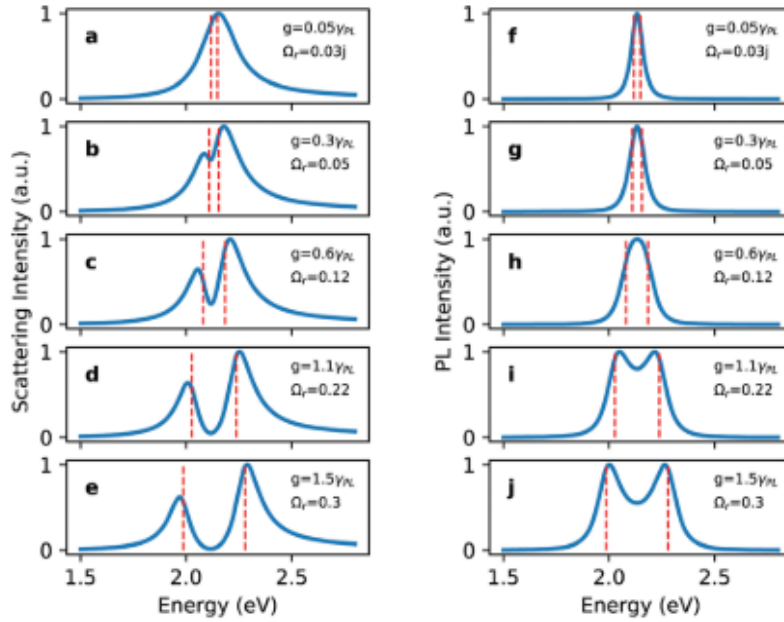
Figure 4.5. Scattering and photoluminescence (PL) spectra calculated for a sample with increasing *g*. As the coupling increases, the single signal initially present splits into two peaks. In the scattering spectra the splitting can be resolved even in the intermediate regime, whereas in the PL spectra it appears only in strong coupling conditions. Reprinted from ref.[7]

5.   Plexcitons and polaritons dynamics: a brief overview

One of the most interesting features of plexcitons, and, generally speaking, of polaritons, is their coherent dynamic properties. A pre-requisite to observe coherent dynamics is that the SC conditions (section 4.4) are satisfied, as reported in some computational study.[80] Coherent phenomena were already measured in the infrared region for polaritonic samples composed of QEs and microcavities.[81,82] Contrarywise, resolving coherences among plexcitonic states is a challenging task, yet not fully achieved in the literature. Indeed, the electronic states from which plexcitons arise have high dissipation rates and, consequently, high $\hbar\Omega_R$ values are required to fulfil the SC conditions. This, in turn, requires a very demanding time resolution, below 10 fs, to capture the oscillations typically associated with coherent superpositions of states. The number of studies devoted to investigating plexcitonic dynamics in the time domain of 10-100 fs is scarce.[83–85] Vasa et al. have already reported evidence of plexcitonic coherence by using pump and probe spectroscopy.[86] However, complete comprehension and characterization of quantum coherences cannot be reached by mono-dimensional spectroscopies because population decay and coherence signals cannot be resolved one from the other. 2-Dimensional Electronic Spectroscopy (2DES) overcomes this problem by decongesting the final optical response within 2D maps that correlate excitation ω_1 and emission ω_3 energies (instead of mono-dimensional maps) as a function of the delay time t_2 (chapter 10). [87,88]

The polaritons' dynamics for timescale above 100 fs are much more studied, and the debate about the interpretation of the various dynamic phenomena is particularly vibrant. Generally, it is expected that UP relaxes fast to dark uncoupled excitonic states,[69] which, in turn, populate LP through electron-electron scattering and emission (or absorption) of molecular vibrational quanta.[69,89,90] However, the exceptions to this picture are numerous because of the vast variability of QEs and cavities, the significant amount of variables for the assembly of the nanohybrids, as well as the experimental parameters. For instance, several authors reported polaritons' lifetimes in the order of magnitude of 1-10 ps,[86,91-95] with a UP dynamics faster than the LP, as a result of a non-markovian regime[96] and the influence of the dark and uncoupled excitons.[69] Not all the experimental works, however, agree with this general evidence.[97]

In some paper, the samples were excited at energies higher than the polaritons (off-resonance excitation).[58,95,98-103] In this scenario, hot carriers and uncoupled excitons must be considered too. However, the timescale of these dynamics does not change sensitively from the on-resonance excitation, or it is just slightly shortened (0.1-10 ps). Conversely, increasing pump fluences reduces the coupling, shortens tremendously the overall dynamics, and reduces the Rabi splitting of the polaritons.[56,57,86,99] Sometimes, high pump fluences reveal Bose-Einstein Condensation short lifetimes that prevail over the longer ones of the uncoupled exciton (see for example ref.[56,57,69]). To our knowledge, there are just a few examples that differ from this picture: Schwartz et al.[104] did not find any of these variations as a function of the pump fluence. Furthermore, anthracene-based microcavities do not support any evidence of reduced coupling,[98] suggesting a huge molecular density and an efficient bimolecular annihilation, which inhibits the build-up of a crowded reservoir of exciton population.[99]

Moreover, there are some issues rather unexplored. For instance, vibrational-assisted relaxation mechanisms were scarcely investigated.[94,101] They cannot be easily resolved by standard 1D time-resolved techniques, and more often they are detected by Raman spectroscopy,[105,106] which, however, cannot reveal the process to whom they are associated, requiring complementary experiments such as stationary and time-resolved fluorescence.[74,89,90,107] 2DES is instead a valuable technique to resolve the vibrations and analyse their contribution to the overall dynamics. Another underexplored topic is the dynamics of hybrids in the intermediate regime and the Fano plexcitons. Although computational results report dynamics slower than polaritons,[108] experimental works found lifetimes in the same order of magnitude.[11,16,109] Balci et al., indeed, observed that the transition from strong to weaker coupling regimes is accompanied by

shortened lifetimes that, however, remain in the same order of magnitude.[93] Furthermore, Fano plexcitons seem to possess the same pump fluence dependence of the polaritons.[109]

Considering the lack of literature and experimental evidence, it is not possible to establish if the differences in the fs dynamics of polaritons in the strong or intermediate coupling regime influence the subsequent relaxation pathways. However, if this was true, it would explain the baffling variability discussed so far.

II Materials preparation and characterization techniques

Here, I will give some technical information about the experimental results of part III. First, I will describe the synthesis and the characterization of three different gold nanoparticles, namely, the "big" and the "small" nanospheres and the nanourchins. Then, I will report on the assembly of different nanohybrids. Finally, different characterization techniques will be described, with a particular focus on the pump and probe technique and the on the two-dimensional electronic spectroscopy (2DES).

6.   Materials preparation

All the solvents and reactants were obtained from Sigma-Aldrich (Merck KGaA, Darmstadt, Germany) and used as received without further purification. The 8-trimethylammonium octylthiol (TMAOt) capping molecule was synthesized following the procedure described in ref [110]. The 4,4′,4″,4‴-(Porphine-5,10,15,20-tetrayl) tetrakis(benzenesulfonic acid) was bought by PorphyChem. Cy75 and TDBC were purchased from Few Chemicals; Styryl 9M and Rhodamine B from Lambda Physik, Rhodamine 640 from Exciton. The other dyes were obtained from Sigma-Aldrich (Merck KGaA, Darmstadt, Germany). Also in this case the dyes were used as received without further purification.

6.1   Synthesis and characterization of gold "big" TMAOt-nanospheres (BNSs)

Synthetic procedure. Citrate capped gold "big" nanospheres were prepared according a reported procedure with small modifications.[111] Typically, 1.65 mL of sodium citrate (510 mM), 250 µL of silver nitrate (10 mM) and 500 µL of tetrachloroauric acid (253 mM) were sequentially added to 5.6 mL of water, under vigorous stirring. The resulting solution was further stirred for 5 min. During this time, the color changed from the initial yellow to green. The solution was then quickly added to 117 mL of boiling water. The resulting suspension was kept boiling for 1 h (using a condenser to avoid evaporation), becoming wine-red after a few seconds. The citrate-capped nanoparticles suspension was then allowed to cool down to room temperature. Subsequently, 2 mL of the 8-trimethylammonium octylthiol solution (33mM) were added and the solution was allowed to react overnight under stirring. The solution was filtered by a 0.2 μm syringe filter to remove large aggregates and then concentrated and resuspended in water five times using a centrifuge tube equipped with a 100 kDa cutoff filter (Amicon® - Ultra, previously rinsed three times with 1:1 EtOH:water), to eliminate the citrate impurities.

Characterization. Figure 6.1a shows a TEM image relative to a BNSs sample. The average diameter is 11±2 nm (300 measurements). I do not expect that the polydispersity of NSs significantly affects the optical proprieties of the nanohybrids. Indeed, the electronic properties of the plasmon and the curvature radius of the particle do not vary significantly for NSs with diameters in the range 9-13 nm.[21] TGA analysis of a sample of TMAOt-BNSs under air atmosphere is shown in figure 6.1b.

The average formula, calculated based on TEM diameter and TGA analysis using a spherical approximation for the gold core and a density of 59 gold atoms per nm^3, is $Au_{30891}(TMAOt)_{2426}$.

According to this formula, for convenience, the nanosphere concentration has been converted into concentration of TMAOt units grafted on their surface by multiplying by 2426.
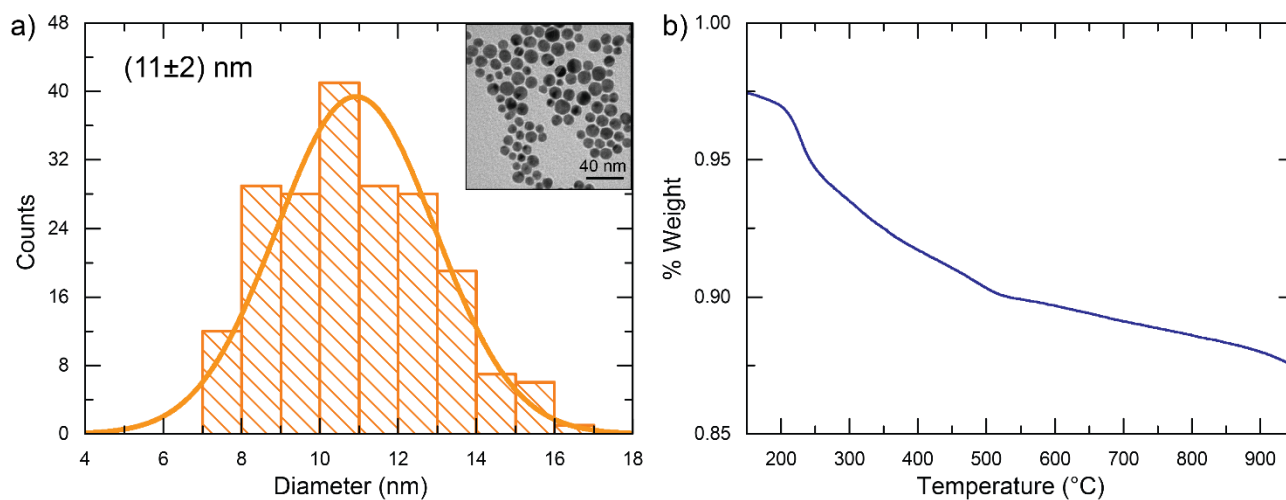
Figure 6.1. a) TEM histogram of the BNSs diameter measured. In the inset, a TEM image. The average diameter is reported in the image and the error bars correspond to the half width at half maximum of the size distribution; b) TGA analysis of a sample of BNSs under air atmosphere.

NMR analysis (figure 6.2) was used to verify the formation of the thiol monolayer, as proved by the massive broadening of all the thiol signals.

Figure 6.2. 1H-NMR (500 MHz) spectra of the nanoparticles with 8-trimethylammonium octylthiol in D_2O (upper spectrum) and of 8-trimethylammonium octylthioacetate bromide in MeOD (lower spectrum). The upper spectrum reveals only very broad signals in the same chemical shift regions typical of the coating thiol (1.0-2.0 ppm and 2.5-3.5 ppm). Other signals arise from isotopic impurities of the solvent and traces of other contaminants. This confirms the grafting of the thiol to the nanoparticles (the broadening results from the reduced tumbling rate and mobility of the thiols due to the grafting to the nanoparticles) and their effective purification (no major free organic species are present in the spectrum).

6.2 Synthesis and characterization of gold "small" TMAOt-nanospheres (SNSs)

Synthetic procedure. "Small" gold nanoparticles were prepared according to a previously reported two-step procedure.[112] Glassware in contact with gold nanoparticles was washed with aqua regia before and after its use and rinsed with distilled water.

A solution of HAuCl$_4$·3H$_2$O (50 mg, 0.127 mmol, 1 equiv) in water (2 mL) was extracted with a solution of tetraoctylammonium bromide (0.175 g, 0.318 mmol, 2.5 equiv) in N$_2$-purged toluene (125 mL). Dioctylamine (0.613 g, 2.539 mmol, 20 equiv) was added to the resulting reddish-orange organic solution (the amount of dioctylamine was calculated in order to obtain 2 nm nanoparticles).[112] The mixture was vigorously stirred under N$_2$ for 3,5 hours. During this period of time, the colour of the mixture faded. Then the solution was cooled at 0°C and a NaBH$_4$ solution (47.0 mg, 1.257 mmol, 10 equiv) in H$_2$O (0.5 mL) was rapidly added. The color of the solution turned rapidly to black and after 1.5 hours of stirring at 0°C, the aqueous layer was removed. To the obtained nanoparticle solution, the thiol (0.123 mmol, 1 equiv) dissolved in 2 mL of MeOH was rapidly added. The reaction mixture was stirred overnight at 0°C. All the formed SNSs were insoluble in toluene, hence the solvent of the reaction was poured out and the sample was rinsed 3 times with toluene. The resulting crude solid, was resuspended and pelleted four times by centrifugation, using MeOH and toluene. The resulting SNSs were finally dissolved in water and purified by gel permeation chromatography with Sephadex G-25.
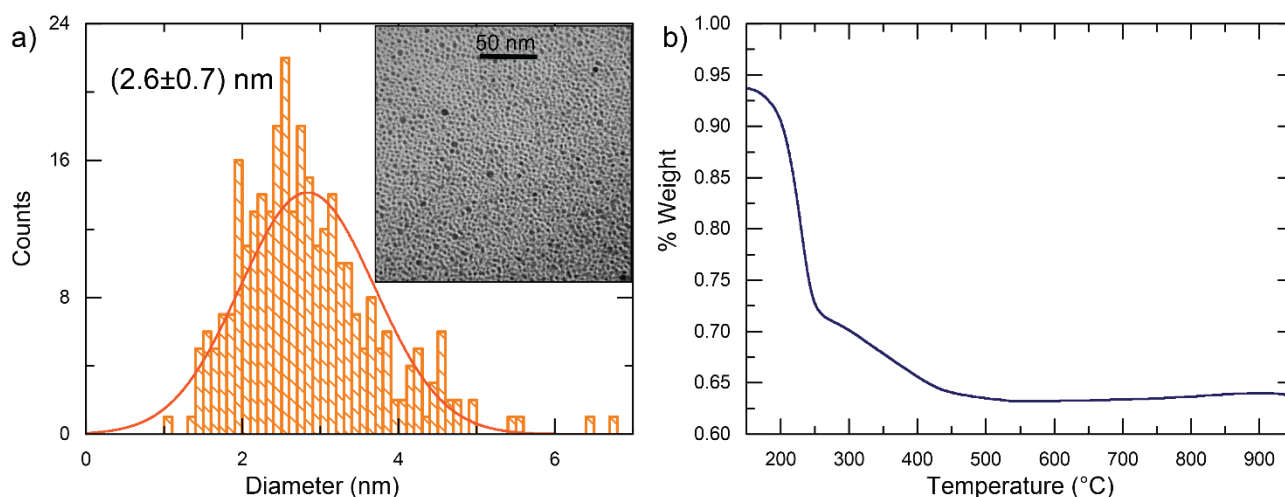
Figure 6.3. a) TEM histogram of the SNSs diameter measured. In the inset, a TEM image. The average diameter is reported in the image and the error bars correspond to the half width at half maximum of the size distribution; b) TGA analysis of a sample of SNSs under air atmosphere.

Characterization. The average diameter of SNSs, retrieved with TEM images analyses, is 2.6±0.7 nm (300 measurements, figure 6.3a). TGA analysis of a sample of TMAOt-SNSs under air

atmosphere is shown in figure 6.3b. The formula, calculated based on TEM diameter and TGA analysis, is $Au_{566}(TMAOt)_{241}$. NMR analysis (figure 6.4) was used to verify the formation of the thiol monolayer, as proved by the broadening of all signals. The extinction of figure 11.2b confirms the presence of a weak plasmon due to the nucleation and growth of the nanoparticles. The SNSs concentration has been converted into TMAOt units grafted on their surface by multiplying by 241.

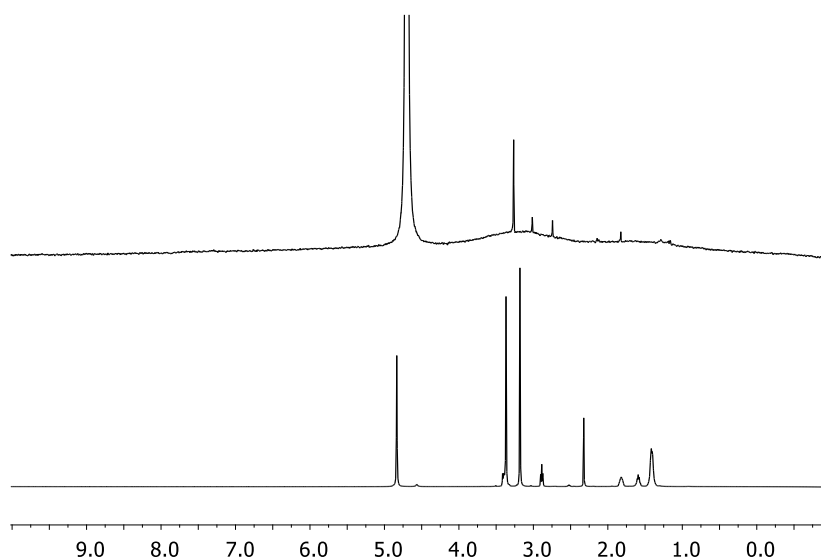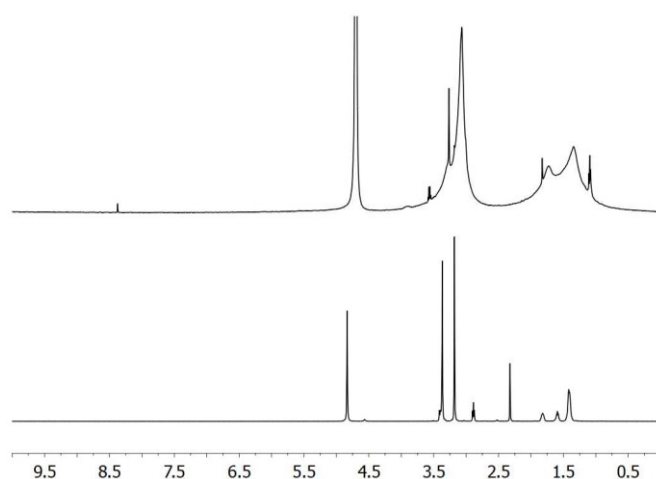Figure 6.4. 1H-NMR (500 MHz) spectra of SNSs with 8-trimethylammonium octylthiol in D_2O (upper spectrum) and of 8-trimethylammonium octylthioacetate bromide in MeOD (lower spectrum). As for BNSs, the upper spectrum reveals only very broad signals in the same chemical shift regions typical of the coating thiol (1.0-2.0 ppm and 2.5-3.5 ppm). This confirms the grafting of the thiol to the nanoparticles and their effective purification.

6.3 Synthesis and characterization of gold nanourchins (NUs) capped with different capping layers

Synthetic procedure. Gold nanourchins (NUs) of different sizes were synthesized by using a modified two step literature procedure.[113] The first step consisted of the preparation of the gold seeds. A $HAuCl_4 \cdot 3(H_2O)$ stock solution (253.9 mM) was centrifuged for 1 h to remove the clusters (15000 rpm). 30 mL of ultrapure water and 28.69 μL of the gold solution were poured into a 100 mL round bottomed flask equipped with a condenser. The temperature was set to 100°C under stirring. As soon as the solution boiled, 900 μL of a 10% m/V citrate solution were added and the color turned to red. After 10 minutes, the heating was removed and the solution was left to cool under stirring. This seed solution has an estimated concentration of 0.046 mg/mL and must be used within the day. The second step was the growth of NUs from the seeds. An aliquot of the gold seeds solution was added to 9.5 mL of MilliQ water in a 20 mL scintillation vial under stirring. 15 μL of the $HAuCl_4 \cdot 3(H_2O)$ stock solution, 22 μL of the citrate solution and 1 mL of hydroquinone solution (30 mM) were added to a scintillation vial in this order. After the addition of the

hydroquinone addition, the solution changed color from light blue to dark purple as a function of the amount of seeds solution previously added. The solution was left at room temperature for 30 minutes under stirring and then used for further functionalization.

SOt molecules synthesis and characterization. 8-sulfonate-octylthiol (SOt) was prepared according to the following scheme:
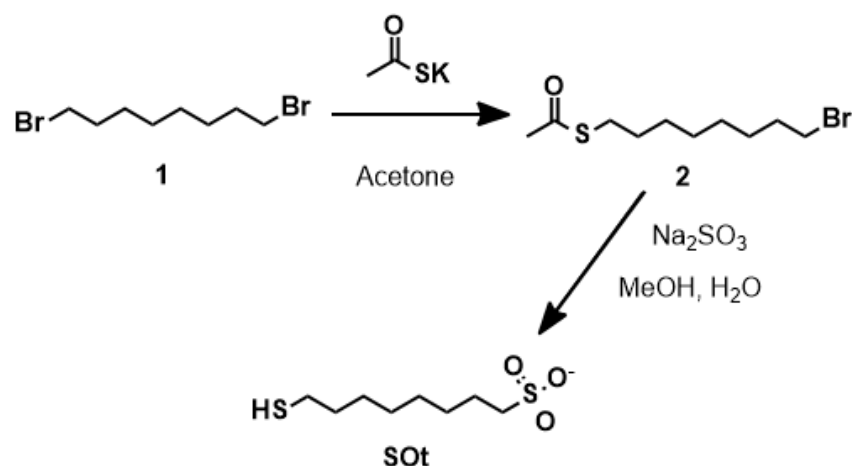
Scheme 6.1. SOt synthetic scheme.

Synthesis of 8-thioacetyl-1-bromo-octane (2). 1,8-dibromoctane **1** (1 mL, 5.43 mmol) was dissolved in acetone (15 mL). Potassium thioacetate was added (443 mg, 3.88 mmol) and the resulting mixture was kept at 35°C overnight. After evaporation of the solvent, the yellowish solid was dissolved with CH_2Cl_2 and extracted with water (3 x 40 mL). The organic phase was dried with $MgSO_4$. After solvent evaporation, the crude product was purified by flash chromatography (silica gel, eluent: petroleum ether: CH_2Cl_2 3:2 , rf= 0.62). 602.5 g (41%) of **2** were obtained as a yellowish oil. 1H-NMR ($CDCl_3$, 500 MHz), d: 3.32 (t, 8Hz, 2H), 2.78 (t, 8Hz, 2H), 2.24 (s, 3H), 1.77 (qn, 8 Hz, 2H), 1.48 (qn, 8Hz, 2H), 1.24 (br, 8H).

Synthesis of 8-merapto-1-sulfonate octane (SOt). (251.1 mg, 0.936 mmol) Na_2SO_3 (281 mg, 2.23 mmol) and benzyl trimethyl ammonium bromide (10 mg, 0.035 mmol) were added in a 10 mL round flask. Successively, 4.5 mL of MilliQ water and 2 mL of MeOH were poured into. The resulting mixture was kept at 95°C under reflux overnight. The solution was evaporated adding CH_2Cl_2 and EtOH to remove water without producing bubbles. We washed the crude mixture with diethyl ether to remove the traces of **2**. Flash chromatography (silica gel, eluent: CH_2Cl_2:MeOH 7:3) was used for further purification. 133.5 mg (63%) of **SOt** were obtained as a white powder. 1H-NMR (MeOD, 500 MHz), d: 2.80 (t 4.5 Hz, 2H,), 2.51 (t, 7 Hz, 2H), 1.80 (m, 2H), 1.60 (m, 2H), 1.34

(m, 8H). 13C-NMR(MeOD, 500 MHz), d: 52.3, 33.8, 28.9, 28.5, 28.3, 27.9, 24.5, 23.5. ESI-MS (negative): (MeOH, [M]$^-$): 224 m/z.

NUs functionalization with TMAOt and SOt. NUs batches were centrifuged for 8 minutes at 5000 rpm and the supernatant was removed to eliminate most of the citrate and hydroquinone molecules free in solution. NUs were successively redispersed in 1 mL ultrapure water and sonicated for 10'. SOt molecules were added in a 100:1 SOt:NUs ratio (we considered NUs as spheres of 100 nm diameter with a thiol footprint of 0.15 nm^{-2}). They were incubated for 90' and successively purified twice from the impurities. Each purification step consisted of centrifugation (3', 10000 rpm), removal of the supernatant, redispersion in 1 mL of ultrapure water. NUs capped with TMAOt (TMAOt-NUs) were prepared with a similar procedure. Pristine NUs batches were centrifuged (10', 5000 rpm) and redispersed in 1 mL of 5 mM solution of NaNO$_3$ to prevent tips etching due to the joint action of trimethyl ammonium residues and bromide anions.[114] TMAOt molecules were added in 800000:1 TMAOt:NUs ratio. They were incubated overnight and successively purified from the impurities three times with the same protocol of SOt-NUs.

6.4   Assembly of nanohybrids

Assembly of the NS-TPPS nanohybrids (chapter 11). To prepare the NS-TPPS hybrids with different Porphyrin-per-Particle ratios (PPP ratio), suitable volumes of MilliQ water (pH=2.2, HCl) and of a concentrated BNSs solution (5 mM) were added in this order to a 1 mM solution of H$_2$-TPPS^{2-} at pH 3.2. Table 6.1 reports the exact volumes used to prepare NS-TPPS_100, NS-TPPS_1040 and NS-TPPS_5200 samples (the number that labels each sample corresponds to the PPP ratio). The PPP values for these samples have been selected as relevant examples because they allow exploring all the possible coupling regimes achievable in these systems, as further explained in chapter 11.

Table 6.1. Volumes used for the preparation of the nanohybrids samples.

	MilliQ water, µL	BNSs (5 mM), µL	H$_2$-TPPS^{2-} (1 mM), µL
NS-TPPS_5200	995	1	4
NS-TPPS_1040	998	1	1
NS-TPPS_100	994	6	0.5

The resulting solution was gently shaken to obtain a homogeneous solution and allowed to rest for a night. The final pH is 2.2.

For the samples of Figure 11.2d, MilliQ water (pH=2.2, H_2SO_4), a concentrated NSs solution (5 mM) and a 1 mM solution of TPPS (pH=7) were used. In particular, the sample represented by the purple curve was prepared with the same volumes used for the NS-TPPS_1040 and the sample represented by the pink curve with the same volumes of NS-TPPS_5200. In this latter, MilliQ water was 1M in Na_2SO_4, in order to promote the aggregation of H_2-TPPS^{2-}.

The absorption and PL spectra were recorded the day after the synthesis in order to allow the coupling among NSs and H_2-TPPS^{2-} to be complete. The NS-TPPS_1040 photoluminescence (PL) spectra were recorded after three washing steps, each one consists of (i) centrifugation at 10000 rpm for 10', (ii) removal of the supernatant, (iii) addition of MilliQ water at pH=2.2 and, finally, (iv) sonication for 20'.

Assembly of the BNSs- and SNS-TPPS nanosystems (chapter 12). To prepare the NSs-porphyrin hybrid samples in acidic (basic) conditions, suitable volumes of MilliQ water at pH=2.2, HCl (pH=11, NaOH) and of a 5mM NSs solution were added in this order to a 1 mM solution of H_2-TPPS^{2-} at pH 3.2 (TPPS^{4-} at pH 11). Table 6.2 reports the exact volumes used to prepare them.

Table 6.2. Volumes used for the preparation of the nanohybrids samples. I omitted the part of the acronym regarding the pH because the volumes do not change as a function of it.

	MilliQ water, μL	NSs (5 mM), μL	TPPS (1 mM), μL
BNSs, PAP=0.35	998	1	1
BNSs, PAP=3.5	994	6	0.5
SNSs, PAP=0.35	998	0.5	1
SNSs, PAP=3.5	996	2.5	1

All the absorption and emission spectra were measured the day after the synthesis of the samples to allow the system to react completely. The samples were sonicated before the measurements for 15'. All the Dynamic Light Scattering (DLS) measurements were measured 1h after the synthesis to avoid strong aggregation and precipitation.

Assembly of NUs nanohybrids (chapter 14). Typically, 100 μL of a 1 mM solution of dye were added to 500 μL of a solution of NUs with plasmon peak extinction equal to 1, corresponding to a concentration of about 1.5 μg/mL. Only in the case of PIC, 1 μL of supersaturated solution of PIC in EtOH was added to 500 μL of NUs solution. The mixture was incubated overnight and then

purified to remove the excess of dye. The purification protocol consisted of centrifugation (5', 7500 rpm), removal of the supernatant and redispersion in MilliQ water (0.4 mL).

Reproducibility of nanohybrids. Each nanohybrid sample was prepared at least three times and analysed at the UV-Vis spectrophotometer. These analyses confirmed the reproducibility of the coupling and the main optical properties of the nanohybrids prepared in the same conditions.

7. Standard Techniques for the NPs characterization

TEM analysis was performed with a Jeol 300 PX electron microscope and the collected images were analysed with ImageJ software.

Thermogravimetric analysis (TGA) was run on 1 mg nanoparticle samples using a Q5000 IR model TA. The measurement was set to reach 100°C and to keep this temperature for 10', in order to remove completely the water traces, and then to 1000 °C under a continuous air flow.

NMR spectra were recorded using a Bruker AV III 500 spectrometer operating at 500 MHz for 1H. Chemical shifts are reported relatively to the internal standard Me4Si. Multiplicity is given as follow: s = singlet, d = doublet, t = triplet, q = quartet, qn = quintet, m = multiplet, br = broad peak.

ESI-MS mass spectra were obtained with an Agilent Technologies LC/MSD Trap SL mass spectrometer.

A Zetasizer Nano ZS was used for DLS measurements. The instrument was equipped with a 633 nm laser and a detector in configuration NIBS (non-invasive backscatter system – 173°). The temperature was kept at 25°C during the measurement and 0.197 was used as the refractive index of the NPs. Zetasizer software was used to analyse the data.

8.   Standard Techniques of optical spectroscopy

Extinction spectra were recorded with a Cary 5000 spectrophotometer, while a Jobyn Yvone FluoroMax 3 was employed for PL measurements. All the PL spectra have been recorded using a KV550 longpass filter (Newport®) before the detector to remove the unwanted contribution of scattered light below 550 nm. This filter was added between the sample and the detector.

9.   Pump and Probe technique

The pump and probe technique can give information about the relaxation dynamics of the electronic excited states in the time domain between about 100 fs and 1 ns. For this reason and for its highly versatility,[115–117] it is one of the most known and widespread time resolved techniques.

In this context, the dynamics of several polaritonic samples have been investigated with this technique.

9.1   Intuitive picture of a pump and probe experiment

This technique employs the interaction with two laser pulses: the pump and probe, with the pump intensity typically noticeably stronger than the probe one. In this experiment, the pump and probe beams are spatially overlapped on the sample, and what is measured is the variation of the probe intensity after the sample at different probe delays to the pump (figure 9.1).
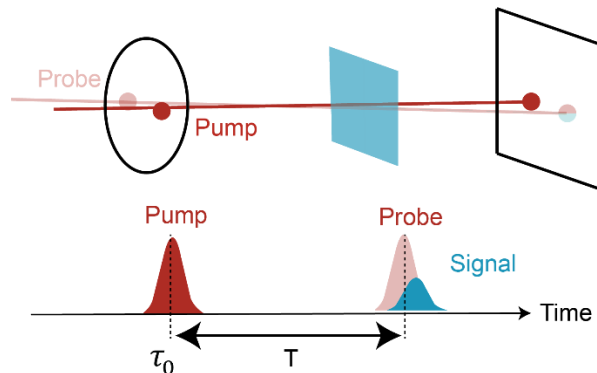
Figure 9.1. Excitation geometry (upper line) and pulse sequence (lower line) for a pump–probe experiment. The signal (blue) is emitted in the same direction as the probe.

Let us consider the simple case of a sample with two energy levels (ground state, g, and excited state, e) and a pump and probe setup with both pulses resonant with the g-e transition (figure 9.2).
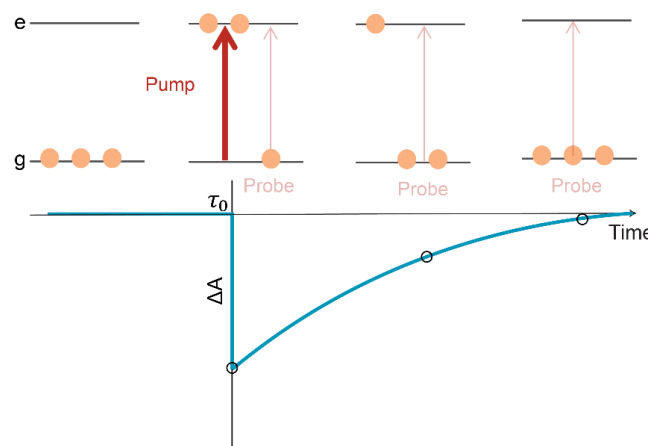
Figure 9.2. Time evolution of a two-level sample addressed in a pump and probe experiment (upper line) and the resulting signal output measured as a function of the delay time between pump and probe pulses (lower line).

At the time τ_0, the pump pulse excites the sample, with a consequent absorption. If the probe pulse arrives at τ_0 too, the system will absorb less photons than in the absence of the pump pulse. This phenomenon is called Ground State Bleaching (GSB), and becomes less and less important moving at longer delays, until the sample completely relaxes to g. In this situation, the GSB will be completely recovered. The measured signal, the differential absorbance, ΔA is obtained as:

$$\Delta A = -\log\left(\frac{I_P}{I_{NP}}\right) = A_P - A_{NP} \tag{9.1}$$

with I_P and I_{NP} the intensity of the signal with or without the pump pulse. Analogously, A_P and A_{NP} are the absorbance values in the presence and absence of the pump, respectively. Thus, the GSB is measured as a negative signal, which then, increasing the delay time, tends to zero with a time equal to the characteristic time of the relaxation from e to g of the sample considered (figure 9.2).

The GSB is not the only phenomenon detectable with a pump and probe setup. Considering the two-level sample again, the probe pulse can stimulate the relaxation from e to g (Stimulated Emission, SE, figure 9.3a), which induces a negative signal in the pump and probe spectra. Eventually, in samples with a more complex level structure, the probe can excite the sample from e to higher energy states. This phenomenon is named Excited State Absorption (ESA, figure 9.3b), which contributes with a positive signal in the spectrum.
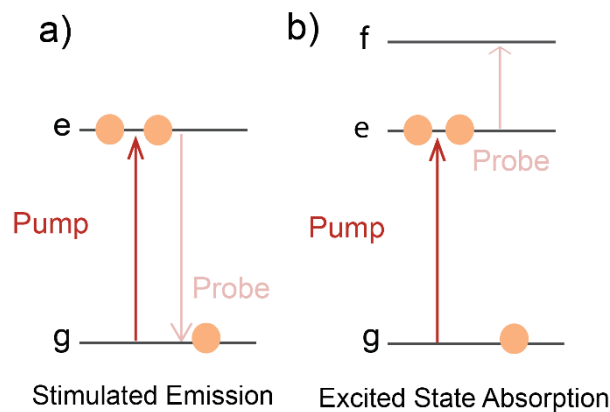
Figure 9.3. Sketch of a) stimulated emission and b) excited state absorption.

The pump and probe technique can be classified as one-color when the pump and the probe pulses have the same wavelength or as a two-color pump and probe when they are different. In this latter case, the probe is often a white light continuum, whose different wavelength components are then resolved by a spectrometer before the detector. In this case the

experiment can also provide the Transient Absorption (TA) spectrum where ΔA is analyzed both as a function of the delay t and the wavelength of the probe.

9.2   Optical setup

Our laboratories are equipped with the home-built pump and probe setup described in figure 9.4.
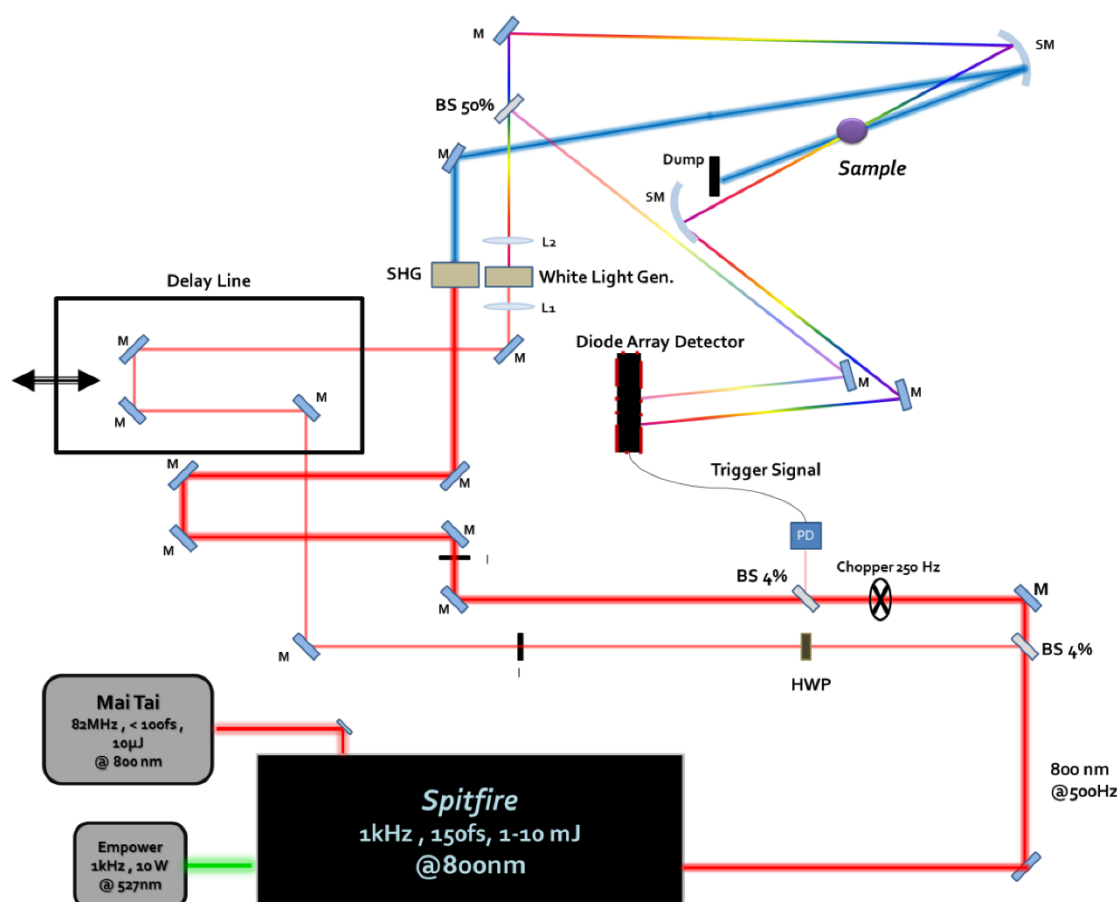
Figure 9.4. Pump and probe setup built in our laboratories. Reprinted from Ref.[118].

The pump and probe beams are generated by an amplified Ti:Sapphire laser (SpitFire, Spectra Physics) seeded by a femtosecond pulsed Ti:Sapphire oscillator (Mai-Tai, Spectra Physics). The laser pulses are emitted at 800 nm, with a power of 0.8 mJ per pulse, a repetition rate of 1 kHz, and a 160 fs pulse duration. The output laser beam is split by a 4% beam splitter into two paths. The weaker one generates a super-continuum white light in a thin sapphire plate and is used as the probe. The pump pulse at 400 nm is obtained via a second harmonic generation in a BBO thin crystal. The pump fluence is tuned from 170 to 730 $\mu J/cm^2$ using OD filters and its repetition rate is halved to 500Hz through an optical chopper.

The collimated pump pulse and the focused probe pulse hit the samples in an overlapping region. In this region, the pump beam diameter is about 60-80 μm and the probe 20-30 μm. The delay between pump and probe pulses was controlled with a motorized linear stage. The transmitted light is dispersed and directed to a linear CMOS diode array. The quality of the TA signal, i.e., ΔA values (differential absorption), is improved through repeated measurements and averaging (150-200 measurements were averaged to obtain a sufficient signal-to-noise ratio). The obtained spectra are numerically processed to minimize white light chirping effects, by using a home-made Matlab routine. Each measure is repeated at least twice to verify the reproducibility of the phenomena.

9.3   Fitting models

Our protocol for the fitting of the TA measurements consisted of selecting at least three decay traces in the region of interest and fitting them with a global fit with shared time constants. The following fitting models have been used for the analysis performed in chapter 13. In general, all the parameters were left free to change. Only for UR$_B$ dynamics, due to the complexity of the fitting, I fixed τ_{e-e}.

For the analysis of free TPPS J - aggregates, we fitted the decay with a four exponentials decay (4D):

$$\Delta A(t) = \Delta A_0 + A_1 e^{-t/\tau_1} + A_2 e^{-t/\tau_2} + A_3 e^{-t/\tau_3} + A_4 e^{-t/\tau_4} \tag{9.2}$$

where ΔA_0 is the background value, τ_i the different times constants and A_i their corresponding pre-exponential factors. I used the same model without the fourth term to also retrieve the time constants of the TPPS aggregated in the sample NS_TPPS-UNC and I called it '3D' fitting model. For the analysis of **NSA** sample and the 520-580 nm region in NS-TPPS_100 and NS-TPPS_1040 samples , I used a slightly different model as reported in the literature:[119]

$$\Delta A(t) = \Delta A_0 + H(t - \tau_0)\left\{ A_1 \left(1 - e^{-\frac{t-\tau_0}{\tau_{e-e}}}\right) e^{-t/\tau_{e-ph}} + A_2 \left(1 - e^{-\frac{t-\tau_0}{\tau_{e-e}}}\right) e^{-t/\tau_{ph-env}} \right\}, \tag{9.3}$$

where the Heaviside function $H(t - \tau_0)$ maintains the causality principle, τ_0 is the zero-delay time, τ_{e-e} is the characteristic electron-electron scattering time constant, τ_{e-ph} the electron-phonon scattering time constant and τ_{ph-env} the phonon-environment time constant, further explained in chapter 13. This model is called raise-decay-decay (RDD) because a raising exponential is convoluted to the sum of the exponential decays. Finally, for the study of the UR$_B$ GSB I used a RDD modified model, in which only one decay is convoluted to the exponential rise (RD+2D model):

$$\Delta A(t) = \Delta A_0 + H(t - \tau_0) \left\{ A_1 \left(1 - e^{-\frac{t - \tau_0}{\tau_{e-e}}} \right) e^{-t/\tau_{e-ph}} + A_2\, e^{-t/\tau_{plex,1}} + A_3\, e^{-t/\tau_{plex,2}} \right\}. \qquad (9.4)$$

For the study of the LR_Q GSB, the third decay component was set to zero.

10. Two-Dimensional Electronic Spectroscopy (2DES)

2DES was developed in the first years of 2000 as a primary tool for the investigation of the coherent dynamics of energy transport in biological antenna systems.[120] Indeed, the high time resolution of this technique, which can arrive up to 5-10 fs, and the capability of spreading the signals along multiple frequency dimensions allows 2DES to experimentally capture quantum phenomena and couplings with high precision. Although 20 years later the relevance of quantum phenomena in biological processes is still intensely debated,[121,122] 2DES has been welcoming to other aiming, among which the characterization of the dynamics in complex inorganic[123,124] and hybrids systems such as polaritonic samples.[81,83]

2D electronic spectroscopy, like the pump and probe technique, is a non-linear optical spectroscopy, which means that the setup utilizes intense light sources (in our case, lasers) that stimulates a nonlinear response in the systems. Furthermore, both 2DES and pump and probe techniques belong to the family of the four-wave mixing techniques, which investigate ultrafast dynamics where the signal (the 'fourth' wave) is stimulated by three light-matter interactions. The main difference between these two techniques is that the pump and probe is a 1D technique, because two of the three exciting pulses are temporally superposed in the pump pulse (figure 10.1a). Consequently, ΔA can be resolved only in the probe frequencies and in the delay time τ. Contrarywise, 2DES has an extra dimension because the time delays between each couple of pulses can be controlled (figure 10.1b). In a typical 2DES experiment, the signal is a 3D matrix of data, where the signal is plotted as a function of: (i) the delay time, t_2, called in this framework population time, which is the time between the second and the third pulse; this time is analogous to the delay time τ in a pump and probe experiment; (ii) the Fourier Transform (FT) of the other two time intervals t_1 and t_3, (ω_1 and ω_3 respectively). In analogy with the pump and probe technique, ω_3 is the probe frequency (here called emission frequency), while ω_1, also reported as excitation frequency, is the FT of the time interval between the first and the second laser pulse. This is the dimension that the pump and probe technique is not able to resolve and modulate. Figure 10.1 describes these concepts. The main difference between the 1D and 2D non-linear techniques is the ability of the latter to decongest the different signal contributions, by introducing a further dimension.

The 2DES technique is more complex and less known than pump and probe. For this reason, it is worthy of giving a more formal treatment of the signals obtained by 2DES. The purpose is to provide some basis for understanding the observed phenomena reported in part III. For a more detailed and complete discussion, the reader is referred to Refs.[125,126].
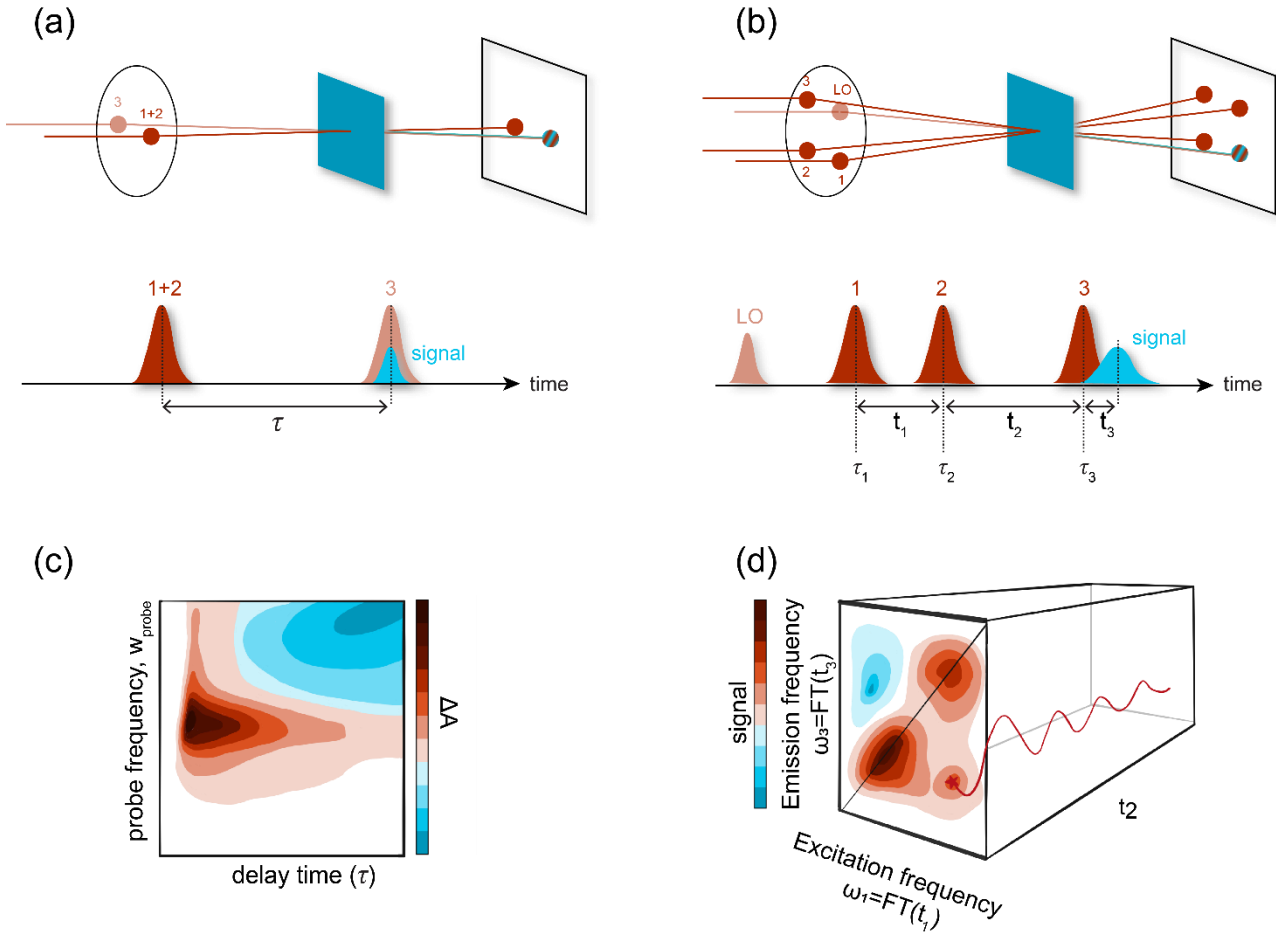
Figure 10.1. Excitation geometry (upper line) and pulse sequence (lower line) for a) pump–probe and b) 2DES experiments in the BOXCARS geometry. The pump and probe geometry has been redrawn to highlight the three exciting pulses (the first two of them represent the 'pump'). The main difference in these experiments is the added dimension in the 2DES: to visualize this concept, a pictorial representation of the signals obtained from c) pump and probe and d) 2DES experiments are reported. Adapted from Ref.[79].

10.1   Theoretical background

Density matrix. A useful tool in the 2DES framework is the density matrix ρ, which describes a statistical ensemble of quantum states interacting with the environment-bath:[127,128]

$$\rho(t) = |\psi(t)><\psi(t)| \tag{10.1}$$

where $\psi\ (t)$ is the wavefunction describing that ensemble, which in a perturbative approach can be expressed a liner combination of eigenstates i calculated as solutions of the time-independent Schrodinger equation:

$$\psi\ (t) = \Phi_n e^{-i\omega_n t}.$$ (10.2)

Φ_n is the solution of the time-independent Schrodinger equation of the system and the exponential is a phase factor which depends on the energy of the eigenstate. For instance, for a two-level (1 and 2) system, the matrix representation is:

$$\rho(t) = \begin{pmatrix} b_1(t)b_1^*(t) & b_1(t)b_2^*(t) \\ b_2(t)b_1^*(t) & b_2(t)b_2^*(t) \end{pmatrix}$$ (10.3)

$\rho(t)$ introduces the concepts of population and coherence. Considering equation (10.3), the diagonal elements of the matrix are called "populations" and represent the probability that the system is described by the i-th eigenstate, while the elements out of the diagonal are called "coherences" because they represent a superposition of the two different states. The associated probability oscillates at a frequency corresponding to the energy difference of the states themselves. This is the same phenomenon described in chapter 4, where Rabi splitting and plexcitonic coherences are commented.

The time-evolution of $\rho(t)$ can be obtained resolving the Liouville-von Neumann equation:[125]

$$i\hbar \frac{\partial \rho}{\partial t} = [H, \rho]$$ (10.4)

whose solution, in the perturbative approach, can be obtained through the definition of the time evolution operator U such that:[129]

$$\rho(t) = U^+ \rho(0) U$$

$$U = exp_+ \left[-\frac{i}{\hbar} \int_0^t d\tau H(\tau) \right]$$ (10.5)

With this notation the time dependence is enclosed in U, derived as a time ordered exponential. The physical meaning underneath these equations is that, considering the transition from an eigenstate to another, all the pathways at the different orders of the perturbation must be included and summed in a specific order.

Response theory. 2DES signal can be formalized into the perturbative approach, which allows expressing the polarization $\boldsymbol{P}$ as a perturbative expansion in powers of the incoming fields. Specifically, the detected signal is proportional to the third order polarization $\boldsymbol{P}^{(3)}$, because the

signal is stimulated by the interaction with 3 exciting fields. Indeed, the first order (linear) polarization is detected by linear spectroscopies techniques, while $\boldsymbol{P}^{(3)}$ is this the first nonlinear significant term of the polarization series expansion for absorptive phenomena. It is defined as the convolution of the three exciting electric fields $\boldsymbol{E}_j(k_j, t)$ with the non-linear response function at the third order $\boldsymbol{R}^{(3)}(t_1, t_2, t_3)$ of the system:

$$\boldsymbol{E}_j(k_j, t) = A_j(t - \tau_j)e^{-i\omega(t-\tau_j)+i\boldsymbol{k}_j \cdot \boldsymbol{r}+i\phi_j} + complex\ conjugate$$

$$\boldsymbol{P}^{(3)}(t_1, t_2, t_3) \propto \int_0^\infty dt_3 \int_0^\infty dt_2 \int_0^\infty dt_1 \cdot \quad (10.6)$$

$$\cdot \boldsymbol{R}^{(3)}(t_1, t_2, t_3)\boldsymbol{E}(t - t_3)\boldsymbol{E}(t - t_3 - t_2)\boldsymbol{E}(t - t_3 - t_2 - t_1)$$

with t_j and τ_j the time intervals and the time of the pulse arrival as described in figure 10.1, k_j, $A_j(t), \phi_j$ the wavevector, the temporal envelope and the phase of the j-th field, respectively. From the response theory, $\boldsymbol{R}^{(3)}(t_1, t_2, t_3)$ can be defined as:[125]

$$\boldsymbol{R}^{(3)}(t_1, t_2, t_3) = \left(-\frac{i}{\hbar}\right)^3 \sum_{i=1}^{4}(R_i - R_i^*) \quad (10.7)$$

where:

$$R_1 = \text{Tr}[\mu U(t_3)U(t_2)U(t_1)\mu(0)\rho(-\infty)U^+(t_1)\mu U^+(t_2)\mu U^+(t_3)]$$

$$R_1^* = \text{Tr}[\mu U(t_3)\mu U(t_2)\mu U(t_1)\rho(-\infty)\mu(0)U^+(t_1)U^+(t_2)U^+(t_3)]$$

$$R_2 = \text{Tr}[\mu U(t_3)U(t_2)\mu U(t_1)\rho(-\infty)\mu(0)U^+(t_1)U^+(t_2)\mu U^+(t_3)]$$

$$R_2^* = \text{Tr}[\mu U(t_3)\mu U(t_2)U(t_1)\mu(0)\rho(-\infty)U^+(t_1)\mu U^+(t_2)U^+(t_3)]$$

$$R_3 = \text{Tr}[\mu U(t_3)\mu U(t_2)U(t_1)\rho(-\infty)\mu(0)U^+(t_1)\mu U^+(t_2)U^+(t_3)] \quad (10.8)$$

$$R_3^* = \text{Tr}[\mu U(t_3)U(t_2)\mu U(t_1)\mu(0)\rho(-\infty)U^+(t_1)U^+(t_2)\mu U^+(t_3)]$$

$$R_4 = \text{Tr}[\mu U(t_3)\mu U(t_2)\mu U(t_1)\mu(0)\rho(-\infty)U^+(t_1)U^+(t_2)U^+(t_3)]$$

$$R_4^* = \text{Tr}[\mu U(t_3)U(t_2)U(t_1)\rho(-\infty)\mu(0)U^+(t_1)\mu U^+(t_2)\mu U^+(t_3)]$$

where μ is the dipole moment operator and $\rho(-\infty)$ the equilibrium density matrix before the perturbation.

Liouville pathways and Feynman diagrams. Each of the R_i-th terms in the equation (10.8) represents a so-called "Liouville pathway", i.e. one of the possible pathways of evolution that the fields can promote in the system. The density matrix operator is composed of a *ket* and a *bra*,

as reported in equation (10.1): the time evolution operator can act on both of them, from the left or the right, respectively. Thus, considering for instance R_1, its time evolution can be visualized as follow.

Before any excitation, the system is in thermal equilibrium ($\rho(-\infty)$). The first field-operator is $\mu(0)$, which acts at time 0 on the *ket* side of the density matrix ($\mu(0)\rho(-\infty)$). After time 0, the excited system evolves under $U(t_1)$ until the second pulse arrives ($U(t_1)\mu(0)\rho(-\infty)U^+(t_1)$). At the second pulse arrival, now μ acts on the *bra* side, and its time evolution is described by $U(t_2)$ until the third pulse arrival, which acts again on the *bra* side. After the time evolution ruled by $U(t_3)$, a final dipole moment μ is used to calculate the trace and, thus, the signal $P^{(3)}$. Figure 10.2 helps to visualize these steps.

$$R_1 = \text{Tr}[\mu U(t_3)U(t_2)U(t_1)\mu(0)\rho(-\infty)U^+(t_1)\mu U^+(t_2)\mu U^+(t_3)]$$
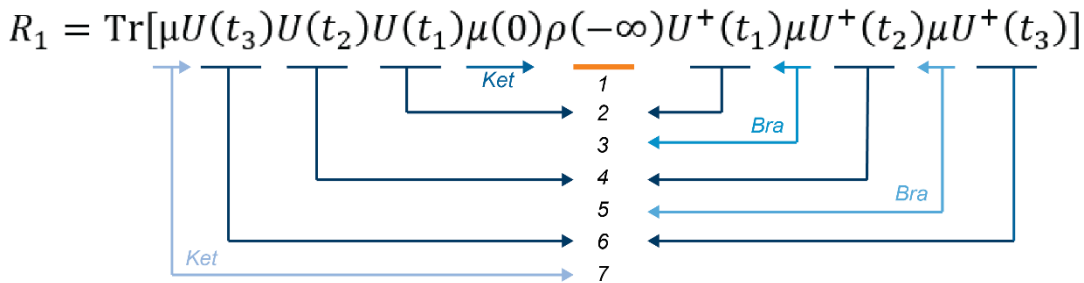
Figure 10.2. Visual representation of the Liouville pathway R_1. The numbers indicate the order of the temporal events.

An intuitive way to picture the Liouville pathways is the use of the double-sided Feynman diagrams. They are composed of two vertical lines, the left one representing the *ket* and the right one the *bra*, while the time evolution of the system goes upwards. Each interaction with the field is represented by an arrow, which can point towards (absorption) or outwards (emission) and can act on the *ket* or on the *bra*. Between two arrows, different ρ states are divided by a line and evolve under $U(t_i)$. The last arrow is dashed because it represents the signal and it is conventionally assigned to the *ket* side (except for R_4^*). During the temporal evolution of ρ, the density matrix can be found in a coherence, where the *ket* and *bra* are different, or in a population, if they are in the same state.

The Feynman diagrams of a three-level system, the same represented in figure 9.3b, are represented in figure 10.3. However, generally speaking, the number of the Feynman diagrams, as well as the Liouville pathways, depend on the photophysics of the system and on the number of its states.
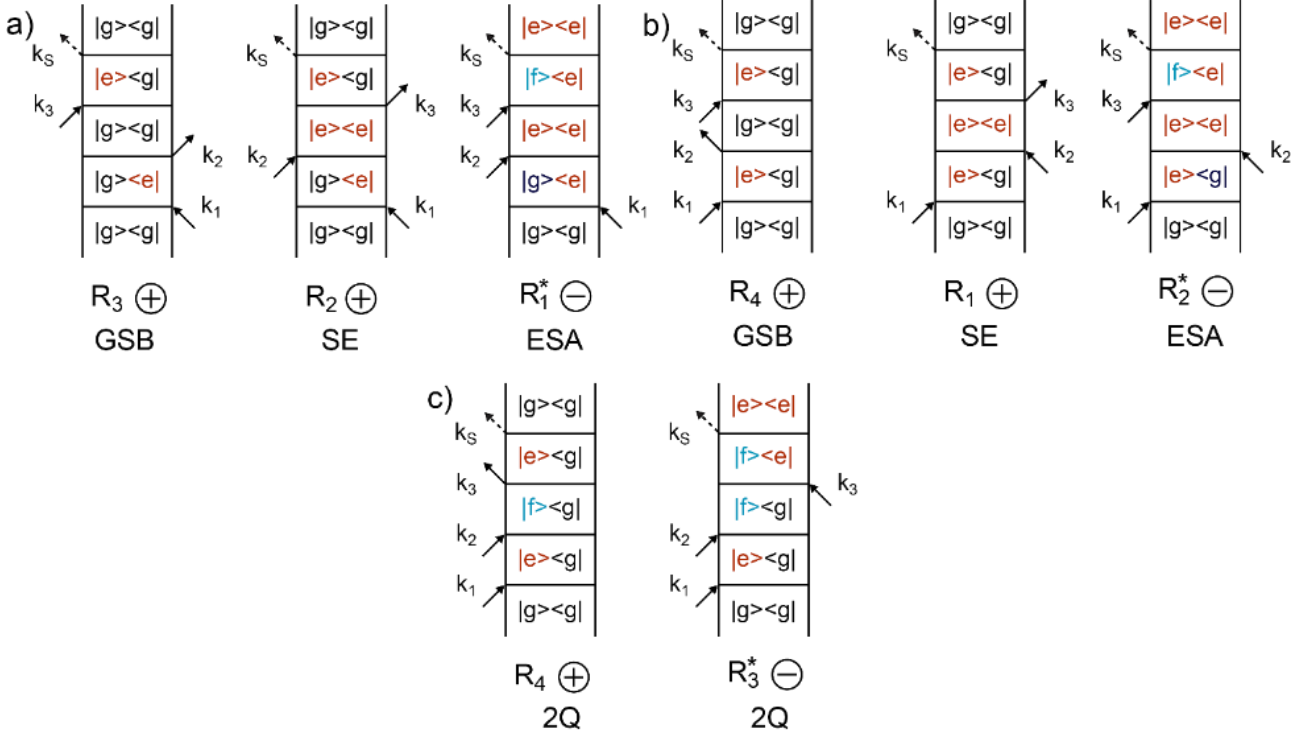
Figure 10.3. Feynman diagrams contributing to a) rephasing, b) non rephasing, and c) double-quantum signals[130] for a three level system with a ground state g and two excited states e and f. Adapted from Ref.[79].

Let us now consider the field contribution, which is convoluted to the response function in the calculation of $P^{(3)}$. Since the overall field comprises three laser pulses, it contains six terms (equation 10.6), generating 864 signals. Luckily, it is possible to reduce them with three approximations. The first one is the *time ordering in the semi-impulsive limit*. Considering the temporal width of the pulses far shorter than the overall time of the experiment and the time intervals t_i, each pulse can be considered as a δ-function in the time domain, still maintaining its wavevector and frequency. This approximation also assures that each interaction can be assigned to a specific field. The *Rotating Wave Approximation* considers only the positive or negative contributions of the field, while when the field contributes with both of them, it is considered negligible. Finally, the third-order response is generated along a precise direction, described by the *phase matching* conditions:

$$k_{sign} = \sum_{i=1}^{3} \pm k_n. \tag{10.9}$$

This means that it is possible to distinguish between different Liouville pathways choosing properly the exciting geometry. In particular, in this PhD thesis two particular families of signals will be analyzed:

$$\boldsymbol{k}_{sign}^{R} = -\boldsymbol{k}_1 + \boldsymbol{k}_2 + \boldsymbol{k}_3$$

$$\boldsymbol{k}_{sign}^{NR} = +\boldsymbol{k}_1 - \boldsymbol{k}_2 + \boldsymbol{k}_3.$$

(10.10)

$\boldsymbol{k}_{sign}^{R}$ indicates *rephasing* signals, while the $\boldsymbol{k}_{sign}^{NR}$ *non rephasing* signals. These names are due to the phase evolution of ρ along t_1 and t_3. While, indeed, the phase of the *rephasing* signal after the coherence in t_1 is restored during t_3, which has the opposite sign, this is not achievable for *non rephasing* signals.

These three approximations reduce the number of terms of the third-order polarization to four independent contributions, and their complexes conjugated, which are actually the number of the Liouville pathways considered in the third-order response function.

To conclude this paragraph, let us analyze the different kinds of Liouville pathways in figure 10.3. The phenomena attributed to them are the same already commented in the pump and probe signal description: SE, GSB and ESA. SE signals (R_1 and R_2), indeed, analyze indirectly the Stimulated Emission from the excited state and are able to reveal its population dynamics. GSB signals (R_3 and R_4) report the dynamics of g recovery. Unlike the pump and probe technique, here these contributions have a positive sign. The ESA signals (R_1^* and R_2^*), instead, consider the dynamics that involve the f state and are negative. Finally, two other signals can be detectable, namely R_3^* and R_4^*. They are called Double Quantum signals and report the coherence between e and f during the population time. The reader is referred to significant theoretical works for further information.[125,130]

10.2   2DES: concepts and maps interpretation

2DES signal is represented by 2D maps measured at different t_2, each of which reports in the axes the FT of t_1 and t_3, ω_1 and ω_3, respectively. The measured signal is thus written as: $S = S(\omega_1, t_2, \omega_3)$.

Considering the Feynman diagrams reported in figure 10.3, the coherences evolving in the first and third periods are Fourier-transformed and their frequencies become the x and y coordinates of the maps. The population dynamics after the second pulse is evaluable considering the time evolution of each coordinate of the (ω_1, ω_3) maps along t_2. In this thesis Rephasing and Non Rephasing experiments were performed. When rephasing and non-rephasing signals are summed up, *Total* or *Purely absorptive* maps are obtained, that report only real (and, thus, absorptive) contributions to the signal.[125]

To ease the interpretation of the maps reported in the experimental part, below two significant models are reported.[131]
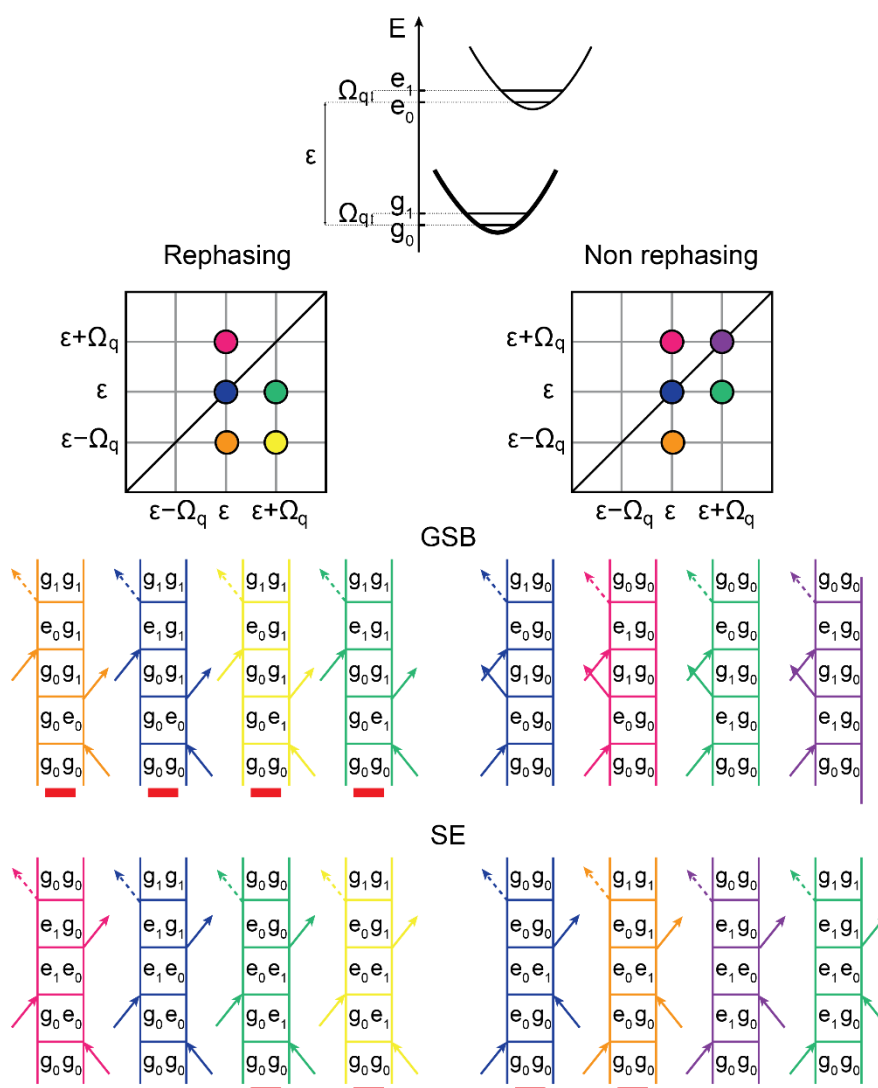
Figure 10.4. Displaced harmonic oscillator model. A nuclear coordinate-energy scheme of this model is represented on the top. In the middle the vibronic coherences are sketched in the rephasing (left) and non rephasing (right) maps and their Feynman diagrams are represented on the bottom, following the color code. Red lines pinpoint Feynman pathways leading to electronic coherences having positive oscillation frequency. The *ket* and *bra* are omitted for clarity. Adapted from Ref.[131].

Displaced harmonic oscillator model. With the first model the reader is introduced to the 2DES response of a vibronic system, i.e. a system in which electronic and vibrational degrees of freedom are coupled. The simplest model is represented by two electronic states, e and g, (ground and excited state, respectively), with an energy gap ε, each one coupled to a single vibrational nuclear coordinate q with frequency Ω_q.[132] Figure 10.4 lists the Feynman pathways with an oscillating contribution in t_2, both for the rephasing and non-rephasing experiment. A colour code links the coloured dots on the 2DES map to the corresponding Feynman diagrams

that describe the signal contributing at those coordinates. This model features the typical "chair pattern" for the signals in the rephasing maps, while in the non rephasing this pattern is flipped upside-down. When several vibrational modes q_i are coupled to the electronic transition, many other beatings with frequency Ω_{q_i} contribute to the overall signal at specific coordinates determined by Ω_{q_i} and ε.
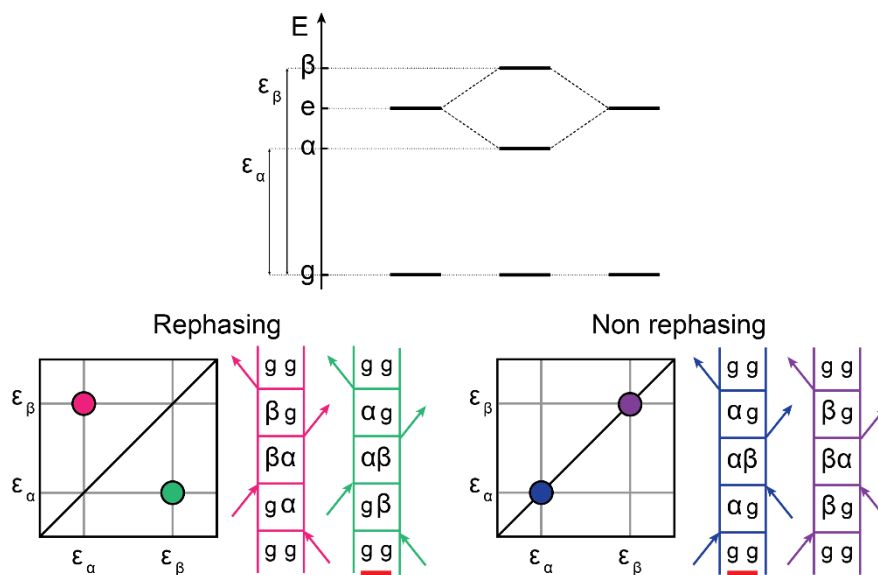
Figure 10.5. Excitonic dimer model. An energy scheme of the model is represented on the top. Below, the electronic coherences signals are reported in the rephasing (left) and non rephasing (right) maps and their Feynman diagrams are represented aside, following the color code. Red lines pinpoint Feynman pathways leading to electronic coherences having positive oscillation frequency. The *ket* and *bra* are omitted to allow better visualization. Adapted from Ref.[131].

Exciton dimer model. This model allows us to understand how electronic coherences appear in 2D maps and it can be applied to any pair of coupled electronic states that are simultaneously excited by the laser spectrum, for instance SC plexcitons. Let us consider a dimer of two identical two-level molecules, excitonically interacting with a resonance coupling J.[133] The resulting system, called excitonic dimer, has two new eigenstates whose energy difference is $2J$[134] and it is represented in the top of figure 10.5. The oscillating signals are generated by coherent superpositions of excitonic states, and the number of possible contributions is drastically reduced compared to the previous model. In both rephasing and non rephasing maps only two Feynman pathways produce signals oscillating with frequency $|\varepsilon_\alpha - \varepsilon_\beta|$, where ε_α and ε_β are, respectively, the frequency of α and β exciton transitions. These beatings appear at cross-peaks (or antidiagonal position) $(\varepsilon_\alpha, \varepsilon_\beta)$ and $(\varepsilon_\beta, \varepsilon_\alpha)$ in the rephasing experiment, and on the diagonal positions $(\varepsilon_\alpha, \varepsilon_\alpha)$ and $(\varepsilon_\beta, \varepsilon_\beta)$ in the non rephasing maps.
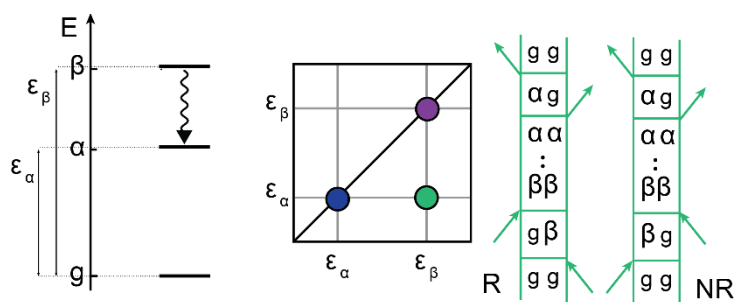
Figure 10.6. Incoherent energy transfer. An energy scheme is represented on the left. In the middle, the purple and blue dots depict signals involving the populations of β and α, respectively. The green dot represents the incoherent energy transfer signal. On the right, the Feynman diagrams are reported either for rephasing (R) and non rephasing (NR) experiment, following the color code. The *ket* and *bra* are omitted to allow better visualization.

Incoherent energy transfer. In the previous model, the two coupled levels coherently share the excitation until the coherent superposition is damped by the environment. This phenomenon can be described also in terms of coherent or wavelike energy transfer. Another common energy transfer mechanism is the incoherent energy transfer, where the energy is transferred directionally from the higher to the lower energy level, without any superposition of states (the off-diagonal elements of ρ are nulls). This model is generally described with the classical Foster or Dexter theory in the case of energy transfer between molecules, or with more complex models in the case, for instance, of plasmonic systems.[53,135,136] In this case, being α the lower energy level with frequency ε_α and β the higher one with frequency ε_β (figure 10.6, left), a lower cross peak at coordinates $(\varepsilon_\alpha, \varepsilon_\beta)$ will appear in both rephasing and non rephasing maps. This incoherent energy transfer also affects the population signals (figure 10.6, centre). In particular, β will experience a further depopulation mechanism, detectable as a new exponential decay in the diagonal signal at coordinates $(\varepsilon_\beta, \varepsilon_\beta)$. Contrarywise, a rise can be revealed in the diagonal signal at the coordinates $(\varepsilon_\alpha, \varepsilon_\alpha)$, with the same time constant of the β exponential decay.

10.3   Setup and data analysis

Our laboratories are equipped with a home-made 2DES setup with a BOXCARS geometry, where the laser pulses propagate along the vertexes of an ideal square. Figure 10.7 schematically depicts the setup. This section is intended to give a brief description of the main components of the setup. For further insights, the reader is referred to Ref.[137].

Laser source and wavelength conversion. The laser source is a Coherent ®Libra. Its output consists of a train of pulses with a repetition rate of 3 kHz, where each pulse has a duration of about 100 fs, energy of 0,8 nJ and a bandwidth of 12 nm, centered at 800 nm. When the output is produced, it first passes through a beam stabilizer device (Newport® Guide Star II). Two

piezoelectric mirrors and two cameras compensate for any spatial deviations over time and guarantee the beam stability during the alignment and the experiments. Then, the beam wavelength is converted from 800 nm to a broadband spectrum between 500 and 900 nm using a Light Conversion® TOPAS White, a non-collinear optical parametric amplifier. The 800 nm light, once in the TOPAS While, is split into three parts. First, 1% of the beam is used to produce white light with a sapphire plate through non-linear effects. It is then collimated with spherical mirrors and focused into a pulse shaper that allows controlling the chirp of the pulse and the bandwidth of the final amplified pulse. The remaining 99% is used to generate a second harmonic 400 nm beam by a barium-boron-oxide (BBO) crystal. This beam is furtherly split in two. The interaction of the three beams onto a second BBO crystal allows amplifying different components of the white light by carefully tuning the angle of the crystal and the 400 nm beams delays. The goal is to maximize the output in terms of broadness of the spectrum and intensity of the beam. After a collimation step, the beam exits the TOPAS as a train of pulses with a duration of 20 fs, bandwidth of 80-100 nm and energy between 1 and 15 μJ. The broadband spectrum can be measured with an Avantes® fiber-optic spectrometer.
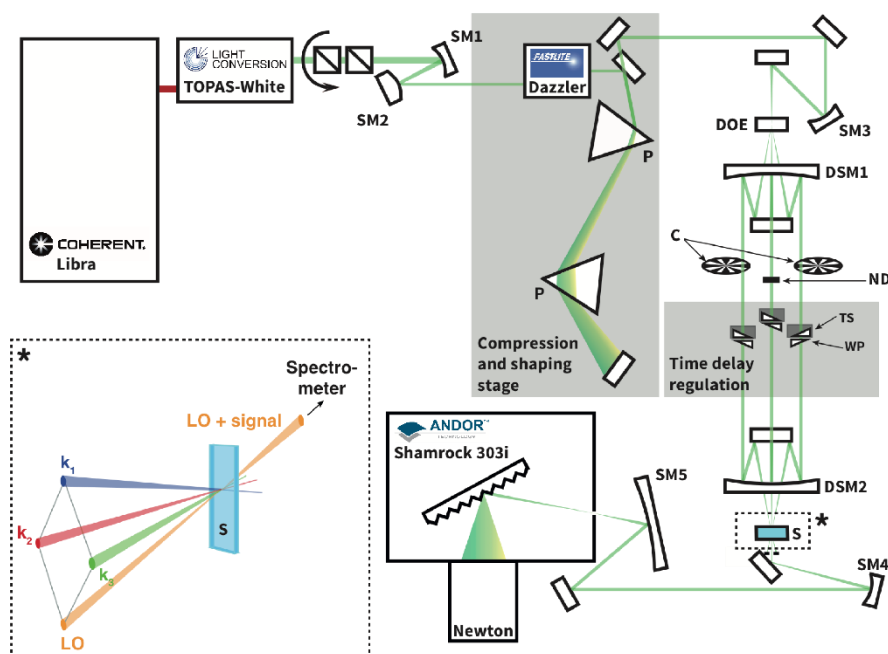
Figure 10.7. Schematic setup for 2DES. Abbreviations: (SM) spherical mirror, (P) prism, (DOE) diffractive optical element, (DSM) donut spherical mirror, (C) chopper, (ND) neutral density filter, (WP) wedge pair, (TS) translational stage, (S) sample. Inset: schematic representation of BOXCARS geometry. Reprinted from Ref.[131].

Pulse shaping. When ultrashort laser pulses propagate through a medium with a frequency dependent refractive index, the different components of the pulse light acquire different speeds. This causes the broadening of the pulse duration and different phase shifts. This phenomenon,

called "chirp", can induce systematic errors in the 2DES measurements and reduce the resolution of the measurements. To compensate for the chirp, coarse adjustments were made by a prism compressor, while the fine tuning by an acousto-optic programmable dispersive filter. The prism compressor consists of a couple of prisms, built in a material with a suitable wavelength-dependent refractive index, that can reduce the chirp acting on their distance and relative angle. The dispersive filter, Fastlite® Dazzler, contains an ultra-compact uniaxial birefringent crystal and a piezoelectric device, which generates acoustic waves. The latter, controlled via software, can adjust the phase and the amplitude up to the fourth order. The Dazzler and prisms' parameters are optimized with the calibration routine described later.

Delay regulation and heterodyne detection. The beam is then split into four identical replicas using a diffractive optic element. These four beams are spatially arranged along the vertexes of an ideal square. Three of them will be used as excitation, while the fourth is called local oscillator (LO) and is needed for detection purposes. The time delay between them is finely controlled using three couples of antiparallel CaF_2 wedges. Each wedge is positioned on a linear stage (Aerotech® Ant95) and controlled via software, allowing time delays with a precision of 0.07 fs and scanning times up to 2 ps. LO is considered as the temporal reference for the other delays, so it does not require any delay, but it is just lowered in power (of a 10^4 factor) by a D4 gradual neutral density filter. The role of LO is to interfere with the signal: the interference is then spectrally resolved by a spectrometer (Andor® Shamrock 303i) and detected by the Andor® Zyla 5.5 scientific Complementary Metal-Oxide Semiconductor camera with 5.5 Megapixel. This kind of detection is called "heterodyne detection". It provides an enhanced signal-to-noise ratio and it allows separating the real and imaginary part of the electric field of the signal.

A further refinement of the signal is given by the double lock-in detection,[137] which removes spurious contributions, e.g. the scattering from the exciting pulses. Two of the incoming pulses, are modulated with two optical choppers operating at 250 Hz and 50 Hz, which are synchronized with the laser repetition rate and the operating frequency of the detector; moreover, one is opportunely chosen as an integer multiple of the other, to have a right phase-locking of the signal. Thus, a new restriction is imposed, i.e. the signal can be recorded only at the sum or difference of the modulation frequencies so that the majority of the scattering contributions (caused by the exciting pulses) is prevented from being detected.

Calibration. First, to verify that the four beams are at the corners of the ideal square with a constant intensity and possess the same size and shape, a CCD camera is positioned in the place of the sample holder. The prism compression is modified to correct possible errors. Then, the

zero position of the wedges, the coefficients that convert the stages position into time delays, and Zyla calibration are obtained performing a calibration routine by using a pinhole placed at the focus of the four beams. The final calibration step consists of a series of FROG (frequency resolved optical gating) experiments performed on a non-resonant sample (typically DMSO solvent), which allows us to estimate the pulse duration and thus the temporal resolution of the experiment. Iterative FROG measurements, performed while tuning the Dazzler parameters, allow optimizing the quality of the light beam.

Data processing and analysis. The output of the 2DES experiment, i.e. the heterodyned signal, is stored in a 3D matrix, where the signal is resolved as a functions of the three time intervals of the experiment t_i. The first steps are: (i) a pre-processing to eliminate the spurious scattering contributions; (ii) the deconvolution of the inference pattern from the LO spectrum to achieve the signal; (iii) the data average (if many experiment in the same conditions were performed). After that, the signal is phased. This is a critical task, which requires to define exactly the phase between the signal and LO, in order to isolate the real and the imaginary part of the signal. Using the projection-slice theorem, the projection on the ω_3 axes are matched with the real absolute T signal with an experimental pump and probe spectrum, measured with the same setup.[138]

Therefore, the obtained signal is analysed through a global fitting methodology using the software MATLAB®.[137,139] The temporal evolution of the 2DES maps along t_2 includes either oscillating components, due to the vibronic or electronic coherences, and non-oscillating decays, mainly due to the time evolution of populations. The fitting is based on a multi-exponential model built as a sum of complex exponentials which account for non-oscillating and oscillating components.[139]. The fitting algorithm is able to globally fit all the (ω_1, ω_3) signals along t_2 for the rephasing, non rephasing and total maps in one step. The final outputs are the time constants for the populations decay, and the frequency and damping times of the oscillating components. Moreover, for each process, an amplitude map is obtained, which is called DAS (decay-associated spectra) for the population processes and CAS (coherent decay-associated spectra) for the coherence ones. In the real part of a DAS, a positive(negative) signal is associate to a decay(rise). The CAS are instead analysed in their absolute form. DAS and CAS allow to locate into the 2DES maps the regions in which a precise process, described by a time and/or frequency constant, occurs.

Moreover, the oscillating dynamics can be studied also with an alternative approach. Indeed, the population dynamics can be removed by subtracting them from the signal. The remaining matrix only includes oscillating residues. The simplest methodology to analyse the frequencies of the

oscillations is to integrate the 2D maps of residues along ω_1, ω_3 and to apply a Fourier transform (FT) along t_2. The final spectrum is called power spectrum and represents the intensities of the beatings that oscillate along the population time.

To retain more information about the dephasing time of these oscillations, Smoothed-Pseudo-Wigner-Ville (SPWV) transform can be used. Briefly, the oscillating residues are extracted at a specific coordinate (ω_1, ω_3) of the 2D map and then transformed with a complex procedure, that involves the combination of a bilinear transform with a linear transform. In this way, the signal is shown as a function of the population time (x-axis) and of the frequency of the oscillating components (y-axis). SWPV transform is preferred over the conventional FT because it can provide information on the frequency and time properties of the beatings at the same time, allowing a more immediate visualization of the damping behaviour of the different oscillating components. For further insights of this kind, the reader is referred to Ref.[139].

III Results and Discussion

In this part, two families of Colloidal Plexcitonic Materials (CPMs) are discussed. Chapter 11 describes the results obtained on a nanohybrid built by conjugation of gold nanospheres and a polyanionic porphyrin in different aggregation states. The nanohybrid presents two sets of plexcitonic resonances, which can be selectively turn on and off through supramolecular interactions and contribute collectively to the system relaxation. Further insights about the supramolecular interactions, which regulate the aggregation state of the porphyrin onto the nanospheres surface, will be given in Chapter 12. Chapter 13, instead, is focussed on the dynamics of this system characterized by pump and probe. The second family of CPMs is produced using gold nanourchins. In Chapter 14, a library of plexcitonic nanohybrids was designed and studied to understand the role of the capping layer and the dye molecules in the plexcitonic assembly. Two of the most promising hybrids were studied in the following chapters to unveil their ultrafast dynamics with the 2DES technique. The focus of Chapter 15 is the dramatic difference between strong and weak coupling dynamics for TDBC-NUs nanohybrids. Finally, Chapter 16 reports the study of the role of molecular vibrations in PIC-NUs nanohybrids.

11.   Gold nanospheres and polyanionic porphyrins: Selective Switching of Multiple Plexcitons

11.1   Motivations: preparing a "responsive" dynamic nanohybrid

Although strong light-matter coupling with organic molecules has been known for about 40 years, and the polaritonic chemistry for nearly a decade,[140] attention has been so far focused on fundamental investigations on "static" systems, where coupling parameters are tuned by modifying either the detuning (δ) or the number of coupled QEs (N) to obtain hybrid states with suitable properties[11,77,92,141,142] (chapter 4). On the other hand, another category of systems – the "dynamic" plexcitonic materials can potentially be prepared. In this new category, almost unexplored in literature, the plexcitons can be activated and modulated by external stimuli, making the material a functional material. This may offer the possibility to realize new plexcitonic devices, useful in several fields such as nanophotonics, solar cells or quantum technologies (chapter 3).

Taking inspiration from this concept, I focused the attention on the possibility of exploiting the supramolecular interactions at play between the two entities (NS and QE) forming the plexciton. Such interactions are indeed compelling to achieve the necessary spatial proximity between the colloidal NS and the QE and determine their mutual arrangements. Moreover, their dynamic nature could allow the controlled activation or de-activation of the coupling conditions necessary for the efficient formation of hybrid plexciton states. Accordingly, here I present the first of the two plexcitonic families reported in this thesis: a "responsive" dynamic nanohybrid in solution, where, depending on controllable external conditions, two sets of plexcitonic resonances in different coupling regimes can be selectively activated, and, in turn, different optical properties can be achieved. By controlling the supramolecular dye-dye, Nanospheres (NS)-NS, and dye-NS interactions, it is possible to selectively turn on and off the two sets of resonances (Table 11.1). Moreover, when they are both present, they do not act as independent transitions but collectively contribute to the system's relaxation.

11.2   Design of the hybrid systems

To prepare responsive hybrid systems, I exploited the self-organization of the diprotonated form of the anionic dye 5,10,15,20-tetrakis-4-sulfonato-phenyl porphyrin (H_2-TPPS^{2-}) on cationic NS (Figure 11.1a). Indeed, the ability of this dye to form molecular aggregates with relevant spectroscopic properties in a controlled way is well-known.[143–146] At pH values below 3, the porphyrin is doubly protonated at the tetrapyrrolic core and the resulting charge distribution

favors the formation of J-aggregates. Effective aggregation requires however also the presence of other concurrent co-factors such as high concentration, high ionic strength, or the presence of polycationic templating agents like polymers or nanoparticles.[144,147–154] Our hypothesis was hence that cationic nanoparticles could attract TPPS molecules on their surface and also template their aggregation depending on the dye concentration.
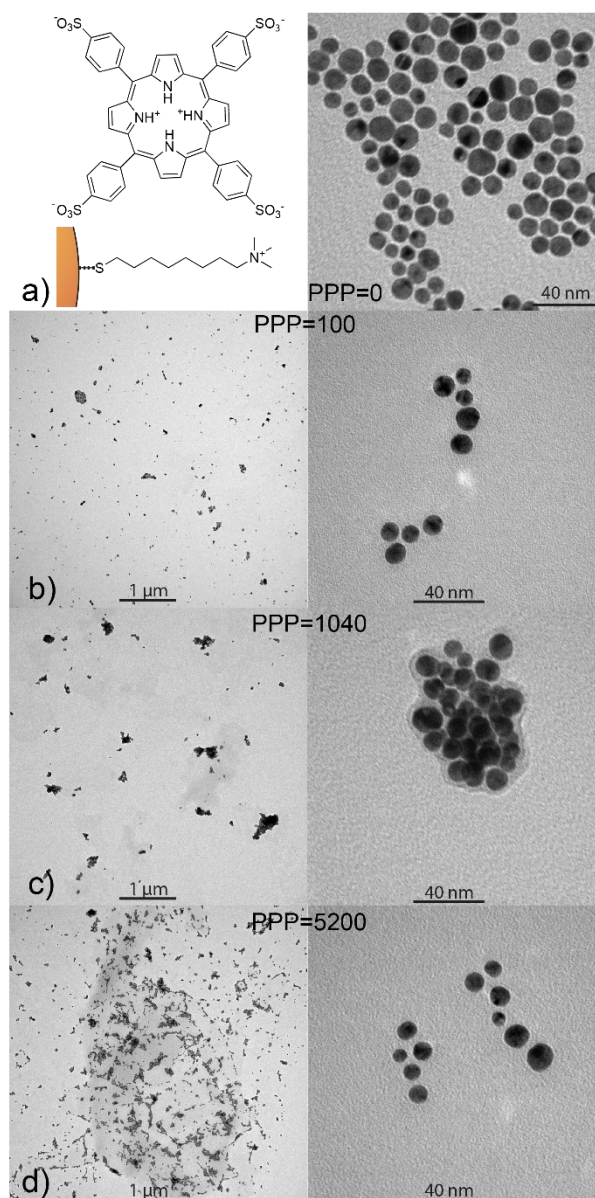
Figure 11.1. a) Molecular structure of diprotonated H_2-TPPS^{2-} and TMAOt capping molecule (left) and TEM image of cationic NSs (right, scale bar 40 nm). b)-d) TEM images of NS-TPPS nanohybrids prepared with different values of the 'porphyrin-per-particle' (PPP) parameter at two different magnifications (scale bars: 1 μm on the left and 40 nm on the right); b) PPP=100; c) PPP=1040; d) PPP=5200. At intermediate values of PPP (PPP~1000), the formation of a more significant amount of NSs' aggregates is found.

On these bases, we prepared NSs with an average diameter of 11±2 nm by a modified Turkevich procedure and coated them with TMAOt (Figure 11.1a) as described in section 6.1.[110] NSs of this

size can both support strong plasmons and give rise to stable suspensions in water. The hybrid nanosystems were then assembled by simply mixing NSs (5-30 μM) and H_2-TPPS^{2-} (0.5-4 μM) in water at pH 2.2 (6.3 mM HCl). In these low-concentration conditions and in the absence of NSs, the porphyrin is primarily present as free monomers and the formation of aggregates can only occur by the nanoparticle templating action. As expected, I found that the nature of the hybrid formed is mainly controlled by the ratio between H_2-TPPS^{2-} and NSs concentration in solution. For this reason, I defined the 'porphyrins-per-particle' (PPP) parameter, calculated as the ratio between the nominal concentrations of H_2-TPPS^{2-} and NSs in the final solution. Geometrical calculations indicate that depending on the orientation they assume on the particle surface, the number of porphyrin units necessary to coat the whole surface of a nanoparticle with a diameter of 11 nm ranges from about 300 ("parallel" orientation) to 1400 ("perpendicular" orientation).

I explored the supramolecular assembly of NSs and H_2-TPPS^{2-} for PPP values going from 0 (only NSs) to 10400, comparing the modifications of the extinction spectra of the resulting solutions with respect to those of the bare constituents. In the following, nanohybrids obtained at a specific value of PPP will be labeled as NS-TPPS_PPP. The nanohybrids obtained were characterized by TEM analyses (figure 11.1). Figure 1b), 1c) and 1d) report, as an example, the TEM micrographs collected for three nanohybrids samples with PPP=100, 1040, and 5200.

11.3   Extinction spectra

Figure 11.2b shows the extinction spectra of nanohybrids (blue) obtained at selected values of PPP. As a term of comparison, the spectrum of the NSs at PPP=0 (red), and of the monomeric and J-aggregate forms of H_2-TPPS^{2-} (figure 11.2a-c) are reported. The extinction spectrum of the NSs is characterized by the typical plasmonic resonance at about 530 nm.[47]

H_2-TPPS^{2-} in the monomeric form features two main groups of absorption bands. At higher energies, the so-called B-band at 434 nm can be identified, while at lower energies, the weaker Q-bands are found at 650 and 580 nm. In the J-aggregate, the presence of intermolecular excitonic interactions causes the splitting of each of the monomer bands into a blue-shifted and a red-shifted band.[143,155,156] This is particularly evident in the B band region where two new excitonic bands appear at 420 and 490 nm. The effect is less pronounced in the Q band region where the excitonic interactions are lower and the presence of a vibronic progression makes the identification of the bands more difficult. The absorption properties of this porphyrin in different aggregation states have been the object of several investigations, and more details can be found for example in refs.[147,151,155]. In figure 11.2, dashed green lines (dashed for the monomer,

dotted for the aggregate) pinpoint the most intense bands (434 and 650 nm for the monomer, and 490 and 710 nm for the J-aggregate).
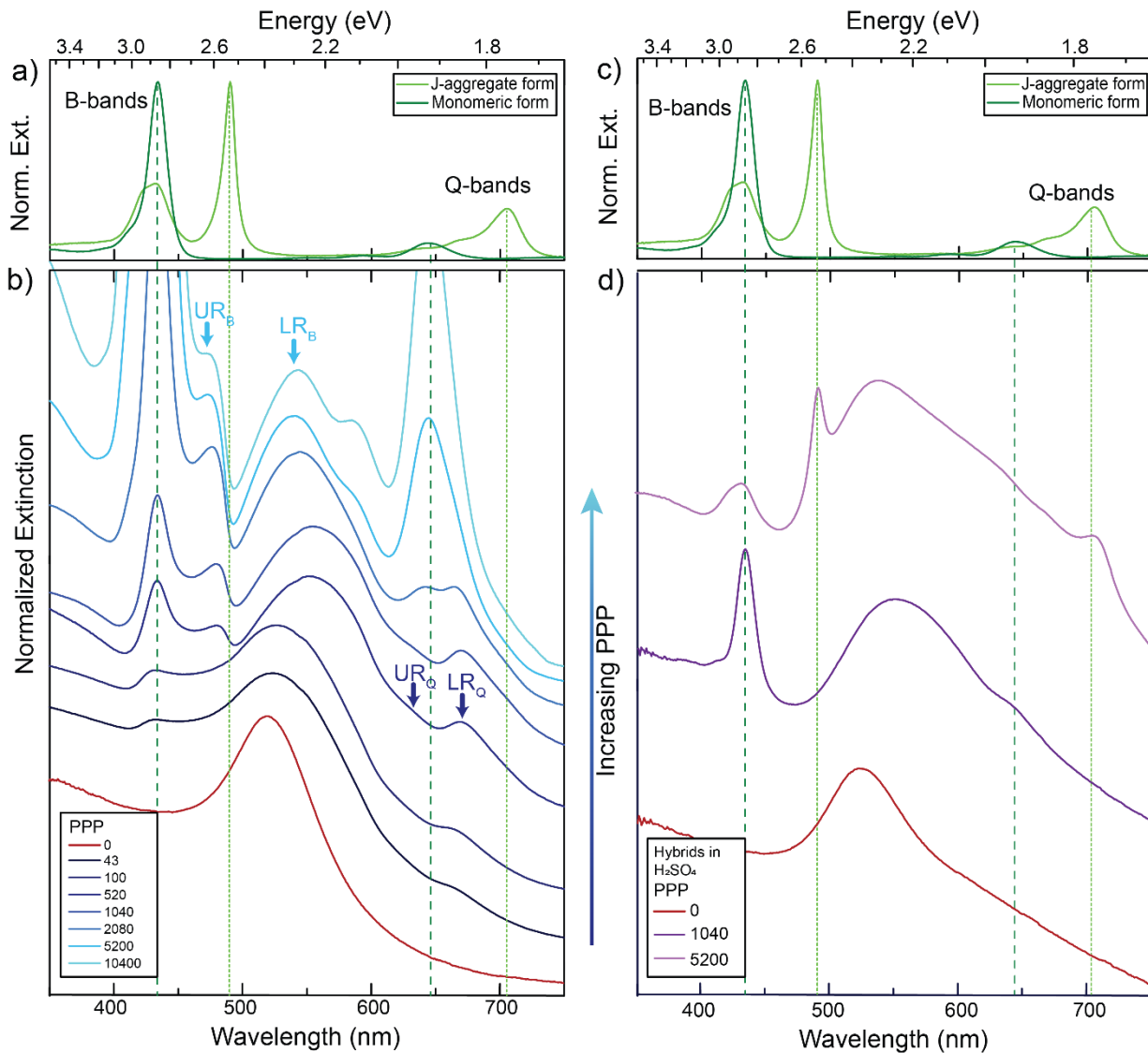
Figure 11.2. Normalized extinction spectra of a)-c) H_2-TPPS^{2-} in its monomeric and J-aggregate form and b)-d) nanohybrids at increasing values of PPP from PPP=43 to PPP=10400; the red line represents the extinction spectrum of bare NSs (PPP=0). The spectra are shifted vertically to ease the comparison. Vertical dashed lines pinpoint the position of the main absorption bands of H_2-TPPS^{2-} in its two forms. Light blue (dark blue) arrows indicate the position of the UR$_B$/LR$_B$ (UR$_Q$/LR$_Q$) plexciton resonances. d) nanohybrids were prepared as the samples in Figure b) but replacing HCl with H_2SO_4. Sulfate ions switch off the plexciton interactions. PPP=0 (only NSs, red); PPP= 1040 (purple) and PPP= 5200 (pink). In this latter sample, the H_2-TPPS^{2-} aggregation was promoted by the addition of Na_2SO_4 to ease the comparison with the spectra of the non-interacting species (see the section 6.4 for more details on the preparation of these samples).

When the spectra of the hybrids systems are analyzed, it is immediately apparent that they do not correspond to the mere sum of the NSs and H_2-TPPS^{2-} spectra, and this is the first evidence for the presence of significant interactions between the NSs and the porphyrins at the surface. Clear trends can be identified as a function of the PPP. At high values of PPP (PPP>1000), the

III Results and Discussion

overall amount of H_2-TPPS^{2-} is in large excess and it is high enough to ensure the complete saturation of the NSs surface even in the "perpendicular" configuration. In these conditions, the formation of porphyrin aggregates on the surface of the particles is expected.[152] More generally, it is also known that NPs are able to template the formation of aggregates onto their surface.[48,157–162] The extinction spectra clearly suggest the presence of both free H_2-TPPS^{2-} (strong and sharp bands at 434 and 650 nm and nanoparticle-adsorbed J-aggregates. These are revealed by the shoulder at 710 nm and, in particular, by a pronounced dip in the B band region in correspondence of the exciton band of the aggregate at 490 nm, accompanied by two side peaks at about 477 and 540 nm (light-blue arrows in figure 11.2b). These bands present the typical anti-crossing behavior expected when plexcitonic resonances are formed. Similar features were also reported for H_2-TPPS^{2-} J-aggregates strongly coupled with Al nanodisks[163] and nanostructured silver films.[103,164] Therefore, these two bands can be attributed to the formation of an upper and lower plexcitonic resonances, arising from the strong coupling between the 490 nm exciton resonance of H_2-TPPS^{2-} J-aggregates and the plasmon resonance of NSs. These plexciton resonances will be denoted from now on as UR$_B$/LR$_B$ where the B subscript highlights their involvement in the B-bands range. The estimated $\hbar\Omega_R$ from the difference of the UR$_B$ and LR$_B$ energies is 430 meV (equation 4.18), while $\hbar k$ and $\hbar\gamma$ were estimated 175 meV and 31 meV, respectively, from the extinction spectra reported in figure 11.2a and b. This leads to a coupling $\hbar g$ of about 200 meV (equation 4.18). An error of about 20% has been estimated for this value because of the uncertainty in precisely selecting the position and the width of the experimental bands. Nevertheless, the estimated value is in good agreement with previous findings[103,163,164] and the strong coupling condition (equation 4.23) holds in any case.

At intermediate values of PPP (PPP~1000), a significant amount of free H_2-TPPS^{2-} cannot be observed because all the H_2-TPPS^{2-} can be accommodated on the particles' surface available. In the B-band region, the features attributed to the UR$_B$/LR$_B$ are still identified, although weaker. The LR$_B$ band previously detected at 540 nm appears now red-shifted (the maximum at PPP=1040 is at 560 nm) and wider with respect to the analogous band at higher PPP. This behavior can be justified by invoking the formation of a more significant amount of NSs' aggregates,[165] as it is also apparent from the comparison of the TEM images of Figure 11.1 c and d, and the consequent redshift of the corresponding plasmonic band. Moreover, in the Q-bands region, a second dip, although less pronounced, is present at about 650 nm, corresponding to the most intense Q band of the monomer. Two adjacent maxima at about 620 and 670 nm could also be identified (blue arrows). These latter features appear around PPP = 2080 and remain

present also at lower values of PPP (PPP<100), where the signals due to UR_B/LR_B are not visible any more.

I attribute the modification of the spectra in the Q bands region to the formation of a second set of resonances, denoted as UR_Q/LR_Q, arising from the coupling between the 650 nm resonance of the monomeric H_2-TPPS^{2-} and the red tail of the plasmon resonance of NSs. I calculated $\hbar\Omega_R$, $\hbar k$ and $\hbar\gamma$ being 170, 175 and 50 meV, respectively, which brings to a $\hbar g \approx 100$ meV (equation 4.18), with an uncertainty of about 20%. This value does not satisfy the plexcitonic existence condition (equation 4.22), which suggests that UR_Q/LR_Q, rather than be the expression of a Rabi splitting, represents a Fano-like plexciton (section 4.2).

At low PPP values (PPP<100) the B-band region is dominated by a weak and broadened signal at about 434 nm corresponding to the B-band of the monomeric H_2-TPPS^{2-}, suggesting the presence in the samples of only NS-adsorbed porphyrin monomers. Noteworthy, the plasmon band in the 500-550 nm region shifts back to the blue with a maximum of 533 nm and accordingly also the TEM images capture a lower degree of NSs aggregation (Figure 11.1b).

As further verification of the establishment of a strong coupling between NSs and H_2-TPPS^{2-} both in monomeric and J-aggregate forms, nanohybrids with the same PPP values were prepared using H_2SO_4 instead of HCl. The doubly negatively charged sulfate anions, present in large excess, inhibit the binding of the porphyrins as a result of effective competition. As expected, the extinction spectra of the obtained nanohybrids, except for a slight red shift of the plasmonic resonance due to NSs aggregation caused by sulfate anions,[166] are basically superpositions of the spectra of the non-interacting species (Figure 11.2d).

11.4 PL spectra: evidence for a plexciton relaxation cascade

Since the photoluminescence (PL) quantum yield of plexcitons is known to be very low, if any,[78] (section 4.4), the emission of residual traces of unbound molecules of H_2-TPPS^{2-} is expected to contribute significantly to the PL spectrum in most cases. To minimize this contribution, the nanohybrid samples were purified by the excess of unbound porphyrin using a series of centrifugation and resuspension cycles. The integrity of the nanohybrids and the reduction of unbound porphyrin molecules were checked by recording the extinction spectrum before and after each centrifugation cycle.

In figure 11.3a I reported the PL spectra measured for the NS-TPPS_1040 sample at different excitation wavelengths. A weak PL signal at 668 nm, typical of the uncoupled H_2-TPPS^{2-} monomer,[147] is recorded when the excitation wavelength is tuned close to one of the absorption

bands of the porphyrin (λ_{exc}=470 and 550 nm). Upon excitation at 510 nm, however, a blue-shifted emission band centered at 655 nm appears. The presence of this band is reproducible across different batches of samples prepared in the same conditions. At 510 nm, the oscillator strength of the non-coupled H_2- $TPPS^{2-}$ is very low and therefore its contribution at this exciting wavelength is minimized. This emission signal has only one maximum at a wavelength located in between the UR_Q and LR_Q resonances, which indicate an intermediate (Fano) coupling regime (section 4.4), as also supported by the estimated value of $\hbar g$.
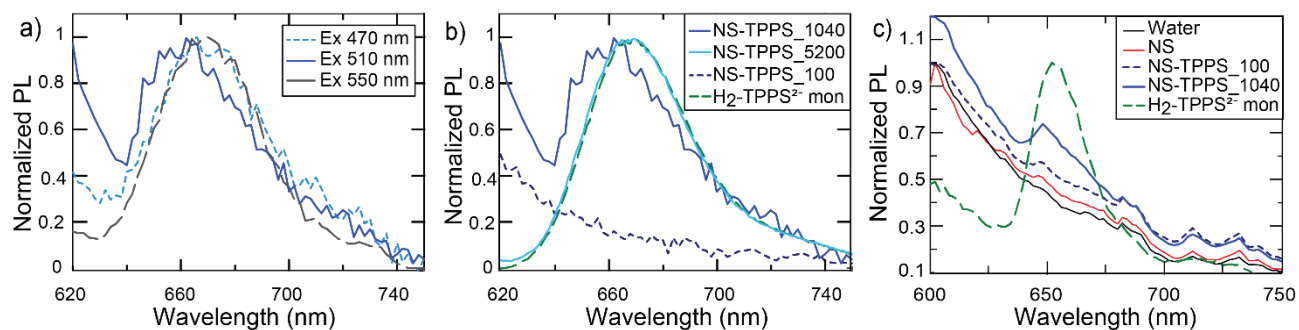
Figure 11.3. a) Normalized PL spectra recorded for the sample NS-TPPS_1040 at different excitation wavelengths; b) Comparison between the normalized PL spectra of NS-TPPS_1040 (blue line), NS-TPPS_100 (dotted black line), NS-TPPS_5200 (light blue solid line) and H_2-$TPPS^{2-}$ in the monomer form (green dashed line), obtained exciting at 510 nm; c) PL spectra measured at 77K.

It is also worth noting that this emission in the Q bands region is promoted by excitation at 510 nm, resonant with the LR_B band. This immediately suggests that the signal detected at 655 nm can be likely attributed to the PL from the UR_Q/LR_Q resonances, following the relaxation from the initially excited LR_B. Because of the low PL signal, the excitation spectrum of the sample did not give any meaningful information. However, as control experiments, I also recorded, at the same excitation wavelength, the PL of solutions of the nanohybrids NS-TPPS_5200 and NS-TPPS_100, where only UR_B/LR_B and UR_Q/LR_Q are predominant, respectively (figure 11.3b). The inspection of the spectra reveals that no emission is observed in the NS-TPPS_100 sample, suggesting that the UR_Q/LR_Q cannot be directly excited at 510 nm. In contrast, in the NS-TPPS_5200 sample only the emission at 668 nm due to residual uncoupled H_2-$TPPS^{2-}$ is detected. Also, no emission is observed for both the samples in the wavelength region between 470 nm and 550 nm, suggesting that the UR_B/LR_B manifolds are not emissive. Finally, I repeated the extinction and PL measurements on the same samples at 77K (figure 11.3c). The extinction spectra at 77K present the same features already found also at room T, with bands slightly narrower. Also the PL behavior is similar, except that the PL signal at 655 nm is strongly quenched. This implies that the mechanism of population of the emitting state is annihilated at

low temperature, suggesting that phonons and coupling with vibrational modes may have a non-negligible role in the relaxation dynamics.[167]

11.5   Two different kinds of tunable plexcitons with the same molecule

While the appearance of the UR_B/LR_B at high PPP is in line with previous findings and falls clearly into a regime of strong coupling, more intriguing is the behavior of UR_Q/LR_Q. As I will discuss in part IV, the formation of plexcitons with monomeric QEs is a rare phenomenon for CPM. Moreover, in our specific case, not only the extinction coefficient of the Q band of the monomer is modest, but also its spectral overlap with the NSs plasmon is relatively poor. Consequently, the formation of plexcitonic resonances between monomeric H_2-$TPPS^{2-}$ molecules and a single NS seems unlikely.

I suggest that the peculiar behavior in the Q bands region could be attributed to the formation of plasmon nanogaps[168] where the H_2-$TPPS^{2-}$ molecules are trapped between two closely adjacent metal nanostructures. Similar geometries have already been discussed in chapter 2, even though they were prepared with a plasmonic surface and a NP, while here the nanogaps are between dispersed NSs. In our conditions, the resonant peak of two interacting particles is red-shifted from that of a single particle because of near-field coupling.[165,169–171] This, in turn, would reduce the detuning δ with the Q band transition. Experimentally, the hypothesis of nanogaps formation in aggregates of NSs is supported by the TEM images, which indeed capture a higher degree of aggregation exactly for conditions where the UR_Q/LR_Q resonances appear more intense (PPP~1000, figure 11.1c). The same behavior is verified looking at the changes of the plasmonic band in the 500-550 nm region as a function of PPP, which red-shifts and becomes broader concurrently with the appearance of the bands at about 620 and 670 nm, assigned to the formation of UR_Q/LR_Q plexciton resonances. Moreover, the width of the interstitial spaces recorded in the TEM images, significatively increased when H_2-$TPPS^{2-}$ is added, is compatible with the possibility of the presence of tilted molecules of H_2-$TPPS^{2-}$ crosslinking the NSs (figure 11.4).

All these experimental findings point toward the reasonable attribution of the UR_Q/LR_Q features to plexciton resonances in the intermediate coupling regime. Nevertheless, it is known that even without the formation of hybrid plexcitonic states, the plasmon-mediated interaction between the excitations of co-adsorbed molecules can result in modifications of the absorption properties of the molecular moieties, including the appearance of bands' splitting, shifts, and asymmetric line shapes.[172] The first evidence against this argument is that in this case dependence of the

spectral modifications on the degree of coverage is typically recognized,[172] which is not the case here.
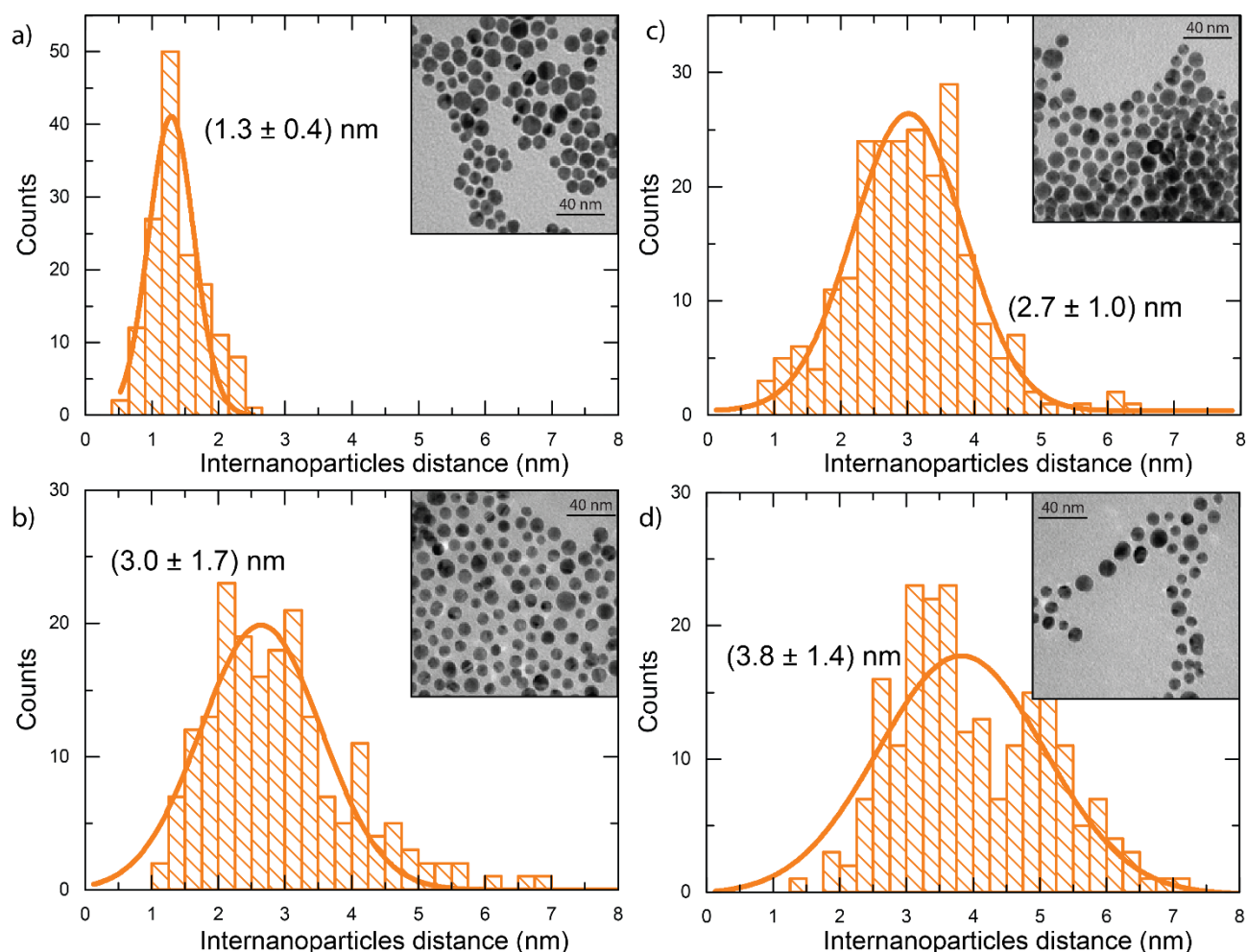
Figure 11.4. a), b), c), d) Distribution of the inter-nanoparticle distances of each sample and gaussian fit of the data of the sample NS-TPPS_0, NS-TPPS_100, NS-TPPS_1040 and NS-TPPS_5200, respectively. The insets report the respective TEM micrographs. The centroid and the half width at half maximum of the fitting are reported into the figure for each graph as mean value and error, respectively. Data relative to the NS-TPPS_5200 sample can also be fitted with a bimodal gaussian fit yielding the average interparticle distances of 2.3 and 4.6 nm.

To further corroborate the hypothesis on the nature of the plexcitonic states UR_B/LR_B and UR_Q/LR_Q, Boundary Element Method (BEM) electrostatic calculations have been performed in collaboration with the group of professor S. Corni (Università degli Studi di Padova). NSs with a diameter of 11 nm were simulated with two symmetrical promontories of J-aggregates to consider the anisotropic optical response of the porphyrins (cartoon inset in Figure 11.5). The extinction spectrum obtained in these conditions, compared with the experimental extinction spectrum at PPP=520 successfully predicts the formation of plexciton bands in the B-band region, supporting our interpretation of UR_B and LR_B (Figure 11.5a). In the case of NSs interacting with H_2-TPPS^{2-} in the monomer form, several arrangements of NSs aggregates and various

III Results and Discussion

distances between NSs inner cores have been explored. In particular, it was found that large linear aggregates of NSs can be tuned to be resonant with the monomer Q band and promote the building of an intermediate coupling regime and the formation of the UR_Q/LR_Q resonances (Figure 11.5b).
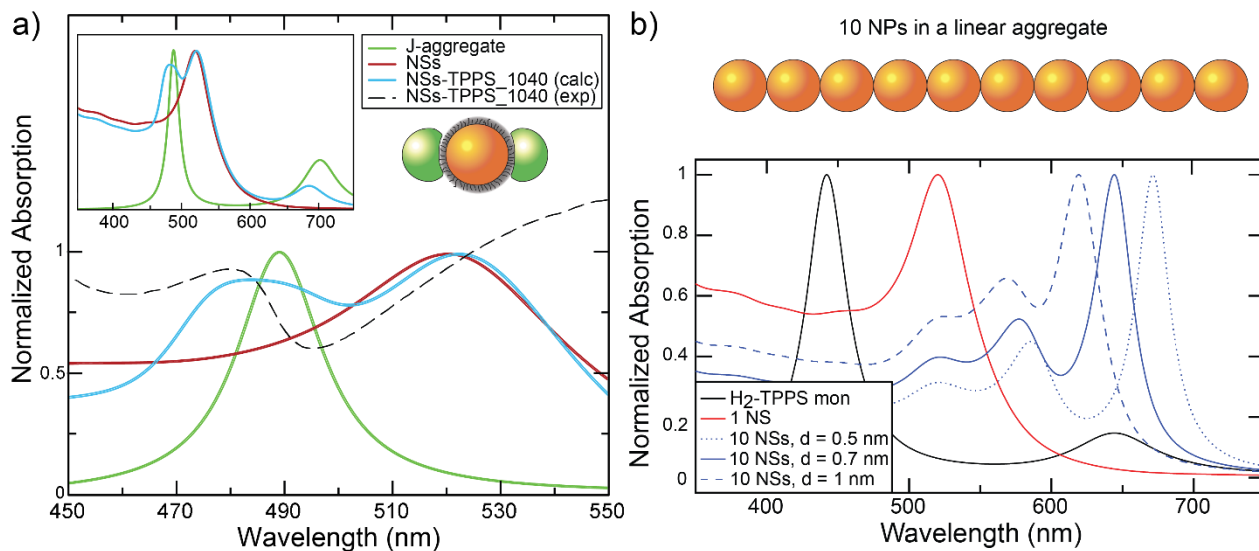
Figure 11.5. a) Simulated normalized absorption spectrum in the 450-550 nm wavelength range of a capped gold NS of 11 nm diameter (red), a H_2-TPPS^{2-} J-aggregate sphere (green), and a NS with two symmetrically located J-aggregate promontories (light blue). The experimental extinction spectrum at PPP=520 is also reported for comparison (dashed black line). The cartoon schematizes this model depicting the NS (orange sphere) and the J-aggregate promontories (green spheres). The simulated spectra in the full 350-750 nm range are reported in the inset. b) Simulated normalized absorption spectrum for a H2-TPPS^{2-} monomer (black), a capped gold NS (red), and a 10 NSs necklace-like aggregate (cartoon on top) at a different inter-particle distance (blue).

These findings demonstrate that in our systems, one or two sets of plexciton resonances can be selectively activated by controlling the aggregation state of the porphyrin on the particle surface, and the particles aggregation, as summarized in table 11.1. This, in turn, is essentially obtained by tuning the relative ratio between particles and dyes in the samples. However, a fundamental contribution is also provided by the multivalent nature of H_2-TPPS^{2-} which, thanks to the four peripheral negative charges, can act as nanoparticles crosslinker both in the monomeric and J-aggregate form. When the H_2-TPPS^{2-} concentration is low enough, only individual dye molecules are present on the unsaturated particle surface. These conditions promote the aggregation of the particles with nanogaps formation and the sole UR_Q/LR_Q plexciton is observed. It can be speculated that nanoparticles aggregation might induce H_2-TPPS^{2-} molecules to take a perpendicular (or anyway tilted) orientation with respect to the particle surface and this in turn reinforce the crosslinking ability of the dye. In the light of this, it

is clear that a fine control of the orientation of the porphyrins on the metallic surface may reveal to be a crucial, although challenging, task, further studied in the next chapter.

As their concentration increases, porphyrins start to form J-aggregates on the surface of the nanoparticles, and this turns on the UR_B/LR_B plexciton. Eventually, the whole particle surface is coated by J-aggregates. This circumstance reduces the aggregation of the nanoparticles, as reported by Dynamic Light Scattering (DLS) measures reported in the next chapter and increases the interparticle distance (Figure 11.4). At high PPP the sole UR_B/LR_B plexciton is observed, likely because few or no particle-bound monomers are present in the sample. Finally, all the plexcitons can be easily deactivated by adding a species, as the sulfate anions, with a higher affinity for the particle surface.

Table 11.1. Summary of the obtained regimes: one or two sets of plexciton resonances (UR_B/LR_B and UR_Q/LR_Q) can be selectively activated by controlling the PPP parameter. Gold NSs are represented as orange spheres, while H_2-$TPPS^{2-}$ in the monomer (J-aggregate) form is depicted as blue (green) ellipses. In the first column, purple circles represent sulfate anions, hindering the coupling between porphyrin and NSs. In the insets: experimental TEM images.

with sulfate anions	PPP=100	PPP=1040	PPP=5200
NO plexciton resonances	UR_Q/LR_Q plexciton (intermediate 'Fano' regime)	UR_Q/LR_Q + UR_B/LR_B plexcitons: plexciton relaxation cascade	UR_B/LR_B plexciton (strong 'Rabi' regime)

These nanohybrids represent a substantial step further with respect to the few examples of 'tunable' plexcitons reported so far in the literature.[77,92,141] Indeed, the degree of external control reached by our systems is not limited to a change in the coupling regime of the same plexciton resonance. Instead, by exploiting the higher complexity of the porphyrin dye and its supramolecular interactions with nanoparticles, more than one plexciton resonance can be

promoted, and each resonance can be selectively activated or deactivated acting on external conditions such as dye concentration and addition of anions (table 11.1).

The presence of coherent channels has already been verified in H_2-TPPS^{2-} J-aggregates and the possibility to self-assemble these aggregates within suitably designed nanostructured environments has already been proposed as a viable strategy to control energy and charge transport.[174] Indeed, the combination of molecular excitons and plasmons in strongly coupled hybrid systems is particularly attractive because of the very extensive control over the plasmon modes supported by metallic nanostructures. Such control derives from an established knowledge between the details of the nanostructure and the associated plasmon mode.[9] Here I have demonstrated the feasibility of this approach preparing hybrid nanostructures where indeed a cascade relaxation channel can be activated or deactivated according to externally controlled conditions.

It should also be noted that the situation achieved at intermediate values of PPP, with the simultaneous presence of two sets of plexciton resonances, is quite different from the so-called 'double Rabi splitting'[175], or 'hybrid polaritons'[54] where different molecular species are coupled with the plasmonic substrate and undergo optically driven mixing. Here the UR$_B$/LR$_B$ and UR$_Q$/LR$_Q$ resonances can be modulated independently, and, most importantly, they are formed starting from the same molecule in different aggregation forms rather than by multiple functionalization. Moreover, the two sets of plexciton resonances are connected by a relaxation phenomenon that promotes the PL emission from UR$_Q$/LR$_Q$ only upon excitation of LR$_B$, whereas the PL is not activated by direct excitation. The presence of this relaxation channel, furtherly characterized in chapter 13, might imply a polaritonic-assisted mechanism, analogously to polariton-assisted energy transfer, recently demonstrated between different species coupled to the same plasmonic structure.[54]

The activation of a relaxation cascade mechanism among the two plexciton resonances opens exciting perspectives to control the flow of excitation energy for example in light-harvesting applications. From a general point of view, the presence of strong coupling among units involved in energy transport processes is currently recognized as a key design factor to control the mechanisms of energy transfer, through the activation of coherent transport channels.[88,121]

12. Controlling the formation of plexcitons by manipulating the aggregation of dyes on ligand-shell protected gold nanospheres

12.1 Introduction

In the last chapter, I characterized a responsive and tuneable CPM, consisting in the assembling of H_2-TPPS^{2-} (figure 12.1a) on cationic gold nanoparticles (figure 12.1b). In particular, the coupling between the Q band of the monomeric H_2-TPPS^{2-} and the NSs produced intriguing Fano-like resonances. Not only the dipole moment of the Q band of the monomer was modest, but also its detuning with the NSs plasmon was relatively high. This peculiar behaviour was attributed to two phenomena: i) the aggregation of the NSs induced by H_2-TPPS^{2-} that red-shifts the particles' plasmon to a more favourable wavelength and ii) the consequent formation of plasmon nanogaps[168] entrapping the H_2-TPPS^{2-} molecules, where the strongly confined electromagnetic field enhances the dyes' absorption. The templating action of NSs in the production of porphyrin J-aggregates and the crosslinking of nanoparticles due to H_2-TPPS^{2-} were both not trivial.

At neutral pH, the porphyrin bears four negative charges located at the peripheral sulfonate groups, while its two inner pyrrolic nitrogen are deprotonated (TPPS^{4-}). The charged groups provide the necessary polarity to grant solubility in water and prevent aggregation by electrostatic repulsion. When the pH is reduced, the protonation of the two inner pyrrolic nitrogens (pK_a~4.8) takes place (figure 12.1a). [176,177,178] The protonation results not only in a modification of the overall net charge and charge distribution but also in a conformational change. Indeed, the peripheral aryl moieties become nearly coplanar with the tetrapyrrole ring, which, in turn, adopts a saddle conformation.[176,179,180] The consequence of these modifications is a greater tendency of H_2-TPPS^{2-} to form J-aggregates, due to the reduced repulsion, the better surface overlap, and the possibility of charge pairing.[152,177,178,180–182] On the other hand, the formation of H-aggregates is hampered because of the unfavourable charge distribution.

Besides the decrease of the pH, the formation of aggregates often requires other factors, such as the increase of the dye concentration, the ionic strength, and, most relevant, the presence of templating agents[148,182–186]. Indeed, polycationic species such as cationic polymers or peptides usually induce the formation of J-aggregates.[146,187] Consequently, the ability of cationic nanoparticles to perform a similar templating role, as seen in the previous section, was not unexpected. However, the few examples reported so far in the literature reveal that different results are obtained depending on the properties of the nanoparticles and conditions used. Gold

nanorods[152,188] and carbon nanodots[189] coated with positively charged species were shown to template the formation of J-aggregates at acidic pH and also the formation of H-aggregates at basic pH. However, plexcitons formation has never been observed with these nanoparticles. Cationic maghemite (γ-Fe$_2$O$_3$) nanoparticles, on the other hand, did not template any aggregation. Instead, they partially deprotonated the dye molecules absorbed on the particle surface to get the TPPS^{4-} form, even at acidic pH.[190] These apparently contradictory examples confirm that different, and so far partly elusive, parameters control the self-assembly of the various porphyrin aggregates and, in the case of gold nanoparticles, the formation of monomeric plexcitons.

To get more insights into the role of the NSs in the formation of UR$_Q$/LR$_Q$ and their templating capability, I performed a comprehensive investigation of the effects of different parameters (size of the nanoparticles, pH, and concentration) in the interaction between nanoparticles and porphyrins. The results obtained suggest that the system is peculiarly sensitive to all these parameters, disclosing the possibility of exploiting nanoparticle templates to engineer the physicochemical properties of the hybrid assemblies.

12.2 Synthesis and photophysical characterization of the components of the hybrid nanosystems

I studied the aggregation behaviour of the porphyrin in the presence of cationic gold nanoparticles with different sizes, to explore the effect of the different particle curvature. NSs with an average diameter of 11 ± 2 nm ('big' nanospheres, BNSs) were prepared as reported in the previous chapter, while NSs with an average diameter of 2.6 ± 0.5 nm ('small' nanospheres, SNSs) were prepared with a modified Brust and Schiffrin protocol using dioctylamine as surface stabilizing agent and NaBH4 as reductant.[112] Both BNSs and SNSs were coated with a TMAOt shell by ligand exchange. For further information about synthesis and characterization of the NSs, the reader is referred to the chapter 6. The extinction spectra of the suspensions of the two NSs' samples are reported in figure 1b. BNSs featured their plasmon band at 520 nm, typical of gold nanospheres with a core diameter larger than 3 nm. This resonance band is barely detected in SNSs. Variation of the pH in the interval 2-11 did not affect the NSs spectra. The thermogravimetric analysis (chapter 6) allowed us to estimate similar surface ligand densities, with each thiol occupying (0.10 ± 0.02) nm^2 of the BNSs surface and (0.09 ± 0.02) nm^2 of the SNSs surface.

a)

H_2TPPS^{2-} $TPPS^{4-}$

pKa ≈ 4.8

b)

c)

d)
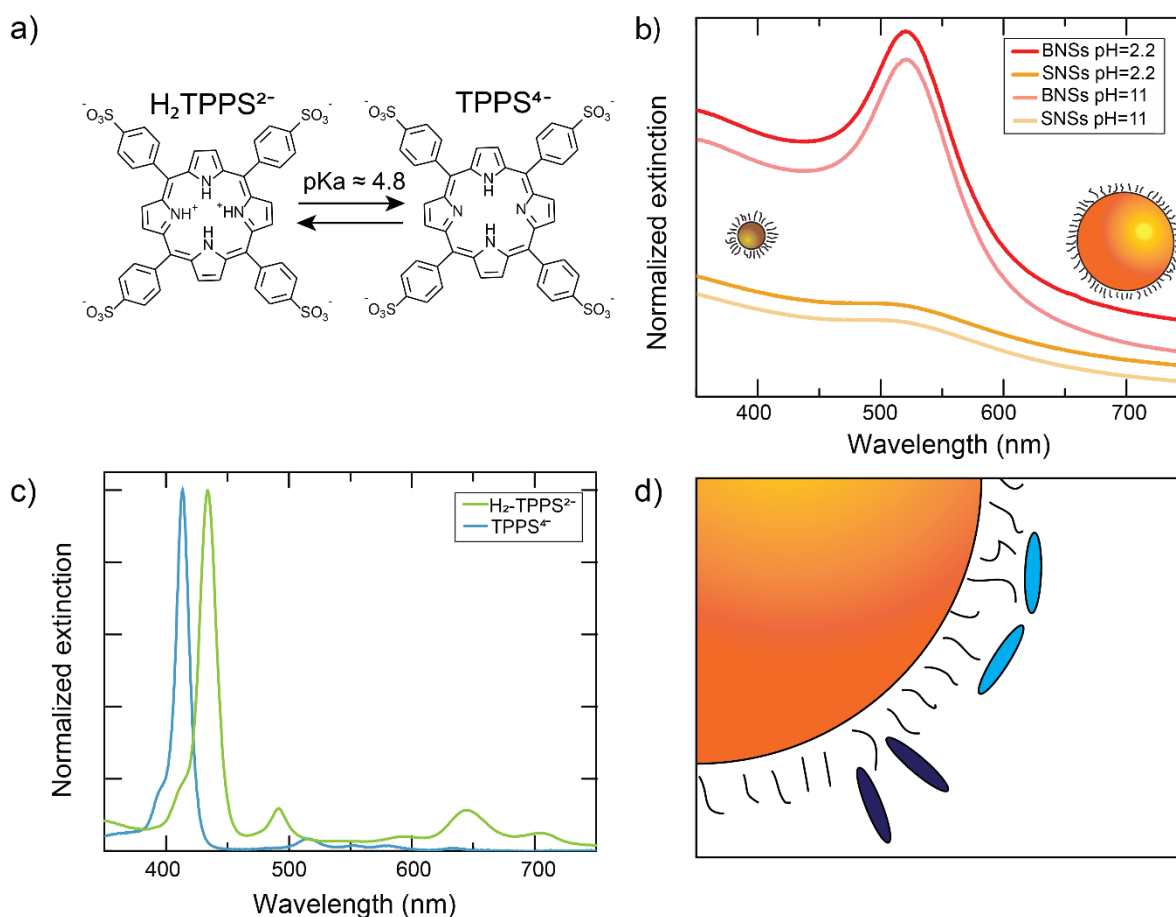
Figure 12.1. a) Molecular structures of diprotonated and free base porphyrin, labelled H_2-TPPS^{2-} and TPPS^{4-}, respectively; b) extinction spectra of big (BNSs) and small (SNSs) nanoparticles at different pH. The spectra are shifted vertically to ease the comparison. The cartoons of big and small nanospheres are represented in scale; c) Normalized extinction spectra of H_2-TPPS^{2-} at pH=2.2 and of TPPS^{4-} at pH=11 (1 μM solutions in MilliQ water); d) Perpendicular (dark blue) and parallel (light blue) orientation of the porphyrins on a nanoparticle surface.

DLS analysis of BNSs at pH=2 (table 12.1) yielded the average hydrodynamic diameter of 12.0 ± 0.8 nm, which might suggest a TMAOt shell of about 1 nm, as confirmed by TEM measurements reported in the previous chapter. Contrarywise, when the pH was set to 11, the hydrodynamic diameter raised to (28 ± 8) nm, suggesting the presence of a modest particles' aggregation, not detectable in the extinction spectra. This phenomenon can be attributed to the increased concentration of OH$^-$ ions, which likely bind to the nanoparticles' surface more strongly than Cl$^-$ ions and reduce the repulsion among the nanoparticles favouring their aggregation.

Figure 11.1c reports the reference spectra of the porphyrin at 1 μM concentration. At basic pH, the typical TPPS^{4-} spectrum, with the B band at 413 nm and the four Q bands at 515 nm, 550 nm, 580 nm, and 635 nm, was retrieved.[176,179,180] By decreasing the pH to 2.2, the spectrum turned into that of the protonated H_2-TPPS^{2-} with a modest amount of J-aggregate (see chapter 11).[176,179,180] Hence,

in the absence of NSs, the typical signatures of TPPS^{4-}, H$_2$-TPPS^{2-} and its J-aggregate could be detected in the extinction spectra of the porphyrin in the pH range explored.

Based on these results and the available literature, I pinpointed two main parameters expected to have the most relevant effect on the porphyrin aggregation. First, the pH, which was set at 2.2 and 11.0 to ensure that in these conditions H$_2$-TPPS^{2-} and TPPS^{4-} are present, respectively. Second, the Particle Area Per Porphyrin (PAP) parameter, which expresses the dye concentration in terms of the ratio between the average nanoparticle surface area and the number of porphyrin molecules in the sample. In particular, I chose PAP values capable of ensuring either the full saturation of the particles' surface or a partial coating. To do so, I estimated that the surface covered by a single porphyrin should range from 0.4 nm^2 ('perpendicular' orientation) to 2 nm^2 ('parallel' orientation) of the NSs surface (figure 12.1d).[191] Consequently, I set the PAP values used in the experiments to 0.35 nm^2 (surface saturation condition) and 3.5 nm^2 (surface subsaturation condition). With respect to the PPP parameter defined in the previous chapter, PAP allows a better comparison between BNSs and SNSs, since it also keeps into account the surface of the NPs, which changes significantly between the two NPs considered.

Thus, I performed a systematic spectroscopic investigation of the photophysical behaviour of the porphyrin in the presence of either SNSs or BNSs at the selected pH and PAP values. Each sample was independently prepared by adding the dye (final concentration: 1 μM) to a suspension of NSs adjusted at the required pH. Extinction and emission spectra were recorded after 16 h incubation at room temperature.

12.3   Porphyrin aggregation in the presence of big NSs

The first set of experiments was performed using BNSs at PAP=0.35 nm^2 (surface saturation conditions). The extinction spectra of the samples at pH 2.2 and 11 are reported in figure 12.2a.

The analysis of the spectrum at pH 2.2 revealed the already reported results (section 11.2): H$_2$-TPPS^{2-} is present prevalently as J-aggregates adsorbed onto the NSs, as attested by the UR$_B$/LR$_B$ in the B band region and the diagnostic Q band present as a shoulder at 710 nm. Hence, in these conditions BNSs template the self-assembly of H$_2$-TPPS^{2-} to form J-aggregates, which are barely present at the same pH and porphyrin concentration in the absence of nanoparticles. Moreover, the presence of residual H$_2$-TPPS^{2-} monomers not involved in aggregates is also ascertained by the formation of the plexciton Q in the extinction spectra and the typical emission of H$_2$-TPPS^{2-} monomer upon excitation at 430 nm in the emission spectra (figure 12.2d). Fluorescence measurements revealed the emission of the Q plexciton upon excitation of LR$_B$ at

510 nm, too, as previously described. The aggregation of BNSs in the presence of H_2-TPPS^{2-}, which induces a red-shift of the plasmon band and reduces the detuning with the Q bands, has also been confirmed by DLS measurements (table 12.1) as well as by the TEM measurements reported in the previous chapter.
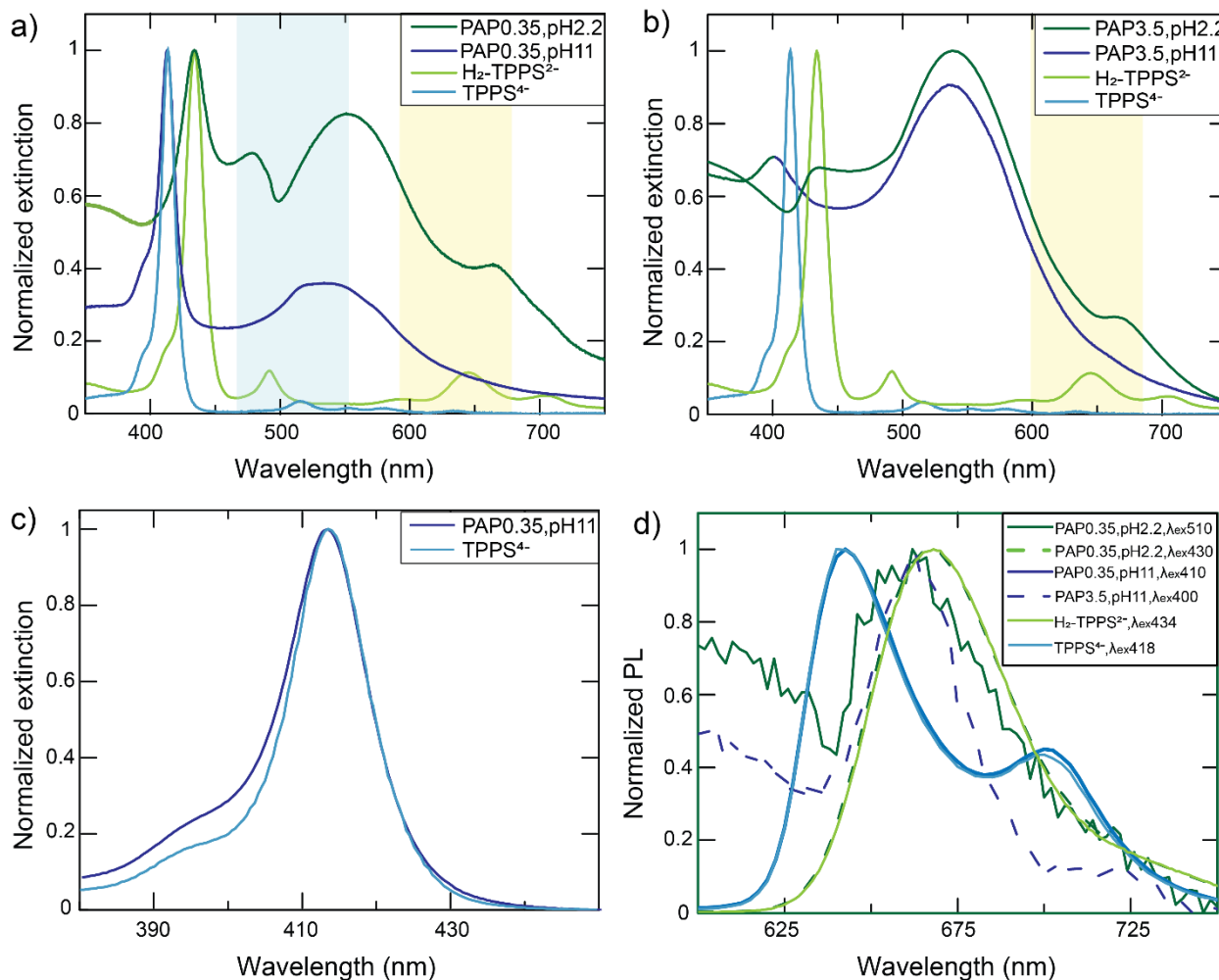
Figure 12.2. Overall perspective of extinction and emission spectra of BNSs. a) Extinction spectra of the hybrids at PAP=0.35 nm^2. H_2-TPPS^{2-} and TPPS^{4-} absorption spectra at pH 11 and 2.2, respectively, are reported as a reference; b) Same as a) but for PAP= 3.5 nm^2. The blue (yellow) area highlights the presence of UR$_B$/LR$_B$ (UR$_Q$/LR$_Q$) plexciton resonances. c) Extinction spectrum of BNSs at PAP=0.35 nm^2 and at pH=11 after subtraction of the extinction spectrum of BNSs. TPPS^{4-} absorption spectrum is reported as reference. d) Normalized PL of nanohybrids in different conditions compared with the emission spectra of H_2-TPPS^{2-} (pH=2.2) and TPPS^{4-} (pH=11). The excitation wavelengths are reported in nm.

It is relevant to note that the building up of an effective plexcitonic coupling requires that the transition dipole moments of the nanoparticles and the dyes are parallel.[50] In our case, the porphyrin has two degenerate and perpendicular transition dipole moments, both laying on the molecule plane.[176] On the other hand, the transition dipole moment of nanoparticles is orthogonal to their surface.[192] As a consequence, it can be reasonably supposed that plexcitonic coupling in

this system can be effectively established when the porphyrin molecular plane is perpendicular (or slightly tilted) to the NS's surface. In turn, this means that H_2-TPPS^{2-} monomers bound to the particles can employ at maximum two sulfonate groups to enact the formation of close contact ion pairs with the ammonium headgroups on the nanoparticles' surface.

When the pH is raised to 11.0, the extinction spectrum of the hybrid sample (figure 12.2a) appears as the simple superimposition of those of NSs and TPPS^{4-}. Also, the fluorescence spectrum recorded at various excitation wavelengths always reveals only the typical emission of monomeric TPPS^{4-} (figure 12.2d). Hence, the sample appears to be composed mostly of non-aggregated NSs (as proved by the negligible red shift of the LSPR band) and dye monomers. However, a closer inspection of the spectrum in the B bands region (figure 12.2c) suggests that the shoulder at 400 nm is more intense than expected. The presence of a signal blue shifted than that of monomeric TPPS^{4-} might indicate the formation of H-aggregates, likely templated by the nanoparticles.[146] No plexcitons are observed at this pH. There are several possible reasons for this result. First, absorption bands of H-aggregate and TPPS^{4-} poorly overlap with the plasmon of the NSs. Second, the TPPS^{4-} molecules should be bound in parallel orientation onto the BNSs surface to optimize the ion pairing interaction with the cationic surface. However, this orientation would minimize the alignment of the transition dipole moments and hamper any plexcitonic hybridization. Third, nanospheres aggregation is much less relevant than at pH 2.2 (Table 12.1), which, in turn, reduces the number of nanogaps.

Table 12.1. Centroid of the hydrodynamic diameter and relative full width half maximum.

Sample	Hydrodynamic diameter (nm)
BNSs pH=2.2	12.0±0.8
BNSs pH=11	28±8
BNSs, PAP 3.5, pH=2.2	32±8
BNSs, PAP 0.35, pH=2.2	780±60
BNSs, PAP 3.5, pH=11	1330±80
BNSs, PAP 0.35, pH=11	200±20

In the samples with PAP = 3.5 nm^2 (partial surface coverage, figure 12.2b) a different behaviour is recorded. At acidic pH, only UR$_Q$/LR$_Q$ can still be detected. Hence, in these conditions, even the presence of the nanoparticles does not induce the H_2-TPPS^{2-} aggregation, likely because the NSs/dye ratio in the sample is too low to favour the hydrophobic interaction between the dyes over the charge repulsion. Consequently, H_2-TPPS^{2-} monomers are the main species present in

the sample and can build plexcitons with the NSs through nanogaps formation. No fluorescence could be detected for this sample upon excitation in the B plexciton region (510 nm).

In the extinction spectra at pH=11 (figure 12.2b), a peak at 403 nm is the only visible feature besides the BNSs plasmon band. This band is attributed to the formation of H-aggregates. Such attribution is supported by the fluorescence spectra where two peaks at 665 nm and 725 nm have been recorded, in agreement with previous literature on H-aggregates (figure 12.2d).[146]

The results so far described indicate that BNSs can template the formation of either H-aggregates or J-aggregates, depending on the pH and PAP value.

At basic pH, the particles template the formation of H-aggregates in all the conditions investigated. In subsaturation regime (PAP = 3.5 nm^2) these are the only species present. This is somewhat counterintuitive because tetranionic TPPS^{4-} molecules present in the sample are not enough to saturate the NS surface and consequently one would expect TPPS^{4-} to bind to the cationic particle surface in the monomeric form. However, this observation is in agreement with the fact that when saturation conditions (PAP=0.35 nm^2) are reached, H-aggregates are still detected, but a large amount of TPPS^{4-} monomers, in excess with respect to the total surface available, remains free in solution.[193] The presence of TPPS^{4-} bound in the monomeric form onto BNSs surface in saturation conditions is unlikely, because of the massive amount of TPPS^{4-} and, thus, low surface availability. This indicates that the available nanoparticles' surface is fully coated by H-aggregates, and it requires only a small fraction of the porphyrins present. DLS investigations (table 12.1) also indicate that H-aggregates coating the particles in subsaturation conditions act as strong nanoparticles crosslinkers, while this effect is substantially reduced at saturation conditions (table 12.1). This could be due to the formation of a denser H-aggregates "corona" on the particles' surface in the saturation regime.

At acidic pH, the system evolves more intuitively upon the increase of the porphyrin amount, switching from nanoparticle-bound monomers to nanoparticle-bound J-aggregates as the amount of dye molecules in solution is increased.

The modulation of the system properties can also be followed from a different perspective by analysing the effect of changing the pH while keeping the PAP value constant. Let us start from a basic pH solution and with a large amount of TPPS^{4-}, where H-aggregates saturate the NSs' surface, and free monomers are present in solutions. When the pH is decreased below the pK$_a$, the porphyrins get protonated and form J-aggregates, which grow essentially by recruiting most monomers from the solution. The starting situation is not so different at basic pH and at low

concentrations of porphyrin, where again there are H-aggregates absorbed on the particles' surface, but not free monomers. In this case, however, aggregates evolve upon protonation with the disassembly of the aggregates to form surface absorbed monomers.

12.4   Characterization of the small nanoparticles nanosystems

Figure 12.3 reports the extinction spectra obtained by mixing SNSs with the porphyrin. In this case, being the SNS almost devoid of the plasmon band, observation of plexciton resonances is unlike in any condition. In addition, the effective volume cannot be sufficiently large to include enough dye molecules to result in an observable plexciton.[194,195]

In surface saturation conditions (PAP=0.35 nm^2, figure 12.3a and 12.3b), as in the case of BNSs, an extensive porphyrin J or H aggregation was observed. At acidic pH, J-aggregates (peaks at 490 nm and 705 nm) were predominant. Fluorescence spectra confirmed the presence of J-aggregates and revealed the additional presence of residual H_2-TPPS^{2-} monomers (figure 12.4): upon excitation at 418 nm, the typical emission of H_2-TPPS^{2-} monomers and a shoulder at 710 nm characteristic of the J-aggregates were recorded,[146,182] while excitation at 434 nm produced only the monomeric H_2-TPPS^{2-} emission spectrum.

At basic pH (figure 12.3a and 12.3b), the extinction spectra revealed instead the presence of H-aggregates, through the appearance of the band at 403 nm, and TPPS^{4-} monomers (band at 419 nm).

Surprisingly enough, in subsaturation conditions (PAP = 3.5 nm^2, figure 12.3c and 12.3d), the dye is always present as TPPS^{4-}, no matter the pH. At acidic pH (pH 2.2), only monomers were observed. The interaction with the positively charged monolayer reduces the apparent pK_a of the pyrrole residues, preventing their protonation even in these conditions. Effective binding of TPPS^{4-} to the nanoparticles was confirmed by the fact that the samples are not fluorescent (data not shown), because of the quenching properties of the NSs.[196] Moreover, it must be noted that the position of the B band is redshifted by 5 nm (from 414 nm to 419 nm). This suggests a certain degree of interaction between the conjugated aromatic rings of the porphyrin and the surface of the nanoparticle, through phenomena like image charge effect[197,198] or electromagnetic interactions.[199] In the sample at basic pH, on the other hand, a shoulder at about 400 nm is visible in the spectrum and can be ascribed to H-aggregates formation (figure 12.3c and 12.3d).

Hence, similarly to BNSs, also SNSs template the formation of H-aggregates at basic pH and J-aggregates at acid pH. At basic pH, the increase of the dye amount results in the rise of the fraction of H-aggregates over the particle-bound monomers. It is however noteworthy the fact

that also in this case H-aggregates are observed in subsaturation conditions. At acidic pH, the system changes from nanoparticle-bound monomers, which in this case are deprotonated TPPS^{4-} molecules, to nanoparticle-bound J-aggregates. Apparently, dyes aggregation is accompanied at this pH by their protonation. Indeed, the TPPS^{4-} form, detected as the sole species present in the samples at high PAP, does not form J-aggregates.
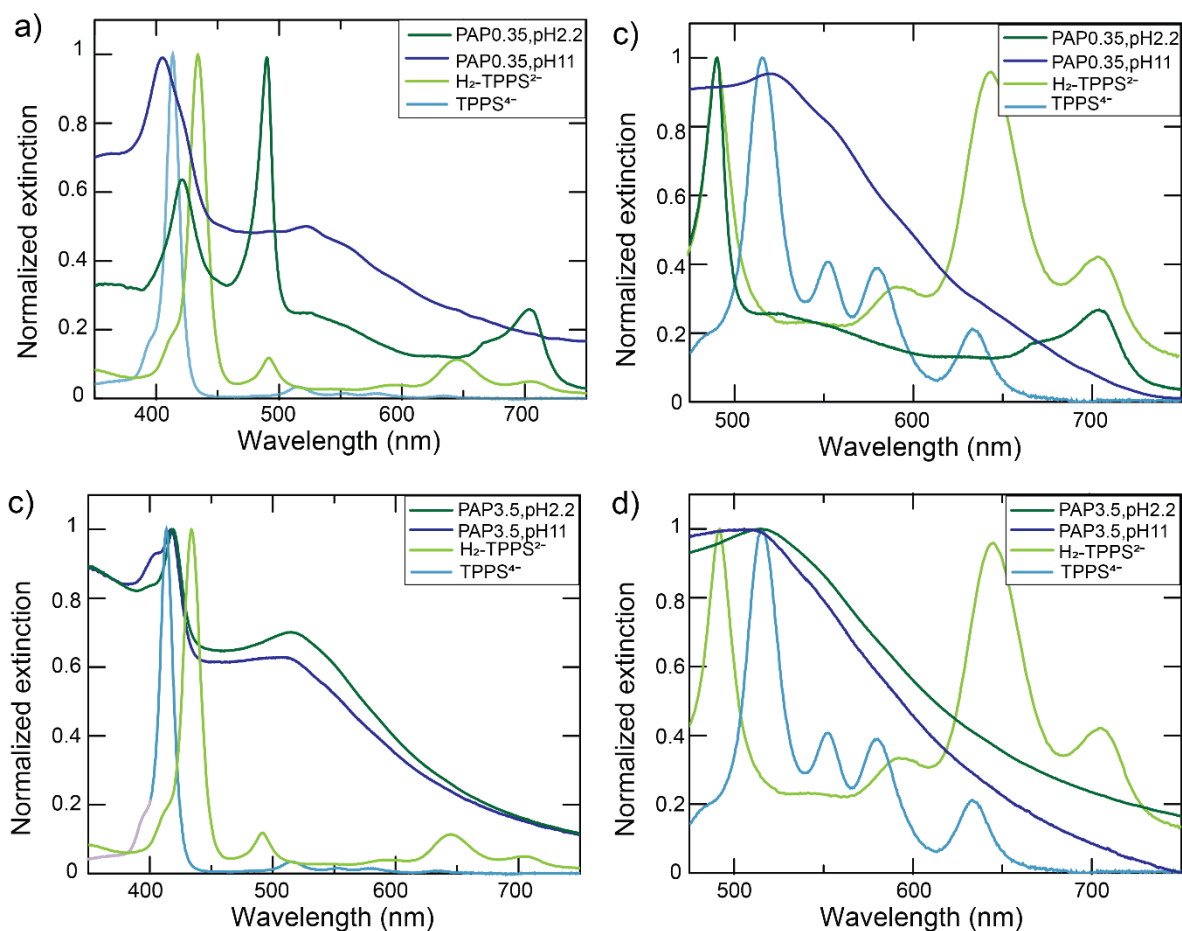
Figure 12.3. Normalized extinction spectra of SNSs, H$_2$-TPPS^{2-} (pH=2.2) and TPPS^{4-} (pH=11) at a) PAP = 0.35 and c) 3.5 nm^2. A zoom of the 480-750 nm region of each plot is reported in panel b) and d), respectively.

Looking at the systems also from the perspective of pH changes at constant PAP is again quite interesting. In saturation conditions, the protonation of TPPS^{4-} consequent to the pH decrease converts H-aggregates into J-aggregates. In subsaturation conditions, quite surprisingly, pH decrease does not produce any porphyrin protonation but the sole disassembly of H-aggregates into monomers.
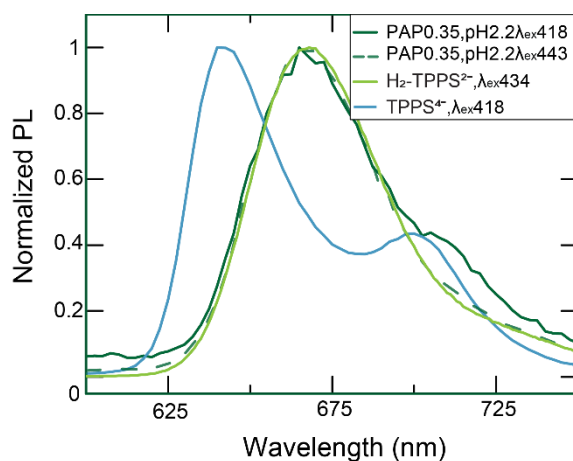
Figure 12.4. Normalized PL of the nanohybrid sample prepared with SNSs at PAP=0.35 nm^2, compared with the fluorescence of H$_2$-TPPS^{2-} (pH=2.2) and TPPS^{4-} (pH=11) as reference.

12.5   Discussion of the results

Overall, the results reported here reveal that the interactions of cationic gold nanoparticles with the tetra-phenyl-porphyrin result in a series of different structures depending on the dye/nanoparticle ratio, the pH, and the particle size. These are graphically summarized in figure 12.5.

When the dye is present in a sufficient amount to saturate their surface, the nanoparticles can template the formation of dye aggregates. I found that, regardless of the particle radius, J-aggregation is promoted in acidic conditions and H-aggregation in basic conditions, in agreement with previous studies.[152,162,188,190] The role of nanoparticles is likely to attenuate the electrostatic repulsion between the negatively charged dyes, favouring the attractive hydrophobic interactions, and to template the aggregates. This was also previously reported for other CMP-s assembled either via electrostatic interactions.[106,161,200,201]

However, it is surprising that H-aggregates are formed at basic pH even in subsaturation conditions, both with large and small NSs. H-aggregation formation is a phenomenon rarely observed because of the relevant charge repulsion of the peripheral sulfate groups, which in water is not fully counterbalanced by the hydrophobic effect. For this reason, the absorption of individual TPPS^{4-} molecules on the surface of the NSs appears to be at first sight the most likely event in subsaturation conditions, with H-aggregation occurring only in saturation conditions, when the available nanoparticles' surface cannot accommodate all the dye molecules. The counterintuitive behaviour observed here could be ascribed to the presence of OH$^-$ ions forming close ion pairs with the ammonium headgroups. If this were the case, OH$^-$ ions would reduce both the electrostatic stabilization of the nanosphere and the nanosphere surface available for ion

pairing interactions. Noticeably, the expected reduction of colloidal stability is confirmed by DLS experiments discussed above, which indicated that BNSs undergo some aggregation at pH 11. The parallel reduction of the surface available is the most likely explanation of the observation of H-aggregates also in subsaturation conditions since the decrease of the dye amount is counterbalanced by the decrease of the number of binding sites on the particles. H-aggregates' formation is quantitative in the case of BNSs, and only partial with SNSs, suggesting that binding of OH$^-$ ions could be less effective in the case of smaller NSs.
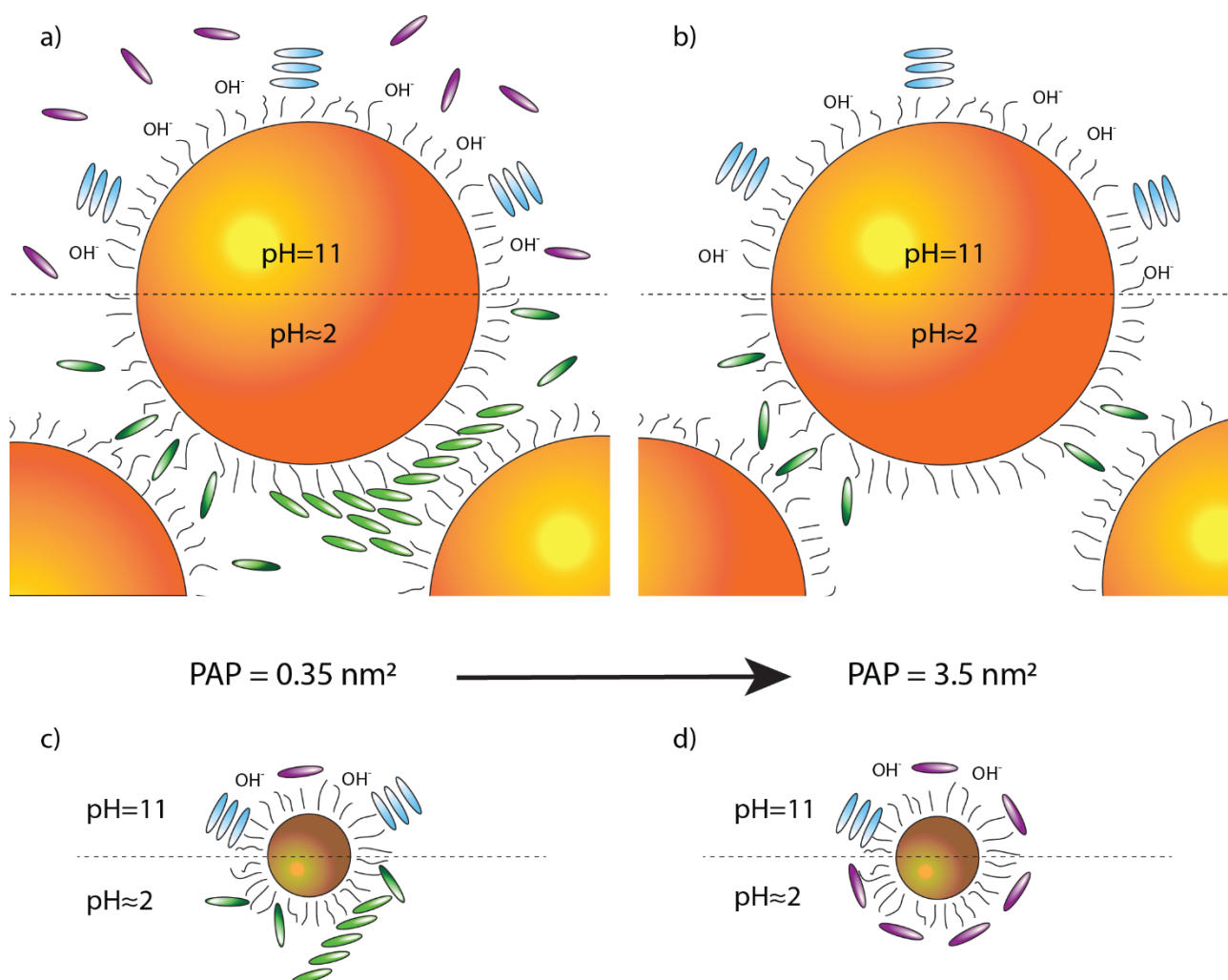
Figure 12.5. Overview of the interactions between NSs and porphyrin dyes. The structures templated by BNSs and SNSs are schematized in panels a), b) and c), d), respectively. Interactions at pH=11 (pH=2.2) are at the top (bottom) of each image. Panels a) and c) refer to PAP=0.35 nm^2, while panels b) and d) to PAP=3.5 nm^2. Each porphyrin species is pinpointed by a different colour: monomeric TPPS^{4-} (H$_2$-TPPS^{2-}) is dark purple (dark green), while H (J) aggregates are light blue (light green).

Another unexpected result in subsaturation conditions is obtained with SNSs at acidic pH. At basic pH, TPPS^{4-} has four negative charges. The binding of a tetranionic molecule to a cationic ligand shell-protected gold nanoparticle has been reported to be very strong, as expected in the case

of four ion pairing interactions providing additive contributions to the overall affinity.[110,202,203] Simple considerations based on the Coulomb law suggest that the optimal interaction is reached when the molecule lies flat on the particle surface (Appendix A.i). In this position, the distance between the sulfate groups and the ammonium headgroups of the coating thiols is minimized. This parallel orientation is also supported by the observed formation of H-aggregates in these conditions. When TPPS^{4-} is converted in the H$_2$-TPPS^{2-} form, the most stable orientation should still be the same (see later), even if a considerable charge repulsion should be generated between the positively charged pyrroles and the underlying ammonium headgroups. Our results suggest indeed that such repulsion is so relevant to prevent the protonation of the pyrrolic nitrogen atoms even at pH 2.2, in the case of small nanoparticles. This behaviour is similar to that described with cationic maghemite nanoparticles of similar size.[190]

On the other hand, in the case of big nanoparticles, the observed behaviour is different. In this case, protonation of the pyrrolic nitrogens of the dye to form H$_2$-TPPS^{2-} occurs, and the dye leaves the most favourable horizontal position to get an (almost) perpendicular position, which allows the coupling with the nanoparticle plasmon to form the plexciton. In the (almost) perpendicular position, two sulfate groups are in contact with the surface, while the other two are more distant from the surface than the positively charged pyrroles. The Coulomb repulsion experienced by the pyrroles is stronger than the attraction experienced by the outer sulfate groups. Hence, an energy cost is required to get in this less favourable orientation, which is compensated by the interaction with a second nanoparticle, leading to the formation of a nanoparticle aggregate. Remarkably this series of events, namely pyrrole protonation, transition to the (almost) perpendicular position and nanospheres' aggregation occurs only in the case of big nanospheres, but not with the small ones. The only relevant difference between the two systems is the curvature of the particles' surface. This suggests that nanosphere aggregation could be a cooperative process, where several H$_2$-TPPS^{2-} are necessary to crosslink the nanoparticles effectively. Being H$_2$-TPPS^{2-} a substantially rigid molecule, the necessary simultaneous bridging action of several dye molecules can effectively occur only in the case of less curved surfaces.

Theoretical simulations, performed in collaboration with prof. S. Corni, are currently underway to support these hypotheses.

12.6 Final remarks

This study revealed that the interaction between TPPS and cationic nanoparticles can result in the formation of a large variety of different structures. Overall, the self-assembly behaviour of

III Results and Discussion

the system is controlled by the balance of electrostatic and hydrophobic interactions established by the two entities. Negatively charged TPPS, in any form, is strongly attracted by the cationic particles' surface. Nanosphere binding attenuates the electrostatic repulsion between the dye molecules favouring the formation of aggregates, whose structure is controlled by the charge distribution of the dye itself. It is a noteworthy that the elusive $TPPS^{4-}$ H-aggregates are easily formed both with large and small nanospheres, suggesting that this is a general process and should be observed with most cationic nanoparticles. On the other hand, the formation of J-aggregates from H_2-$TPPS^{2-}$ in the presence of polycationic species is a quite recognized process and the behaviour of cationic nanospheres is in line with expectations.

The most elusive entity observed in this system is of course UR_Q/LR_Q, which consists of the coupling of the plasmon of aggregated BNSs and H_2-$TPPS^{2-}$. Indeed, monomeric plexcitons are rare for CPMs (see part IV) and, to our knowledge, this is the only example of a plexcitonic set of resonances that occurs in solution using a plasmon nanogap. Our results indicate that its formation is the result of a delicate balance of mutual interactions and structural factors. On the one hand, only a rigid and multiply charged molecule as H_2-$TPPS^{2-}$ can behave as an effective particle crosslinker. On the other hand, only large nanospheres can favour the formation of multiple interparticle bridges. Eventually, only nanospheres' aggregation can allow the dye to assume a favourable orientation, to form the nanogaps necessary to enhance its absorption and to shift the position of the plasmons to meet the coupling conditions.

13. Time-resolved dynamics of multiple plexcitons in colloidal materials

13.1 Introduction

The study of the polaritonic and plexcitonic dynamics is crucial in the fields of the quantum technologies, solar cells, nanophotonics, and numerous other applications, as listed in chapter 3. Light-matter coupling, indeed, is a vast research field to which different coupling regimes concur with different related phenomena (chapter 4). Moreover, even considering the same coupling regime, the study of different cavities and QEs, and using different experimental conditions led to rather inconsistent and discontinuous results, to the extent that it is very complicated to get a general picture. For these reasons, the debate in literature is still vivid and bright (chapter 5).

Within this framework, in chapter 11, I characterized the colloidal multi-plexcitonic material prepared by assembling NSs and H_2-TPPS^{4-} in different aggregation states. Static emission measurements revealed a relaxation cascade mechanism among the two plexcitonic resonances, where the emission from UR_Q/LR_Q occurred exciting UR_B/LR_B. In this chapter, the discussion of this phenomenon and the general dynamics of the two plexcitons will be analyzed further through transient absorption (TA) experiments. Interestingly, the results suggest that the interaction between the two plexcitons is modulated by the NSs plasmon, and that their dynamics are sensitive to the pump fluences.

13.2 Linear optical properties

Figure 13.1 summarizes the extinction spectra of the samples used for the ultrafast dynamic characterization. I considered nanohybrids with PPP=100 and 1040, where only the UR_Q/LR_Q and both UR_Q/LR_Q and UR_B/LR_B are present, respectively. In order to achieve a meaningful comparison, considering that in the nanohybrids samples the NSs are aggregated (the plasmon peak is shifted from 520 nm to ca. 550 nm, as reported in chapter 11), a solution of aggregated NSs (NSA) with a plasmonic peak in the same region (540-550 nm) was used as reference. This sample was obtained using H_2SO_4 (pH=2.2). H_2-TPPS^{2-} J-aggregates were prepared by adding HCl to a pH=7 TPPS^{4-} and analyzed as reference too. A sample in which NSs and J-aggregates of H_2-TPPS^{4-} are simultaneously present but uncoupled was token as further reference (sample NS-TPPS_UNC, figure 13.1). This sample was prepared using H_2SO_4 instead of HCl, because doubly negatively charged sulfate anions, in large excess, inhibit significatively the binding of the porphyrins within the effective volume of the NSs (chapter 11).
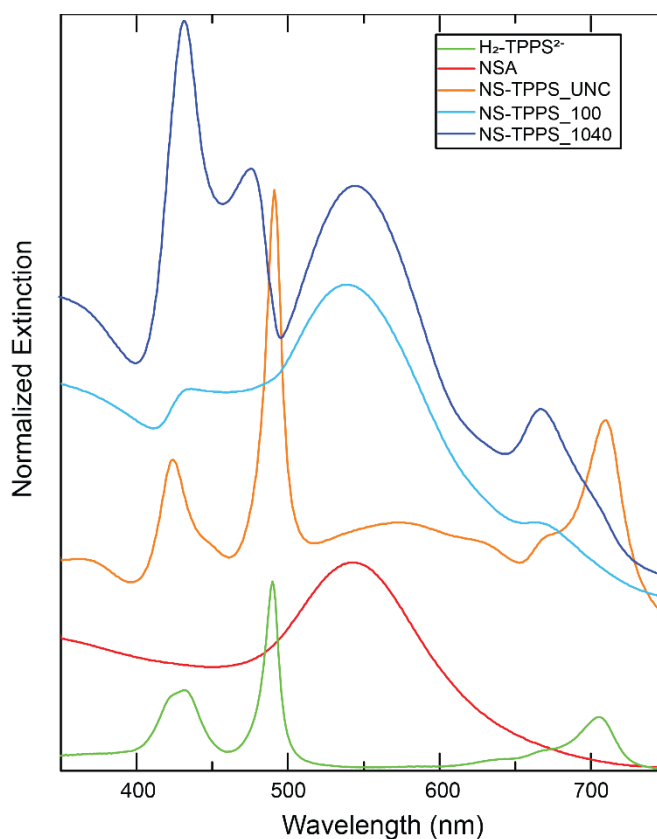
Figure 13.1. Normalized extinction spectra of J-aggregates of H_2-TPPS^{4-}, NSA, NS-TPPS_UNC, NS-TPPS_100 and NS-TPPS_1040 samples. The spectra were normalized to the plasmon peak in the 500-600 nm spectral region. The spectra are shifted vertically to ease the comparison.

13.3 Ultrafast dynamics of uncoupled systems and NS-TPPS_UNC

TA spectra of H_2-TPPS^{4-} at selected values of delay time and the signal decay at a probe wavelength of 490 nm are reported in figure 13.2a and 13.2b, respectively. In full agreement with previous literature,[145,204] the TA spectra feature two characteristic strong Ground State Bleaching (GSB) signals at 490 and 706 nm, in correspondence of the two main excitonic bands B and Q. An additional weaker GSB at 665 nm (vibronic band of S_1) and a broad Excited State Absorption (ESA) signal between 510 and 650 nm are also recorded. The decays at different probe wavelengths, analysed with a multi exponential global fit 4D (section 9.3), are described by four main time constants: $\tau_1 = 0.6$ ps, $\tau_2 = 4$ ps, $\tau_3 = 30$ ps and $\tau_4 = 230$ ps. The subpicosecond kinetic (τ_1) is attributed to the B to Q bands fast relaxation, τ_2 and τ_3 to intra-aggregate and aggregate-solvent energy redistribution and, finally, τ_4 is the Q band lifetime.[204]
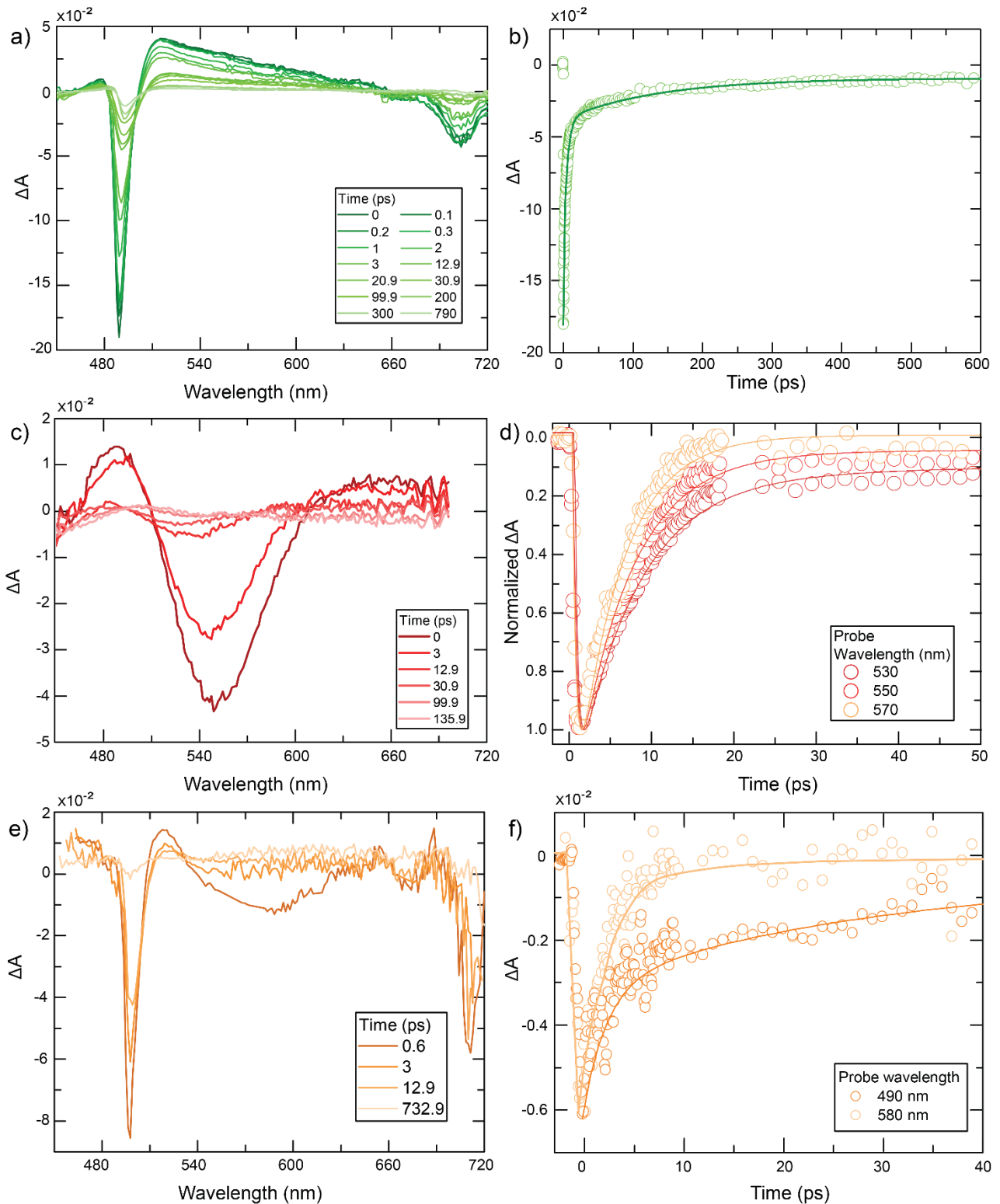
Figure 13.2. a) – c) - e) transient spectra of, respectively, free H_2-TPPS^{4-} J-aggregates, NSA and NS-TPPS_UNC at different times; b) – d) – f) their respective dynamics (open circles are the data, while the lines their fittings). Pump fluence is 470 μJ/cm^2 for TPPS and NSA, 740 μJ/cm^2 for NS-TPPS_UNC.

The TA spectra of NSA and the dynamics at selected probe wavelengths are reported in figure 13.2c and 13.2d, respectively. Also in this case, my findings nicely reproduce previous literature results. [47,119] A strong GSB in correspondence of the plasmon peak dominates the TA spectra. The

relaxation dynamics is described by three kinetic components: i) a sub-picosecond rise, due to electron-electron scattering (τ_{e-e}, about 0.2 ps), ii) a fast decay associated with electron-phonon scattering (τ_{e-ph}, between 1 and 3 ps depending on the pump fluence), and iii) a slower decay due phonon-environment coupling (τ_{ph-env}, average value of 120 ps). All kinetic constants are summarized in appendix A.ii, Table A1. A more detailed comment on the NSA dynamics goes beyond the scope of this work, also considering the wide wealth of literature already devoted to that. It is however interesting to highlight that the τ_{e-ph} gets shorter as the probe wavelength increases (figure 13.2d). This is a typical feature when probing aggregates of increasing dimensions.[205]

Figure 13.2e reports the TA spectra of NS-TPPS_UNC sample at selected times. Qualitatively, the TA spectra roughly appear as the sum of the H_2-TPPS^{2-} and NSs aggregate nonlinearities: two strong GSB signals at about 500 and 700 nm indicate the presence of H_2-TPPS^{4-} J-aggregates, while the GSB at 580 nm is due to the aggregated NSs. However, a closer look reveals that the GSB of the B band of H_2-TPPS^{4-} and the GSB of the NSs plasmon resonance are both slightly redshifted (from 490 to 500 nm and from 550 to 580 nm, respectively). Although this could be partially justified considering the overlap with ESA signals, it is not unlikely that the red shift is a consequence of the specific organisation of the J-aggregates around the NSs, a similar behaviour is captured also in figure 13.1. Indeed, recent theoretical findings suggest that the 3D organisation of molecules around the surface of a spherical metal nanoparticle in weak coupling conditions, lead to the modification of the dipole-dipole interactions and to possible spectral shifts in the optical response.[172,206] This interpretation is supported by the analysis of the dynamic behaviour. Furthermore, the redshift of the plasmon peak could be due to different and probably higher extent of NSs aggregation.

Figure 13.2f shows the time profiles at two relevant probe wavelengths. The dynamics in the spectral region dominated by the NSs response (see for example the trace at 580 nm in figure 13.2f) presents a behaviour very similar to what already found for the bare NSA sample, although the overlap with the ESA signal of H_2-TPPS^{4-} partially hindered the recognition of all the features and the kinetic constants. For example, it was not possible to clearly identify here the τ_{ph-env} component because of the predominance of the H_2-TPPS^{4-} ESA signal after the first ten ps. Also, it was not possible to ascertain the dependence of τ_{e-ph} on probe wavelength, which seems to remain constant at 2.5 ps. The dynamics at 500 nm, corresponding to the strong GSB signal of the B-band of the H_2-TPPS^{4-} J-aggregates, fitted with a 3D fitting model (section 9.3), is described by three time constants: τ_1 = 2.3 ps, τ_2 = 22 ps and τ_3 = 200 ps. The overall shortening of the H_2-

TPPS[4-] kinetics is a clear indication of the presence of a coupling, although weak, between the J-aggregates and the NSs.[6,8]

13.4   Ultrafast dynamics of multi plexcitonic nanosystems
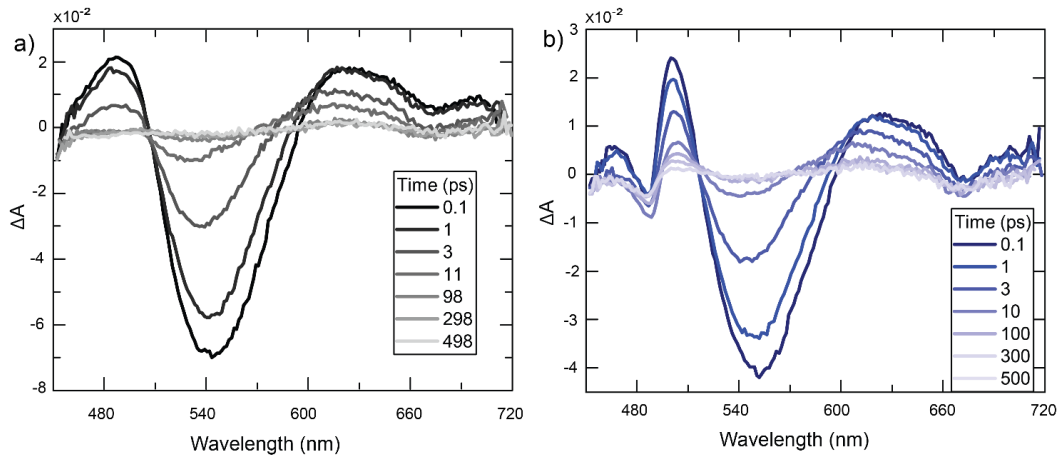
Figure 13.3. a) TA spectra of NS-TPPS_100 and b) NS-TPPS_1040, reported at different times. Pump fluence is 714 µJ/cm².
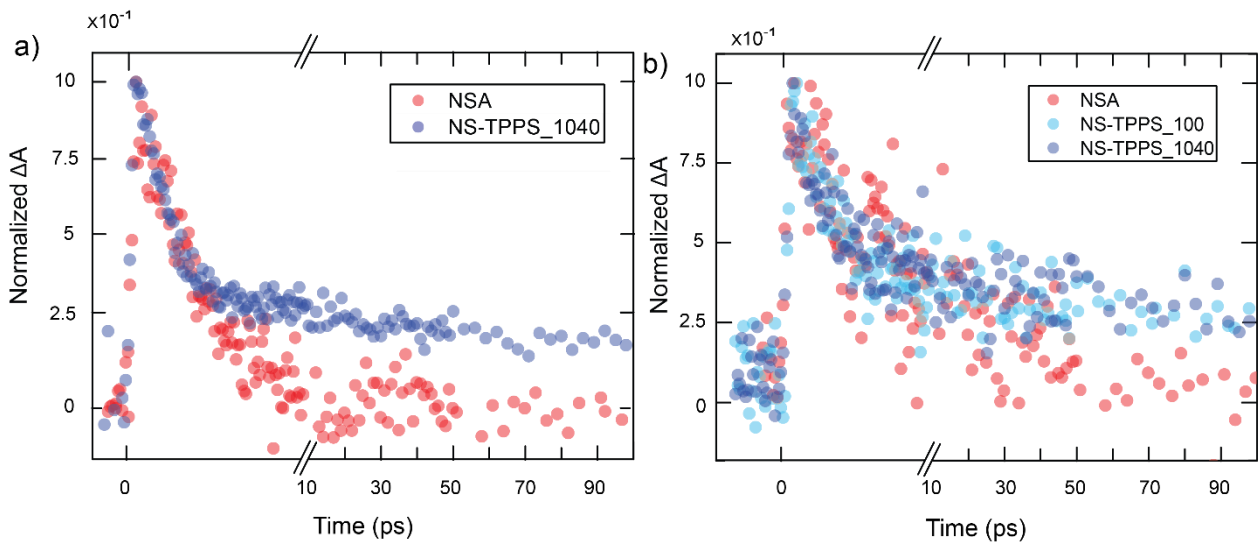
Figure 13.4. a) Decay trace at 500 nm of NSA and NS-TPPS_1040 and b) decay trace at 625 nm of NSA, NS-TPPS_100 and NS-TPPS_1040. In both figures the pump fluence is 173 µJ/cm² for the plexcitonic samples and 165 µJ/cm² for NSA.

In figure 13.3, the TA spectra measured at different delay time of NS-TPPS_100 and NS-TPPS_1040 are reported. The spectra of all the samples are dominated by the typical broad GSB signal of the aggregated NSs at ca. 550 nm. In addition, the features of UR_B/LR_B and UR_Q/LR_Q plexcitons are evident: NS-TPPS_100 and NS-TPPS_1040 present a GSB at 670 nm attributed to LR_Q; NS-TPPS_1040 possesses another GSB at 480 nm, attributed to UR_B. Note that the UR_B GSB could be slightly redshifted because it overlaps with the ESA of aggregated NSs. Another

plexcitonic feature is a strong ESA between the GSB signals.[86,91–93,97,104] UR_B/LR_B and UR_Q/LR_Q plexcitons have strong ESA in the region of 500 nm and 630 nm, respectively. The presence of an additional slow decay component absent in NSA (figure 13.4), supports the plexcitonic origin of these features. However, no evidence of UR_Q was found, probably because of its low extinction coefficient, which make it barely visible also in the linear extinction spectra (figure 13.1). LR_B GSB is also not visible, probably hidden under the huge signal of NSs GSB at about 550 nm, as will be later discussed.

Figure 13.5 reports the dynamics of LR_Q and UR_B for NS-TPPS_100 and NS-TPPS_1040 at wavelengths corresponding to the bleaching of the associated transitions. At early times (0-10 ps), the decay traces are dominated by a short rise, below 1ps, and a fast decay within 3-10 ps, this latter fluence dependent (Appendix A.ii, Table A2 and A3). Since this is the typical behaviour of NSA, this first part of the dynamics is tentatively attributed to the plasmonic moieties. Note that, in NS-TPPS_1040 LR_Q dynamics, the fast rise is barely visible at high pump fluence and cannot be resolved for the lower one (figure 13.5b). The long-time dynamics, from 10 ps to 400-500 ps, consist of the recovery of the GSB. This feature is not present in NSA, and, since it appears at UR_B and LR_Q wavelengths, it is attributed to a plexcitons dynamics. These long-time dynamics are described by only one time constant for LR_Q and by two time constants for UR_B, both fluence dependent.

Based on that evidence, I fitted the dynamics dividing the fast plasmon dynamics from the slow plexciton GSB recovery (fitting models are reported in section 9.3). The obtained plexciton time constants τ_{plex} are plotted as a function of the pump fluence in figure 13.6, while a comprehensive table of the fitting results is reported in (Appendix A.ii, Table A2 and A3). Interestingly, when UR_B/LR_B is present, UR_Q/LR_Q doubles its time constant. Moreover, the fittings confirmed the linear dependence of τ_{plex} on the pump fluence, in stark contrast with what reported in the literature (see chapter 5).
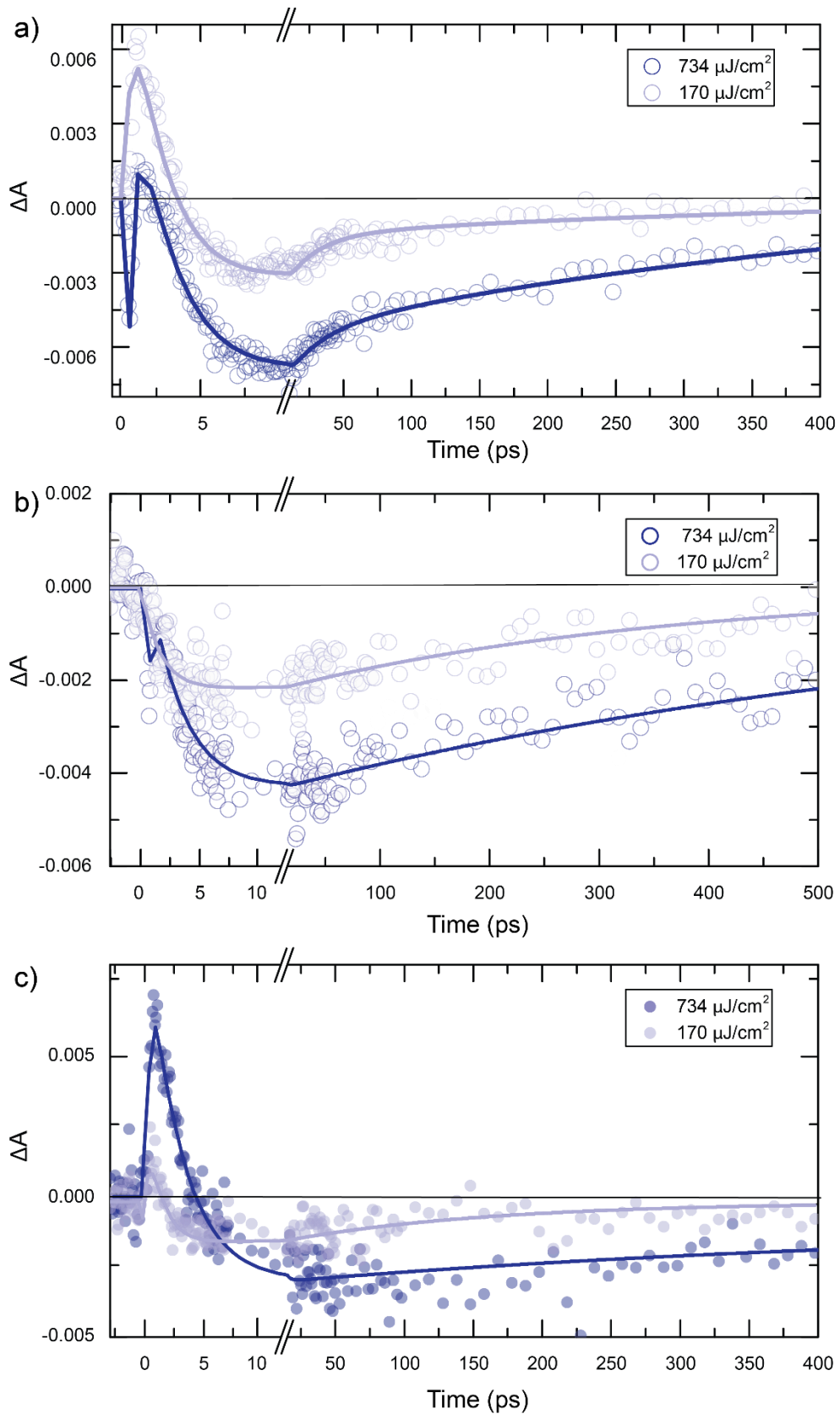
Figure 13.5. a) Dynamics of UR_B at 480 nm for the sample NS-TPPS_1040 at different pump fluences; b) and c) dynamics of LR_Q at 670 nm at different pump fluences for NS-TPPS_1040 and NS-TPPS_100, respectively. The circles represent the experimental data, while the lines are their fittings. The x axes present a break at 10-15 ps to allow a better visualisation of both the fast and slow part of the dynamics.
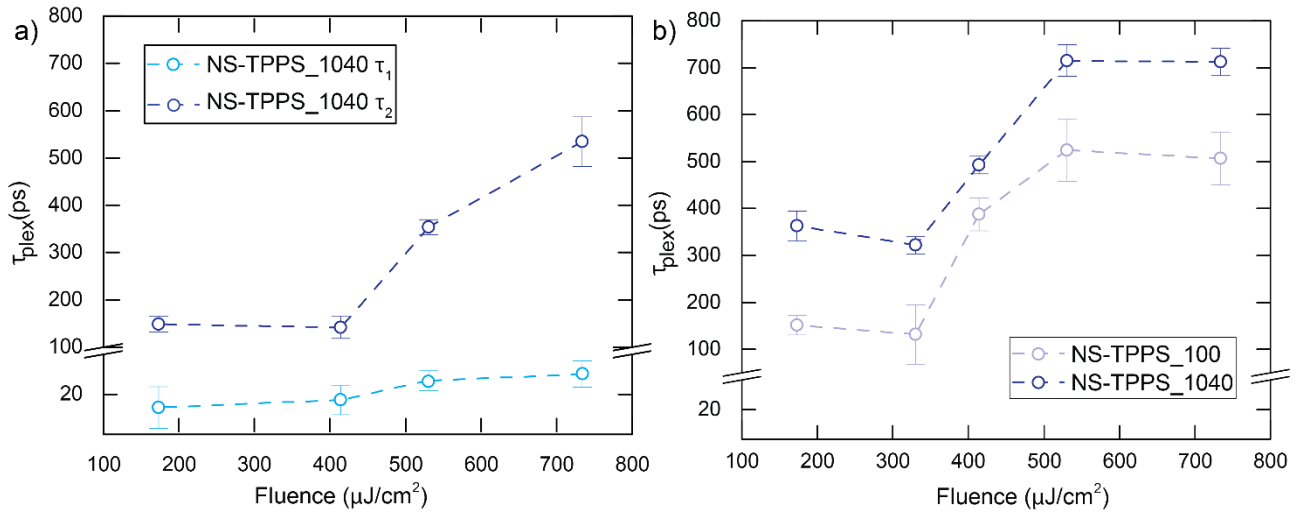
Figure 13.6. plexcitons time constants τ_{plex} as a function of pump fluence for NS-TPPS_100 and NS-TPPS_1040. a) reports τ_{plex} for UR_B, while b) for LR_Q.
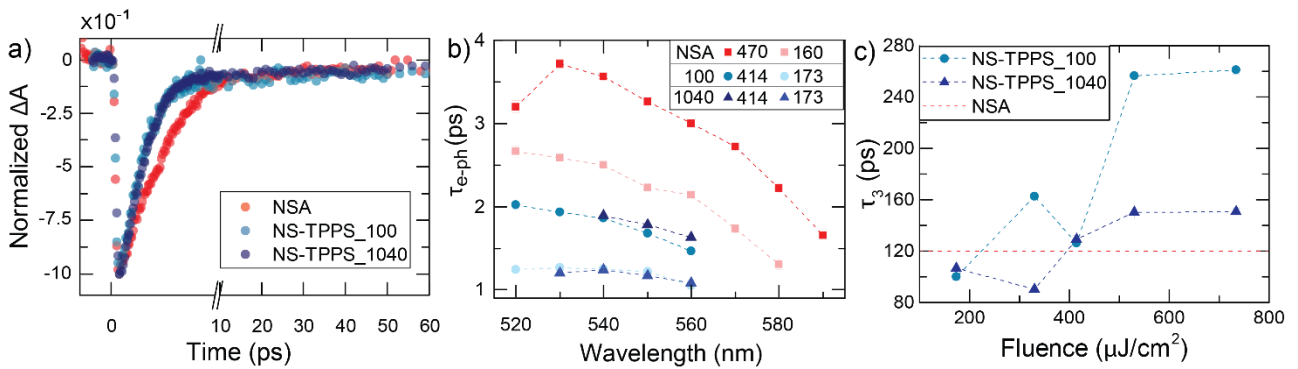
Figure 13.7. a) normalized dynamics at probe wavelength 550 nm for NSA (pump fluence = 470 $\mu J/cm^2$), NS-TPPS_100 (pump fluence = 414 $\mu J/cm^2$) and NS-TPPS_1040 (pump fluence = 414 $\mu J/cm^2$). The break at 10 ps allows a better visualisation. b) τ_{e-ph} of NSA, NS-TPPS_100 and NS-TPPS_1040 as a function of the probe wavelength. In the legend, 100 stands for NS-TPPS_100 and 1040 for NS-TPPS_1040; the pump fluences are expressed in $\mu J/cm^2$; c) averaged τ_3 reported for NS-TPPS_100 and NS-TPPS_1040 as a function of the pump fluence. τ_3 of NSA, reported as reference, is represented by the red dashed line.

Let us now focus the attention on the 520-590 nm region, where the strong plasmonic GSB dominates the TA spectra. The same fitting model used of NSA (RDD, section 9.3) seems to be a reasonable choice here, since the NSA signal is the most prominent and in this spectral region the NS-TPPS_100 and NS-TPPS_1040 dynamics are very similar to NSA (figure 13.7a). A comprehensive table of the fitting results is reported in (Appendix A.ii, Table A1). In figure 13.7b, τ_{e-ph} for NSA, NS-TPPS_100 and NS-TPPS_1040 are plotted. The pump fluence and the probe wavelength dependences are respected also for plexcitonic samples, confirming the plasmonic nature of the GSB here discussed. Surprisingly, NS-TPPS_100 and NS-TPPS_1040 have similar τ_{e-}

$_{ph}$, while NSA has a longer time constant. This difference can be justified by the presence of different anions (H_2-TPPS^{4-} and sulfate) in the nanohybrid samples, which can influence the nature of the coupling between electrons and phonons and thus slightly change $\tau_{e\text{-}ph}$. Evidence that corroborates the importance of the NSs capping layer environment for $\tau_{e\text{-}ph}$ is also reported by Shabaninezhad et al.[207]

NS-TPPS_100 and NS-TPPS_1040 have a second slower decay whose time constant goes from 100 ps to about 300 ps for increasing values of the pump fluence (figure 13.7c). However, this fluence dependence was not found in bare NSs,[47] that in our case have a time $\tau_{ph\text{-}env} \approx 120$ ps. Hence, the two sets of plexcitonic resonances and the plasmon manifold seems to have a cooperative behaviour, which will be later further analysed.

13.5   Discussion

Nanohybrids in three different coupling regimes have been studied by pump and probe technique. In NS-TPPS_UNC, Purcell effect reduces the time constants as consequences of the weak coupling. In this sample however, the NSs and TPPS maintain their individuality as also proved by the recorded dynamics. In NS-TPPS_100 and NP-TPPS_1040, instead, the stronger coupling promotes the formation of hybrids state with a completely different behaviour than the non-interacting plasmonic and dye components.

I found clear signatures of coupling between UR_B/LR_B and UR_Q/LR_Q plexcitons, which behave collectively, giving rise to several unexpected phenomena and trends. For instance, the emission of UR_Q/LR_Q plexciton upon excitation of UR_B/LR_B plexciton was already interpreted in terms of the strong correlation between the two sets of resonances (chapter 11). Moreover, the time constant of LR_Q doubles in the presence of UR_B in the NP-TPPS_1040 sample (figure 13.6b) and both the plexcitons show the same dependence on the pump fluence (figure 13.6). While further investigations are needed for a more thorough understanding of these complex dynamics, it is worth mentioning that a possible mixing or correlation of the UR_B/LR_B and UR_Q/LR_Q plexcitons, despite their significant energy difference, should not sound as a completely new phenomenon. Indeed, B and Q plexcitons are hybrid states originating from the B band of TPPS J-aggregates and the Q band of monomeric TPPS. It was demonstrated that B and Q bands of this molecule are coupled and share oscillator strength.[174] Consequently, their hybrid states could have inherit this property. In this hypothesis, rather than considering the B and the Q plexcitons as two separated sets of states connected by an energy transfer, they should be described as a unique manifold originating from the mixing of both B and Q bands with the plasmon resonance.

Particularly subtle is also the role of uncoupled plasmonic resonance, whose dynamics seems to be to some extent intertwined and related to the already coupled dynamics of UR_B/LR_B and UR_Q/LR_Q plexcitons. First, the plasmon resonance falls in a spectral range (520-570 nm) that is exactly in between the two plexcitonic sets of resonances and the coupling with different states of the H_2-TPPS^{4-} molecules occurs exactly on the NSs surface. Second, the pump wavelength is set at 400 nm ("off-resonance" pump condition), that can directly excite the *sp* to *d* bulk interband transition of gold NSs. For these two reasons, it is expected that NSs plasmon resonance contributes significantly to the overall dynamics of nanohybrids.

The first experimental clue of this behaviour is the typical plasmonic strong signal at early times (0-10 ps) captured for both NS-TPPS_100 and NS-TPPS_1040 in UR_B and LR_Q regions, due mainly to electron-phonon scattering. The associated time constant gets longer increasing the pump fluence and it is wavelength dependent in the typical plasmon region (520-570 nm). These two trends are typical of plasmonic NSs, as discussed above. Although this could be an independent contribution due to uncoupled (or less coupled) NSs, also the long-time dynamics (attributed to plexcitons) are fluence dependent. For this reason, it seems that the presence of a plasmon manifold in between the two plexciton resonances could modulate the overall plexcitonic dynamics.

Several previous works that analysed plexcitonic or polaritonic dynamics in "off-resonance" pump conditions reported a reduced plexcitonic time constants increasing the pump fluence. Indeed, they mainly excited the uncoupled excitonic states, leading to their decoupling.[99,100,102] However, as previously noticed, the "off-resonant" pump used here does not excite the excitonic resonance, but the bulk gold transitions of the NSs. Probably for this reason, the nanosystem is subject to longer dynamics. Similar findings are also reported in the work of Hranisavljevic *et al.*[158], although the authors did not investigated the fluence dependence.

13.6 Final remarks

In this chapter, pump and probe measurements of the NS-TPPS plexcitonic nanosystems revealed deeper insights on the nature of their coupling. By using static experiments, we already demonstrated the presence of a relaxation cascade mechanism between two sets of plexcitons. Pump and probe experiments provided a more detailed picture suggesting the presence of more subtle coupling effects. This coupling makes their time constant longer when both are present: UR_Q/LR_Q constant is increased of 3 times when also UR_B/LR_B is present.

III Results and Discussion

To complete the picture, the role of the plasmon manifold should be carefully considered. Indeed, the off-resonance excitation configuration adopted here allows to directly excite the bulk electrons of the gold NSs, which then relaxes to the plexcitonic resonances. Surprisingly, the fast electron-phonon mechanisms typical of gold NS seems to modulate also the plexcitonic time constants.

The time constants here reported are far longer than the average time constants typically reported for other plexcitonic and polaritonic systems, which are in the order of 0.1-10 ps (chapter 5). Moreover, the possibility of controlling these constants as a function of the number of the plexcitons and the pump fluence is remarkable. The use of a multiple plexcitons nanosystem, as well as the direct excitation of the NSs bulk transition, open a possible interesting perspective for using these materials in photonic devices.

14. Plexcitonic Nanohybrids Based on Gold Nanourchins: the Role of the Capping Layer

14.1 Introduction

Assembling CPMs dispersed in solution requires a fine tailoring of the supramolecular interactions between the NPs and the QEs. In this framework, the CL of NPs clearly plays a crucial role in controlling these interactions. In the previous three chapters, for instance, the interactions between the tetra anionic H_2-TPPS^{4-} and the NSs were ensured by the cationic capping layer of TMAOt molecules. In that case, the spatial proximity of the porphyrin to the surface of the NSs, the formation of J-aggregates, the inhibition of the coupling by using SO_4^{2-} anions and the reduction of the NS available surface due to OH^- ions are all phenomena in which that cationic CL was necessarily involved.

Although many works in the literature investigated the main physico-chemical parameters that regulate the plexcitonic coupling strength (see for example Ref.[41,50,161,208–211]), the role of the capping layer has never been examined in depth. For this reason, I designed and prepared a library of nanohybrids by coupling gold nanourchins (NUs)[113] covered with different CL, and several QEs featuring suitable photochemical properties. The results suggest that stronger couplings are achieved when direct adsorption of the dye to metal surface can be established than when segregation and electrostatic interactions are exploited. Moreover, it was also found that the conditions that regulate the aggregation of QEs play an important role in the formation of plexcitonic hybrids.

14.2 Design of the nanohybrids' library

To build the library considered in this work, I started by identifying a wide enough number of organic dyes to be used as excitonic moieties. I selected 12 dyes (**1-12**, figure 14.1a) belonging to the classes of triarylmethanes, rhodamines, cyanines, benzothiazoliums, and naphthoxaziniums. The following criteria drove the selection of the dyes. First, they all have strong absorptions in the 550-650 nm region of the visible spectrum and therefore they fulfill the resonance conditions necessary to establish an effective coupling with the majority of plasmonic colloidal nanoparticles.[6,9,142,212,213] Secondly, they all have a net charge, which can provide an essential contribution to the interaction with the plasmonic nanoparticles. Both negatively and positively charged molecules were included. About half of the molecules selected are known to form H- or J-aggregates (table 14.1). As already discussed in chapter 4, the high transition dipole moments

and the narrow bandwidths typical of the J-aggregates absorption bands make them particularly suited for the formation of plexcitons,[41] as proven by the vast wealth of examples available in the literature (see for instance Refs.[17,48,161,214–217]). Instead, the formation of plexcitons with molecular excitations coming from organic molecules in the monomeric form is seldom observed with nanoparticles dispersed in solution.[14,17,31,218–220] Contrarywise, to the best of our knowledge, there is no report of formation of CPM dispersed in solution with H-aggregates. Therefore, the dyes have also been selected in view of exploring the conditions for the possible plexciton formation with non-aggregated molecules, J-aggregates and H-aggregates.
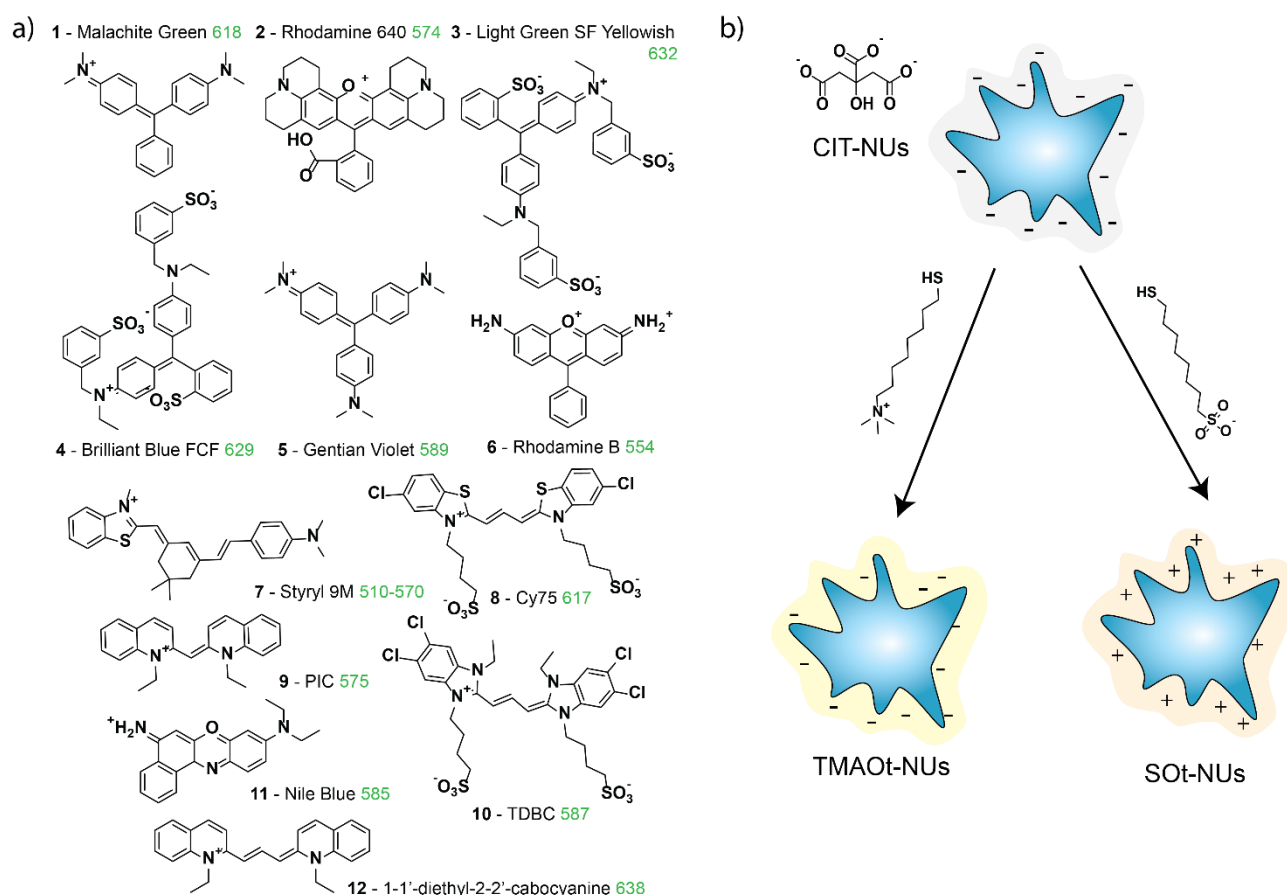
Figure 14.1. a) molecular structure of the QEs considered. For each of them, the wavelength of the main maximum absorption is reported in green; b) Schematization of the different capping layers and their exchange process. CIT-NUs were exploited to study the role of direct dye-metal interactions, while SOt-NUS (TMAOt-NUs) were employed to assess the role of weak interactions between the capping layer and positively (negatively) charged dyes.

As plasmonic materials, gold nanourchins (NUs), i.e. short-tipped gold nanostars, were chosen for two main reasons. The first one is that, as for nanostars, the tip plasmon is easily tunable from 550 nm to the infrared region by controlling the synthetic conditions, and this guarantees to achieve an adequate overlap with the dyes' absorption.[113] Second, the NUs structure features

strong electric fields at the tips, which should positively contribute to the establishment of strong couplings.[221]

I analyzed NUs coated with three different CL in order to have insights about different QE-NU interactions. First, NUs stabilized with the weak capping agent citrate (CIT-NUs)[48,159,217,222] were studied, with the aim of understanding to what extent the possibility of a (partial) exchange of CIT with dye molecules could lead to direct adsorption of the dye onto the metal surface. I also considered NUs covered with the cationic TMAOt (TMAOt-NUs) and the anionic SOt (SOt-NUs), (figure 14.1b). In both cases, differently from CIT-NUs, the capping molecules are strongly attached to the metal surface and the dye molecules can thus interact with the NUs only through electrostatic interactions with the sulfate or ammonium groups or through hydrophobic interactions with the alkyl portion of the coating layer.

Table 14.1. Photophysical properties, wavelength of the main absorption peaks and capability of giving rise to plexcitonic coupling with NUs for the 12 organic dyes used in this work. In the column of the photophysical properties, the conditions necessary to obtain the aggregates are reported between brackets. In the main peaks and coupling columns, M stands for monomer and J(H)-agg for J(H)-aggregates.

Dye	Photophysical properties	Main Peaks	Coupling
1	Apolar, cationic.	510nm - 570nm (solvatochromic)	Yes
2	Polar, cationic	618 nm	No
3	Polar, cationic	589 nm	No
4	Polar, cationic	554 nm	No
5	Polar, neutral	574 nm	No
6	Polar, Polyanionic	632 nm	No
7	Polar, polyanionic	629 nm	No
8	Polar, polyanionic J-aggregates (NaCl, 50μM)	552 nm (M), 617 (J-agg)	Yes (J-agg)
9	Slightly polar, cationic. J-aggregates (NaCl, 5mM)	520 nm (M), 575 nm (J-agg)	Yes (J-agg)
10	Polar, polyanionic. J-aggregates (high concentration)	520 nm (M), 587 nm (J-agg)	Yes (J-agg)
11	Polar, cationic H-aggregates (NUs)	585 nm (H-agg), 636 nm (M)	No
12	Slightly polar, cationic H-aggregates (high concentration)	638 (H-agg), 698 nm (M)	No

14.3   Preparation of the NUs and the nanohybrids
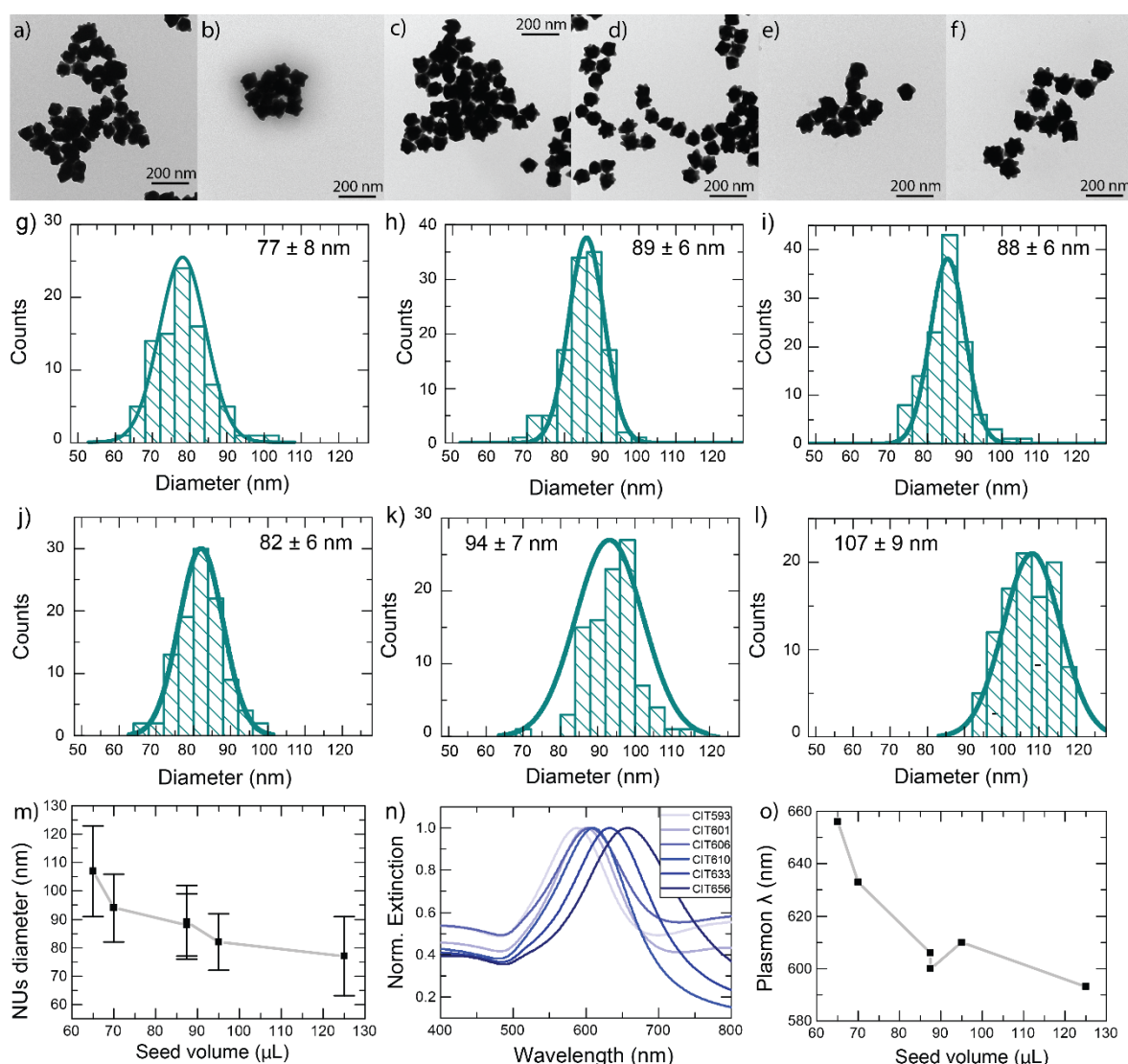
Figure 14.2. Characterization and functionalization of NUs. Each NUs sample is labeled with an acronym where the first part denotes the capping layer (CIT, SOt or TMAOt), and the second one the plasmon wavelength. a)-f) TEM images of CIT593, CIT601, CIT606, CIT610, CIT633, CIT656, respectively (scale bar: 200 nm) and g)-l) their histogram with gaussian curve fits. m) NUs diameter as a function of the injected volume of seeds solution (the seed solution has a concentration of 0.046 mg/mL). The diameters reported on the y axis are estimated as the central values of the NUs size distribution fitted with a Gaussian function. The error bars correspond to the half width at half maximum of the size distribution. n) Normalized extinction spectra of CIT-NUs. o) Wavelength of the maximum plasmonic resonance as a function of the injected volume of seeds solution.

NUs with different sizes were prepared according to a previously reported protocol as described in section 6.3.[113] In this protocol, the size and plasmonic properties of the NUs are determined by the amount (volume) of seeds solution injected into the growth solution. Transmission Electron Microscopy (TEM) micrographs of six samples and their size analysis are reported in figures 14.2a-f and 14.2g-l, respectively. As expected, the size of NUs decreases by increasing the number

of seeds (figure 14.2m). The extinction spectra of the NUs (figure 14.2n) are characterized by two plasmon resonances: a first weak signal at about 520 nm is due to the plasmon of the core and a second more intense band above 550 nm is instead attributed to the plasmon of the tips.[221] The maximum of this second band is sensitive to the size of the NUs, and therefore it depends on the volume of seeds solution injected during the synthesis: a blue shift is recorded for increasing volumes of seeds solution (figure 14.2o).

Pristine NUs prepared with this protocol are capped with citrate (CIT-NUs). We then prepared TMAOt-NUs and SOt-NUs using capping exchange procedures (chapter 6). The Z-potential values of CIT-NUs, SOt-NUs and TMAOt-NUs are -30 mV, -20 mV and +4 mV, respectively. The more negative Z-potential of CIT-NUs with respect to SOt-NUs can be ascribed to the polyanionic nature of the citrate, which contributes with more than one negative charge to the effective surface charge, compared with the single charge per molecule of the SOt capping layer. I also found that the capping layer exchange does not affect the SOt-NUs extinction spectra (figure 14.3). TMAOt-NUs, besides having a slightly positive Z-potential, clearly show aggregation phenomena, as proved by the rising of a band at about 700 nm in the extinction spectrum (figure 14.3). These findings suggest the presence of citrate counterions strongly bound to the TMAOt-NUs monolayer, which reduces the overall measured Z-potential and promotes the particles aggregation.
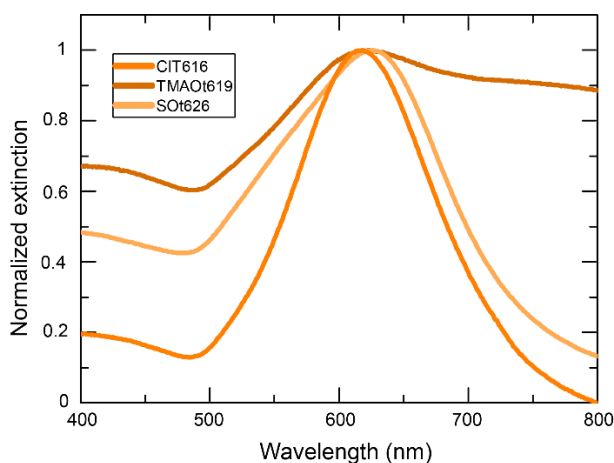
Figure 14.3. Extinction spectra of three samples of NUs coated with the three different capping layers.

Eventually, I prepared the nanohybrids library by mixing each of the 12 dyes with (i) CIT-NUs and (ii) with the NUs capped with the thiol of opposite charge. 24 combinations were thus obtained. Spectroscopic analysis after 1 day of incubation revealed the typical rising the two plexcitonic resonances only in 5 cases. Below I describe the properties of these 5 successful examples of

plexciton formation, classified in terms of the aggregation state of the QE and the nature of the interactions between dye and NUs (weak interactions, meaning segregation and/or electrostatic or direct metal-dye interaction, see also part IV).
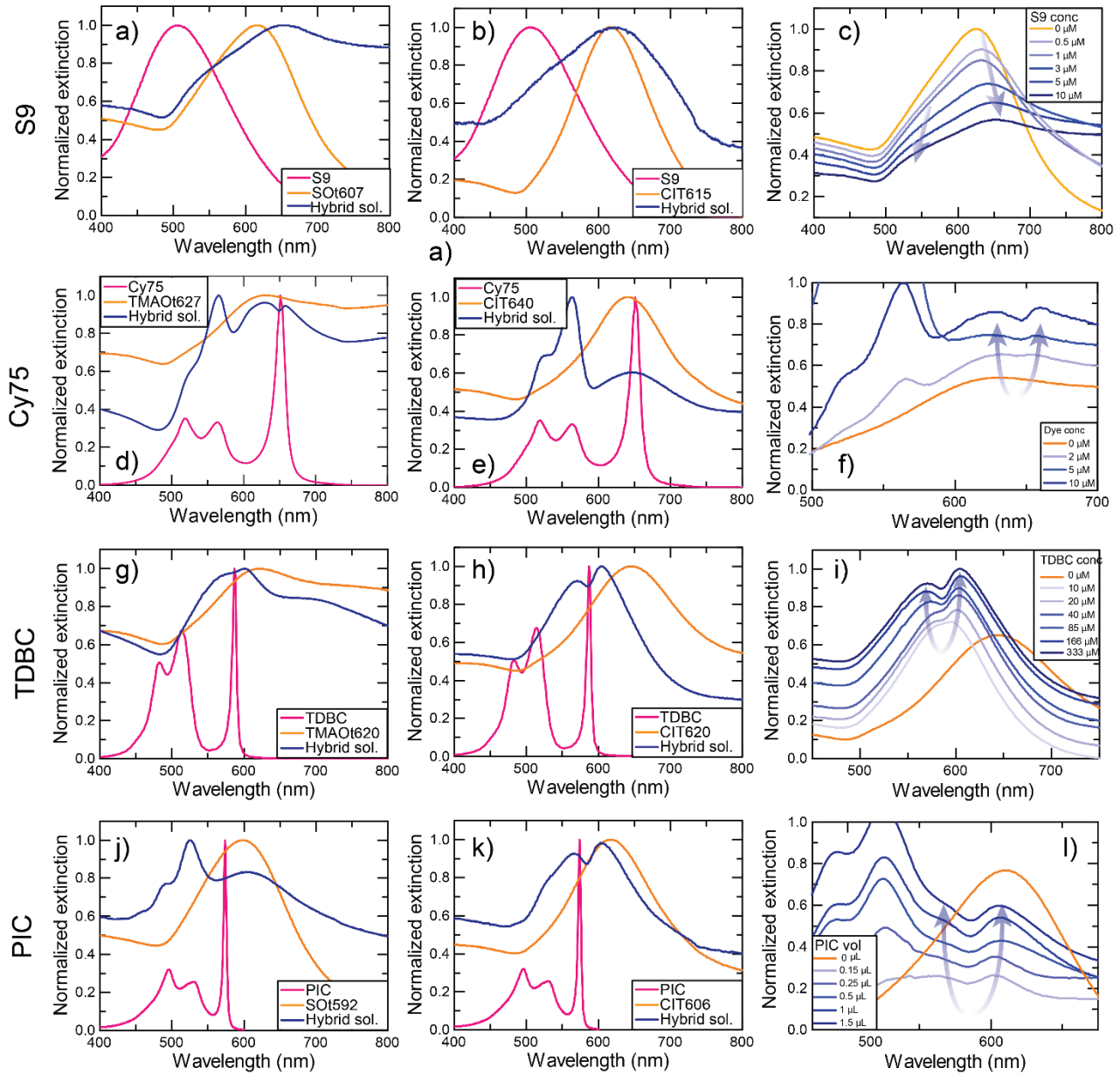
Figure 14.4. Normalized extinction spectra of dyes, NUs, and nanohybrids solutions (pink, orange, and dark blue lines, respectively) obtained using as organic dye: a)-c) S9, d)-f) Cy75, g)-i) TDBC and j)-l) PIC. The first column a), d), g) and j) refers to nanohybrids prepared with thiol capped-NUs exploiting non-covalent interactions; the second column b), e), h) and k) relates to nanohybrids prepared with CIT-NUs controlling metal-dye interactions. The third column c), f), j) and l) reports the typical concentration trend of $\hbar\Omega_R$, which increases as the dye concentration is raised.

14.4 Plexcitonic nanohybrids with non-aggregated molecules: styryl 9M

Dyes **1-7**, including styryl 9M (S9, **7**), triarylmethanes and rhodamines, do not form aggregates when dissolved in water. Among them, I observed plexcitonic resonances only in nanohybrids prepared with cationic S9 and SOt-NUs (figure 14.4a). To the best of our knowledge, this is the first time that a plexciton with S9 is reported. S9 is a solvatochromic dye: its maximum absorption peak undergoes a red-shift when the polarity of the solvent is decreased.[223] As an example, the absorption maximum is found at 510 nm in a 99:1 water:acetone solution and at 570 nm in acetone solution (table 14.1). The extinction spectrum of S9/CIT-NUs hybrids appeared just as the sum of the spectra of the single components and therefore no relevant interactions between the NUs and the dyes are established in these conditions (Figure 14.4b). Contrarywise, in the case of S9/SOt-NUs, two peaks could be detected at about 652 nm and 526 nm, which I attributed to the formation of two plexciton resonances. From the energy separation among these two peaks a Rabi splitting energy ($\hbar\Omega_R$) of ≈ 450 meV can be estimated. This assignation is supported by the fact that the distance between the two peaks increased by increasing the S9 concentration (Figure 14.4c). Indeed, this behavior is typical of plexcitonic resonances, whose Rabi splitting is proportional to the square of the number of coupled molecules (section 4.3). It is remarkable that in these nanohybrids, the plexcitonic resonance forms even if the plasmon band of NUs (625 nm) poorly overlaps with the dye's absorption band. I suggest that the dye, embedded in the nanoparticle coating layer, experiences a low polarity environment and red shifts its absorbance peak, reducing the detuning and allowing an effective plexcitonic coupling. TEM analysis of SOt-NUs before and after the addition of S9 did not reveal any structural modification in the NUs morphology (figure 14.5a-b).

14.5 Plexcitonic nanohybrids with J-aggregating molecules.

Dyes **8-10**, all belonging to the cyanines family, easily form J-aggregates in the appropriate ionic strength, concentration, or temperature conditions.[38,224] For all these molecules, I observed the formation of plexcitons after conjugation with the NUs.

Cy75 (**8**) is an anionic dye that aggregates in water solutions at high ionic strength values (NaCl 0.05 mM, figure 14.4d).[51] This dye in its J-aggregate form has already been employed to prepare plexcitonic materials in the form of film-coupled nanocube cavities.[51] When Cy75 was mixed with CIT-NUs, it did not produce plexcitonic resonances nor aggregates formation (figure 14.4e). Instead, in the presence of TMAOt-NUs the typical features associated with the formation of

plexcitonic resonances appeared (figure 14.4d): a dip in correspondence of the excitonic band of Cy75 J-aggregates (650 nm) and two side peaks (629 nm and 658 nm, $\hbar\Omega_R \approx$ 85 meV).[210,220] As for S9, the concentration trend supports the attribution of these two new peaks to plexciton resonances (figure 14.4f). Also in this case, the TEM analysis of TMAOt-NUs before and after the addition of Cy75 did not reveal any significant structural modification (figure 14.5c-d).
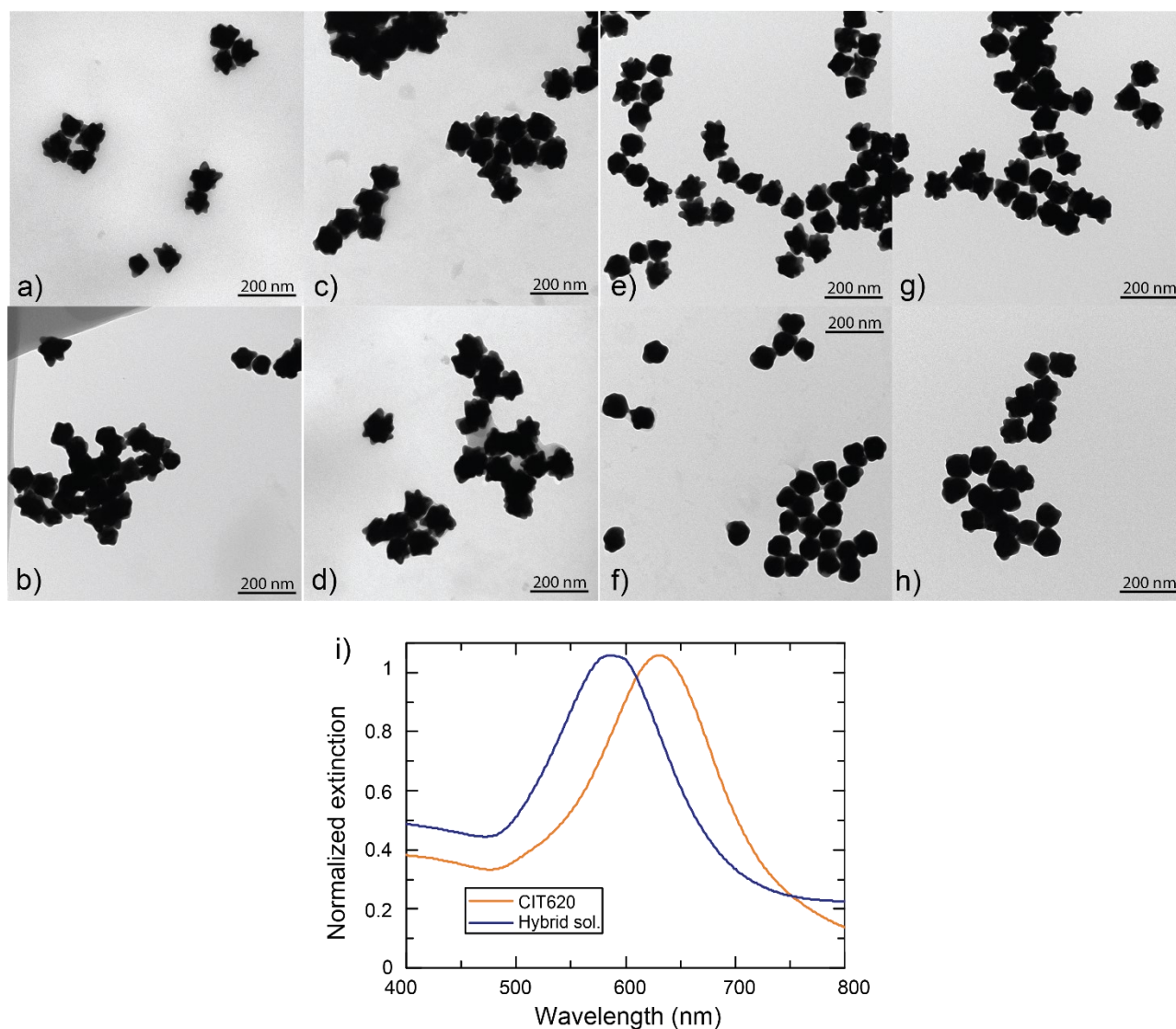
Figure 14.5. a)-h) TEM images (scalebar: 200 nm) of different NUs before and after dye addition. SOt607 a) before and b) after S9 addition; TMAOt627 c) before and d) after Cy75 addition; CIT620 e) before and f) after TDBC addition; CIT606 g) before and h) after PIC addition. i) as an example, the extinction spectra of CIT620 before (orange line) and after (dark blue line) TDBC addition (final TDBC concentration: 10 μM).

TDBC (**10**) is an anionic dye well-known for the formation of J-aggregates at high concentrations[156,225] and it is often used for preparing plexcitonic materials, see for instance Ref.[92,208,210,217]. With this dye I observed the formation of plexcitonic resonances independently on the NUs capping layer (figure 14.4g and h), although with slightly different coupling values: I

estimated $\hbar\Omega_R$ = 120 meV for TDBC/CIT-NUs, while 95 meV for TDBC/TMAOt-NUs. Also in this case, the dependence of the Rabi splitting on the dye concentration was confirmed (figure 14.4i). Differently from the two previously described systems, the TEM images of CIT-NUs before and after the addition of TDBC revealed the smoothing of the tips after the functionalization with the dye (figure 14.5e-f), which induced a blueshift of the absorption band associated with the tip plasmon, even at low TDBC concentration (figure 14.5i and figure 14.4h). This reshaping is a clear proof that TDBC exchanged CIT molecules on the NU surface, establishing a direct interaction with the metal surface. I estimated an average blue shifting due to the TDBC etching of 113 meV by repeating four times the experiment in figure 14.5i. These insights allowed me to assembly the CIT-plexcitonic samples with (almost) zero δ (see for instance 14.figure 3h).
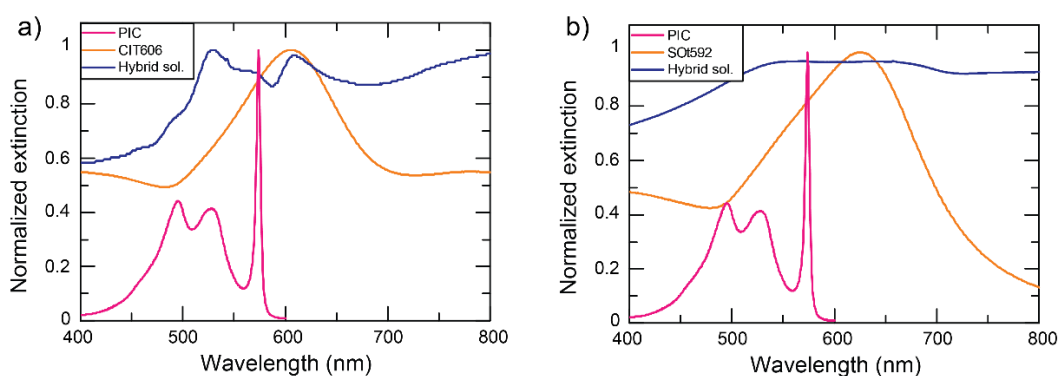
Figure 14.6. Extinction spectra of a) PIC, CIT606 and their nanohybrids, b) PIC, SOt592 and their nanohybrids. In this case PIC molecules were added to NUs already in the J-aggregate form.

PIC (**9**) is a positively charged dye (figure 14.1a) that aggregates at high temperature (85°C) and in high ionic strength conditions.[156,225] With TDBC, it is one of the most used dyes for preparing plexcitonic materials (see for instance Ref.[41,106,226,227]). I found that, adding non aggregated PIC to CIT-NUs and SOt-NUs, the plexcitonic coupling was established only with the former (figure 14.4k), with a Rabi splitting energy of 130 meV. No plexciton formation nor dye aggregation were observed in the presence of SOt-NUs. I also tried to prepare the nanohybrids adding pre-aggregated PIC to the NUs. In both cases a broad and intense band above 700 nm, due to NUs aggregation, dominates the extinction spectra of the hybrids (figure 14.6). Despite that, plexciton resonances appeared again only with CIT-NUs. In the light of these results, it can be concluded that the inability of SOt-NUs to produce plexcitonic coupling with PIC is not related to the capability of templating the dye aggregation. Like for TDBC/CIT-NUs nanohybrids, I noted a reshaping of CIT-NUs (figure 14.5g-h) and a blueshift of the plasmon peak (see, for instance, figure 14.4k) after the addition of the dye molecules. Therefore, also in this case, the formation

of direct interactions between the dye and the metal surface consequent to CIT exchange could be established. The estimated blueshift due to TDBC was considered the same for PIC molecules.

14.6   Nanohybrids with H-aggregating molecules

Nile blue (**11**), which is usually present in solution as a monomer, formed H-aggregates in the presence of SOt-NUs (figure 14.7a), as also reported for anionic SnO_2 and SiO_2 nanoparticles, but no plexciton resonance was observed both with CIT- and SOt-NUs.[228] 1-1'-diethyl-2-2'-carbocyanine (**12**) typically forms H-aggregates.[229] Here I neither observed the nucleation of H-aggregates onto NUs surface, nor any plexciton formation both with CIT- and SOt-NUs. However, I observed the blueshift of the tip plasmon, likely due to the tips' smoothing, in the case of CIT-NUs (figure 14.7b).
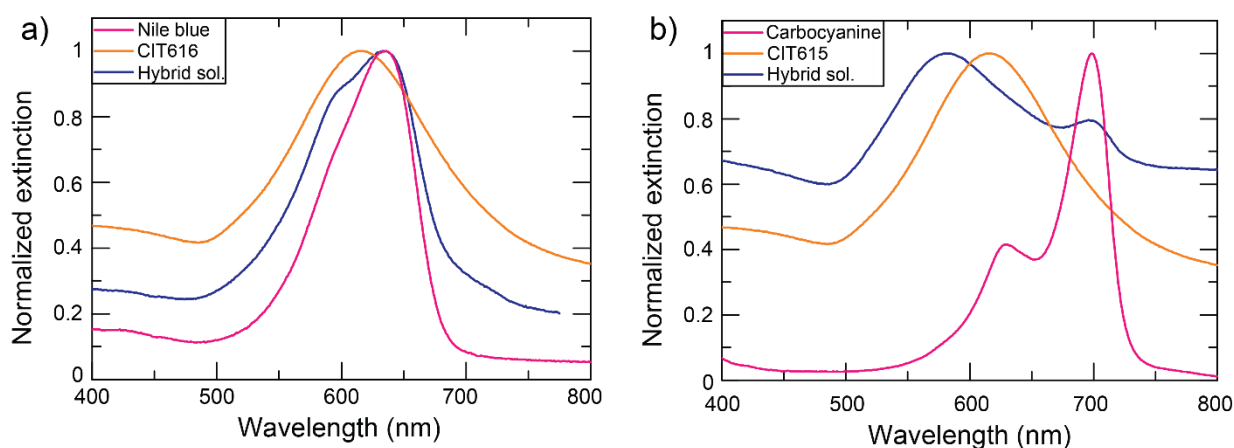
Figure 14.7. a) Extinction spectra of CIT616, Nile blue and their nanohybrids; here the presence of H aggregates is indicated by the shoulder of the main peak at 585 nm; b) Extinction spectra of CIT616, carbocyanine and their nanohybrids; the presence of interactions at the NPs surface is highlighted by the blueshift of the plasmon peak.

14.7   Discussion

The results reported in this chapter allowed building the first example of a library of plexcitonic materials based on colloidal NUs. To the best of our knowledge, similar systems have been studied so far only by Melnikau *et al.*, who reported a preliminary investigation on plexcitons promoted by the coupling of gold nanostars and two cyanine dyes.[215] Our deep and complete characterization of these systems definitely proved the high suitability of NUs to couple with organic dyes. As mentioned, the easy tunability of the tip plasmon and the enhancement of the electric fields at the tips make these structures particularly suited in view of achieving strong coupling with organic dyes and the effective formation of hybrid plexcitonic resonances.

III Results and Discussion

Despite the relatively wide range of families of organic dyes taken into consideration, cyanine dyes were revealed to be the most effective in the formation of plexcitons, especially in their J-aggregate form, confirming a trend already widely established in the literature.

More interesting are the different behaviors manifested by the cyanine molecules in the coupling with NUs stabilized by different capping agents. Two classes of capping agents have been considered. On the one hand, I found evidence that, with CIT-capped NUs, the dyes can establish direct interactions with the metal surface after the (partial) exchange of the capping molecules. The reshaping of the NUs' tips after the functionalization with the dye, as proved by the TEM analysis and the blue shift of the plasmonic resonance, is a clear indication of a partial exchange of the CIT by the cyanine molecules and the establishment of direct metal-dye interactions. On the other hand, in the case of thiol-capped NUs negatively or positively charged the direct interaction is not possible, as confirmed by the absence of any reshaping or plasmon shifts, and the association between the dyes and the NUs is due to electrostatic interactions with dyes of opposite charge and possibly to weak interactions between the non-polar portions of the dyes and the inner alkyl part of the capping layer.

I found that, while TDBC interacts both with thiol-capped NUs and CIT-capped NUs to form plexciton hybrids, PIC can form plexcitons only with CIT-NUs and Cy75 only with thiol-capped NUs. These findings confirm that the interaction between the metal nanostructures and the organic dye molecules in plexciton formation is strongly modulated by the nature of the capping agent, which therefore requires a careful evaluation. In particular, the TDBC case allows the direct comparison of the effectiveness of indirect non-covalent and direct metal-dye interactions by examining the TMAOt-NUs/TDBC and CIT-NUs/TDBC hybrids. Stronger coupling is observed in CIT-NUs ($\hbar\Omega_R \approx 120$ meV) than in TMAOt-NUs ($\hbar\Omega_R \approx 95$ meV),.[194,230] Indeed, in the case of weak CL and dye-metal interaction, QEs can easily displace the CL molecules, reducing their distance between the surface of the nanoparticles and increasing the number of dyes within the NUs effective volume. This trend is again confirmed by CIT-NUs/PIC ($\hbar\Omega_R \approx 130$ meV) and TMAOt-NUs/Cy75 ($\hbar\Omega_R \approx 85$ meV), although the molecules compared are different.

Indeed, in the interplay between dye-nanoparticle interactions and the formation of plexcitonic hybrids also the properties of QEs must be kept into account. The Cy75 dye, whose structure is similar to that of TDBC, forms a plexcitonic hybrid only with TMAOt-NUs but not with CIT-NUs. With respect to TDBC, Cy75 features benzothiazole rather than benzimidazole groups and lacks two chlorine atoms at the 6,6' positions and the ethyl groups at the 1,1' positions of the heterocycles. These structural differences explain its lower tendency to aggregation in water

solutions[38,224] and might also be responsible for its reduced capability of exchanging CIT molecules and forming aggregates on the metal surface. In this framework, I also found that S9 is the only non-aggregating dye, among the other 7 molecules tested, capable of producing plexcitonic resonances. It is probably not a case that S9 is the only species presenting an elongated structure with a polymethine chain connecting two (hetero) cyclic terminal groups, very similar to the cyanine structure. Moreover, the lower polarity environment provided by the capping layer also seems to favor the plexcitonic coupling by reducing the detuning between the molecular and the plasmonic resonances.

These findings suggest that mere electrostatic forces between oppositely charged capping molecules and organic dyes, while important,[210] are not enough to establish a strong coupling. Most likely, a delicate balance between electrostatic, dispersion, and hydrophobic forces both between dyes and between dyes and capping molecules determine the final coupling regime.

14.8   Final remarks

In conclusion, I systematically explored the formation of plexcitonic resonances in a library of colloidal hybrids prepared by coupling gold nanourchins and different dyes. The attention was focused particularly on the still underexplored role of the capping layer in mediating the interaction and the coupling between the organic dye and the plasmonic substrate.

Beyond providing new examples of plexcitonic hybrids never reported before, I found that the nature of the capping layer is crucial to determine the establishment of the coupling between dyes and plasmonic substrate, which is the result of a delicate and complex balance between a wealth of various dye-dye and dye-capping molecules interactions: electrostatic, dispersive, and hydrophobic forces.

These results suggest that stronger couplings are achieved when a direct metal-dye interaction can be established after the exchange of capping molecule by dye molecules. These insights also shed light on a still unexplored aspect of the plasmon-exciton interactions and open new perspectives for the design of novel and performative plexcitonic nanohybrids.

15. Coherent dynamics of plexciton systems studied by 2DES

15.1 Introduction

One of the most intriguing phenomena that might be attained in SC plexcitonic materials is the possibility of exploiting quantum coherences between their states (chapter 4). Indeed, although quantum plasmonics has been recently identified as a new frontier in the study of the fundamental physics of surface plasmons and in the realization of quantum-controlled devices (including single-photon sources, transistors and ultra-compact circuitry at the nanoscale),[231] their effective use is limited by the rapid loss of coherence of plasmonic resonances, which typically get damped in timescales comparable or faster than 10 fs.[45-47]

One of the possible ways recently identified to mitigate the effect of plasmonic dissipative losses is to hybridize plasmonic resonances with molecular excitonic states, typically characterized by much longer coherent times. In other words, moving from plasmons to plexcitons. In facts, however, although the dephasing times of quantum coherences in plexciton materials have been predicted to last for a period longer than 10 fs,[80,232] the experimental proofs are scarce, and, precisely in the plexcitonic panorama, almost absent.

The direct characterization of plexcitonic quantum coherences and their dephasing times is a particularly challenging task because of their fast oscillation period, which is far below 100 fs. Classical pump and probe experiments with the typical resolution of 100 fs cannot resolve them. 2DES can potentially overcome this issue as well as decongest coherent signals from other dynamic contributions.

In this chapter, I will present the 2DES study of two plexcitonic nanohybrids prepared by covering gold nanourchins (NUs, figure 15.a) with TDBC J-aggregates (figure 15.1b). The two samples differ for the coupling regime established between the plasmonic and the organic moieties: in one case we achieved SC conditions (equation 4.22), while in the other just the plexcitonic CE (equation 4.23). The aim was to verify possible differences in the dynamics as a consequence of the different coupling regime. The 2DES analysis revealed that, while energy relaxation follows an incoherent path in the intermediate regime, electronic quantum coherences dominate the early times relaxation of the strongly coupled plexcitonic sample, extending the plasmon coherence time constant of about one order of magnitude. It is worth highlighting that the results obtained here (unpublished), to the best of our knowledge, represent one of the few works currently

available on the 2DES response of plexciton systems[83,84] and the first one characterizing their coherent dynamics.

15.2 Preparation and preliminary linear characterization of the nanohybrids to be used in 2DES measurements
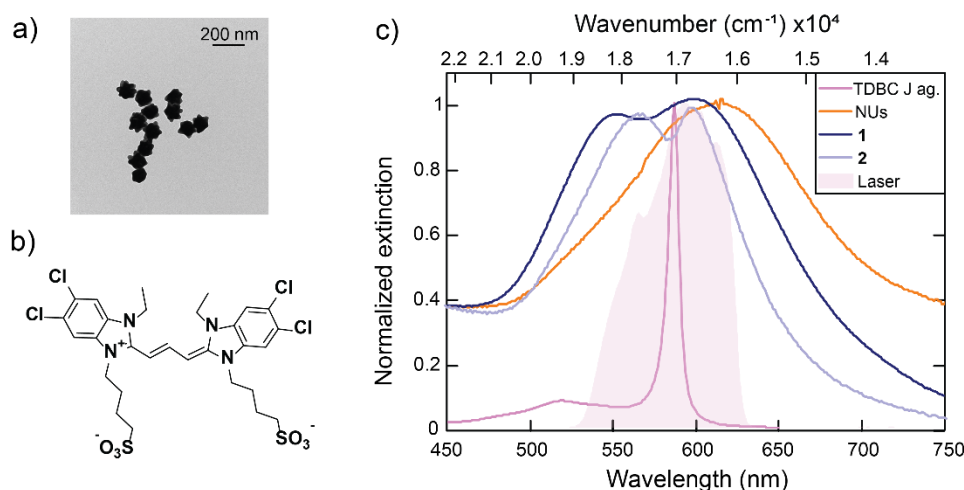
Figure 15.1. Morphological and linear characterization of the nanohybrids used in the 2DES characterization. a) TEM image of citrate-capped NUs (scalebar: 200 nm); b) Molecular structure of the TDBC molecule; c) normalized extinction spectra of the nanohybrids and their constituents. The laser profile used for 2DES measurements is represented as a pink area.

Starting from the vast wealth of plexcitonic materials prepared and described in the previous sections, we identified two interesting samples, whose properties appeared particularly suited for 2DES analysis. In particular, we selected two TDBC-NUs hybrids with tip plasmon centered at 610 nm (2030 meV, 16390 cm^{-1}, figure 15.1c) and average diameter of (82 ± 6) nm, (figure 15.1a).

The two nanohybrid systems are characterized by different coupling strength between plasmonic nanoparticles and dye molecules. Different coupling regimes have been achieved controlling the number of dye molecules on metallic nanoparticles, [92] exploiting the dependence of the Rabi splitting on the excitons concentration within the effective volume of the NUs.[20] Figure 15.1c compares the extinction spectra of the two nanohybrids with the spectra of pristine NUs and TDBC aggregates. The extinction spectrum of nanohybrid **1** presents an Upper Plexcitonic Resonance (UPR) at 548 nm (2260 meV, 18250 cm^{-1}) and a Lower Plexcitonic Resonance (LPR) at 602 nm (2060 meV, 16600 cm^{-1}), with a calculated Rabi splitting (Ω_R) of 1510 cm^{-1} (187 meV). In nanohybrid **2**, instead, the Rabi splitting was reduced to 890 cm^{-1} with UPR and LPR at 567 nm (2190 meV, 17637 cm^{-1}) and 597 nm (2080 meV, 16750 cm^{-1}), respectively. As already discussed in section 4.4, the conditions for strong coupling are achieved when $\Omega_R^2 > (\gamma_{TDBC}^2 + \gamma_{NUs}^2)/2$,[9,10] being

γ_{TDBC} and γ_{NUs} the associated amplitude decay rates of TDBC J-aggregates and NUs, quantified as spectral widths (half-width at half-maximum).[8] According to that, only **1** satisfies the condition of strong coupling regime, while **2** can be classified in an intermediate coupling regime (table 15.1).

Table 15.1. Summary of the experimental parameters and calculation of the coupling regime for **1** and **2**. UPR, LPR, γ_{TDBC} and γ_{NUs} were retrieved from the extinction spectra of figure 15.1c. Ω_R is the difference UPR and LPR energy. γ_{TDBC} and γ_{NUs} were calculated as the half width at half maximum of the respective extinction peaks, fitted with gaussian fits. I could not estimate directly γ_{NUs}, because TDBC reshapes NUs surface and shifts its plasmon peak. Consequently, I prepared five nanohybrids with low amount of TDBC (final concentration: 10 µM). These sample did not present any plexcitonic signature, but, still, they have blue-shifted plasmon peak (average blue-shift: 113 meV). Their average γ is 170.8 meV, which we reported here and used hereafter. The condition for strong coupling can be rearranged as $\Omega_R{}^2 - (\gamma_{TDBC}{}^2 + \gamma_{NUs}{}^2)/2 > 0$, as reported in the last line of the table: only **1** satisfies the strong coupling conditions.

Parameters	**1**	**2**
UPR (nm)	552	567
UPR (meV)	2246	2187
LPR (nm)	602	597
LPR (meV)	2059	2077
Ω_R (meV)	187	110
γ_{NUs} (meV)	170.8	170.8
γ_{TDBC} (meV)	15.2	15.2
$\Omega_R{}^2 - (\gamma_{TDBC}{}^2 + \gamma_{NUs}{}^2)/2$ (meV^2)	20097	-2629

2DES measurements have been performed on suspensions of nanohybrids **1** and **2** and compared with the 2DES response of the uncoupled constituents, i.e., TDBC J -aggregates and NUs water suspensions, measured in the same conditions. Since I was mainly interested to investigate the ultrafast coherent behavior, I focused on a time window of 400 fs after photoexcitation, still largely underexplored. The dynamics of plexcitonic systems at longer timescales have instead been studied in numerous other works.[16,86,91,93]

15.3   Ultrafast dynamics of the uncoupled systems

Figure 15.2 summarizes the 2DES response of the uncoupled systems. Panel a) shows selected purely absorptive 2DES maps for TDBC J-aggregates in water, while in panel c) the decay of the signal at relevant coordinates is depicted. The obtained data are in full agreement with the results of previous investigations on the same system. [83,233,234] The main feature appearing in the maps is a diagonal peak at 17040 cm^{-1}, composed of contributions from GSB and SE of the J band dominating also the linear absorption spectrum. In addition, a negative ESA peak is found

at slightly blue-shifted emission frequencies, which is due to transitions from the one- to the two-exciton bands.[233]

A global multiexponential fitting analysis[139] was employed to quantify the kinetic constants regulating the relaxation dynamics. I identified a short (40 fs) and a long (>400 fs) non-oscillating decaying components, whose amplitude distribution across the 2D maps are reported in the form of 2D-DAS (2D decay associated spectra[139] (figure 15.2b). In agreement with previous ultrafast experiments,[83,235,236] they have been attributed to relaxation into dark exciton states and to slower deactivation processes (including exciton-exciton annihilation and relaxation back to the ground state), respectively. [233,237] No relevant oscillating components were detected.

Figure 15.2d reports the 2DES response of a suspension of NUs. Here the dynamics is more complex and reflects the different steps of the equilibration of the nonequilibrium electron Fermi gas generated after the plasmon-resonant excitation. This electron gas equilibrates through a series of sequential steps that span the femtosecond to picosecond time scales, including ultrafast electronic plasmon dephasing, electron–electron scattering, subpicosecond electron–phonon scattering, and energy dissipation to the nanoparticle surroundings over tens to hundreds of picoseconds.[47] The global fit revealed that the NUs dynamics is dominated by three time constants (<10 fs, 125 fs and >>400 fs) whose amplitudes are reported in the form of DAS in figure 15.2e. The two slower kinetic constants (125 and >>400 fs) contribute mainly to the diagonal peak as rising and decaying component, respectively. This behavior can be appreciated also looking at the decay extracted at diagonal coordinates (square, blue trace in figure 15.2f). Based on their amplitude distribution, the value of the decay constants, and the comparison with previous results, these two kinetics can be likely attributed to the electron-electron scattering and electron-phonon scattering, respectively.[47,238–240] The shortest component depicts dynamics which develop in a timescale comparable with the pulse duration. Several phenomena can contribute to this ultrafast relaxation dynamics, including scattering, pulse overlap effects, induced polarization decay, Landau damping and wavevector randomization and electronic coherent dephasing.[83] While these dynamics is too fast to disentangle the contribution of different kinetic components, I can nonetheless reliably state that the dephasing of the plasmon coherence prepared by the ultrafast excitation must happen in a timescale <10 fs. This value is in line with previous estimates which report a 3-10 fs time for the plasmon dephasing.[45–47,83]
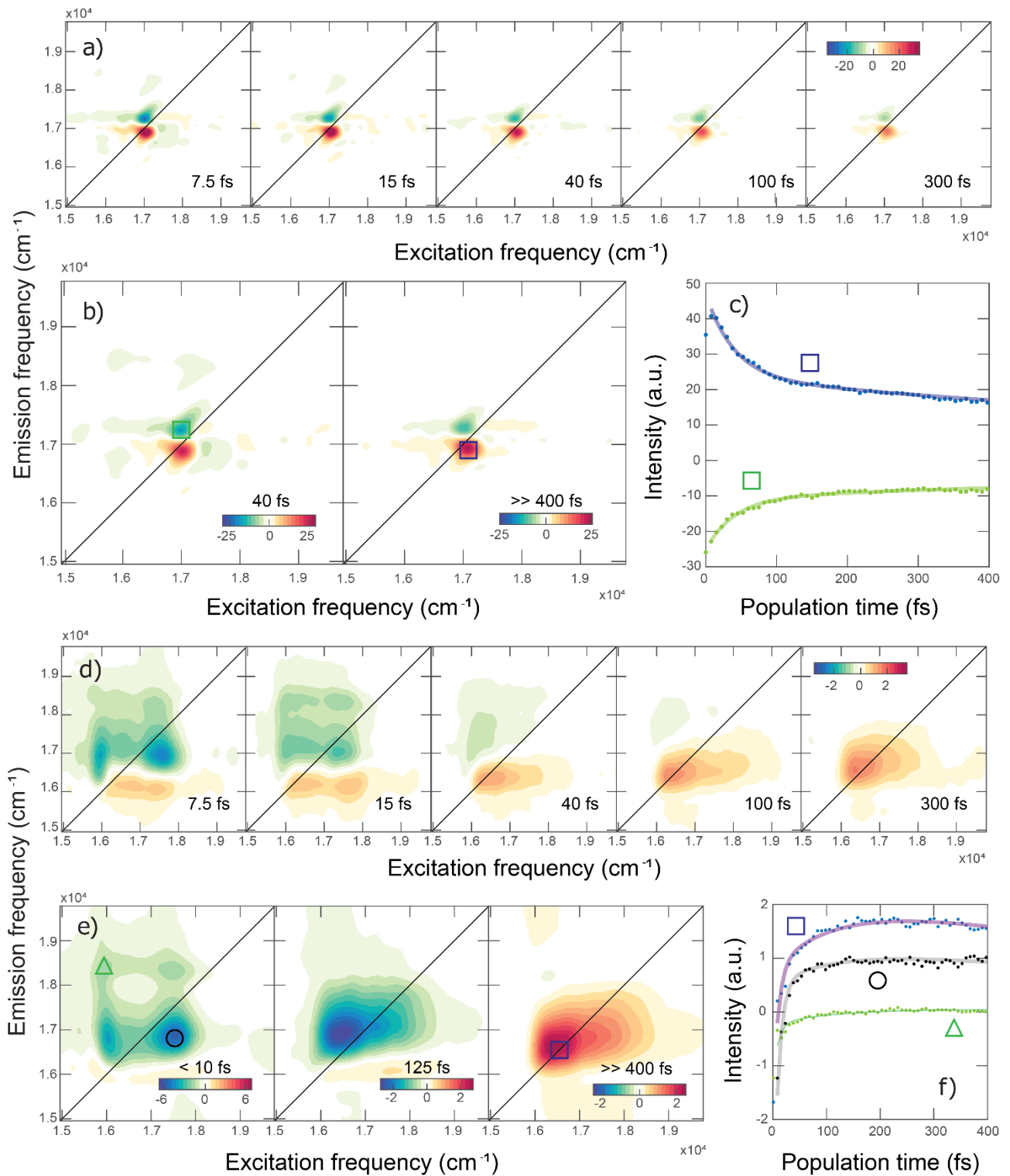
Figure 15.2. 2DES response of the uncoupled components: TDBC J-aggregates a)-c) and NUs d)-f). a) Purely absorptive 2DES maps for TDBC J-aggregates at selected values of population time t_2; b) DAS reporting the amplitude distribution of the two kinetics constants regulating the time evolution of the transient signal as emerging from the global fitting analysis; c) Signal decay extracted at diagonal coordinates (17040, 17040 cm^{-1}), blue square, and at coordinates (17040, 17300 cm^{-1}), green square; d) Purely absorptive 2DES maps for NUs suspensions at selected values of population time t_2, e) same as b), but for NUs. f) Signal decays extracted at diagonal and off-diagonal coordinates pinpointed by the markers.

15.4   2DES analyses of SC plexcitonic nanohybrids. Nanohybrid **1**

The early time 2DES maps of the strongly coupled nanohybrid **1** (figure 15.3a) display a 'square' signal distribution with two diagonal peaks at coordinates 16200 cm^{-1} and 18000 cm^{-1}, and the respective antidiagonal peaks at cross positions. The two diagonal peaks have coordinates which correspond, within the approximation due to the convolution with the laser spectral profile, to the two plexciton resonances already individuated in the extinction spectrum and labelled as UPR and LPR. They enclose contributions from GSB and SE of these transitions. The presence of cross peaks is indicative of the coupling between the plexciton states via the common ground state and via energy exchange. This shape is typical of strongly coupled systems where a coherent coupling between transitions is established.[241] A similar pattern has recently been observed in the 2DES response of another cavity-based polariton system.[85]

During the investigated time evolution, the diagonal peak corresponding to LPR (UPR) shows a progressive blue (red) shift. This trend appears particularly clear if I plot the signal on the diagonal as a function of t_2 (figure 15.3b). This phenomenon has been already detected in other plexciton systems and has been attributed to the transient reduction of the Rabi splitting.[86] It also accounts for the dispersive shape of the LPR diagonal peak, which manifest a bigger shift than UPR.[83,86,241,242]

The overall evolution of the transient signal in the 2D maps is driven by two time components: a fast decay with a time constant of approximately 16 fs and a slower components that remain constant up to 400 fs and accounts for most of the spectral shift described before. Their DAS are shown in figure 15.3c and 15.3d, respectively. The faster component contributes more to the relaxation of the signal at cross coordinates while diagonal signals decay predominantly with the slower time constant (see also the examples of signal decay shown in figure 15.3d-g).

The attribution of these time constants to specific relaxation mechanisms can be done through the comparison with the response of the uncoupled components, the analysis of the DAS and the comparison with the literature. The slower component accounts for all the processes occurring on a timescale longer than the investigated time window. Nonetheless, the clear negative amplitude signal at the cross-peak coordinates below diagonal (18000, 16000 cm^{-1}) in the associated DAS (figure 15.3d), suggests that in this timescale also an incoherent energy transfer from the upper to the lower plexciton branch is occurring.

The faster dynamics has a time constant comparable with the transfer to dark states found in the bare J-aggregates and also with the ultrafast redistribution processes that take place in less

than 10 fs within the non-functionalised NUs. Nonetheless, the amplitude distribution of this fast time constant is completely different in nanohybrids and uncoupled components, suggesting a completely different origin. Therefore, while contributions from ultrafast transfer to J-aggregate dark states and ultrafast electron equilibration in the metal nanoparticle cannot be completely ruled out in this timescale, it can be hypothesized that the 16 fs time constant in nanohybrids **1** corresponds to the damping of an electronic coherence between the two plexciton branches prepared by the broadband photoexcitation.

This attribution is supported by the presence of an oscillating component contributing at the same coordinates and characterized by a very similar damping time (figure 15.3g). The analysis through the global fitting identified for these beatings a frequency of 1500 cm^{-1} and a damping time τ_d of 16 fs. These coherent sub-100 fs oscillations are mainly detected at cross-peaks positions in the rephasing data and at diagonal positions in the nonrephasing spectra, as shown in the amplitude distribution maps in figure 15.3e,f. As already anticipated in section 10.2, this is the typical behavior expected for electronic coherences (excitonic dimer model).

The frequency, damping time and amplitude distribution of this beatings strongly suggest that they originate from an electronic quantum coherences between UPR and LPR. These oscillations represent the smoking gun for the presence of coherent population transfer among the two plexciton branches and represent the first direct experimental real time observation of this phenomenon in colloidal plexciton systems. As further proof for this interpretation, the frequency of these beating (1500 cm^{-1}) coincides with the Rabi splitting measured from the linear absorption spectrum (1510 cm^{-1}, figure 15.1c).
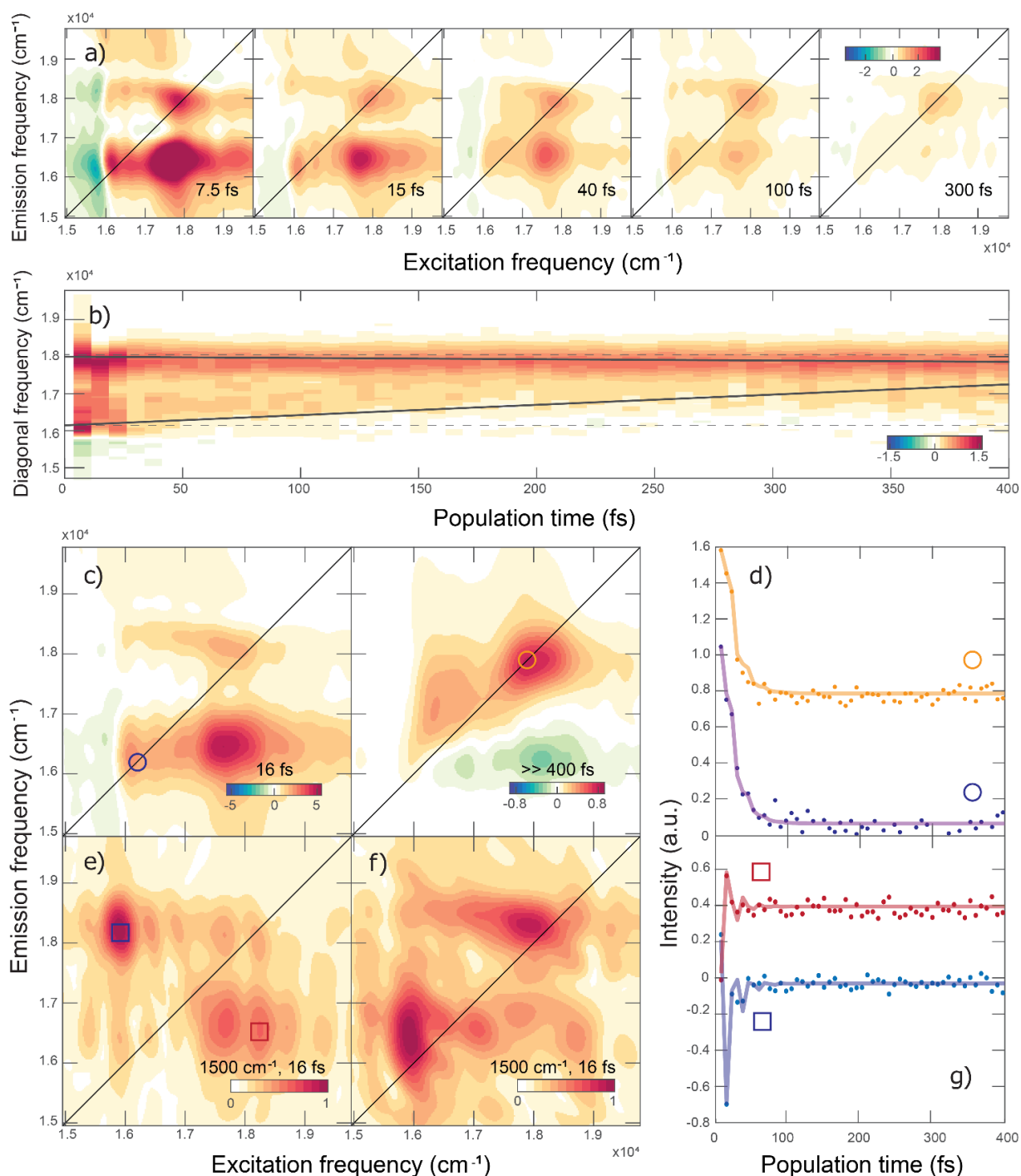
Figure 15.3. 2DES response of nanohybrid **1**: a) Purely absorptive 2DES maps at selected values of population time t_2; b) Diagonal slice of the 2DES maps plotted as a function of t_2. Solid lines highlight the transient reduction of the Rabi splitting; c) DAS associated with the two identified kinetic constants (values reported at the bottom) dominating the dynamics of the nanohybrid. d) Signal decays extracted at the diagonal coordinates pinpointed by the markers: UPR, extracted at (17950,17950) cm^{-1} (orange circle) and LPR at (16150,16150) cm^{-1} (blue circle). Dots and solid lines represent the experimental data and the fittings, respectively. e) Normalized amplitude distribution maps (absolute value CAS[139]) obtained from the global fitting of the rephasing signal relative to an oscillation with central frequency 1500 cm^{-1} and damping time 16 fs. f) Same as e) for the nonrephasing signal. g) Signal decays extracted at cross peaks coordinates pinpointed by the markers: (18070,16450) cm^{-1} (red square) and (16100,18210) cm^{-1} (blue square).

15.5 2DES analyses of intermediate regime plexcitonic nanohybrids. Nanohybrid **2**

The 2DES maps of nanohybrid **2** (figure 15.4a) present a completely different signal distribution than in **1**. At early times (t_2<40 fs) the maps are dominated by a positive feature at 17200 cm^{-1}, corresponding to the energy of the UPR and a negative signal at about 16900cm^{-1}, corresponding to the energy position of the dip between the two plexciton resonances (figure 15.1c). After 40 fs, a positive diagonal signal at 16600 cm^{-1} starts developing. For t_2 > 100 fs, I clearly recognized the two positive features, attributed to UPR and LPR. In addition, in the same timescale a cross peak in the lower diagonal portion of the 2D maps at cross coordinates between the two main diagonal peaks become visible.

The time evolution of all these features can be quantified also in this case by the global fitting analysis, which retrieved three time constants (18 fs, 93 fs, >>400 fs, 2D-DAS in figure 15.4e). The first time constant mainly contributes to the decay of the signal at UPR coordinates. Based on the amplitude distribution of this component and on previous measurements on similar systems, this kinetics can be attributed to a combination of radiation damping and transfer from UPR to J-aggregates dark states.[57,89,243] The second time constant has an amplitude distribution typical of incoherent relaxation dynamics from upper to lower energy states and therefore can be associated to the energy transfer from UPR to LPR. Finally, the slowest time constant mainly captures LPR relaxation processes. The time traces also exhibit fast oscillations on top of the population decays (figure 15.4d). The global fitting captured two principal beating frequencies of 700 cm^{-1} and 1200 cm^{-1} with dephasing times in the order of hundreds of fs, which correspond to the most intense TDBC vibrational modes. Their amplitude distributions (CAS) are reported in appendix A.iii. In the next chapter the nature of these beatings will be further evaluated.
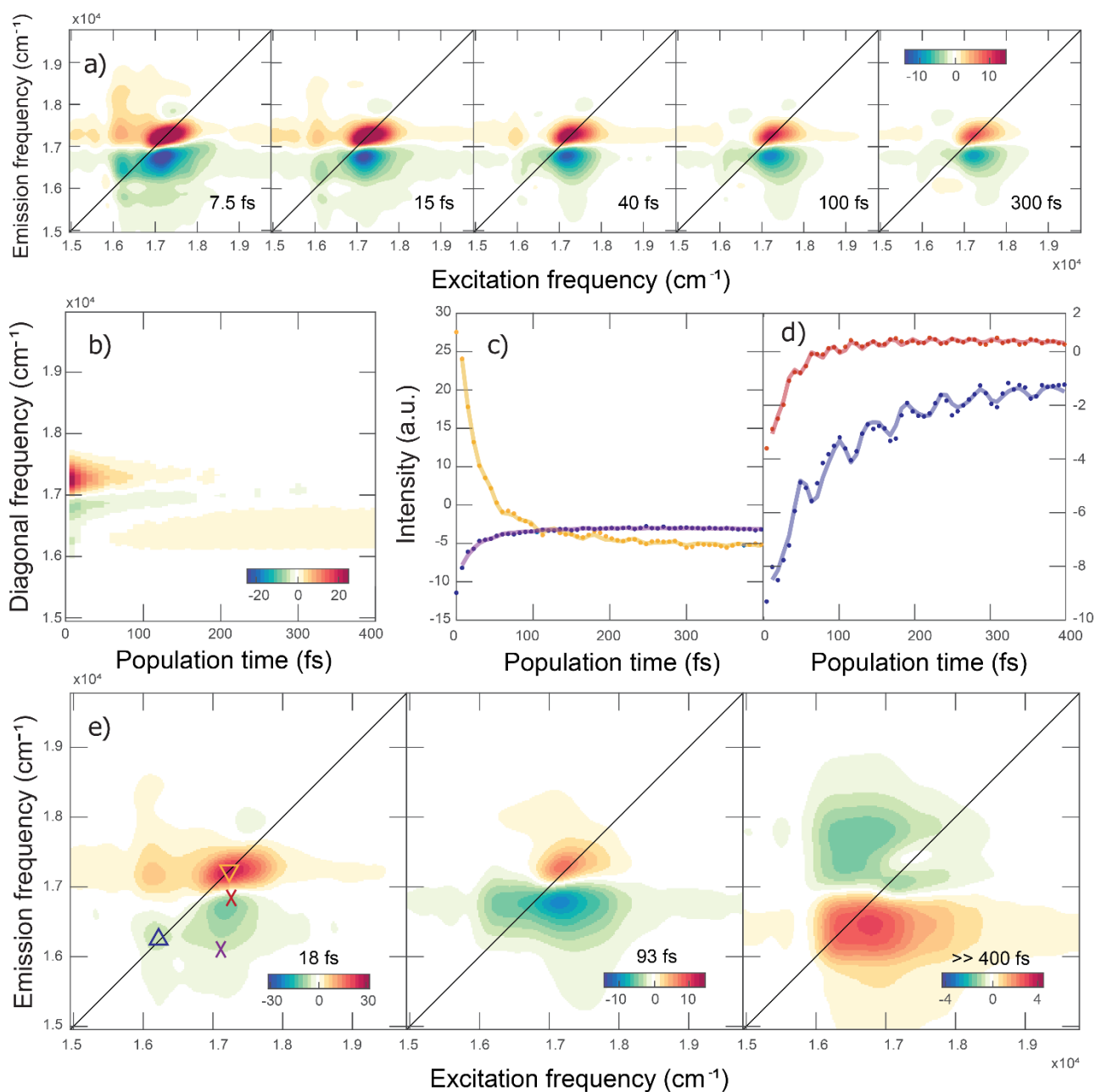
Figure 15.4. 2DES response of nanohybrid 2: a) Purely absorptive 2DES maps at selected values of population time t_2; b) Diagonal slice of the 2DES maps plotted as a function of t_2; c), d) signal decays extracted at relevant coordinates pinpointed by the markers: orange triangle (17220,17220) cm^{-1}, blue triangle (16310,16310) cm^{-1}, red cross (17137, 16077) cm^{-1} and blue cross at (17324,16920) cm^{-1}. The dotted lines represent the experimental signals while the solid lines the corresponding fits; e-f) DAS associated with the three identified kinetic constants (values reported at the bottom) dominating the dynamics of the nanohybrid **2**.

15.6   Discussion and final remarks

Although the challenging nature of the 2DES responses reported in figure 15.3 and 15.4 requires further analyses, currently underway, the experimental findings reported here are strongly suggesting that:

(i) the ultrafast dynamics of plexcitonic nanohybrids is strongly affected by the coupling regime. This could explain the often scattered and contradictory interpretation of the dynamics offered by literature works. These findings call for a more conscious and careful definition of the coupling regime when investigating the plexciton ultrafast dynamics;

(ii) the coherence lifetime of plasmonic substrates can be effectively tuned modulating the level of hybridization with molecular excitons, forming plexciton states.

This second aspect is particularly meaningful in view of the application of plasmonic moieties in quantum devices. Theoretical predictions suggested that the system-bath coupling properties can be controlled using the polaron decoupling effect, in which a coherent interaction between molecular excitons and photons reduces the reorganization energy, leading to significant changes in the rates of photophysical processes.[69] These theoretical predictions have been recently experimentally demonstrated by 2DES applied to a periflanthene derivative film in a microcavity.[84] It was suggested that the strong light-matter coupling established in this system suppresses the dephasing of electronic coherences, possibly supporting coherence-assisted processes. This approach appears highly promising towards the development of quantum technologies devices where the promotion of hybrid polariton states can control the dephasing of quantum coherence.

On the one hand, it is expected that 2DES measurements will play an essential role in achieving a better understanding of the physical and dynamic phenomena at the base of this still underexplored but encouraging effect.[83] 2DES technique is indeed universally recognized as one of the most powerful tools for the investigation of the ultrafast coherent dynamics in complex systems. In recent years, the enormous potential of 2DES techniques to impact the field of nanosystems, semiconductors, quantum technologies, and quantum devices started to be recognized.[241,244] In this context, the first applications of 2DES to plexciton systems are appearing to complement ultrafast pump and probe studies.

On the other hand, the experimental evidence is still very scarce and the mechanisms underneath the enhancement of coherent behavior still unknown. This call for a significant experimental effort in the design of plexciton systems library and the systematic investigations of their optical properties to devise clear structure-to-property relationships. All the experimental results described in this Thesis aim towards this final achievement.

16. Incoherent relaxation pathways and role of vibrational mechanisms for non-strongly coupled plexcitonic systems

16.1 Introduction

In the previous chapter evidence for a peculiar mechanism of amplification of the molecular vibrational modes was found in a nanohybrid that cannot satisfy the SC conditions. To shed more light into this phenomenon, I explored the dynamics of another plexcitonic system in between Fano and the SC regime. This regime has never been studied in the 10-500 fs time domain, and thus its characterization could allow a better comprehension and rationalization of the overall polaritonic dynamics.

The system under investigation is a CPM prepared by mixing gold nanourchins (NUs, figure 16.1a) and PIC J-aggregates (PIC-J, figure 16.1b), in a regime which satisfies the condition of existence (equation 4.22) but not the SC one (equation 4.23). The results suggest that this regime produces real plexcitonic states, whose photophysical properties are closer to the SC than to the Fano-like regime, although their dynamics are mainly incoherent. Moreover, the analysis revealed an unusual UP to LP energy transfer, which seem to be, at least partially, vibrationally assisted.

16.2 Nanohybrid assembly

Also in this case the system of interest was selected among the vast library of NUs-based materials described in chapter 14. I selected a CPM prepared by coupling citrate-capped NUs (plasmon peak centred at 607 nm= 16475 cm^{-1}, average diameter 88 ± 5nm, figure 16.1a) with PIC molecules (figure 16.1b) in its J-aggregate form.

In the extinction spectrum of the hybrid (figure 16.1c) two new plexcitonic resonances appeared at 566, Upper Plexciton Resonance, UPR and 591 nm, Lower Plexciton Resonance, LPR (17668 and 16920 cm^{-1}, respectively), while the PIC-J exciton region around 579 nm (17271 cm^{-1}) presents the typical plexcitonic "dip".[142]

From the analysis of the extinction spectrum, in the same way of the last chapter, the following parameters were estimated: k = 170 meV, γ = 12.6 meV and Ω_R = 93 meV (see chapter 4.3 for more insights about the meaning and the calculation of these parameters). Consequently, using equation 4.19, g were estimated being 92 meV. With these parameters, this CPM satisfies the existence conditions, but not the SC conditions, which is the same situation of nanohybrid **2** investigated in the previous chapter.
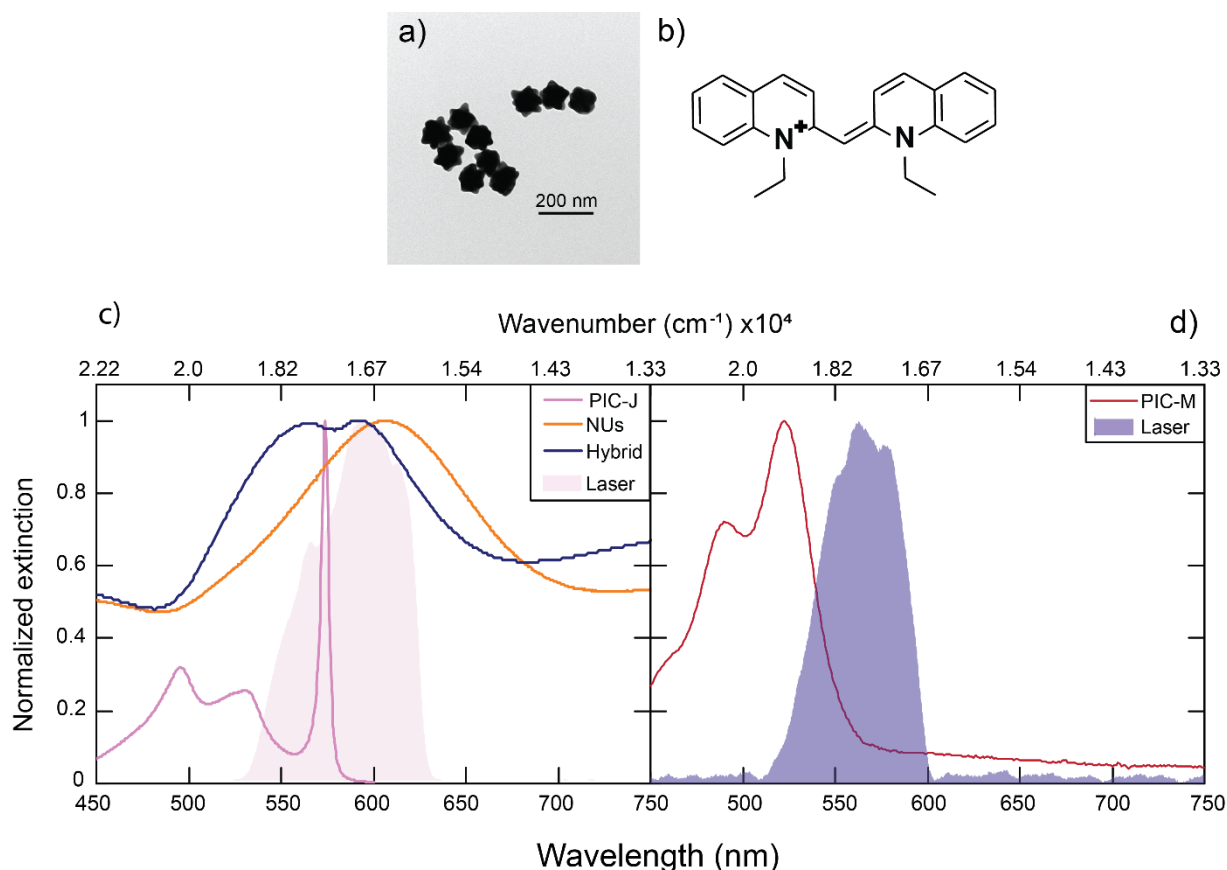
Figure 16.1. a) TEM image of NUs; b) molecular structure of the PIC molecule; c) normalised extinction spectra of NUs, PIC-J-aggregates and the nanohybrid, compared to the laser profile used in 2DES (pink area); d) normalised extinction spectrum of monomeric PIC molecules and laser profile used for their 2DES characterisation (blue area).

16.3   2DES analyses of uncoupled systems

Also in this case, the dynamics of the hybrid have been compared with the dynamics of the uncoupled systems: PIC in the monomeric form (PIC-M), PIC in the J-aggregate form (PIC-J), and citrate capped NUs.

PIC J-aggregates. 2DES maps reporting the rephasing, non rephasing and total signals recorded for a solution of PIC J-aggregates are reported in (figure 16.2a and A6a, A7a in Appendix). The maps are dominated by a diagonal peak at 17400 cm^{-1} (574 nm), which corresponds to its excitonic peak. A global multiexponential fitting was performed to evaluate the dynamics along the population time t_2.[139] PIC-J exciton dynamics was fitted with two exponential decays (40 fs and >>500 fs). The shorter time was tentatively attributed to the fast intra-band relaxation and the slower time to all the processes characterized by time constants longer than the investigated time window, among which fluorescence.[245] Figures 16.2b reports the associated DAS, while the signal decay and the relative fitting at the coordinate of the

excitonic peak are shown in figure 16.2c. The dynamics of PIC-J do not present any oscillating component, as also reported in the Fourier Transform (FT) of the fitting residues (figure 16.3). The coupling with specific molecular vibrations, indeed, are (at least partially) suppressed in aggregates.[156,246,247]
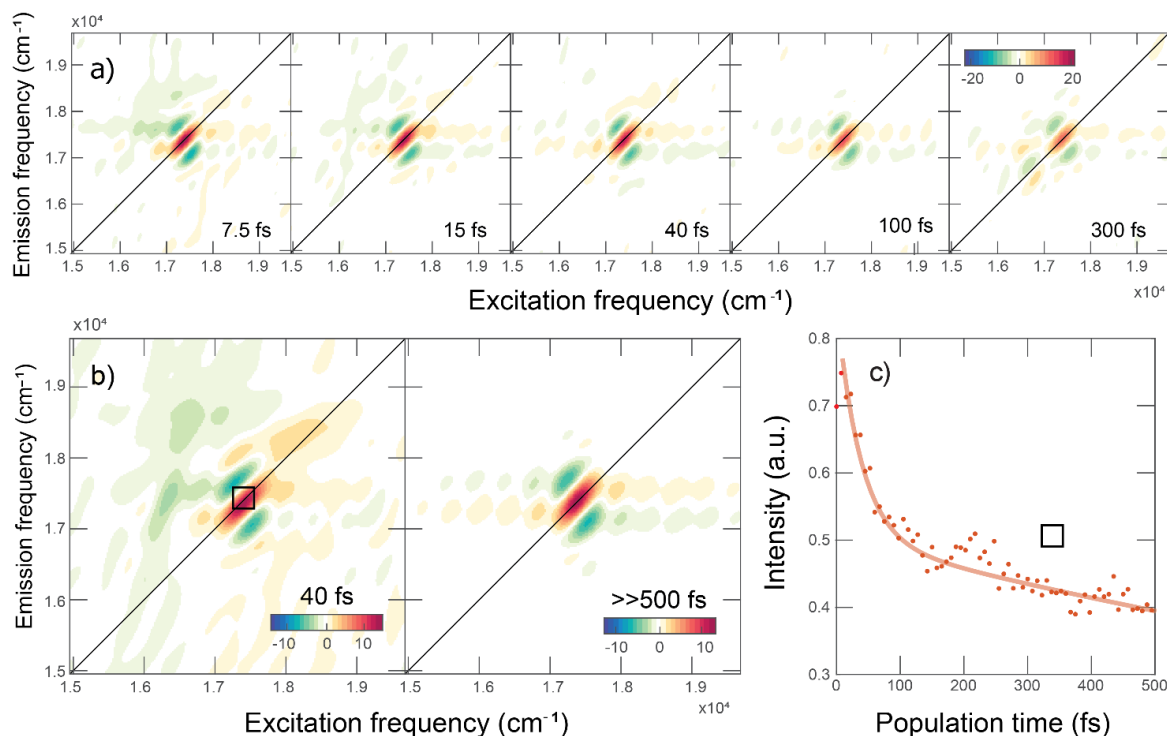
Figure 16.2. 2DES experiments and analysis for the PIC-J sample: a) 2DES rephasing maps at selected values of t_2; b) DAS associated to the two time constants emerging from the global fitting (40 fs and >>500 fs); c) PIC-J excitonic peak evolution along t_2 (dots) and its fitting (red line), extracted at coordinates (17390, 17390 cm^{-1}).

For further insights on the molecular vibrations in PIC, I also analysed a solution of PIC in the monomeric form (PIC-M). In this experiment, the laser profile was tuned on the blue side of the spectrum to maximize the overlap with the absorption spectrum of PIC-M (figure 16.1d). Note that for technical reasons (associated with the performances of noncolinear optical parametric amplification, see section 10.3), it was not possible to push the excitation profile further to the blue to achieve better resonance conditions.

2DES maps for PIC-M are reported in figure 16.3a (rephasing) and A6d-A7d in appendix A.iii (non rephasing and total, respectively). The global fitting revealed a dynamics more complicated than in PIC-J, with two non-oscillating components (133 and >>500 fs, DAS in figure 16.3b), superimposed to several beating frequencies. Among them, three main oscillating components were identified at 135, 334 and 1410 cm^{-1} (CAS in figure 16.3b), corresponding ti the typical vibrational modes of PIC molecules.[245,248,249] Insights on decays and fittings are reported in figure

16.3c. These vibrations are clearly visible in the FT of the residues (figure 16.4), in stark contrast with PIC-J.
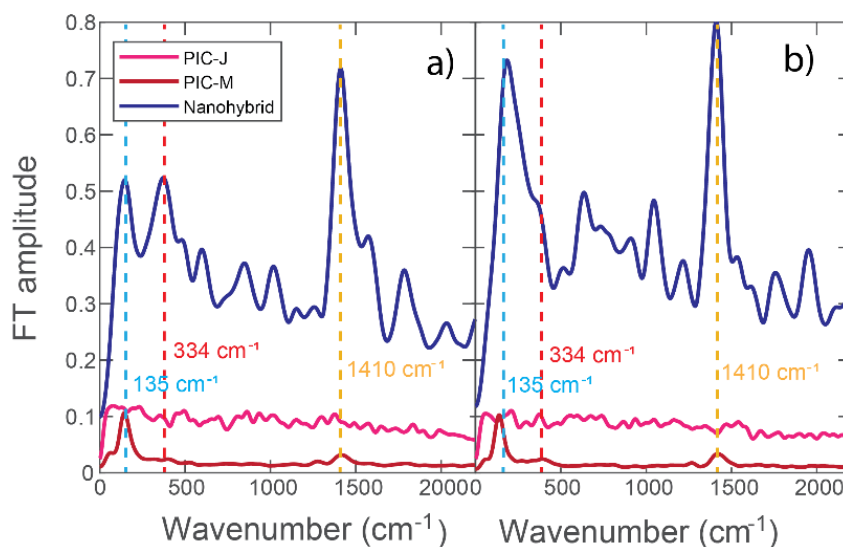
Figure 16.3. FT of the oscillating residues of the global fitting obtained from a) the rephasing and b) the non rephasing experiments for PIC-J (pink), PIC-M (red) and the nanohybrid (blue). The three most intense vibrations are pinpointed by vertical dashed lines.

NUs. Rephasing, non rephasing and total maps (figure 16.5a, A6b and A7b in appendix, respectively) measured for a suspensions of NUs show a broad diagonal peak at 16666 cm^{-1} (600 nm), whose intensity progressively increases with increasing t_2. This peak can be easily attributed to the plasmon resonance of NUs. This behaviour is qualitatively the same reported for the NUs studied in the previous chapter. Indeed, also in this case an ultrafast relaxation dynamics (<10 fs) was found, due to several phenomena, including induced polarization decay, Landau damping and wavevector randomization, electronic coherent dephasing and plasmon dephasing.[83] As already commented in the previous chapter, these phenomena cannot be fully resolved from scattering and pulse overlap effects, because they have timescales faster or comparable with the experimental pulse duration (see figure A8 in appendix). At longer times, the typical electron-electron scattering (243 fs) and electron-phonon scattering (556 fs) dominate the dynamics.[47] The DAS associated with these three phenomena are reported in figure 16.5b, and signal decay traces extracted at relevant coordinates are reported in figure 16.5c.
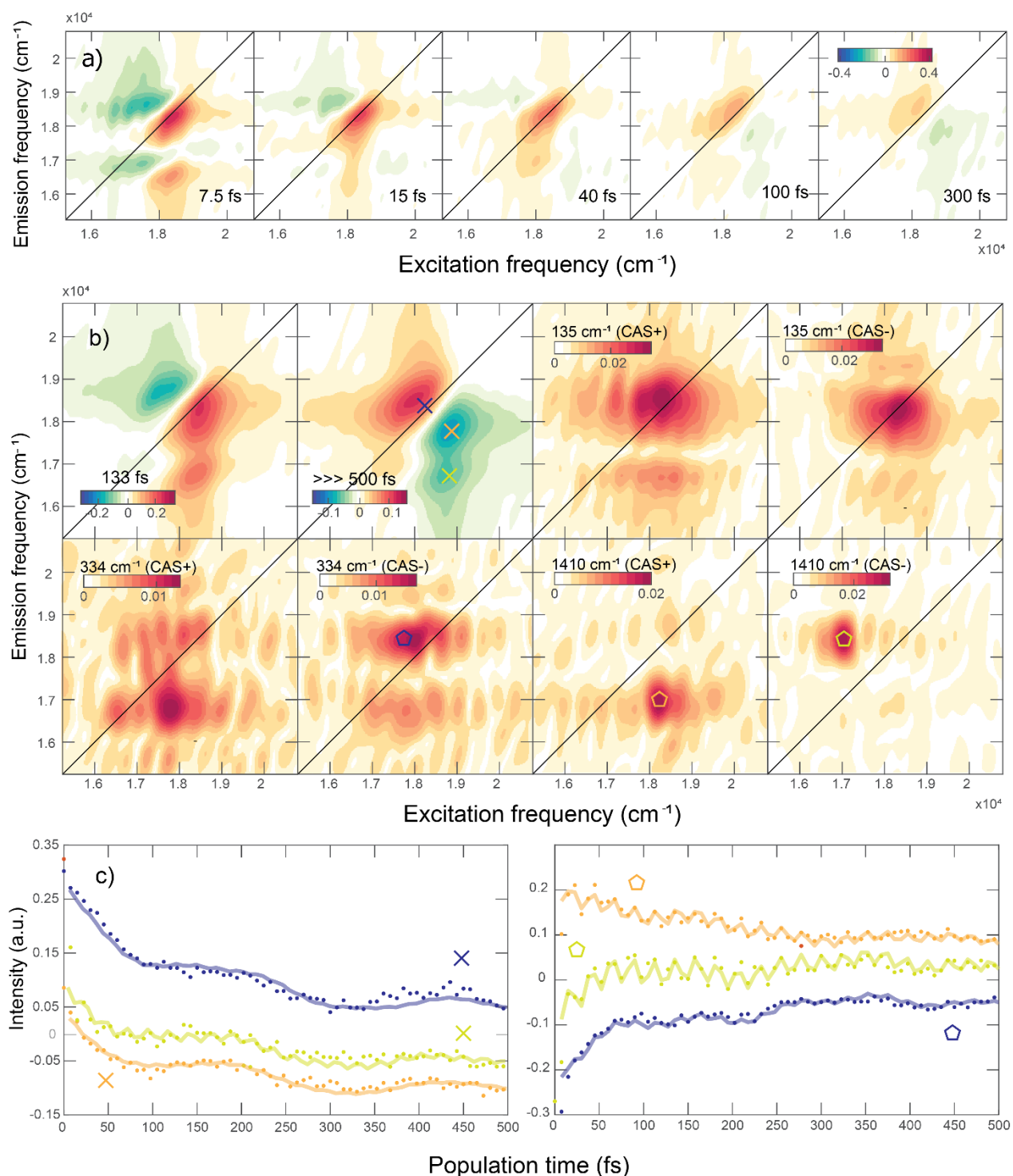
Figure 16.4. 2DES experiments and analysis for the PIC-M sample: a) 2DES rephasing maps at selected values of t_2; b) DAS associated to the two time constants emerging from the global fitting (133 and >>>500 fs) and CAS associated with vibrational modes of frequency 135, 334 and 1410 cm^{-1}; c) Signal decay traces as a function of t_2 (dots) and their fitting (solid lines) extracted at relevant coordinates, pinpointed by different markers: blue cross (18140, 18140 cm^{-1}), orange cross (18810, 17790 cm^{-1}), green cross (18570, 16410 cm^{-1}), blue pentagon (17600, 18760 cm^{-1}), orange pentagon (18160, 17000 cm^{-1}) and green pentagon (17060, 18490 cm^{-1}).
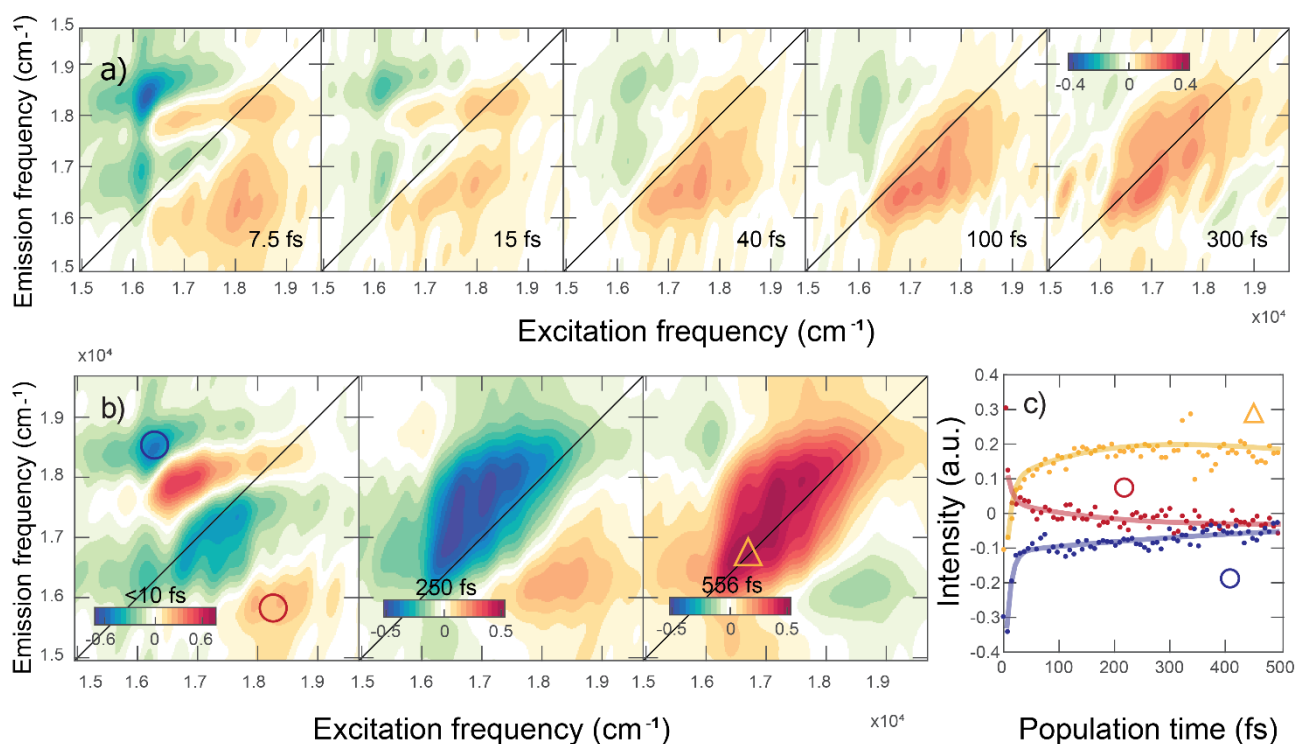
Figure 16.5. 2DES experiments and analysis for the NUs sample: a) 2DES rephasing maps at selected values of t_2; b) DAS associated to the two time constants emerging from the global fitting (<10, 250 and 556 fs, respectively) ; c) Signal decay traces as a function of t_2 (dots) and their fitting (solid lines) extracted at relevant coordinates, pinpointed by different markers: yellow triangle (16780,16780 cm^{-1}), blue circle (16190,18490 cm^{-1}), red circle (18190,15850 cm^{-1}).

16.4   2DES analysis of the nanohybrid

Early times 2DES maps of the nanohybrid (figure 16.6a) are dominated by a strong and quickly decaying diagonal signal at 17200 cm^{-1}; meanwhile, another diagonal signal at 16400 cm^{-1} and a cross-peak at (17200; 16400 cm^{-1}) are rising as t_2 increases. After growing for the first 100 fs, the diagonal signal at 16400 cm^{-1} starts to decay, too. A similar behaviour occurred in non rephasing experiments (figure A6c, appendix) and the pure absorptive maps (figure A7c, appendix).

Similarly to what has been discussed in the previous chapter, and considering the electronic structure as emerging from the extinction spectrum, these two diagonal signals can be attributed to UPR and LPR. Their position in the 2D maps is slightly redshifted compared to the extinction spectrum, but this can be easily justified considering that the 2D signal is a convolution with the laser spectral profile. It was verified that the extinction spectra of the sample after each measurement remained unchanged, evidence that no significant degradation or band shift happened during the analysis (figure 16.7).
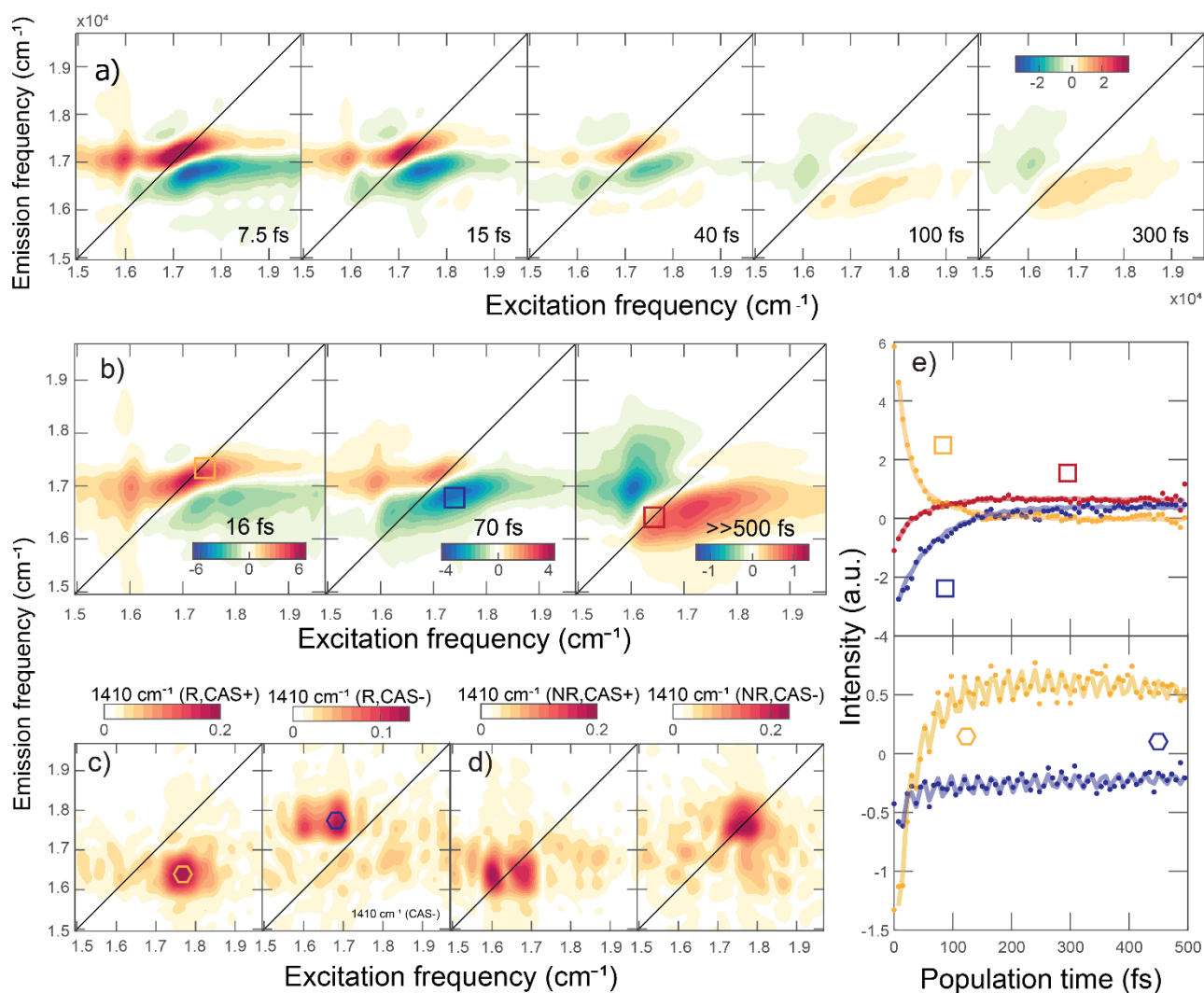
Figure 16.6. 2DES experiments and analysis for the nanohybrid: a) 2DES rephasing maps at selected values of t_2; b) DAS associated to the three time constants emerging from the global fitting (<10, 250 and 556 fs, respectively); c-d) CAS associated with the vibrational mode at 1410 cm^{-1} in the c) rephasing and d) non rephasing signals; e) Signal decay traces as a function of t_2 (dots) and their fitting (solid lines) extracted at relevant coordinates, pinpointed by different markers: orange square (17300,17300 cm^{-1}), blue square (17300, 16900 cm^{-1}), red square (16406,16406 cm^{-1}), orange hexagon (17500,16350 cm^{-1}) and blue hexagon (16660,17450 cm^{-1}).

The global fitting revealed three non-oscillating components of 15, 70 and >>500 fs (DAS in figure 16.6b). The interpretation of the associated physical relaxation phenomena can be done inspecting the amplitude distribution of each kinetic constants in the 2D maps, as shown in the DAS. The first DAS (15 fs) is dominated by a strong decay signal at diagonal coordinates corresponding to UPR (orange square) and by a negative decaying signal at (17200;16666 cm^{-1}, blue square). We attribute these dynamics to a relaxation from UPR to excitonic reservoir (figure 16.6e). Indeed, the blue signal appears at about 500 cm^{-1} below UPR, in correspondence of the plexcitonic "dip" in the extinction spectra, which roughly correspond to the excitonic reservoir[69]. Since these states are dark, no signals are expected on the diagonal at their corresponding

coordinates , but their presence can be ascertained through the presence of ESA (blue negative sign) processes.[79] The second non-oscillating component (70 fs) can be instead attributed to a UPR to LPR incoherent energy transfer, since UPR is depopulating while LPR is rising. The presence of a low antidiagonal rising signal (figure 16.6e, orange hexagon) strongly implies the incoherent transfer (see section 10.2). Finally, the third component can be easily associated with the LPR relaxation back to the ground state (figure 16.6e, orange and red square tracks), characterized by a timescale longer than the experimental time window (500 fs).[91-93] These attributions are in full agreement with results already reported in the previous chapter.
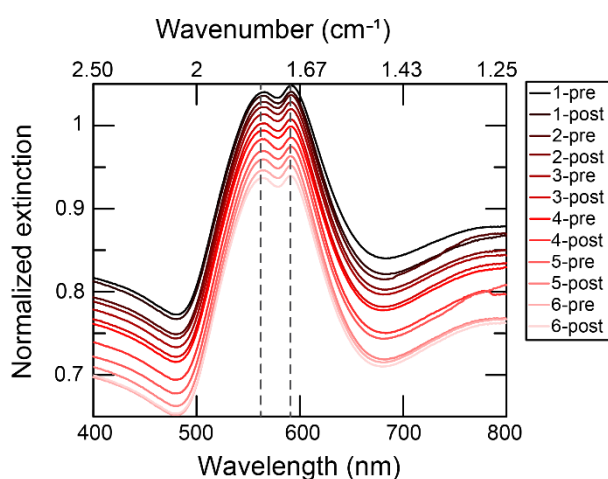
Figure 16.7. Normalized extinction spectra of the nanohybrid before and after each of the six 2DES measurements, as indicated in the legend. The spectra, vertically shifted to ease the comparison, do not present any visible degradation of the plexcitonic bands. Vertical dashed lines, indeed, report the position of the URP and LRP, which result unchanged during the experiment.

In addition to these three decaying components, the global fitting also revealed several beating components. I identified the strongest ones at 135, 334 and 1410 cm^{-1}, as shown in the FT spectra of figure 16.3. These are the same modes appearing also in the monomer dynamics and therefore the most likely interpretation also in this case would be to attribute them to vibrational modes of the PIC molecule. A careful comparison between the FT spectra of the beatings in the PIC-M and nanohybrid samples revealed however a significant enhancement of these modes in the nanohybrids. The enhancement is particularly evident for the mode at 1410 cm^{-1}, characterized by a damping time longer than the experimental time window. The amplitude distribution of this beating mode is shown in the 2D-rephasing CAS in figure 16.6c and 2D-non rephasing CAS in figure 16.6d.
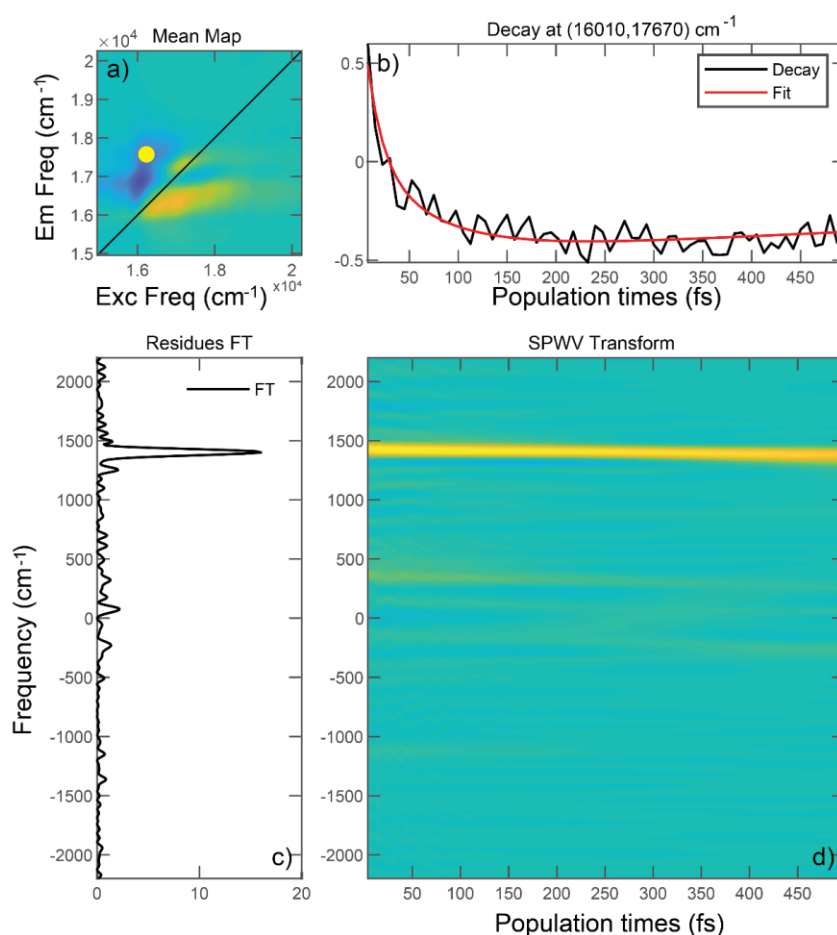
Figure 16.8. a) 2DES rephasing mean map of the nanohybrid; the yellow dot (16010,17670 cm^{-1}) indicates the coordinate at which the analysis was performed; b) experimental decay (black line) and fitting (red line); c) FT of the fitting residues; d) SPWV transform of the fitting residues.

These CAS revealed two signals for the rephasing experiment at off-diagonal coordinates (17500,16350) cm^{-1} and (16660,17450) cm^{-1}, and two signals for the non rephasing experiment at diagonal coordinates (16390,16390) cm^{-1} and (17550,17550) cm^{-1}. This signal distribution does not fully follow the typical behavior expected for vibrational modes (the 'chair' pattern already described in the displaced harmonic oscillator model in section 10.2) and found for the other modes at 135 and 334 cm^{-1}. Instead, the mode at 1410 cm^{-1} seems to contribute mainly at cross peak positions, where signals originating from the UPR/LPR coupling are predicted. This might indicate that the UPR to LPR relaxation occurs also by activating that molecular vibration. To gain more insight on this mechanism, we analysed the beating residues at the cross peak positions applying a smoothed-pseudo-Wigner-Ville (SPWV) transform (figure 16.8-9). The methodology is anticipated in chapter 10. The analysis confirmed that the amplitude of the oscillations does not grow in time, suggesting that they are instantaneously prepared directly by the pulse excitation. The incoherent and vibronic assisted energy transfer from UPR to LPR

must thus be independent mechanisms. If it had not been so, the amplitude of the oscillations would have increased with a time similar to the incoherent UPR to LPR energy transfer (70 fs).

These findings seem to indicate, first, that vibrational modes of PIC are enhanced by the coupling with the plasmonic surface, a well-known phenomenon typically exploited also in Surface Enhanced Raman Spectroscopy (SERS). Second, the peculiar amplitude distribution of the 1410 cm^{-1} mode suggests a more complex origin, involving the coupling with the whole nanohybrid structure. Additional analyses, current underway, are needed for a better comprehension of this behaviour.
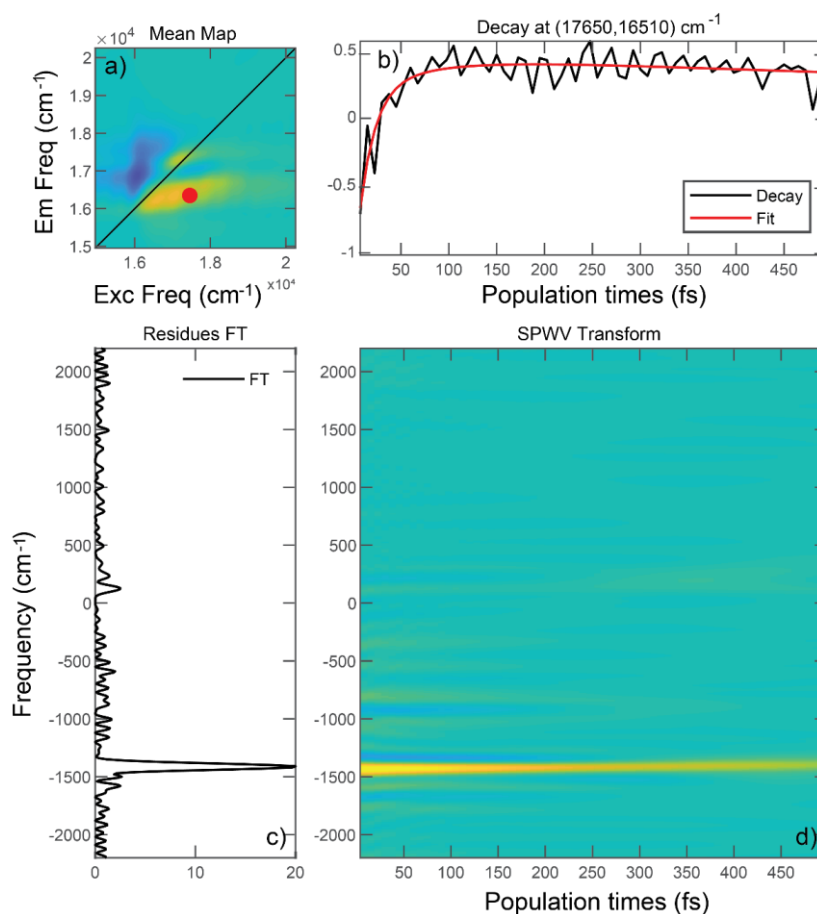
Figure 16.9. a) 2DES rephasing mean map of the nanohybrid; the red dot (17650,16510 cm^{-1}) indicates the coordinate at which the analysis was performed; b) experimental decay (black line) and fitting (red line); c) FT of the fitting residues; d) SPWV transform of the fitting residues.

16.5   Final remarks

The   2DES characterisation of a J-PIC-NU nanohybrid in the intermediate coupling regime revealed interesting and unexpected details of its relaxation dynamics. The relaxation from UPR to the excitons reservoir and to LPR through incoherent

mechanisms were observed and the dynamic behavior was found to be in agreement with the previously studied dynamics of TDBC-NUs hybrids (chapter 15). I also evaluated the role of molecular vibrations, which are enhanced in the nanohybrid in comparison to the molecular vibrations of PIC in aggregated and monomeric forms. The SERS effect cannot (completely) explain this phenomenon. 2DES, indeed, was able to isolate an UPR to LPR vibrationally assisted energy transfer, in addition to the plasmonic enhancement, at least for the vibration at 1410 cm^{-1}. Molecular vibrations have been already reported to assist the relaxations from the dark states of the excitonic reservoir to the LPR,[69] while this is the first observation of this mechanism for the relaxation from UPR to LPR. It can be speculated that the small energy gap between UPR and LPR (900 cm^{-1}) favours the direct relaxation to LPR, while usually the relaxation to the excitonic reservoir is prominent.

Even if this plexctonic sample does not satisfy the strong coupling conditions, the two states have been found to be real, rather than being a Fano interference. This chapter and the previous one proved again that the boundaries between the intermediate Fano regime and the SC one are not well marked (section 4.4). More likely, the transition to the strong coupling regime involves a rich wealth of "coupling shades", also including the situation experimentally analysed here, namely the formation of two real hybrid states, which are however not coupled enough to be coherent. Overall, it seems that, just by tuning the coupling strength by varying the number of molecules onto the surface, completely different dynamics behaviours can be achieved, ranging from electronic quantum coherences (strong coupling) to incoherent relaxation with activation of vibrations. Such a high versatility proves again the importance of plexcitonic and, more generally, polaritonic materials within the chessboard of the quantum technologies and nanophotonics applications.

IV Colloidal plexcitonic materials: first steps to performative hybrids

In this part, I will summarize and critically analyse, when possible, the literature available on Colloidal Plexcitonic Materials (CPMs). The goal of this review is to connect the design of these materials to their optical properties. To this aim, I first analysed the variability of the main components of CPMs (plasmonic NPs, QEs, and capping layer), and then correlated them with optical figures of merit, such as Ω_R and g.

17.   Introduction

In part III, I prepared and analysed several colloidal plexcitonic materials (CPMs), discovering that their dynamics can be tuned either in the fs timescale, where their coherent behaviour can be selectively activable, and at longer times, as reported in the case of nanospheres-TPPS hybrids. Moreover, the study of the nanourchins hybrids revealed that the design of systems capable to achieve the light-matter coupling states might not be trivial.

The field of CMPs is relatively young and still poorly explored: to the best of our knowledge, the first paper on this subject was published in 2001 and the overall literature counts only 70 papers and less than 100 systems studied. Consequently, there are still not clear rules that allow to predict the optical properties of CPMs (Ω_R or g) from the design of their components.

In particular, relevant components of CPMs are two or three, depending on the cases: i) a plasmonic NP, ii) the QEs adsorbed on the NP; iii) the NP capping layer (CL), which stabilizes the NPs and plays the important role of controlling the interactions between the NP and the QEs.[18] It must be noted that the capping layer, while present in most, if not all, of the cases described, is not in principle necessary or it can be formed by the QEs themselves.
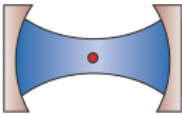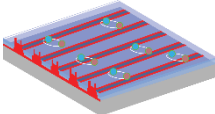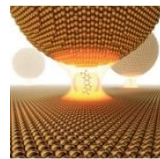
A full understanding of how these components influence important parameters like Ω_R or g is still missing and could be crucial to identify on one hand new guidelines in the design of CPMs, and, on the other, to boost the production of novel and more efficient light-matter hybrids states. To get more insight on this point, I systematically analysed the 70 papers available classifying them on the basis of the nature of the CPM components. The organization of this part is the following: first, I compared colloidal plasmonic nanoparticles to other cavities, to detect their strengths and weaknesses (chapter 18). Then, I presented the historical development in CPMs field (chapter 19). The methods for the data retrieving and processing are reported in chapter 20. The analysis of the literature is reported in chapter 21 and 22, where, respectively, I identified the most common classes of CPMs components and their relationship with Ω_R or g. Finally, an outlook and the future challenges conclude the analysis in chapter 23.

18.   Plasmonic colloidal NPs: an interesting hosting cavity

In chapter 2, several materials that can act as cavities for the light-matter coupling were introduced. They include optical cavities and microcavities, plasmonic surfaces and nanoparticles (NPs), transition metal dichalcogenides and NPs-on-mirror hotspot cavities. Their main properties are summarized in Table 18.1.

Table 18.1. Different cavity systems used for the light-matter coupling. The images in the first row are reproduced from ref.[20] for the microcavity class, ref.[86] for the plasmonic surfaces, ref.[17] for the colloidal NPs and ref.[50] for the hotspot cavities.

	Optical and Micro Cavities	Plasmonic surfaces	Colloidal Plasmonic NPs	Hotspot cavities
Effective volume	High	Low	Low	Very low
Loss	Low	High	High	High
Cavity resonance	Narrow	Broad	Broad	Broad
Synthesis/ Preparation	Sputtering; Evaporation; Chemical vapour deposition	Sputtering; Evaporation; Electrodeposition; Nanolithography	Wet chemistry	Physical and chemical methods
Standard Characterization	Dispersion diagram; Scattering spectrum	Dispersion diagram; Scattering spectrum	Extinction spectrum	Dispersion diagram; Scattering spectrum

Each cavity system has different advantages and drawbacks. Microcavities (as well as classical photonic cavities) have higher effective volume, lower losses and, for this reason, narrower resonances than the other materials. However, colloidal plasmonic NPs have small effective volumes which abundantly overcome their high losses, to the point that coupling strengths equal or stronger than optical cavities are achieved (chapter 2 and 5). Colloidal plasmonic NPs are more synthetically accessible since they are the only ones prepared through a completely chemical approach (wet chemistry). Indeed, microcavities and plasmonic surfaces are usually prepared by physical methods (sputtering, evaporation, chemical vapour deposition, electrodeposition, and nanolithography), while hotspot cavities are prepared by combining physical (for the plasmonic surface) and chemical methods (for the nanoparticles). Moreover, colloidal plasmonic NPs require simpler methods for the characterization of the plexciton: a simple extinction spectrum is sufficient to identify its presence and quantify the main coupling parameters. On the other hand, more elaborate and expensive techniques are needed to obtain the scattering spectrum and the dispersion diagrams of the other kinds of cavities.

Hence, the overall picture emerging from table 18.1, indicates colloidal plasmonic NPs as the most suitable candidates for strong light-matter coupling, at least at the level of fundamental

investigation. However, there are also drawbacks to take in account. The first one is reproducibility. Wet synthesis, indeed, leads in many cases to samples containing collections of NPs with different, albeit close enough, sizes. Each of these particles can potentially couple in a different way with the absorbed QEs. The second significant drawback is the stability of the suspensions and of the particles themselves. Heavy NPs collapse and precipitate because of gravity. Capping layers not always completely hamper NP-NP interactions, allowing or favouring their aggregation, and etching processes, leading to size or shape modifications. It should be noted, however, that the deposition of the NPs onto a solid support could in principle address these problems.

19.   The historical landscape

Although the first publications about plexcitons date to the early '80s (see chapter 2),[42–44] the first two examples of CPMs were published only in 2001 by the groups of Yonezawa[48] and Kawasaki.[157] Reports remained however quite scarce until 2008, with a few papers published by the groups of   Wiederrecht and Yonezawa (see for instance Ref.[48,158–160,211,250,251]). In 2008, Ni *et al.*[218] characterized a CPM with gold nanorods and HITC molecules, while Fofang *et al.*[161] investigated a Fano-like CPM composed of gold nanoshells and DBTC J-aggregates. These are the first two papers where the typical terminology and characterizations commonly used by the community of strongly coupled materials appear. In particular, the typical dye concentration trend (equation 4.10) and the dispersion curve (figure 4.2) were reported. Fofang's work raised considerable and widespread interest (531 citations by now, June 2021). In the following years, several other groups started to be involved in this topic, among which Balci's,[75,83,92,93,214,217,252] Chandra's,[106,201,208,210] Liz-Marzan's,[77,91,175,216] and Rakovich's.[77,91,175,209,215,216,222] Figure 19.1 reports the yearly increase of the number of papers and the relative number of nanosystems studied. In particular, CPMs were classified into two subgroups: the CPMs dispersed in solution (CPM-S), and the CPMs deposited onto a solid substrate (CPM-D). Nowadays, CPM-S are much more studied than CPM-D, since the number of papers about CPM-S doubles the one for CPM-D (48 and 22, respectively) and the number of CPM-S systems is three times the one of CPM-D (68 and 24, respectively).
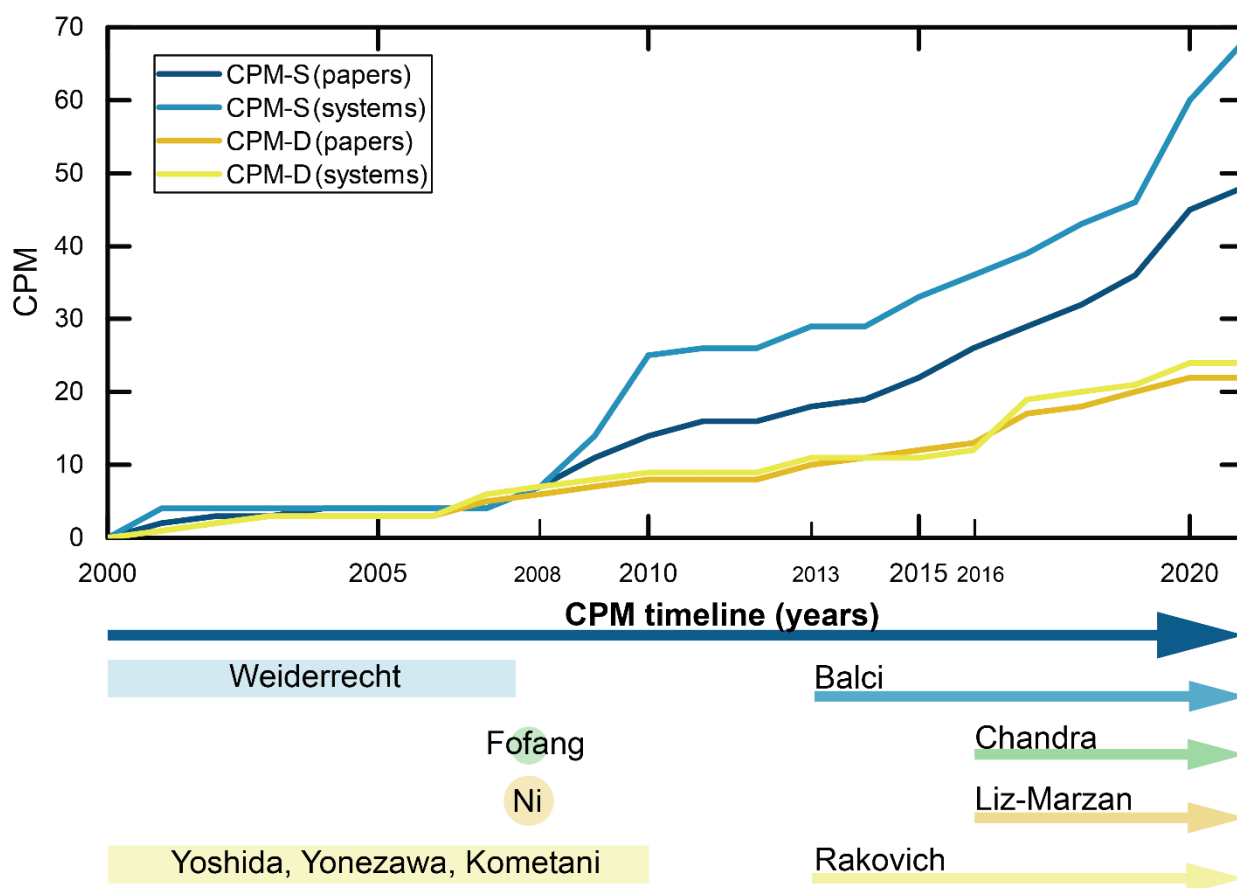
Figure 19.1. Timeline of the study of CPM. On the top, the number of the published papers and the number of studied nanosystems are reported as a function of the time. CPMs are divided into CPM dispersed in solution (CPM-S) and CPM deposited onto a solid support (CPM-D). On the bottom, the timeline of the research work of some of the most important groups whose activities is ceased (rectangles) or still active (arrows) and some of the most important published papers (Ni *et al.*[218] and Fofang *et al.*[161], circles) are reported.

20. Database of Colloidal Plexcitonic Nanosystems

To study systematically the components of the known CMPs, I created a database of all the publications available, maintaining the subclassification in CPM-S (table 20.1) and CPM-D (table 20.2). Tables 20.1 and 20.2 list all the plexcitonic nanosystems in chronological order. The associated data include the relative publication, the features of the plasmonic nanoparticles (material and shape) and of the dye molecules (name, family, state of aggregation) used; the main properties of the capping layer (CL): the molecules that compose it, if it is native or exchanged, and the nature of the interaction between NPs and molecules promoted by the CL). The full name of the dye molecules and the CL molecules are reported in appendix B (table B.1 and B.2). In the last two columns, the coupling parameters $\hbar\Omega_R$ and $\hbar g$ are reported. When these two coupling parameters were not directly determined in the associated publication, I calculated them from the data available. To this aim, I retrieved the plexcitonic peaks maxima in the

extinction spectra using the software https://apps.automeris.io/wpd/ and calculated $\hbar\Omega_R$ as the energy difference between these two peaks. Then, $\hbar g$ can be calculated rewriting equation (4.18) as:

$$\hbar g = \frac{\hbar}{2}\sqrt{\Omega_R^2 + (\gamma - k)^2}.$$

(20.1)

The value of γ was neglected when not available. This is a reasonable approximation considering that γ it is usually one order of magnitude smaller than k. When k was not reported, it was calculated as the half width at half maximum of the plasmon extinction spectra.[8] I estimated an error, in terms of standard deviation, of about 10% for $\hbar\Omega_R$ and $\hbar g$.

All the data contained in tables 20.1 and 20.2 were aggregated using pie charts. The associated numerical tables with data and percentages are reported in appendix B. The $\hbar\Omega_R$ and $\hbar g$ values were instead analysed using histograms.

The obtained data were used to try to establish a correlation between $\hbar\Omega_R$ (or $\hbar g$) and the CPMs classes. In order to improve the statistical analysis, the data relative to CPM-S and CPM-D were analysed together. However, the data relative to CPMs with a high detuning,[48,157–160,200,211,253] or to systems where the plexcitonic band(s) where (almost) hidden by a surplus of free dye in solution were not considered.[219,a]

For each CMP class the average values of $\hbar\Omega_R$ and $\hbar g$ ($\overline{\hbar\Omega_R}$ and $\overline{\hbar g}$) and their standard deviations σ_{Ω_R} and σ_g were calculated. The tables with all the averaged values are reported in appendix B (table B.4). Then, distribution plots where built by plotting the values of $\hbar\Omega_R$ or $\hbar g$ against different CMP classes. Graphs obtained are reported in chapter 22.1 (distribution plot of the Rabi splitting energies) and appendix B (distribution plot of the coupling strength energies).

---

[a] This is the case of the Mohankumar *et al.* work, in which a differential spectrophotometry was proposed to remove the contribution of the uncoupled molecules.[220] In that case it was not trivial to understand the ratio between the coupled and uncoupled dyes, so that over or underestimes would generate a detrimental systematic error.

Table 20.1. Database of CPM-S. The full names of dye molecules are reported in appendix B, table B.1 (J = J-aggregate; M=monomeric form). The full names of the CL molecules are reported in appendix B, table B.2. (N=native; E=exchanged; (i)= direct dye-metal interaction; (iii)= electrostatic interaction; (iv)= segregation). The coupling parameters $\hbar\Omega_R$ and $\hbar g$ are reported in meV.

Chronological				NP		Dye Molecules			Capping Layer			Coupling parameters	
System #	Paper #	First Author & Year	Ref	Material	Shape	Name	Family	J / M	CL molecule	N/E	Interaction	$\hbar\Omega_R$	$\hbar g$
1	1	Kometani 2001	[48]	Au	Sphere	TC	Cyanine	J	BH_4^+	N	(I)		
2	1	Kometani 2001	[48]	Ag	Sphere	TC	Cyanine	J	BH_4^+	N	(I)		
3	1	Kometani 2001	[48]	Ag-Au	Sphere	TC	Cyanine	J	BH_4^+	N	(I)		
4	2	Sato 2001	[157]	Ag	Sphere	TC(Et)	Cyanine	J	BH_4^+	N	(I)		
2	3	Hranisavljevic 2002	[158]	Ag	Sphere	TC	Cyanine	J	BH_4^+	N	(I)		
1	4	Wiederrecht 2004	[159]	Au	Sphere	TC	Cyanine	J	BH_4^+	N	(I)		
2	4	Wiederrecht 2004	[159]	Ag	Sphere	TC	Cyanine	J	BH_4^+	N	(I)		
2	5	Yoshida 2008	[160]	Ag	Sphere	TC	Cyanine	J	BH_4^+	N	(I)		
5	6	Fofang 2008	[161]	Au	Shell	DBTC	Cyanine	J	THPC	N	(I)	120	181
5	6	Fofang 2008	[161]	Au	Shell	DBTC	Cyanine	J	THPC	N	(I)	100	148
6	6	Fofang 2008	[161]	Au	Shell	DBTC	Cyanine	J	Mercapto ethansulphonate	E	(iii)	120	181
7	7	Ni 2008	[218]	Au	Rods	HITC	Carbo cyanine	M	PSS	E	(iii)	425	
1	8	Yoshida 2009	[211]	Au	Sphere	TC	Cyanine	J	BH_4^+	N	(I)		
8	8	Yoshida 2009	[211]	Au	Sphere	TC	Cyanine	J	TMAUt	E	(iii)		
9	8	Yoshida 2009	[211]	Au	Sphere	SO-PIC	Cyanine	J	TMAUt	E	(iii)		
10	9	Yoshida 2009	[200]	Au	Rods	TC	Cyanine	J	TMAUt	E	(iii)		
11	9	Yoshida 2009	[200]	Au	Rods	TC(Ph)	Cyanine	J	TMAUt	E	(iii)	222	125

System #	Paper #	First Author & Year	Ref	Material	Shape	Name	Family	J / M	CL molecule	N/E	Interaction	$\hbar\Omega_R$	$\hbar g$
12	9	Yoshida 2009	[200]	Au	Rods	TC(Et)	Cyanine	J	TMAUt	E	(iii)	168	102
13	10	Juluri 2009	[254]	Au	Rods	DBTC	Cyanine	J	Not reported	N	(I)	92	61
14	11	Choi 2009	[14]	Au	Sphere	Cc	Protein	M	3-mercapto propionic acid	E	(iii)+(iv)		
15	12	Lekeufauck 2010	[255]	Au	Sphere	TDBC	Cyanine	J	Citrate	N	(I)	220	133
16	13	Yoshida 2010	[253]	Ag	Sphere	TC	Cyanine	J	TMAUt	E	(iii)		
17	13	Yoshida 2010	[253]	Ag	Sphere	OC	Cyanine	J	TMAUt	E	(iii)	223	143
18	14	Ni 2010	[219]	Au	Rods	R640	Rhodamine	M	PSS	E	(iii)		
19	14	Ni 2010	[219]	Au	Rods	CV		M	PSS	E	(iii)		
20	14	Ni 2010	[219]	Au	Rods	MG	Triarylmethanes	M	PSS	E	(iii)		
21	14	Ni 2010	[219]	Au	Rods	O720	Oxazine	M	PSS	E	(iii)		
22	14	Ni 2010	[219]	Au	Rods	DOTCI	Carbocy.	M	PSS	E	(iii)		
23	14	Ni 2010	[219]	Au	Rods	O725	Oxazine	M	PSS	E	(iii)		
24	14	Ni 2010	[219]	Au	Rods	HITC	Carbo cyanine	M	PSS	E	(iii)		
25	14	Ni 2010	[219]	Au	Rods	MB	Triarylmethanes	M	PSS	E	(iii)		
26	15	Hao 2011	[256]	Au	Rods	TC(Et)	Cyanine	J	CTAB	N	(iii)	190	102
5	16	Fofang 2011	[16]	Au	Shell	DBTC	Cyanine	J	THPC	N	(iii)	120	181
27	17	Balci 2013	[217]	Ag	Prism	TDBC	Cyanine	J	Citrate	N	(I)	447	259
28	18	Melnikau 2013	[215]	Au	Stars	JC1	Cyanine	J	CTAB + PEI	E	(iii) + (iv)	260	

System #	Paper #	First Author & Year	Ref	Material	Shape	Name	Family	J / M	CL molecule	N/E	Interaction	$\hbar\Omega_R$	$\hbar g$
29	18	Melnikau 2013	[215]	Au	Stars	JC1+S2165	Cyanine	J + M	CTAB + PEI	E	(iii) + (iv)	180+110	
27	19	Balci 2014	[93]	Ag	Prism	TDBC	Cyanine	J	Citrate	N	(I)	447	259
30	20	DeLacy 2015	[226]	Au	Platelets	PIC	Cyanine	J	Citrate + PVP	N	(iii)	207	147
31	21	Nan 2015	[31]	Au	Rods	IR806	Carbo cyanine	M	PAH	E	(iii)	221	114
32	22	Fales 2015	[227]	Au	Sphere	PIC	Cyanine	J	PVSA	E	(iii)		
33	22	Fales 2015	[227]	Au	Rods	PIC	Cyanine	J	PVSA	E	(iii)	129	81
27	23	Balci 2016	[92]	Ag	Prism	TDBC	Cyanine	J	Citrate	N	(I)	447	259
34	24	Melnikau 2016	[77]	Au	Rods	JC1	Cyanine	J	CTAB	N	(iv)	200	123
35	25	Simon 2016	[91]	Au	Rods	JC1	Cyanine	J	CTAB	N	(iv)	260	139
36	26	Hazra 2016	[201]	Ag-Au	Rings	PIC	Cyanine	J	CTAB	N	(iii)		
37	27	Liu 2017	[257]	Ag-Au	Cubes	PIC	Cyanine	J	CTAB	N	(iii)	223	118
38	28	Das 2017	[106]	Ag-Au	Rings	PIC	Cyanine	J	CTAB	N	(iii)	192	137
39	29	Melnikau 2017	[216]	Ag-Au	Rods	JC1	Cyanine	J	DBAC	N	(iv)	175	112
40	30	Thomas 2018	[41]	Ag	Sphere	FITC	Rhodamine	M	PVP	E	(iii)	383	251
41	30	Thomas 2018	[41]	Au	Rods	PIC	Cyanine	J	PSS	E	(iii) + (iv)	229	152
42	31	Walters 2018	[105]	Au	Sphere	TC(Et)'	Cyanine	J	Thiocoline, PAH, PVP, SI	E	(iii) + (iv)	125	101
43	32	Kirschner 2018	[258]	Au	Bipiramids	DBTC	Cyanine	J	CTAB + CTAC	N	(iii)	120	63
44	33	Song 2019	[259]	Au	Cubes	PIC	Cyanine	J	Cl⁻	E	(iii)	100	76

System #	Paper #	First Author & Year	Ref	Material	Shape	Name	Family	J / M	CL molecule	N/E	Interaction	$\hbar\Omega_R$	$\hbar g$
45	34	Melnikau 2019	175	Ag-Au	Rods	JC1+S2165	Cyanine	J	DBAC	N	(iii) + (iv)	175+163	
43	35	Kirschner 2019	260	Au	Bipyramids	TC(Et)'	Cyanine	J	CTAB + CTAC	N	(iii)	120	63
46	36	Balci 2019	214	Ag	Disks	TDBC	Cyanine	J	Citrate	N	(I)	347	187
27	37	Finkelstein-Shapiro 2020	83	Ag	Prism	TDBC	Cyanine	J	Citrate	N	(I)	356	186
47	38	Guvenc 2020	252	Ag	Disks	TDBC	Cyanine	J	Citrate	N	(I)	347	187
48	38	Guvenc 2020	252	Ag-Au	Rings	TDBC	Cyanine	J	Citrate	N	(I)	331	183
38	39	Das 2020	210	Ag-Au	Rings	PIC	Cyanine	J	CTAB	N	(I)	178	130
49	39	Das 2020	210	Ag-Au	Rings	TDBC	Cyanine	J	CTAB	N	(iii)	195	135
50	39	Das 2020	210	Ag-Au	Rings	PIC	Cyanine	J	PSS	E	(iii)	201	138
51	39	Das 2020	210	Ag-Au	Rings	TDBC	Cyanine	J	PSS	E	weak	182	131
52	40	Kumar 2020	208	Au	Rods	TDBC	Cyanine	J	CTAB	N	(iii)	280	254
53	41	Hendel 2020	209	Ag-Au	Rods	JC1	Cyanine	J	CTAB	N	(iv)	235	127
54	41	Hendel 2020	209	Au	Sphere	JC1	Cyanine	J	Not reported	N	(iv)	111	66
55	42	Li 2020	194	Ag-Au	Cubes	TDBC	Cyanine	J	CPC	N	(iii)	162	98
56	42	Li 2020	194	Ag-Au	Rings	TDBC	Cyanine	J	CPC	N	(iii)	186	105
43	43	Kirschner 2020	261	Au	Bipyramids	TC(Et)'	Cyanine	J	CTAB + CTAC	N	(iii)	120	63
57	44	Mohankumar 2020	220	Au	Rods	SQ	Squaraine	M	PSS	E	(iii) + (iv)		
58	44	Mohankumar 2020	220	Ag	Sphere	Cy	Cyanine	M	Citrate	N	(I)		
59	44	Mohankumar 2020	220	Au	Rods	Cy5	Cyanine	M	PSS	E	(iii)		

System #	Paper #	First Author & Year	Ref	Material	Shape	Name	Family	J / M	CL molecule	N/E	Interaction	$\hbar\Omega_R$	$\hbar g$
X14	45	Stete2020	[262]	Au	Rods	TDBC	Cyanine	J	Citrate	N	(I)	227	116
60	46	Krivenkov 2021	[222]	Ag	Platelets	JC-1	Cyanine	J	Citrate	N	(I)	450	274
61	47	Peruffo 2021	[17]	Au	Sphere	TPPS	Porphyrin	M	TMAOt	E	(iii)	173	110
62	47	Peruffo 2021	[17]	Au	Sphere	TPPS	Porphyrin	J	TMAOt	E	(iii)	430	230
63	48	Peruffo 2021	[18]	Au	Stars	Styryl 9M	Carbo cyanine	M	SOt	E	(iii)	456	236
64	48	Peruffo 2021	[18]	Au	Stars	Cy75	Cyanine	J	TMAOt	E	(iii)	87	55
65	48	Peruffo 2021	[18]	Au	Stars	PIC	Cyanine	J	Citrate	N	(I)	130	102
66	48	Peruffo 2021	[18]	Au	Stars	TDBC	Cyanine	J	Citrate	N	(I)	120	98
67	48	Peruffo 2021	[18]	Au	Stars	TDBC	Cyanine	J	TMAOt	E	(iii)	116	68

Table 20.2. Database of CPM-D. The full names of dye molecules are reported in appendix B, table B.1 (J = J-aggregate; M=monomeric form). The full names of the CL molecules are reported in appendix B, table B.2. (N=native; E=exchanged; (i)= direct dye-metal interaction; (ii)= covalent; (iii)= electrostatic interaction; (iv)= segregation). The coupling parameters $\hbar\Omega_R$ and $\hbar g$ are reported in meV.

Chronological				NP		Dye Molecules			Capping Layer			Coupling parameters	
System #	Paper #	First Author & Year	Ref	Material	Shape	Name	Family	J / M	CL molecule	N/E	Interaction	$\hbar\Omega_R$	$\hbar g$
3	1	Kometani 2001	48	Ag-Au	Sphere	TC	Cyanine	J	BH_4^+	Native	(I)	474	336
X1	X1	Hranisavljievic 2002	158	Ag	Sphere	TC	Cyanine	J	PO^{4-}	Exch	(I)		
X2	X2	Itoh 2003	263	Ag	Sphere	R6G	Rhodamine	M	Not reported	Native	(I)	200	103
X3	X3	Liu 2007	63	Au	Sphere	Cc	Protein	M	Cisteine	Exch	(ii)		
X4	X3	Liu 2007	63	Ag	Sphere	Em	Porphyrin	M	Cisteine	Exch	(ii)		
X5	X4	Uwada 2007	264	Au	Sphere	PIC	Cyanine	J	MUA	Exch	(iii)	124	92
2	5	Yoshida 2008	160	Ag	Sphere	TC	Cyanine	J	BH_4^+	Native	(I)	276	
14	11	Choi 2009	14	Au	Sphere	Cc	Protein	M	3-mercaptopropionic acid	Exch	(iii)	112	93
7	X5	Ni 2010	265	Au	Rods	HITC	Carbocyanine	M	PSS	Exch	(iii)	557+188	279+94
27	17	Balci 2013	217	Ag	Prism	TDBC	Cyanine	J	Citrate	Native	(I)	204	179
X6	X6	Zengin 2013	266	Ag	Rods	TDBC	Cyanine	J	Citrate	Native	(I)	100	50
X2	X7	Itoh 2014	267	Ag	Sphere	R6G	Rhodamine	M	Not reported	Native	(I)	200	103
27	X8	Zengin 2015	268	Ag	Prism	TDBC	Cyanine	J	Citrate	Native	(I)	290	147
X7	X9	Roller 2016	269	Au	Sphere	TDBC	Cyanine	J	DNA origami	Exch	(I)	150	90
27	X10	Wersall 2017	75	Ag	Prism	TDBC	Cyanine	J	Citrate	Native	(I)	400	203

System #	Paper #	First Author & Year	Ref	Material	Shape	Name	Family	J / M	CL molecule	N/E	Interaction	$\hbar\Omega_R$	$\hbar g$
37	27	Liu 2017	[257]	Ag-Au	Cubes	PIC	Cyanine	J	CTAB	Native	(iii)	220	118
X8	X11	Rodarte 2017	[230]	Ag	Sphere	AF488	Not reported	M	AUT	Exch	(ii)	603	307
X9	X11	Rodarte 2017	[230]	Ag	Sphere	AF488	Not reported	M	AHDT	Exch	(ii)	436	225
X10	X11	Rodarte 2017	[230]	Ag	Sphere	AF488	Not reported	M	APT	Exch	(ii)	366	191
X11	X11	Rodarte 2017	[230]	Ag	Sphere	AF488	Not reported	M	Thiolated PEG	Exch	(ii)	125	84
X12	X12	Stete2017	[73]	Au	Sphere	TDBC	Cyanine	J	Tween20	Exch	(I)	173	
X13	X12	Stete2017	[73]	Au	Rods	TDBC	Cyanine	J	Tween20	Exch	(I)	144	
X14	X13	Stete2018	[270]	Au	Rods	TDBC	Cyanine	J	Citrate	Native	(I)	232	135
X14	X13	Stete2018	[270]	Au	Rods	TDBC	Cyanine	J	Citrate	Native	(I)	156	102
27	X14	Wersall'19	[76]	Ag	Prism	TDBC	Cyanine	J	Citrate	Native	(I)	250	131
44	33	Song 2019	[259]	Au	Cubes	PIC	Cyanine	J	Cl⁻	Exch	(iii)	130	148
44	33	Song 2019	[259]	Au	Cubes	PIC	Cyanine	J	Cl⁻	Exch	(iii)	330	183
52	40	Kumar 2020	[208]	Au	Rods	TDBC	Cyanine	J	CTAB	Native	(iii)	200	105
55	42	Li 2020	[194]	Ag-Au	Cubes	TDBC	Cyanine	J	CPC	Native	(iii)	156	96
56	42	Li 2020	[194]	Ag-Au	Rings	TDBC	Cyanine	J	CPC	Native	(iii)	200	111

21. Analysis of the databases

21.1 Nanoparticles: material and shape

Figure 21.1 reports the classification of the CPMs on the basis of the metals (or alloys) used to prepare the plasmonic NPs (see also table B.3 in appendix B), while figure 21.2 reports the classification on the basis of the shapes of the plasmonic NPs. Inspection of Figure 21.2 reveals clearly that all the CPMs studied so far rely on nanoparticles made by Au, Ag and Au/Ag alloys. Au is the predominant metal for CMP-s while in the case of CMP-d Au and Ag are equally used.
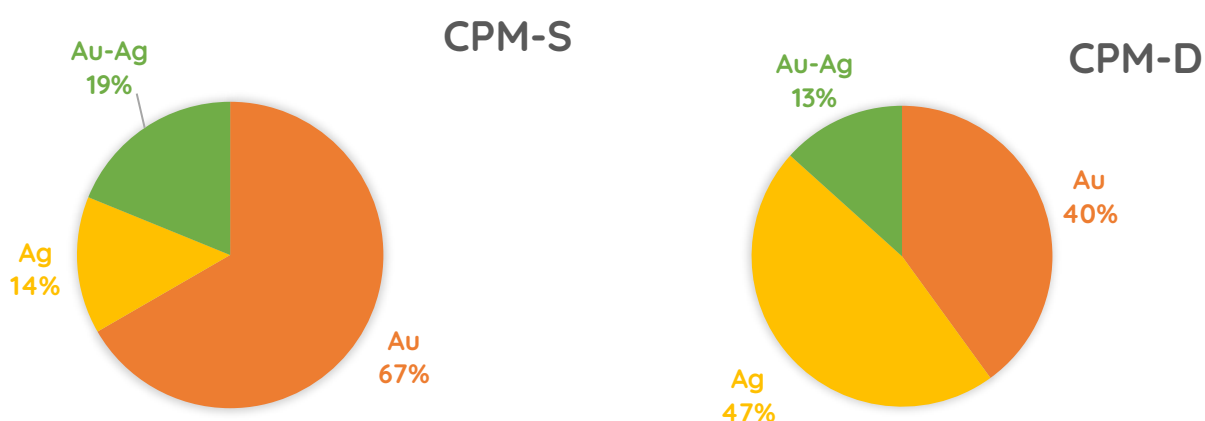
Figure 21.1. Pie charts representing the variability of the NPs materials, classified as CPM-S (left) and CPM-D (right).
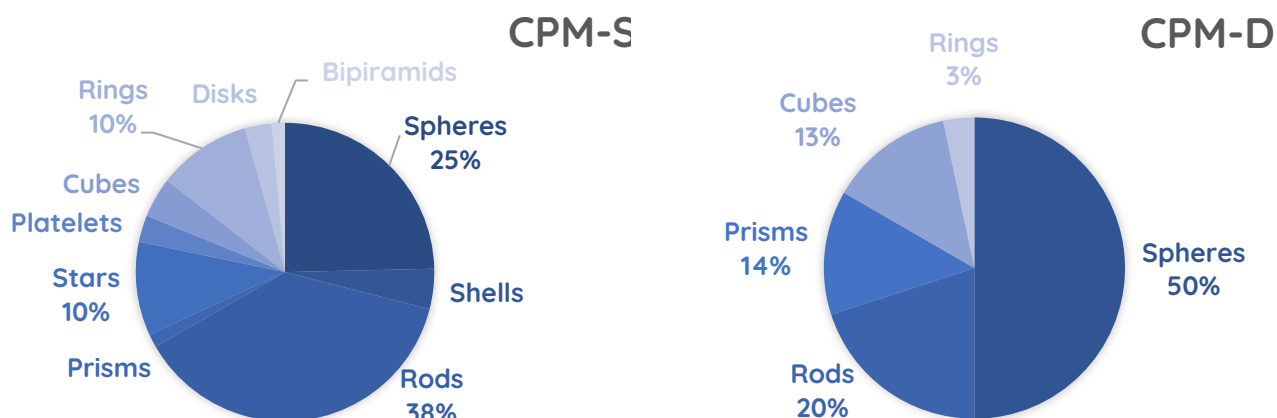
Figure 21.2. Pie charts representing the variability of the NPs shapes, divided in CPM-S (left) and CPM-D (right). In CPM-S chart, only the most frequent shapes are reported. The full list of them is reported in appendix B table B.3.

Shapes of the plasmonic NPs are much more variable, spreading from the simplest geometries, such as rods and spheres, to the more exotic ones such as rings or pyramids. Spheres and rods represent in both cases more than the 60%, probably because they are easily synthesisable and

very common in literature. After them, stars and rings are the most used shapes in the case of CMP-S, while cubes and prisms are preferred in the case of CMP-D.

21.2   Dyes: molecules and aggregation state

Figure 21.3 summarized the different dyes used as QE counterpart. In this case, the choices are much more heterogeneous. More than 30 molecules were used in different CPMs (appendix B, table B.3) and only about ten of them were used more than once. Interestingly, three molecules emerge in the pool of organic QEs so fare used. These are TDBC, PIC and JC1, which alone account for more than 40% of the CMPs reported (figure 21.3).
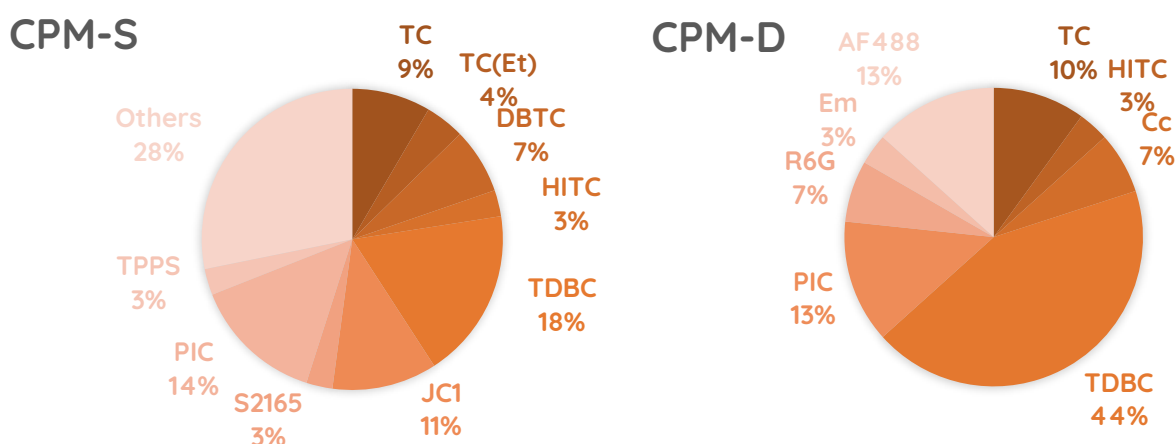
Figure 21.3. Pie charts representing the variability of the dye molecules, divided in CPM-S (left) and CPM-D (right). For CPM-D, dye molecules used just once where reported in "others".

TDBC, JC1 and PIC belong to the cyanines' family and are used in CMPs in the J-aggregate form. Figure 21.4, which groups the dyes according to the classes they belong, confirms that cyanines are by far the most used family of dyes. Besides cyanines, other relevant dyes are porphyrins, also forming J-aggregates, and the carbocyanine used by Ni *et al.* [265] in the form of H-aggregates.

Cyanines are known to easily form J-aggregates with high dipole moment d [38] and low γ. This would produce stronger g, which is directly proportional to d. For this reason, dye aggregation is a relevant feature for the formation of CMPs. Figure 21.5 confirms this intuition revealing that in more than two thirds of the cases, dyes forming the CMPs are aggregated. In addition to the already discussed favourable properties of J-aggregates, they have higher association constants (K_a) to the NPs with respect to their monomeric form, thanks to the higher number of possible anchoring points.
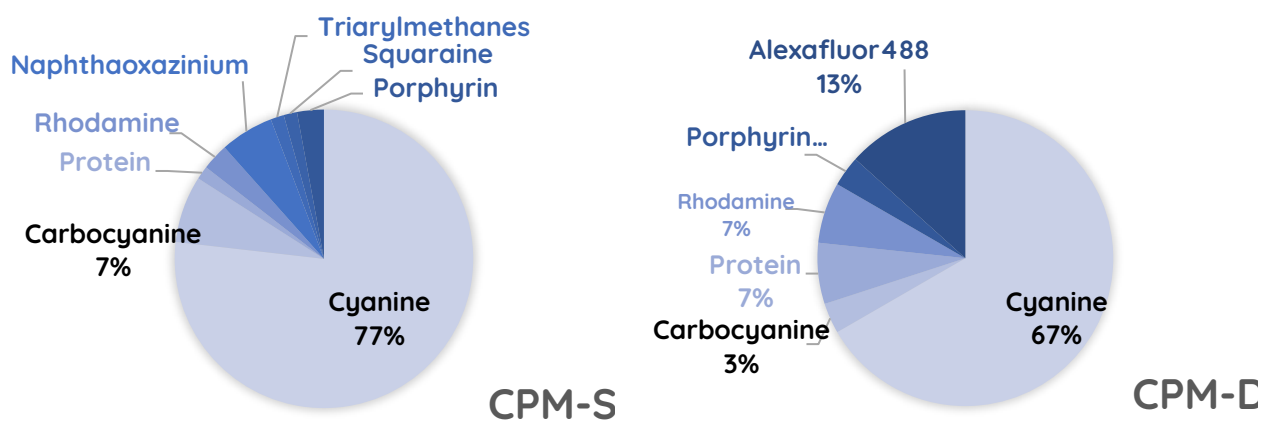
Figure 21.4. Pie charts representing the variability of the families of dye molecules, divided in CPM-S (left) and CPM-D (right).

Noteworthy, with a single exception, all the dye aggregates in figure 11 are of the J-type. Only Ni *et al.* [265], as mentioned, reported a CPM-D plexcitonic material based on H-aggregates of HITC dyes and gold nanorods. Also in this case, however, the real involvement of the H-aggregate is not completely confirmed. Indeed, the scattering spectrum of the nanohybrid presented three peaks (figure 21.6), attributed to the mixing of the plasmonic resonance of the rods, the bright excitonic state of the H-aggregates and the states of the monomeric HITC. Nevertheless, the absorption band of the H-aggregate falls at the same wavelengths of the vibronic band of the monomer.[218] Beyond the interpretation of these results, it remains unclear the reason why H-aggregates are so elusive in plexciton formation.
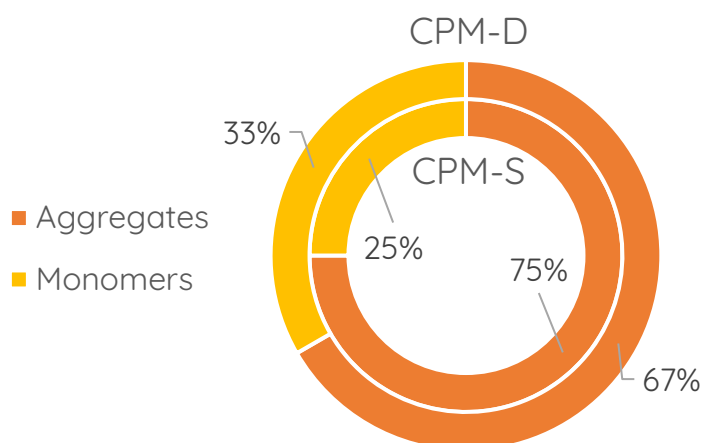
Figure 21.5. Variability of the aggregation state of the dye molecules, divided in CPM-D (external circular crown) and CPM-S (inner circular crown).

137
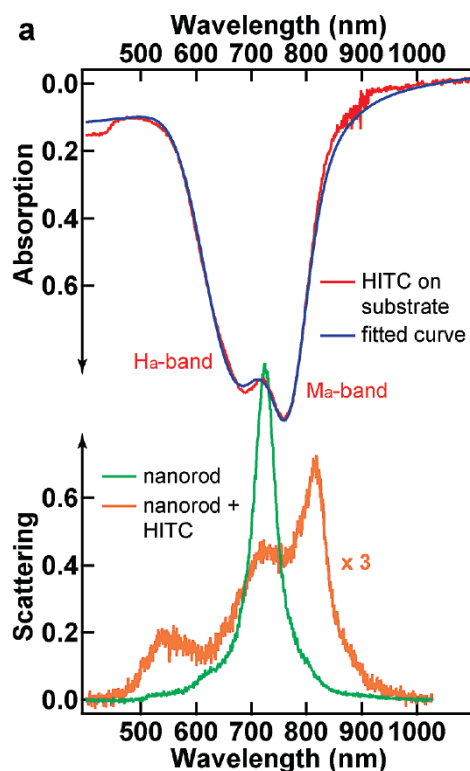
Figure 21.6. Top figure: absorption spectrum of HITC on substrate. The monomeric band (M_a-band) and the H-aggregate band (H_a-band) are labelled. Bottom figure: scattering spectra of the nanorods and the CPM. Reprinted from ref.[265]

The second obvious information extracted from figure 21.5 is that the formation of plexcitonic systems with monomeric molecules is quite infrequent. The main reason is likely due to the lower values of d and K_a of monomeric molecules with respect to their aggregates. In addition, the plexcitonic bands in CMP-S prepared with monomeric dyes are more difficult to detect since they might be (partially) hidden by the stronger signal due to the unbound monomers free in solution, as a consequence of their low K_a. This problem is less relevant in the case of CPM-D, and this could explain the slightly greater percentage of plexcitonic systems based on monomeric dyes found in these systems (figure 21.5).

21.3   Capping layer: molecules and kinds of interaction

Nanoparticles are thermodynamically unstable due to the high surface/volume ratio. For this reason, their fate should inevitably lead to coalescence and formation of massive materials. Nanoparticle coalescence can be prevented by avoiding surface contact because of electrostatic or steric repulsion. In other words, charged nanoparticles cannot aggregate because their reciprocal electric repulsion hampers them to get in contact, while nanoparticle coated with suitable molecules cannot aggregate because of the physical barrier provided by the coating. In most of the cases, with some remarkable exceptions, nanoparticles are not intrinsically charged and hence stabilization is often provided by layers of molecules or ions

adsorbed on their surfaces, which can provide both steric and electrostatic stabilization. The strength of the interactions between the nanoparticle surface and the capping layer ranges from weak absorption to quasi-covalent bonds, depending on the chemical nature of the nanoparticle core and of the capping molecules. It is hence not unexpected that all the plasmonic nanoparticles used for CPM assembly feature a capping layer (see also appendix B, table B.2). Moreover, one can easily expect that the presence of this "intermediate" layer on the surface of the nanoparticles must have an influence on the CMP features. On the one hand, the capping layer influences, or determines, the assembly of the dyes on the nanoparticles. On the other, it may critically affect the relative distance of the two CPM partners.
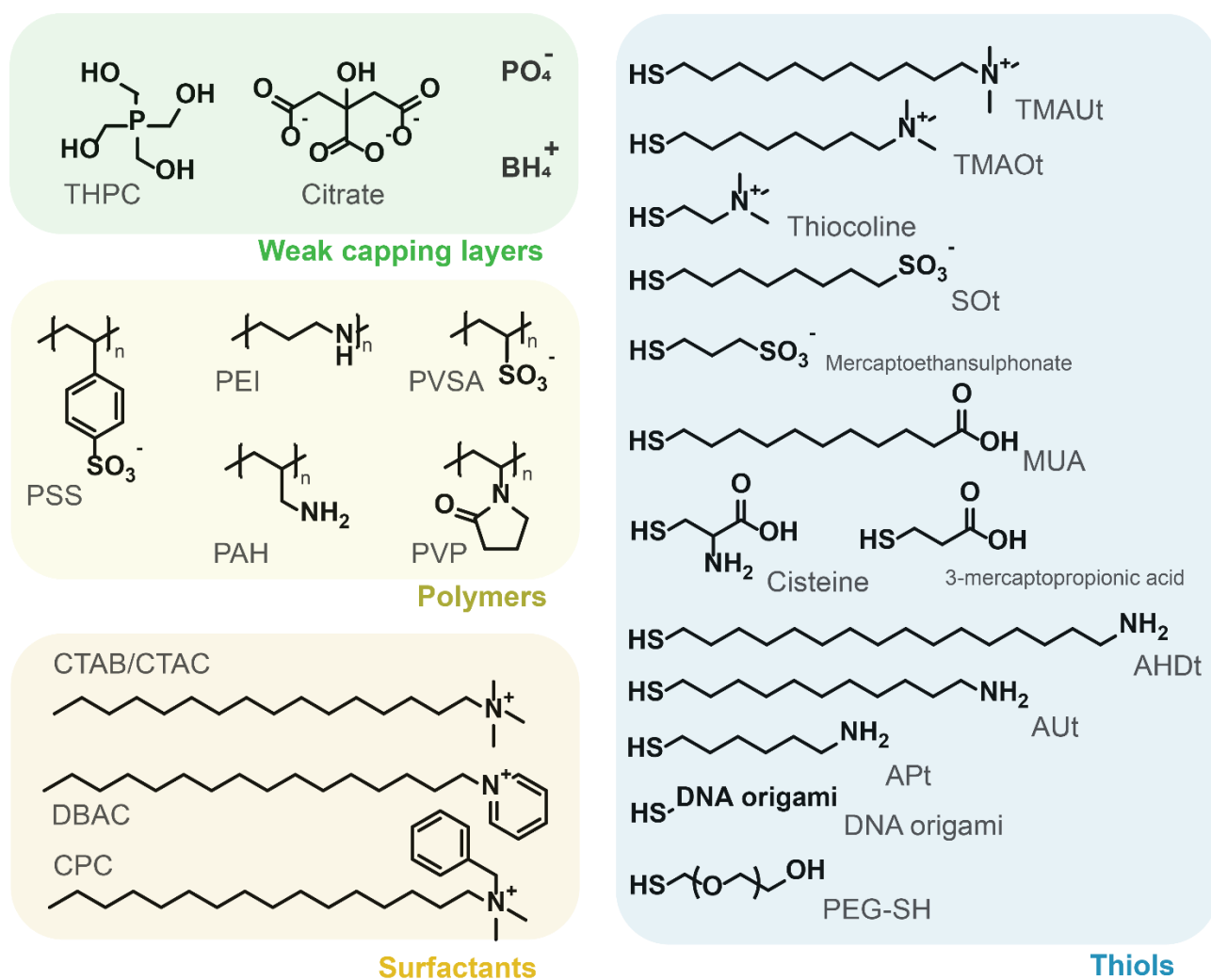
Figure 21.7. Molecular structure of the different capping layer molecules used in the assembly of the CPMs, grouped in 4 classes: weak capping layers, polymers, surfactants, and thiols.

As for dye molecules, a wide variability of CL molecules was found. In an attempt to find some significant correlation, I grouped them into 4 classes: weak capping layers, thiols, polymers, and cationic surfactants. The weak capping layers category includes molecules that can be easily removed, or better exchanged, from the NPs surface because their binding strength is low.[271]

Thiols include molecules featuring an –SH end-group, which is well-known to strongly bind on the Au and Ag surfaces. Polymers can feature both weak and strong interacting groups, but their adhesion on the particles surface is enhanced by their multivalency. Note that PEG and DNA ended with thiol groups were considered thiols and not polymers. Finally, cationic surfactants include molecules with a long aliphatic chain and a cationic head. They are also weakly bound to the surface of NPs, but they usually form a bilayer due to their amphiphilicity.[272]

The pie charts in figure 21.8 show that CPM-S have a quite equilibrate distribution of capping layers, while CPM-D are generally produced using weak capping layers or thiols.

CPM-S

Surfactants 22%
Weak capping layers 24%
Thiols 23%
Polymers 31%

CPM-D

Surfactants 21%
Weak capping Layers 36%
Thiols 32%
Polymers 11%
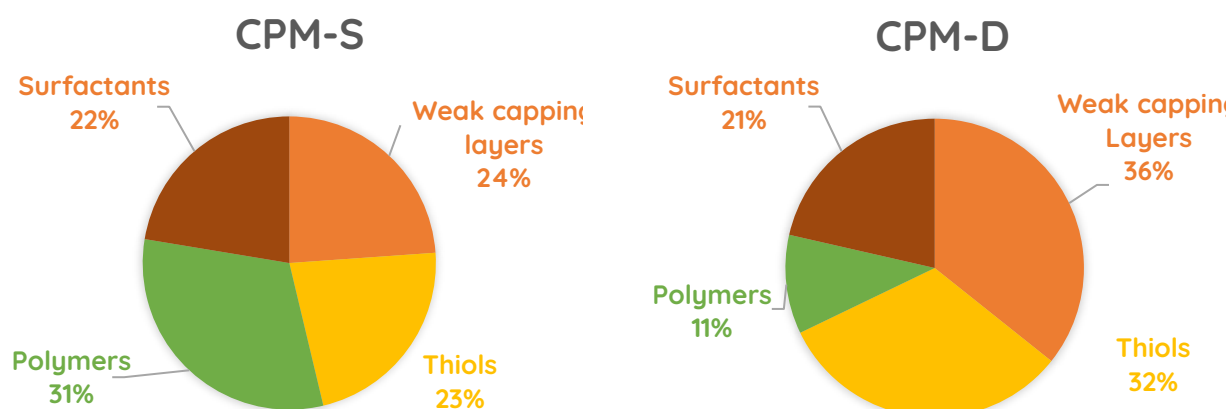
Figure 21.8. Pie charts representing the variability of the capping layer classes, divided in CPM-S (left) and CPM-D (right).

Direct adsorption (i)   Binding with spacer (ii)   Non covalent (iii)   Segregation (iv)

Strong interactions   **Weak interactions**
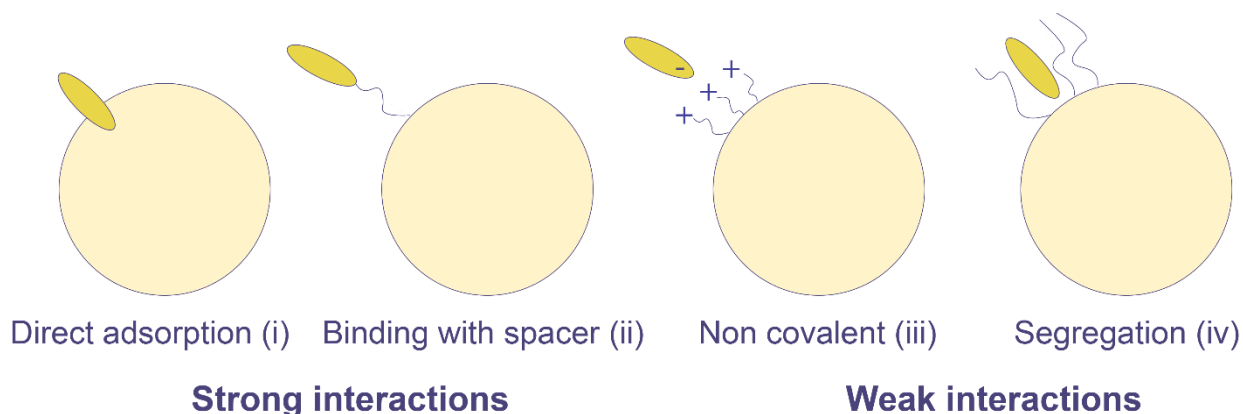
Figure 21.9. Schematization of the main interactions between NPs and dyes observed in CPMs: the dye-metal and the covalent interactions are classified as strong interactions, while electrostatic and segregation interactions as weak interactions.

The interaction of a dye with the plasmonic nanoparticle can occur in different ways, as roughly schematized in figure 21.9: (i) the dye directly adsorbs on the metal surface, in this case the

molecules of the capping layer are exchanged by the dye; (ii) the dye is bound to the NPs surface through a thiolate spacer (or other group with high affinity), also in this case the capping layer molecules are exchanged by the dye; (iii) the dyes is adsorbed on the surface of the capping layer trough non-covalent interactions; (iv) the dye is adsorbed within the capping layer, again as a consequence of non-covalent interactions and solvophobic effects. These different interaction scenarios influence both the QE-NP distance and the QE exchange rate. Interaction (i) places the dye at the shorter distance from the metal surface (contact), while in interactions (ii)-(iv) the distance is controlled by the capping layer or dyes features, and in particular by their molecular structure. The interactions (i) and (ii) can be classified as strong interactions, while the (iii) and (iv) interactions can be classified as weak. It must be noted, however, that the identification of the exact interaction occurring is not always trivial, and in particular the discrimination between (i) and (ii), and between (iii) and (iv) may strongly depend on peculiar features of the capping layer and the dye.

Taking into account these difficulties, I performed my classification on the basis of a few assumptions. It must be noted that the interaction type has been assigned here on the basis of the criteria just discussed, consequently they may not always coincide with the ones originally proposed by the authors.

For instance, the formation of CPMs in nanostructures with edges and capped with citrate was shown in several cases to smooth this fragile parts, modifying their TEM images and extinction spectra.[18,83,92,215,217,262] This evidence confirms the establishment of the direct adsorption of QEs onto the metal surface in these case, and likely also in the cases were nanostructures without edges were coated by citrate of by other weak coatings. For this reason, I considered interaction (i) to be the one occurring in all the cases where nanoparticles were coated by a weak capping layer, i.e. citrate, BH_4^+, THPC and PO_4^- (Table 20.1 and 20.2). It must be noted that at least in one case, namely the paper from Fofang *et al.*[16,161], the interaction was considered by the work authors to be of type (iii) with a THPC capping layer.

As mentioned, the boundaries between type (iii) and type (iv) are quite labile. Thus, I defined the interaction as type (iii) when the capping layer and the QEs had complementary interaction sites, usually opposite net charges, while I opted for interaction (iv) in the other cases, particularly when water was the solvent (which are the cases of Styryl 9M,[18] S2165[175,215] and SQ[220]). In some example, both interactions can be considered.[175,215,220]

Finally, Thomas *et al.* prepared a CPM-S by covering silver spheres with PVP and binding FITC molecules to it through *click* chemistry.[41] In this case, since PVP is not covalently bound to the Ag

surface as a typical thiol molecule, it cannot be defined covalently bonded; for this reason I classified its interaction as (iii).

Table 21.1. The capping layers of CPMs, divided into the four classes, are related to the interactions that they allow between NPs and QEs.

CL classes	Capping layers	Interaction
Weak CLs	BH_4^+	(i)
	THPC	(i)
	PO_4^-	(i)
	Citrate	(i)
Thiols	TMAOt	(iii)
	SOt	(iii) and (iv)
	Mercapto ethan sulfonate	(iii)
	TMAUt	(iii)
	3-mercaptopropionic acid	(iii)
	Cisteine	(ii)
	AUT	(ii)
	AHDT	(ii)
	APT	(ii)
	PEG-S	(ii)
	DNA origami	(ii)
	3-mercaptopropionic acid	(iii)
	MUA	(iii)
Polymers	PSS	(iii) and (iv)
	PEI	(iii) and (ii)
	PVP	(iii)
	PAH	(iii)
	PVSA	(iii)
Surfactants	DBAC	(iii) and (iv)
	CTAC	(iii)
	CTAB	(iii) and (iv)
	CPC	(iii)

Table 21.1 correlates the capping layer categories with the interaction type assigned. As expected, all the type (i) interactions occur with weak CLs. Thiol CLs allow all the other

142

interactions, while polymers and surfactants usually produce type (iii) and more rarely type (iv) interactions.

The pie charts for the NPs-QEs interactions (figure 21.10) reveal that CPM-S have been assembled mainly by type (iii) interactions. Conversely, CPM-D have been prepared mostly using type (i) interactions. These distributions match the capping layer distributions early discussed. In particular, weak capping layer and type (i) interactions prevail in the case of CPM-D. Indeed, deposited system do not need stabilization against coalescence and consequently their preparation with NPs with weak capping layers is easier than in the case of CPM-S.
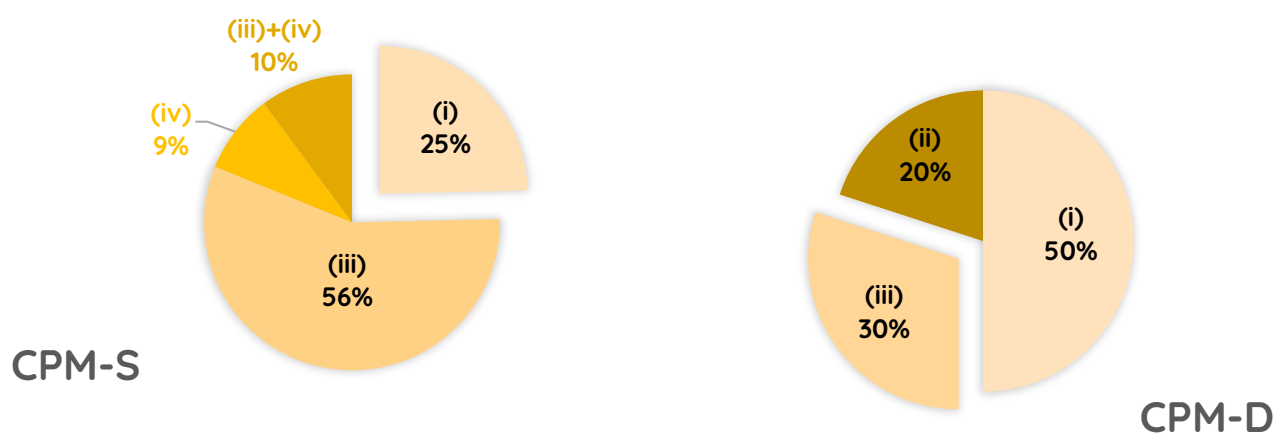
Figure 21.10: Pie charts representing the variability of the kinds of interaction, divided in CPM-S (left) and CPM-D (right). The graphs are divided into two main cloves, which divided the strong interactions (dye-metal (i) and covalent (ii)) from the weak ones (electrostatic (iii), segregation (iv) or both).

21.4   Rabi splitting and coupling strength

The values of $\hbar\Omega_R$ and $\hbar g$ for the different CPMs studied are reported in figure 21.11 and in figure B.1, appendix B for CPM-S and CPM-D. The inspection of the plots confirms that the two categories span similar $\hbar\Omega_R$ values, in the interval 100-500 meV, with most of the systems lying between 200 and 300 meV.
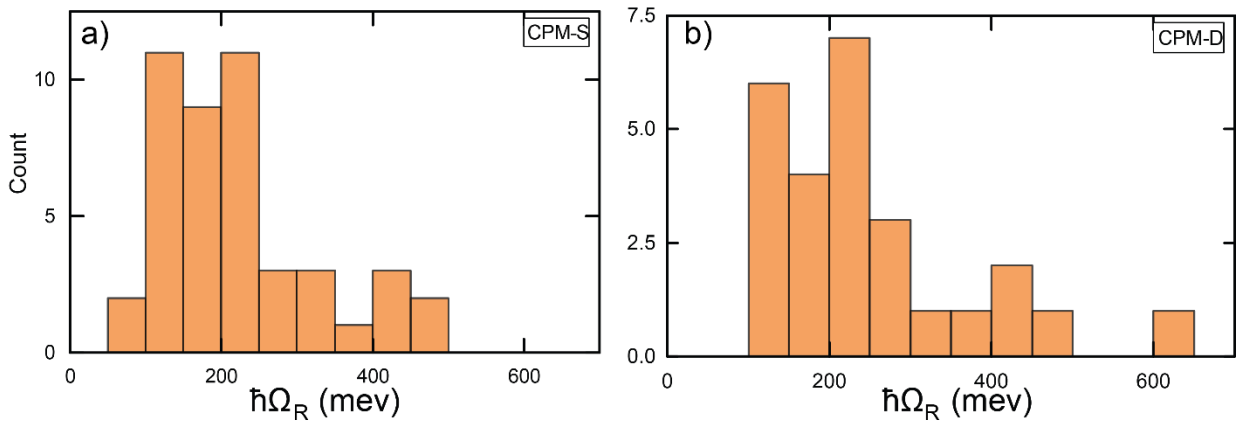
Figure 21.11. Histograms showing the distribution of values of $\hbar\Omega_R$ for a) CPM-S and b) CPM-D.

22. Using the databases to extract structure-to-optical performances relationships

22.1 Evaluating CPM structure-to-optical properties relationship through distribution plots

In order to devise structure-to-optical performances relationships and identify in which conditions the better coupling could be achieved, I prepared distribution plots showing the correlations between the values of $\hbar\Omega_R$ and $\hbar g$ (reported in the y-axes) and the different classes of CPM hybrids (x-axys). In these graphs, each CPM sample is plotted as an open dot, while the blue bars represent the intervals $(\overline{\hbar\Omega_R}+\sigma_{\Omega_R}, \overline{\hbar\Omega_R}-\sigma_{\Omega_R})$ or $(\overline{\hbar g}+\sigma_g, \overline{\hbar g}-\sigma_g)$. Please note that in this case σ_{Ω_R} and σ_g are not due to experimental errors, but just represent the dispersion of $\hbar\Omega_R$ and $\hbar g$ for each class. The blue bars, thus, can be considered as the optical performances of each CPM class, where $\hbar\Omega_R$ and $\hbar g$ have been used as figure of merit. Consequently, it is no relevant whether $\overline{\hbar\Omega_R}$ or $\overline{\hbar g}$ of different classes are compatible or not within the dispersion. Each blue bar represents what intervals of $\hbar\Omega_R$ and $\hbar g$ a peculiar class of CPM can have. The shorter (longer) the bar is, the more localised (dispersed) the performance can be. The higher (lower) is the value of the bar can reach, the higher (lower) is the performances of the CPM class in forming plexcitonic states.

In figure 22.1 and B.2 the distribution plots correlating the coupling parameters with NPs, QEs and CLs classes are reported.

The first parameter analysed is the dependence of the coupling on the NPs composition and shape. The data indicate that nanohybrids made with Ag NPs feature on average stronger $\hbar\Omega_R$ and $\hbar g$ than Au or Ag@Au alloy. The interpretation of these results can be eased by recalling

the conditions of existence, equation (4.22), and of strong coupling (SC), equation (4.23), discussed in chapter 4.4 and here reported again:

$$|2g| > |k - \gamma|; \tag{4.22}$$

$$\Omega_R^2 > \frac{\gamma^2 + k^2}{2}. \tag{4.23}$$

With k and γ the dissipative rates of the plasmon and of the QEs, respectively, retrieved as discussed in chapter 20. Note that generally k is one order of magnitude greater than γ. For this reason, equation (4.22) can be rewritten as $|2g| > k - \gamma$. Thus, high values of k imply stricter conditions of existence, which in turn means that only hybrids featuring stronger coupling will be detected. The analysis of the different k for the different NP composition reveals that the average $\hbar k_{Ag}$, $\overline{\hbar k_{Ag}}$ = (230 ± 100) meV is far bigger than $\overline{\hbar k_{Au}}$ = (160 ± 80) meV, and $\overline{\hbar k_{Au@Ag}}$ = (170 ± 100) meV. Consequently, the conditions imposed in equation (4.22) and equation (4.23) become stricter for Ag NPs. The hybrids which satisfy these conditions will thus have, on average, stronger Ω_R and g.

Moving to the NPs' shapes, the huge variability of shapes used reduces the statistics, which, consequently, is too low to draw a comparison. I tried however to compare nanorings (and hollow nanoprisms) performances because it was recently claimed that they allow reaching high values of Ω_R due to the strong enhancement of the electromagnetic field within their hole.[106,252] However, from the average values reported in table B.4, appendix B, nanorings seem to have the same performances than other geometries such as nanorods or nanospheres, which all have $\overline{\hbar \Omega_R}$ of about 200 meV. It must be noted that in hollow structures the dye molecules are placed not only within the hole, but also in the outer positions, and these might reduce the average coupling value. Further developments of these structures should involve a better control of the molecules position, in order to selectively place them in the hole region where the field gets more effectively enhanced.

Moving the focus to the QEs, the analysis reported in the previous chapter confirmed that more than 40% of CPMs are prepared with PIC, TDBC or JC1. The dispersion plots (figure 22.1b and B.2b) highlight the higher Ω_R performances of TDBC and JC1. A correlation of the coupling parameters with general dye families was instead not possible, since cyanines represent more than 70% of the dye used and, as a consequence, all the other families present not enough cases to be statistically significant.

In figure 22.1c and B.2c, I plotted the distribution graphs for the aggregation states of the QEs. Although monomeric QE plexcitons are much scarcer, they seem to present higher

performances than J-aggregates. This could be tentatively explained considering the low K_a of CPMs with monomeric dyes. Indeed, much higher values of Ω_R would be needed to detect the plexcitonic states in the extinction spectra. However, because of the rarity of these hybrids, more samples are needed to achieve a better comprehension on this topic.

In figure 22.1d and B.2d, the distribution plots relative to the capping layer classes show that the use of thiols and weak capping layers produces stronger interactions. This is also reflected in the distribution plots relative to interactions (figures 22.1e and B.2e), where type (iii) and type iv interactions (mainly achieved by polymers and surfactants) have lower $\hbar\Omega_R$ and $\hbar g$ than type (i) and type (ii), obtained mostly with weak capping layers and thiols (figures 22.1f and B.2f).

To explain this result, we should consider that noncovalent interactions require the presence of the capping layer, which increases the dye-NP distance and partially encumbers the effective volume, reducing the number of dye molecules that can couple. This explanation is further supported by some detailed study addressing the dye-NPs distance parameters. For instance, Li *et al.* reported that, analysing Ag-Au alloy nanocubes and nanorings covered both with TDBC, the latter possess stronger coupling because they have higher effective volume in which store the TDBC dye molecules. Rodarte *et al.*, instead, reported a reduction of the coupling strength by increasing the length of the alkyl spacer connecting the dye and the anchoring thiol used as capping layer (see figure 22.2)[230]. Moreover, a similar discussion was proposed considering the library composed by hybrid dye-nanourchins in chapter 14.[18]
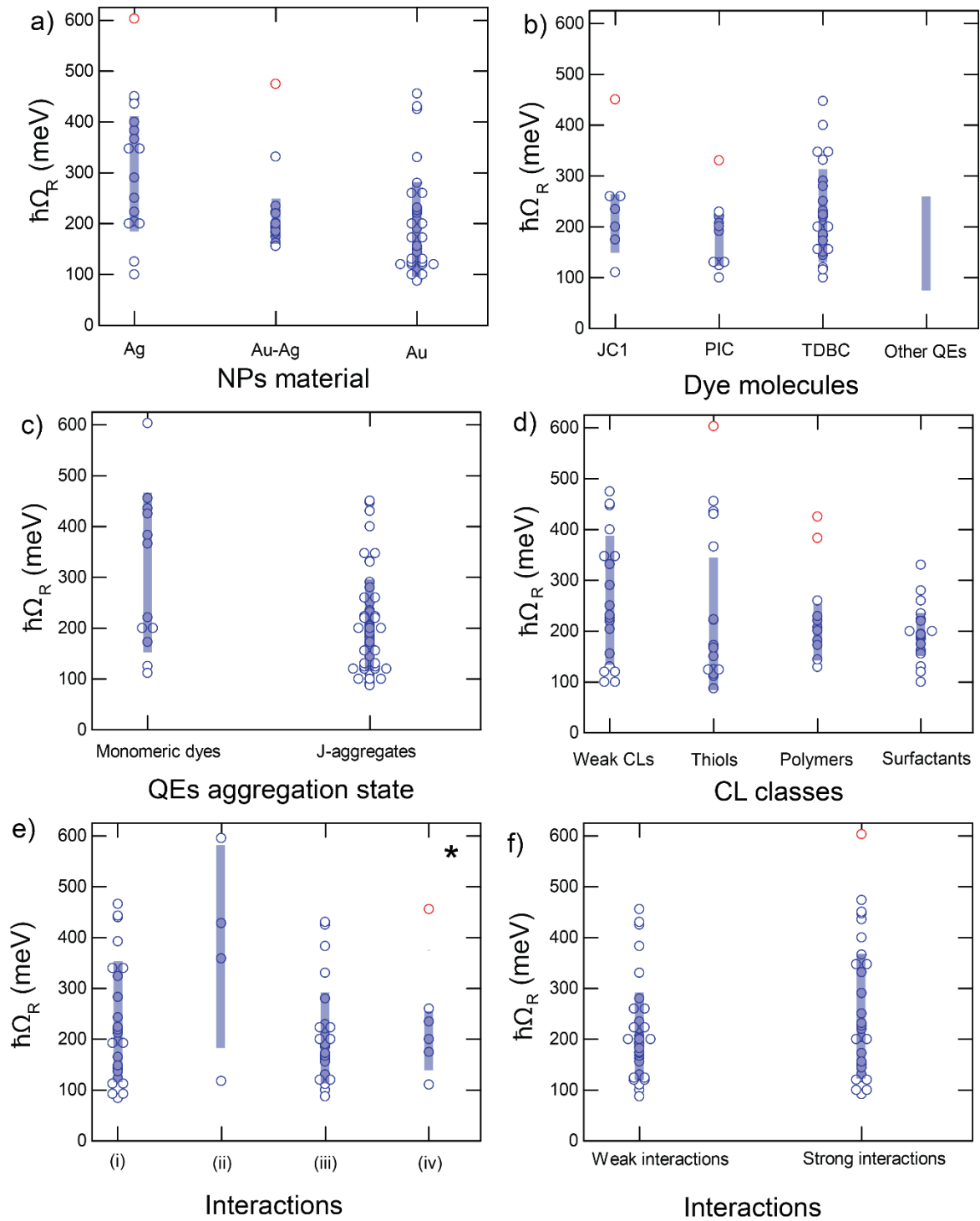
Figure 22.1. Distribution plots correlating $\hbar\Omega_R$ with different classes of CPMs: a) NPs materials, b) dye molecules, c) QEs aggregation state, d) CL classes, e) and f) nature of the interactions. The blue areas represent $\overline{\hbar\Omega_R} \pm \sigma_{\Omega_R}$ intervals, while dots are the values for the single CPMs. Red dots were considered outlier and excluded from the calculation of the average values. In panel e), the covalent interaction is labelled with a star to underline its low statistic.
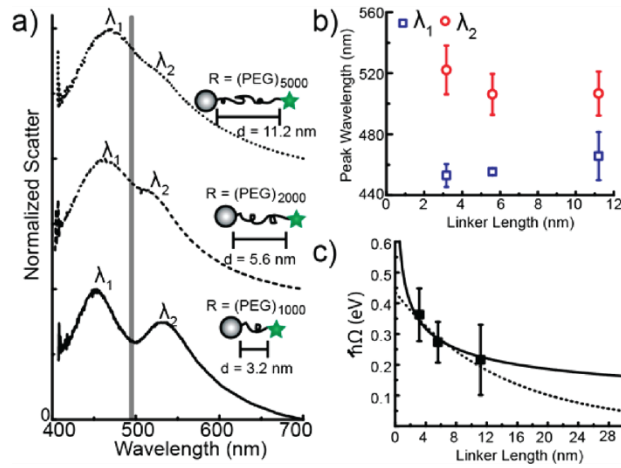
Figure 22.2. a) Scattering spectra collected for ensembles of CPMs using PEG molecules of different length. The grey bar indicates the absorption peak for free dye molecules in solution. b) Plot of the change in peak wavelength for peak 1 (blue) and peak 2 (red) as a function of linker length. c) Plot of the $\hbar\Omega_R$ as a function of linker length.

In the type (i) and type (ii) interactions the dye-NP distance is strongly controlled by the dye structure and by the location of the groups with the greater affinity for the metal surface. With the exception of those dyes designed to include an alkyl spacer, as in figure 19, the dye-NP distance in very short. In addition, it must be noted that all the four CPM with type (ii) interactions come from a single paper[230] and more statistic is necessary to obtain deeper insights.

Finally, the $\hbar\overline{\Omega_R}$ and $\hbar\bar{g}$ of the CPMs with pristine and exchanged capping layers are almost identical. This suggest that the exchange of the capping layer does not significatively alter the plexcitons performances (see appendix Appendix B, table B.4).

22.2 Study of the systems with the strongest coupling

The analysis performed in the previous sections reveals clear correlations between the classes of the component of CPMs that can achieve strong coupling. In table 22.1, I reported the CPM nanohybrids with values of $\hbar\Omega_R$ above 400 meV and $\hbar g$ above 250 meV, which are rather high in the general framework of the these materials.[8,19,40,273] The analysis of this small group confirms that high values of Ω_R can result from all the different possible features above mentioned but specific classes appear to provide more cases. Remarkably, half of the systems are made with monomeric dyes or Ag NPs, although monomeric and Ag CPMs account for only for the 25% of the total number of CPM reported. This confirms the early suggestion that monomeric dyes and Ag NPs are more prone to strong coupling.

Table 22.1. The CPMs with the highest $\hbar\Omega_R$. E=exchanged CL; N =native CL. $\hbar\Omega_R$ are reported in meV. CPMs with * have been measured in conditions of $\delta \neq 0$, which might imply a systematic error.

CPM reference	NPs	CL	QEs	Interaction	$\hbar\Omega_R$	$\hbar g$
CPM-S						
Peruffo 2021 [17]*	Au urchins	SOt, E	Styryl 9M, carbocyanine Monomeric	(iv)	456	236
Krivenkov 2021[222]	Ag platelets	Citrate, N	JC1, cyanine aggregate	(i)	450	274
Balci 2013[217]	Ag prisms	Citrate, N	TDBC, cyanine aggregate	(i)	447	259
Peruffo 2021 [17]*	Au spheres	TMAOt E	TPPS, porphyrin aggregate	(iii)	430	230
Ni 2008 [218]*	Au rods	PSS, E	HITC carboc. monomeric	(iii)	425	
Thomas 2018[41]	Au spheres	PVP, E	FITC, rhodamine monomeric	(iii)	383	251
Kumar 2020[208]	Au rods	CTAB, N	TDBC, cyanine aggregate	(iii)	280	254
CPM-D						
Rodarte 2017[230]	Ag sphere	AUT, E	AF488, monomeric	(ii)	603	307
Kometani 2001[48]*	Ag-Au sphere	BH_4^+, N	TC, Cyanine aggregate	(i)	474	336
Rodarte 2017[230]	Ag sphere	AHDT, E	AF488, monomeric	(ii)	436	225
Wersall 2017[75]	Ag prism	Citrate, N	TDBC, cyanine aggregate	(ii)	400	203
Rodarte 2017[230]	Ag sphere	APT, E	AF488, monomeric	(ii)	366	191
Song 2019[259]	Au cubes	Cl^-, E	PIC, cyanine aggregate	(iii)	330	183

22.3 Comparing CPM in solution with their equivalent deposited

In table 22.2, I compared CPMs which differ only for being dispersed in solution or deposited onto a solid substrate. The main difference between the two kinds of systems, as mentioned earlier, is that in supported systems the QEs are fully "bound" to the nanoparticles, at the closest possible distance, while in dispersed systems the number of QEs in contact with the NPs depend on the reciprocal affinity. I could evaluate the coupling of 11 CPMs whose features were studied both in dispersion or supported. For 5 of them, the coupling was stronger for CPM-D than for CPM-S; for 2 of them the situation was the opposite, and for the remaining 4 the coupling did not change. Apparently, the deposition of the CPM-S is more likely to enhance their performances, or at least

maintain them, with respect to the solution. The data also allow to compare different CPM-D deposited onto the same solid support, which is ITO glass (see rows 8,9 and 11 in table 22.2). Different kinds of solid support do not affect the interactions, because the CPM-D in the three systems considered were respectively higher, equal, or lower than CPM-S ones.

Table 22.2. Comparison between CPM-S and -D. $\hbar\Omega_R$ and $\hbar g$ are reported in meV. Blue rows indicate that CPM-S has stronger coupling than CPM-D (S>D) and orange rows the opposite. For white rows CPM-S and CPM-D have (almost) equal coupling.

CPM-S Ref.	CPM-D Ref.	NPs	CL	QEs	Interaction	CPM-S		CPM-D	
						$\hbar\Omega_R$	$\hbar g$	$\hbar\Omega_R$	$\hbar g$
48	48	Au-Ag sphere	BH$_4^+$	TC, cyanine aggregate	(i)	474	336	474	336
14	14	Au sphere	3-mercapto propionic acid	Cc, protein	(iii)			112	93
218	265	Au rods	PSS	HITC, carbocyanine aggregate	(iii)	425		557+188	
217	217	Ag prism	Citrate	TDBC cyanine aggregate	(i)	447	259	204	179
	268					447	259	290	147
	75					447	259	400	203
	76					447	259	250	131
257	257	Ag-Au cubes	CTAB	PIC cyanine aggregate	(iii)	223	118	220	118
259	259	Ag-Au cubes	Cl$^-$	PIC cyanine aggregate	(iii)	100	76	130	148
259	259	Au cubes	Cl$^-$	PIC cyanine aggregate	(iii)	100	76	330	183
208	208	Au rods	CTAB	TDBC cyanine aggregate	(iii)	280	254	200	105
194	194	Ag-Au cubes	CPC	TDBC cyanine aggregate	(iii)	162	98	156	96
194	194	Ag-Au rings	CPC	TDBC cyanine aggregate	(iii)	186	105	200	111
262	270	Au rods	Citrate	TDBC cyanine aggregate	(i)	227	116	232	135

23.   Concluding remarks

Colloidal Plexcitonic Materials differ from other materials used in the light-matter coupling panorama because they are generated by colloidal plasmonic nanoparticles, which grant low costs and easy processability, besides a facilitated characterization. In this chapter we learnt that they also have excellent photophysical properties, with coupling parameters comparable with other light-matter coupling supports.

However, these materials are still not well understood. Currently, no hints, if not that of a good overlap between the absorption bands of the NPs and the QE, apparently guide the choice of the best candidates. This is why in this chapter I tried to rationalise the properties of the CPMs so far proposed and studied in the literature, focusing on their three main components (the plasmonic NPs, the QEs, and the CLs), to identify the most used and the most performative ones. I also tried to define and classify the four most common kinds of interactions between NPs and QEs. This knowledge could serve as a base for a better design and control of novel nanohybrids with enhanced and controllable performances.

The available data allow to define some meaningful clear-cut correlations. In particular, in the distributions plots, I exploited $\hbar\Omega_R$ and $\hbar g$ as figure of merit for the optical performances of CPMs. The use of Ag NPs, monomeric QEs, and/or a CL which allows strong interactions between NPs and QEs should result in the most strongly coupled CPMs.

The study of the class of molecules forming J-aggregates revealed that TDBC and JC-1 are the most performative. This can be explained considering the peculiar molecular structure of the dyes, as already discussed for the systems reported in chapter 14. Moreover, J-aggregates are far more used because they have more anchoring points. Instead, CPMs prepared with monomeric QEs are rather rare in literature[14,17,31,41,63,215,218,230,263,267], or difficult to characterise[219,220,265] because their K_a is not enough high to maintain their equilibrium shifted to the QE-NP bound form. However, preliminary analyses revealed that the CPMs prepared with monomeric QEs seem to be more performative than the CPMs prepared with J-aggregates. Further analyses are required for a better understanding of this behaviour.

The analysis of the capping layers molecules revealed that the most suitable CL needs to guarantee a strong binding between QEs and NPs and at the same time it should not hinder the effective volume of the NPs, which has to be filled as much as possible with QEs to maximise the coupling.

A possible solution to release some of the identified constraints could be the use of deposited systems. Here, the need of a strong affinity is cancelled and close distances as well as high density of dyes in the effective volume is granted by the solid support itself. Indeed, the use of cumbersome CL is significantly reduced and the number of plexcitonic systems prepared with monomeric QEs higher. In addition, the comparison between CPMs in solution and deposited indicates more favourable performances for CPM-D.

Conclusions

The work presented in this thesis fits in the vast research field of nanomaterials for the exploitation of light-matter coupling and it has followed a twofold aim and perspective: on the one hand, I wanted to identify the main supramolecular features suitable for the efficient assembly of plexcitonic materials, and, thus, study the design of these materials. On the other, to investigate their optical properties and ultrafast dynamics in different coupling regimes. The motivation driving this two-fold approach was to correlate the design to the dynamics and devise guidelines for realizing new functional materials with controlled properties.

The design perspective is a relatively new concept in the scenario of materials for light-matter interaction. Part IV was intended to investigate this issue, to the extent that it became crucial within the overall thesis context to identify the most common and performative CPMs constituents.. Chapter 14 analysed experimentally a nanohybrids library with the same aim. The similarity of the results obtained either experimentally in chapter 14, and in the review research, in part IV validate, overall, a first robust, clear, and rational correlation between the design and the optical properties of CPMs. Moreover, the study of nanospheres-TPPS hybrids in chapters 11 and 12 demonstrated that the CPMs could also be responsive materials, able to adapt their optical properties as a function of different external stimuli.

A second important aspect is the dynamical characterisation of these CPMs. The number of papers devoted to the investigation of the ultrafast dynamics of these systems is still low and they almost entirely make use of the pump and probe technique. In this PhD thesis, instead, the use of 2DES allowed reaching a higher time resolution and decongesting the complex response of the nanohybrids in bidimensional maps. Thanks to these features, using the 2DES, I was able to decipher for the first time the coherent dynamics of the plexcitonic states in the strong coupled regime (chapter 15). When the coupling strength cannot satisfy the strong coupling conditions, plexcitonic states can still be detected, but their excitation exchange becomes incoherent. In this case, I observed energy transfer, assisted by the vibrations of the dyes (chapter 16). Finally, the dynamics of a sample with two sets of plexcitonic resonances were analysed with a pump and probe setup. The results show that the relaxation dynamics can be slowed down up to two orders of magnitude compared to the usual relaxation times of CPMs, just acting on the pump fluence and frequency and on the number of active sets of plexcitonic resonances (chapter 13).

Overall, this Thesis remarks the stark versatility of these materials in terms of dynamics and, in general, optical properties, furtherly enhanced by the more profound understanding obtained by studying their design. From a broader perspective, the correlations between dynamics and system design reported here may help in the development of a new class of devices based on plexcitonic materials.

References

References

1. Fano, U. SULLO SPETTRO DI ASSORBIMENTO DEI GAS NOBILI PRESSO IL LIMITE DELLO SPETTRO D'ARCO. *Nuovo Cimento1* 154– 161 (1935).

2. Dicke, R. H. Coherence in spontaneous radiation processes. *Phys. Rev.* **93**, 99–110 (1954).

3. Tavis, M. & Cummings, F. W. The exact solution of N two level systems interacting with a single mode, quantized radiation field. *Phys. Lett. A* **25**, 714–715 (1967).

4. Cummings, F.W., Jaynes, E. T. Comparison of Quantum and Semiclassical Radiation Theories with Application to the Beam Maser. *Proc. IEEE* 89–109 (1963).

5. Purcell, E. M. Spontaneous emission probabilities at radio frequencies. *Phys. Rev.* **69**, 681 (1946).

6. Marquier, F., Sauvan, C. & Greffet, J. J. Revisiting quantum optics with surface plasmons and plasmonic resonators. *ACS Photonics* **4**, 2091–2101 (2017).

7. Pelton, M., Storm, S. D. & Leng, H. Strong coupling of emitters to single plasmonic nanoparticles: Exciton-induced transparency and Rabi splitting. *Nanoscale* **11**, 14540–14552 (2019).

8. Baranov, D. G., Wersäll, M., Cuadra, J., Antosiewicz, T. J. & Shegai, T. Novel Nanostructures and Materials for Strong Light-Matter Interactions. *ACS Photonics* **5**, 24–42 (2018).

9. Törmö, P. & Barnes, W. L. Strong coupling between surface plasmon polaritons and emitters: A review. *Reports Prog. Phys.* **78**, 13901 (2015).

10. Flick, J., Rivera, N. & Narang, P. Strong light-matter coupling in quantum chemistry and quantum photonics. *Nanophotonics* **7**, 1479–1501 (2018).

11. Nan, F. *et al.* Plasmon resonance energy transfer and plexcitonic solar cell. *Nanoscale* **8**, 15071–15078 (2016).

12. Manuel, A. P., Kirkey, A., Mahdi, N. & Shankar, K. Plexcitonics-fundamental principles and optoelectronic applications. *J. Mater. Chem. C* **7**, 1821–1853 (2019).

13. Srivastava, T. & Jha, R. Plexcitonic nose based on an organic semiconductor. *Appl. Phys. Lett.* **117**, (2020).

14. Choi, Y., Kang, T. & Lee, L. P. Plasmon resonance energy transfer (PRET)-based molecular imaging of cytochrome C in living cells. *Nano Lett.* **9**, 85–90 (2009).

15. Imamo, A. *et al.* Quantum information processing using quantum dot spins and cavity QED. *Phys. Rev. Lett.* **83**, 4204–4207 (1999).

16. Fofang, N. T., Grady, N. K., Fan, Z., Govorov, A. O. & Halas, N. J. Plexciton dynamics: Exciton-plasmon coupling in a J-aggregate-Au nanoshell complex provides a mechanism for nonlinearity. *Nano Lett.* **11**, 1556–1560 (2011).

17. Peruffo, N., Gil, G., Corni, S., Mancin, F. & Collini, E. Selective switching of multiple plexcitons in colloidal materials: directing the energy flow at the nanoscale. *Nanoscale* **13**, 6005–6015 (2021).

18. Peruffo, N., Mancin, F. & Collini, E. Plexcitonic Nanohybrids Based on Gold Nanourchins: The Role of the Capping Layer. *J. Phys. Chem. C* (2021) doi:10.1021/acs.jpcc.1c05862.

19. Frisk Kockum, A., Miranowicz, A., De Liberato, S., Savasta, S. & Nori, F. Ultrastrong coupling between light and matter. *Nat. Rev. Phys.* **1**, 19–40 (2019).

20. Khitrova, G., Gibbs, H. M., Kira, M., Koch, S. W. & Scherer, A. Vacuum Rabi splitting in semiconductors. *Nat. Phys.* **2**, 81–90 (2006).

21. Amendola, V., Pilot, R., Frasconi, M., Maragò, O. M. & Iatì, M. A. Surface plasmon resonance in gold nanoparticles: A review. *J. Phys. Condens. Matter* **29**, (2017).

22. Tame, M. S. *et al.* Quantum plasmonics. *Nat. Phys.* **9**, 329–340 (2013).

References

23. Hugall, J. T., Singh, A. & Van Hulst, N. F. Plasmonic Cavity Coupling. *ACS Photonics* **5**, 43–53 (2018).

24. Fano, U. Effects of configuration interaction on intensities and phase shifts. *Phys. Rev.* **124**, 1866–1878 (1961).

25. Miroshnichenko, A. E., Flach, S. & Kivshar, Y. S. Fano resonances in nanoscale structures. *Rev. Mod. Phys.* **82**, 2257–2298 (2010).

26. Drexhage, K. H. IV Interaction of Light with Monomolecular Dye Layers. *Prog. Opt.* **12**, 163–192 (1974).

27. Jeanmaire, D. L. & Duyne, R. P. VAN. Surface Raman Spectroelectrochemistry Part1. Heterocyclic. *J. Electroanal Chem.* **84**, 1–20 (1977).

28. Kwart, H. & George, T. J. Anomalously Intense Raman Spectra of Pyridine at a Silver Electrode. *J. Am. Chem. Soc.* **4009**, 5215–5217 (1977).

29. Beutler, H. Über Absorptionsserien von Argon, Krypton und Xenon zu Termen zwischen den beiden Ionisierungsgrenzen2P32/0 und2P12/0. *Zeitschrift für Phys.* **93**, 177–196 (1935).

30. Luk'Yanchuk, B. *et al.* The Fano resonance in plasmonic nanostructures and metamaterials. *Nat. Mater.* **9**, 707–715 (2010).

31. Nan, F. *et al.* Unusual and Tunable One-Photon Nonlinearity in Gold-Dye Plexcitonic Fano Systems. *Nano Lett.* **15**, 2705–2710 (2015).

32. Kaluzny, Y., Goy, P., Gross, M., Raimond, J. M. & Haroche, S. Observation of self-induced Rabi oscillations in two-level atoms excited inside a resonant cavity: The ringing regime of superradiance. *Phys. Rev. Lett.* **51**, 1175–1178 (1983).

33. Weisbuch, C., Nishioka, M., Ishikawa, A. & Arakawa, Y. Observation of the coupled exciton-photon mode splitting in a semiconductor quantum microcavity. *Phys. Rev. Lett.* **69**, 3314–3317 (1992).

34. Sanvitto, D. & Kéna-Cohen, S. The road towards polaritonic devices. *Nat. Mater.* **15**, 1061–1073 (2016).

35. Liang, W. Y. Physics Education Related content Recent citations. *Phys. Educ.* **5**, 226–228 (1970).

36. Holmes, R. J. & Forrest, S. R. Strong exciton-photon coupling in organic materials. *Org. Electron.* **8**, 77–93 (2007).

37. Atkins, P. *Physical Chemistry*. (Oxford University Press, 1998).

38. Bricks, J. L., Slominskii, Y. L., Panas, I. D. & Demchenko, A. P. Fluorescent J-aggregates of cyanine dyes: Basic research and applications review. *Methods Appl. Fluoresc.* **6**, 12001 (2018).

39. Pockrand, I.; Brillante, A.; Mobius, D. Exciton – surface plasmon coupling : An experimental investigation Exciton-surface plasmon coupling : An experimental investigation. **77**, 6289–6295 (1982).

40. Hutchison, J. A., Schwartz, T., Genet, C., Devaux, E. & Ebbesen, T. W. Modifying chemical landscapes by coupling to vacuum fields. *Angew. Chemie - Int. Ed.* **51**, 1592–1596 (2012).

41. Thomas, R. *et al.* Plexcitons: The Role of Oscillator Strengths and Spectral Widths in Determining Strong Coupling. *ACS Nano* **12**, 402–415 (2018).

42. Glass, A. M., Liao, P. F., Bergman, J. G. & Olson, D. H. Interaction of metal particles with adsorbed dye molecules: absorption and luminescence. *Opt. Lett.* **5**, 368 (1980).

43. Garoff, S., Weitz, D. A., Gramila, T. J. & Hanson, C. D. Optical absorption resonances of dye-coated silver-island films. *Opt. Lett.* **6**, 245 (1981).

44. Eagen, C. F. Nature of the enhanced optical absorption of dye-coated Ag island films. *Appl. Opt.* **20**, 3035 (1981).

References

45. Link, S. & El-Sayed, M. A. Size and temperature dependence of the plasmon absorption of colloidal gold nanoparticles. *J. Phys. Chem. B* **103**, 4212–4217 (1999).

46. Sönnichsen, C. *et al.* Drastic reduction of plasmon damping in gold nanorods. *Phys. Rev. Lett.* **88**, 774021–774024 (2002).

47. Hartland, G. V. Optical studies of dynamics in noble metal nanostructures. *Chem. Rev.* **111**, 3858–3887 (2011).

48. Kometani, N., Tsubonishi, M., Fujita, T., Asami, K. & Yonezawa, Y. Preparation and optical absorption spectra of dye-coated Au, Ag, and Au/Ag colloidal nanoparticles in aqueous solutions and in alternate assemblies. *Langmuir* **17**, 578–580 (2001).

49. Višić, B. *et al.* Ultrafast nonequilibrium dynamics of strongly coupled resonances in the intrinsic cavity of W S 2 nanotubes . *Phys. Rev. Res.* **1**, 1–7 (2019).

50. Chikkaraddy, R. *et al.* Single-molecule strong coupling at room temperature in plasmonic nanocavities. *Nature* **535**, 127–130 (2016).

51. Chen, Xingxing, Chen, Yu-Hui, Qin, Jian Zhao, Ding, Ding, Boyang, Blaikie, Richard J., Q. M. Mode Modification of Plasmonic Gap Resonances Induced by Strong Coupling with Molecular Excitons. *Nano Lett.* **17**, 3246–3251 (2017).

52. Raimond, J. M., Brune, M. & Haroche, S. Colloquium: Manipulating quantum entanglement with atoms and photons in a cavity. *Rev. Mod. Phys.* **73**, 565–582 (2001).

53. Lunz, M. *et al.* Surface plasmon enhanced energy transfer between donor and acceptor CdTe nanocrystal quantum dot monolayers. *Nano Lett.* **11**, 3341–3345 (2011).

54. Coles, D. M. *et al.* Polariton-mediated energy transfer between organic dyes in a strongly coupled optical microcavity. *Nat. Mater.* **13**, 712–719 (2014).

55. Carusotto, I. & Ciuti, C. Quantum fluids of light. *Rev. Mod. Phys.* **85**, 299–366 (2013).

56. Deng, H., Haug, H. & Yamamoto, Y. Exciton-polariton Bose-Einstein condensation. *Rev. Mod. Phys.* **82**, 1489–1537 (2010).

57. Rahimi-Iman, A. *Polariton Physics*. vol. 229 (2020).

58. Kasprzak, J. *et al.* Bose-Einstein condensation of exciton polaritons. *Nature* **443**, 409–414 (2006).

59. Huynh, A. *et al.* Polariton Parametric Amplifier Pump Dynamics in the Coherent Regime. *Phys. Rev. Lett.* **90**, 4 (2003).

60. Gubbin, C. R., Maier, S. A. & Kéna-Cohen, S. Low-voltage polariton electroluminescence from an ultrastrongly coupled organic light-emitting diode. *Appl. Phys. Lett.* **104**, (2014).

61. Tischler, J. R., Bradley, M. S., Bulović, V., Song, J. H. & Nurmikko, A. Strong coupling in a microcavity LED. *Phys. Rev. Lett.* **95**, 1–4 (2005).

62. Genco, A. *et al.* Bright Polariton Coumarin-Based OLEDs Operating in the Ultrastrong Coupling Regime. **1800364**, 1–6 (2018).

63. Liu, G. L., Long, Y. T., Choi, Y., Kang, T. & Lee, L. P. Quantized plasmon quenching dips nanospectroscopy via plasmon resonance energy transfer. *Nat. Methods* **4**, 1015–1017 (2007).

64. Meystre, P. & Sargent, S. *Elements of Quantum Optics*. (Springer-Verlag, 1991).

65. Grynberg, G., Aspect, A. & Fabre, C. *Introducion to Quantum Optics: From the Semi-classical Approach to Quantized Light*. (Cambridge University Press, 2010).

66. Stete, F. Gold at the Nanoscale Plasmon - Exciton Coupling and Optical Heating. (2020).

67. Yoshle, T. *et al.* Vacuum Rabi splitting with a single quantum dot in a photonic crystal nanocavity.

References

Nature **432**, 200–203 (2004).

68.   Garraway, B. M. The Dicke model in quantum optics: Dicke model revisited. *Philos. Trans. R. Soc. A Math. Phys. Eng. Sci.* **369**, 1137–1155 (2011).

69.   Ribeiro, R. F., Martínez-Martínez, L. A., Du, M., Campos-Gonzalez-Angulo, J. & Yuen-Zhou, J. Polariton chemistry: controlling molecular dynamics with optical cavities. *Chem. Sci.* **9**, 6325–6339 (2018).

70.   Murata, N., Hata, R. & Ishihara, H. Crossover between Energy Transparency Resonance and Rabi Splitting in Antenna–Molecule Coupled Systems. *J. Phys. Chem. C* **119**, 25493–25498 (2015).

71.   Leng, H., Szychowski, B., Daniel, M. C. & Pelton, M. Strong coupling and induced transparency at room temperature with single quantum dots and gap plasmons. *Nat. Commun.* **9**, (2018).

72.   Stete, F. *et al.* Vacuum-induced saturation in plasmonic nanoparticles. *arXiv* **2**, (2020).

73.   Stete, F., Koopman, W. & Bargheer, M. Signatures of Strong Coupling on Nanoparticles: Revealing Absorption Anticrossing by Tuning the Dielectric Environment. *ACS Photonics* **4**, 1669–1676 (2017).

74.   Chovan, J., Perakis, I. E., Ceccarelli, S. & Lidzey, D. G. Controlling the interactions between polaritons and molecular vibrations in strongly coupled organic semiconductor microcavities. *Phys. Rev. B - Condens. Matter Mater. Phys.* **78**, 1–5 (2008).

75.   Wersall, M., Cuadra, J., Antosiewicz, T. J., Balci, S. & Shegai, T. Observation of mode splitting in photoluminescence of individual plasmonic nanoparticles strongly coupled to molecular excitons. *Nano Lett.* **17**, 551–558 (2017).

76.   Wersäll, M. *et al.* Correlative Dark-Field and Photoluminescence Spectroscopy of Individual Plasmon-Molecule Hybrid Nanostructures in a Strong Coupling Regime. *ACS Photonics* **6**, 2570–2576 (2019).

77.   Melnikau, D. *et al.* Rabi Splitting in Photoluminescence Spectra of Hybrid Systems of Gold Nanorods and J-Aggregates. *J. Phys. Chem. Lett.* **7**, 354–362 (2016).

78.   Wang, S. *et al.* Quantum yield of polariton emission from hybrid light-matter states. *J. Phys. Chem. Lett.* **5**, 1433–1439 (2014).

79.   Collini, E. 2D Electronic Spectroscopic Techniques for Quantum Technology Applications. *J. Phys. Chem. C* (2021) doi:10.1021/acs.jpcc.1c02693.

80.   Słowik, K., Filter, R., Straubel, J., Lederer, F. & Rockstuhl, C. Strong coupling of optical nanoantennas and atomic systems. *Phys. Rev. B - Condens. Matter Mater. Phys.* **88**, 1–12 (2013).

81.   Takemura, N. *et al.* Two-dimensional Fourier transform spectroscopy of exciton-polaritons and their interactions. *Phys. Rev. B - Condens. Matter Mater. Phys.* **92**, (2015).

82.   Xiang, B. *et al.* Manipulating optical nonlinearities of molecular polaritons by delocalization. *arXiv* 1–9 (2019).

83.   Finkelstein-Shapiro, D. *et al.* Understanding radiative transitions and relaxation pathways in plexcitons. *Chem* **7**, 1092–1107 (2021).

84.   Takahashi, S. & Watanabe, K. Decoupling from a Thermal Bath via Molecular Polariton Formation. *J. Phys. Chem. Lett.* 1349–1356 (2020) doi:10.1021/acs.jpclett.9b03789.

85.   Mewes, L., Wang, M., Ingle, R. A., Börjesson, K. & Chergui, M. Energy relaxation pathways between light-matter states revealed by coherent two-dimensional spectroscopy. *Commun. Phys.* **3**, 1–10 (2020).

86.   Vasa, P. *et al.* Real-time observation of ultrafast Rabi oscillations between excitons and plasmons in metal nanostructures with J-aggregates. *Nat. Photonics* **7**, 128–132 (2013).

87.   Branczyk, A. M., Turner, D. B. & Scholes, G. D. Two-dimensional electronic spectroscopy for the

References

quantum-optics enthusiast. 1–20 (2013) doi:10.1002/andp.201300153.

88. Collini, E. Spectroscopic signatures of quantum-coherent energy transfer. *Chem. Soc. Rev.* **42**, 4932–4947 (2013).

89. Coles, D. M. *et al.* Vibrationally assisted polariton-relaxation processes in strongly coupled organic-semiconductor microcavities. *Adv. Funct. Mater.* **21**, 3691–3696 (2011).

90. Somaschi, N. *et al.* Ultrafast polariton population build-up mediated by molecular phonons in organic microcavities. *Appl. Phys. Lett.* **99**, (2011).

91. Simon, T. *et al.* Exploring the Optical Nonlinearities of Plasmon-Exciton Hybrid Resonances in Coupled Colloidal Nanostructures. *J. Phys. Chem. C* **120**, 12226–12233 (2016).

92. Balci, S. *et al.* Tunable Plexcitonic Nanoparticles: A Model System for Studying Plasmon-Exciton Interaction from the Weak to the Ultrastrong Coupling Regime. *ACS Photonics* **3**, 2010–2016 (2016).

93. Balci, S. *et al.* Probing ultrafast energy transfer between excitons and plasmons in the ultrastrong coupling regime. *Appl. Phys. Lett.* **105**, (2014).

94. Virgili, T. *et al.* Ultrafast polariton relaxation dynamics in an organic semiconductor microcavity. *Phys. Rev. B - Condens. Matter Mater. Phys.* **83**, 2–7 (2011).

95. Wang, H. *et al.* Hybrid-State Dynamics of Dye Molecules and Surface Plasmon Polaritons under Ultrastrong Coupling Regime. *Laser Photonics Rev.* **12**, 1–7 (2018).

96. Canaguier-Durand, A., Genet, C., Lambrecht, A., Ebbesen, T. W. & Reynaud, S. Non-Markovian polariton dynamics in organic strong coupling. *Eur. Phys. J. D* **69**, (2015).

97. Eizner, E., Akulov, K., Schwartz, T. & Ellenbogen, T. Temporal Dynamics of Localized Exciton-Polaritons in Composite Organic-Plasmonic Metasurfaces. *Nano Lett.* **17**, 7675–7683 (2017).

98. Kéna-Cohen, S. & Forrest, S. R. Room-temperature polariton lasing in an organic single-crystal microcavity. *Nat. Photonics* **4**, 371–375 (2010).

99. Daskalakis, K. S., Maier, S. A., Murray, R. & Kéna-Cohen, S. Nonlinear interactions in an organic polariton condensate. *Nat. Mater.* **13**, 271–278 (2014).

100. De Giorgi, M. *et al.* Interaction and Coherence of a Plasmon-Exciton Polariton Condensate. *ACS Photonics* **5**, 3666–3672 (2018).

101. Ramezani, M., Halpin, A., Wang, S., Berghuis, M. & Rivas, J. G. Ultrafast Dynamics of Nonequilibrium Organic Exciton-Polariton Condensates. *Nano Lett.* **19**, 8590–8596 (2019).

102. Vasa, P. *et al.* Ultrafast manipulation of strong coupling in metal-molecular aggregate hybrid nanostructures. *ACS Nano* **4**, 7559–7565 (2010).

103. Salomon, A., Genet, C. & Ebbesen, T. W. Molecule-light complex: Dynamics of hybrid molecule-surface plasmon states. *Angew. Chemie - Int. Ed.* **48**, 8748–8751 (2009).

104. Schwartz, T. *et al.* Polariton dynamics under strong light-molecule coupling. *ChemPhysChem* **14**, 125–131 (2013).

105. Walters, C. M., Pao, C., Gagnon, B. P., Zamecnik, C. R. & Walker, G. C. Bright Surface-Enhanced Raman Scattering with Fluorescence Quenching from Silica Encapsulated J-Aggregate Coated Gold Nanoparticles. *Adv. Mater.* **30**, 1–6 (2018).

106. Das, K., Hazra, B. & Chandra, M. Exploring the coherent interaction in a hybrid system of hollow gold nanoprisms and cyanine dye J-aggregates: Role of plasmon-hybridization mediated local electric-field enhancement. *Phys. Chem. Chem. Phys.* **19**, 27997–28005 (2017).

107. Mazza, L., Kéna-Cohen, S., Michetti, P. & La Rocca, G. C. Microscopic theory of polariton lasing via vibronically assisted scattering. *Phys. Rev. B - Condens. Matter Mater. Phys.* **88**, (2013).

References

108. Phys, J. C., Zhang, B. & Zhang, B. The vibronic absorption spectra and exciton dynamics of plasmon-exciton hybrid systems in the regimes ranged from Fano antiresonance to Rabi-like splitting The vibronic absorption spectra and exciton dynamics of plasmon-exciton hybrid systems in the regim. **014102**, (2020).

109. Nan, F. *et al.* Unusual and Tunable One-Photon Nonlinearity in Gold-Dye Plexcitonic Fano Systems. (2015) doi:10.1021/acs.nanolett.5b00413.

110. Bonomi, R., Cazzolaro, A. & Prins, L. J. Assessment of the morphology of mixed SAMs on Au nanoparticles using a fluorescent probe. *Chem. Commun.* **47**, 445–447 (2011).

111. Xia, H., Bai, S., Hartmann, J. & Wang, D. Synthesis of monodisperse quasi-spherical gold nanoparticles in water via silver(I)-assisted citrate reduction. *Langmuir* **26**, 3585–3589 (2010).

112. Manea, F., Bindoli, C., Polizzi, S., Lay, L. & Scrimin, P. Expeditious synthesis of water-soluble, monolayer-protected gold nanoparticles of controlled size and monolayer composition. *Langmuir* **24**, 4120–4124 (2008).

113. Li, J. *et al.* Controllable synthesis of stable urchin-like gold nanoparticles using hydroquinone to tune the reactivity of gold chloride. *J. Phys. Chem. C* **115**, 3630–3637 (2011).

114. Rodríguez-Lorenzo, L., Romo-Herrera, J. M., Pérez-Juste, J., Alvarez-Puebla, R. A. & Liz-Marzán, L. M. Reshaping and LSPR tuning of Au nanostars in the presence of CTAB. *J. Mater. Chem.* **21**, 11544–11549 (2011).

115. Bonetti, C. *et al.* Identification of excited-state energy transfer and relaxation pathways in the peridinin-chlorophyll complex: An ultrafast mid-infrared study. *Phys. Chem. Chem. Phys.* **12**, 9256–9266 (2010).

116. Manzoni, C., Polli, D. & Cerullo, G. Two-color pump-probe system broadly tunable over the visible and the near infrared with sub-30 fs temporal resolution. *Rev. Sci. Instrum.* **77**, 1–9 (2006).

117. Dobryakov, A. L. *et al.* Femtosecond pump/supercontinuum-probe spectroscopy: Optimized setup and signal analysis for single-shot spectral referencing. *Rev. Sci. Instrum.* **81**, 1–9 (2010).

118. Bolzonello, L. Ultrafast Relaxation Dynamics of Multichromophoric Systems Through Advanced Optical Spectroscopies. 132 (2016).

119. Del Fatti, N. *et al.* Nonequilibrium electron dynamics in noble metals. *Phys. Rev. B - Condens. Matter Mater. Phys.* **61**, 16956–16966 (2000).

120. Lambert, N. *et al.* Quantum biology. *Nat. Phys.* **9**, 10–18 (2013).

121. Cao, J. *et al.* Quantum biology revisited. *Sci. Adv.* **6**, eaaz4888 (2020).

122. Christensson, N., Kauffmann, H. F., Pullerits, T. & Mančal, T. Origin of long-lived coherences in light-harvesting complexes. *J. Phys. Chem. B* **116**, 7449–7454 (2012).

123. Lenngren, N. *et al.* Hot electron and hole dynamics in thiol-capped CdSe quantum dots revealed by 2D electronic spectroscopy. *Phys. Chem. Chem. Phys.* **18**, 26199–26204 (2016).

124. Collini, E. *et al.* Quantum Phenomena in Nanomaterials: Coherent Superpositions of Fine Structure States in CdSe Nanocrystals at Room Temperature. *J. Phys. Chem. C* **123**, 31286–31293 (2019).

125. Mukamel, S. *Principles of nonlinear optical spectroscopy*. (1995).

126. Mukamel, S. Correlation Spectroscopies of Electronic and Vibrational Excitations. *New York* **51**, 691–729 (2000).

127. Boyd, R. W. *Nonlinear Optics*. (Elsevier, 2008).

128. McHale, J. L. *Molecular Spectroscopy, Second Edition. Molecular Spectroscopy, Second Edition* (2017).

References

129. Tokmakoff, A. *Time-Dependent Quantum Mechanics and Spectroscopy. Lecture* (2014).

130. Nemeth, A. *et al.* Double-quantum two-dimensional electronic spectroscopy of a three-level system: Experiments and simulations. *J. Chem. Phys.* **133**, (2010).

131. Meneghin, E. Coherent Multidimensional Electronic Spectroscopy : From Bioinspired To Biological Systems. (2017).

132. Turner, D. B. *et al.* Quantitative investigations of quantum coherence for a light-harvesting protein at conditions simulating photosynthesis. *Phys. Chem. Chem. Phys.* **14**, 4857–4874 (2012).

133. Butkus, V., Zigmantas, D., Valkunas, L. & Abramavicius, D. Vibrational vs. electronic coherences in 2D spectrum of molecular systems. *Chem. Phys. Lett.* **545**, 40–43 (2012).

134. Kasha, M., Rawls, H. R. & El-Bayoumi, M. A. The Exciton Model In Molecular Spectroscopy. *Pure Appl. Chem.* **11**, 371–392 (1965).

135. Hsu, L. Y., Ding, W. & Schatz, G. C. Plasmon-Coupled Resonance Energy Transfer. *J. Phys. Chem. Lett.* **8**, 2357–2367 (2017).

136. Ozel, T. *et al.* Observation of selective plasmon-exciton coupling in nonradiative energy transfer: Donor-selective versus acceptor-selective plexcitons. *Nano Lett.* **13**, 3065–3072 (2013).

137. Bolzonello, L., Volpato, A., Meneghin, E. & Collini, E. Versatile setup for high-quality rephasing, non-rephasing, and double quantum 2D electronic spectroscopy. *J. Opt. Soc. Am. B* **34**, 1223 (2017).

138. Jonas, D. M. Two-Dimensional Femtosecond Spectroscopy. *Annu. Rev. Phys. Chem.* **54**, 425–463 (2003).

139. Volpato, A., Bolzonello, L., Meneghin, E. & Collini, E. Global analysis of coherence and population dynamics in 2D electronic spectroscopy. *Opt. Express* **24**, 24773 (2016).

140. Hertzog, M., Wang, M., Mony, J. & Börjesson, K. Strong light-matter interactions: A new direction within chemistry. *Chem. Soc. Rev.* **48**, 937–961 (2019).

141. Wurtz, G. A. *et al.* Molecular Plasmonics with Tunable Exciton–Plasmon Coupling Strength in J-Aggregate Hybridized Au Nanorod Assemblies. *Nano Lett.* **7**, 1297–1303 (2007).

142. Ebbesen, T. W. Hybrid Light-Matter States in a Molecular and Material Science Perspective. *Acc. Chem. Res.* **49**, 2403–2412 (2016).

143. Micali, N., Mallamace, F., Romeo, A., Purrello, R. & Monsù Scolaro, L. Mesoscopic Structure of meso-Tetrakis(4-sulfonatophenyl)porphine J-Aggregates. *J. Phys. Chem. B* **104**, 5897–5904 (2000).

144. Occhiuto, I. G. *et al.* The role of counter-anions in the kinetics and chirality of porphyrin J-aggregates. *Chem. Commun.* **52**, 11520–11523 (2016).

145. Misawa, K. & Kobayashi, T. Ultrafast exciton and excited-exciton dynamics in J-aggregates of three-level porphyrin molecules. *J. Chem. Phys.* **110**, 5844–5850 (1999).

146. Maiti, N. C., Mazumdar, S. & Periasamy, N. J- and H-aggregates of porphyrin - Surfactant complexes: Time-resolved fluorescence and other spectroscopic studies. *J. Phys. Chem. B* **102**, 1528–1538 (1998).

147. Castriciano, M. A. *et al.* Aggregation Behavior of Tetrakis(4-sulfonatophenyl)porphyrin in AOT/Water/Decane Microemulsions. *J. Phys. Chem. B* **109**, 12086–12092 (2005).

148. Koti, A. S. R. & Periasamy, N. Self-assembly of template-directed J-aggregates of porphyrin. *Chem. Mater.* **15**, 369–371 (2003).

149. Collini, E., Ferrante, C., Bozio, R., Lodi, A. & Ponterini, G. Large third-order nonlinear optical response of porphyrin J-aggregates oriented in self-assembled thin films. *J. Mater. Chem.* **16**, 1573–1578 (2006).

References

150. Romeo, A., Angela Castriciano, M. & Scolaro, L. M. Spectroscopic and kinetic investigations on porphyrin J-aggregates induced by polyamines. *J. Porphyr. Phthalocyanines* **14**, 713–721 (2010).

151. Rubires, R. *et al.* Self-assembly in water of the sodium salts of meso-sulfonatophenyl substituted porphyrins. *New J. Chem.* **23**, 189–198 (1999).

152. Trapani, M., De Luca, G., Romeo, A., Castriciano, M. A. & Scolaro, L. M. Spectroscopic investigation on porphyrins nano-assemblies onto gold nanorods. *Spectrochim. Acta - Part A Mol. Biomol. Spectrosc.* **173**, 343–349 (2017).

153. Trapani, M. *et al.* Nanohybrid Assemblies of Porphyrin and Au10 Cluster Nanoparticles. *Nanomaterials* vol. 9 1026 (2019).

154. Bolzonello, L., Fassioli, F. & Collini, E. Correlated Fluctuations and Intraband Dynamics of J-Aggregates Revealed by Combination of 2DES Schemes. *J. Phys. Chem. Lett.* **7**, 4996–5001 (2016).

155. Akins, D. L. Structure and Exciton Emission Dynamics of Molecular Aggregates: Cyanines and Porphyrins. in *J-aggregates* (ed. Kobayashi, T.) 67–94 (World Scientific, 1996).

156. Kobayashi, T. *J-aggregates*. (1996).

157. Sato, T., Tsugawa, F., Tomita, T. & Kawasaki, M. Spectroscopic properties of noble metal nano-particles covered with J-aggregates of cyanine dye. *Chem. Lett.* **30**, 402–403 (2001).

158. Hranisavljevic, J., Dimitrijevic, N. M., Wurtz, G. A. & Wiederrecht, G. P. Photoinduced charge separation reactions of J-aggregates coated on silver nanoparticles. *J. Am. Chem. Soc.* **124**, 4536–4537 (2002).

159. Wiederrecht, G. P., Wurtz, G. A. & Hranisavljevic, J. Coherent coupling of molecular excitons to electronic polarizations of noble metal nanoparticles. *Nano Lett.* **4**, 2121–2125 (2004).

160. Yoshida, A., Kometani, N. & Yonezawa, Y. Silver:dye composite nanoparticles as a building unit of molecular architecture. *Colloids Surfaces A Physicochem. Eng. Asp.* **313**–**314**, 581–584 (2008).

161. Fofang, N. T. *et al.* Plexcitonic nanoparticles: Plasmon-Exciton Coupling in Nanoshell-J- Aggregate complexes. *Nano Lett.* **8**, 3481–3487 (2008).

162. Đorđević, L. *et al.* Design principles of chiral carbon nanodots help convey chirality from molecular to nanoscale level. *Nat. Commun.* **9**, (2018).

163. Li, J. *et al.* Dual Strong Couplings Between TPPS J-Aggregates and Aluminum Plasmonic States. *J. Phys. Chem. Lett.* **7**, 2786–2791 (2016).

164. Salomon, A., Wang, S., Hutchison, J. A., Genet, C. & Ebbesen, T. W. Strong light-molecule coupling on plasmonic arrays of different symmetry. *ChemPhysChem* **14**, 1882–1886 (2013).

165. Martínez, Á., Lyu, Y., Mancin, F. & Scrimin, P. Glucosamine Phosphate Induces AuNPs Aggregation and Fusion into Easily Functionalizable Nanowires. *Nanomater. (Basel, Switzerland)* **9**, 622 (2019).

166. Van Haute, D., Longmate, J. M. & Berlin, J. M. Controlled Assembly of Biocompatible Metallic Nanoaggregates Using a Small Molecule Crosslinker. *Adv. Mater.* **27**, 5158–5164 (2015).

167. Wang, H. *et al.* Dynamics of Strongly Coupled Hybrid States by Transient Absorption Spectroscopy. *Adv. Funct. Mater.* **28**, 1–22 (2018).

168. Gu, P., Zhang, W. & Zhang, G. Plasmonic Nanogaps: From Fabrications to Optical Applications. *Adv. Mater. Interfaces* **5**, 1–22 (2018).

169. Su, K.-H. *et al.* Interparticle Coupling Effects on Plasmon Resonances of Nanogold Particles. *Nano Lett.* **3**, 1087–1090 (2003).

170. Jiang, N., Zhuo, X. & Wang, J. Active Plasmonics: Principles, Structures, and Applications. *Chem. Rev.* **118**, 3054–3099 (2018).

References

171. Pramod, P. & Thomas, K. G. Plasmon coupling in dimers of Au nanorods. *Adv. Mater.* **20**, 4300–4305 (2008).

172. Auguié, B., Darby, B. L. & Le Ru, E. C. Electromagnetic interactions of dye molecules surrounding a nanosphere. *Nanoscale* **11**, 12177–12187 (2019).

173. Nan, F. *et al.* Plasmon resonance energy transfer and plexcitonic solar cell. 15071–15078 (2016) doi:10.1039/c6nr02633h.

174. Bolzonello, L., Fassioli, F. & Collini, E. Correlated Fluctuations and Intraband Dynamics of J-Aggregates Revealed by Combination of 2DES Schemes. *J. Phys. Chem. Lett.* **7**, 4996–5001 (2016).

175. Melnikau, D. *et al.* Double Rabi Splitting in a Strongly Coupled System of Core-Shell Au@Ag Nanorods and J-Aggregates of Multiple Fluorophores. *J. Phys. Chem. Lett.* **10**, 6137–6143 (2019).

176. Gouterman, M. *Optical spectra and electronic structure of porphyrins and related rings*. (The porphyrins, 1978).

177. Aggarwal, L. P. F. & Borissevitch, I. E. On the dynamics of the TPPS4 aggregation in aqueous solutions: Successive formation of H and J-aggregates. *Spectrochim. Acta - Part A Mol. Biomol. Spectrosc.* **63**, 227–233 (2006).

178. Castriciano, M. A. *et al.* Structural Rearrangements in 5,10,15,20-Tetrakis(4-sulfonatophenyl)porphyrin J-Aggregates under Strongly Acidic Conditions. *J. Phys. Chem. B* **107**, 8765–8771 (2003).

179. Akins, D. L., Zhu, H. R. & Guo, C. Absorption and raman scattering by aggregated meso-tetrakis(p-sulfonatophenyl)porphine. *J. Phys. Chem.* **98**, 3612–3618 (1994).

180. Akins, D. L., Zhu, H. R. & Guo, C. Aggregation of tetraaryl-substituted porphyrins in homogeneous solution. *J. Phys. Chem.* **100**, 5420–5425 (1996).

181. Ribó, J. M., Crusats, J., Farrera, J. A. & Valero, M. L. Aggregation in water solutions of tetrasodium diprotonated meso-tetrakis(4-sulfonatophenyl)porphyrin. *J. Chem. Soc. Chem. Commun.* **7**, 681–682 (1994).

182. Maiti, N. C., Ravikanth, M., Mazumdar, S. & Periasamy, N. Fluorescence dynamics of noncovalently linked porphyrin dimers and aggregates. *J. Phys. Chem.* **99**, 17192–17197 (1995).

183. Castriciano, M. A., Romeo, A., Zagami, R., Micali, N. & Scolaro, L. M. Kinetic effects of tartaric acid on the growth of chiral J-aggregates of tetrakis(4-sulfonatophenyl)porphyrin. *Chem. Commun.* **48**, 4872–4874 (2012).

184. Koti, A. S. R., Taneja, J. & Periasamy, N. Control of coherence length and aggregate size in the J-aggregate of porphyrin. *Chem. Phys. Lett.* **375**, 171–176 (2003).

185. Romeo, A. *et al.* Kinetic control of chirality in porphyrin J-aggregates. *J. Am. Chem. Soc.* **136**, 40–43 (2014).

186. Micali, N., Villari, V., Castriciano, M. A., Romeo, A. & Scolaro, L. M. From fractal to nanorod porphyrin J-aggregates. concentration-induced tuning of the aggregate size. *J. Phys. Chem. B* **110**, 8289–8295 (2006).

187. Zagami, R. *et al.* Tuning supramolecular chirality in nano and mesoscopic porphyrin J-aggregates. *Dye. Pigment.* **142**, 255–261 (2017).

188. Zhang, L. *et al.* Tetrakis(4-sulfonatophenyl)porphyrin-directed assembly of gold nanocrystals: Tailoring the plasmon coupling through controllable gap distances. *Small* **6**, 2001–2009 (2010).

189. Đorđević, L. *et al.* Design principles of chiral carbon nanodots help convey chirality from molecular to nanoscale level. *Nat. Commun.* **9**, 3442 (2018).

190. Magno, L. N. *et al.* Use of Spectroscopic Techniques for Evaluating the Coupling of Porphyrins on

References

Biocompatible Nanoparticles. A Potential System for Photodynamics, Theranostics, and Nanodrug Delivery Applications. *J. Phys. Chem. A* **121**, 1924–1931 (2017).

191. Fleischer, E. B. The Structure of Porphyrins and Metalloporphyrins. *Acc. Chem. Res.* **3**, 105–112 (1970).

192. P. Prasad. Nanophotonics. in 129–151 (Wiley-Interscience, 2004).

193. Siddhanta, S., Barman, I. & Narayana, C. Revealing the trehalose mediated inhibition of protein aggregation through lysozyme-silver nanoparticle interaction. *Soft Matter* **11**, 7241–7249 (2015).

194. Li, N. *et al.* Strong plasmon-exciton coupling in bimetallic nanorings and nanocuboids. *J. Mater. Chem. C* **8**, 7672–7678 (2020).

195. Eizner, E., Avayu, O., Ditcovski, R. & Ellenbogen, T. Aluminum Nanoantenna Complexes for Strong Coupling between Excitons and Localized Surface Plasmons. *Nano Lett.* **15**, 6215–6221 (2015).

196. Thomas, K. G. & Kamat, P. V. Chromophore-Functionalized Gold Nanoparticles. *Acc. Chem. Res.* **36**, 888–898 (2003).

197. Braun, S., Salaneck, W. R. & Fahlman, M. Energy-level alignment at organic/metal and organic/organic interfaces. *Adv. Mater.* **21**, 1450–1472 (2009).

198. Tanaka, D. *et al.* Strongest π-metal orbital coupling in a porphyrin/gold cluster system. *Chem. Sci.* **5**, 2007–2010 (2014).

199. Darby, B. L., Auguié, B., Meyer, M., Pantoja, A. E. & Le Ru, E. C. Modified optical absorption of molecules on metallic nanoparticles at sub-monolayer coverage. *Nat. Photonics* **10**, 40–45 (2016).

200. Yoshida, A., Uchida, N. & Kometani, N. Synthesis and spectroscopic studies of composite gold nanorods with a double-shell structure composed of spacer and cyanine dye J-aggregate layers. *Langmuir* **25**, 11802–11807 (2009).

201. Hazra, B. *et al.* Hollow gold nanoprism as highly efficient 'Single' Nanotransducer for surface-enhanced raman scattering applications. *J. Phys. Chem. C* **120**, 25548–25556 (2016).

202. Schneider, H. J., Schiestel, T. & Zimmermann, P. The Incremental Approach to Noncovalent Interactions: Coulomb and van der Waals Effects in Organic Ion Pairs. *J. Am. Chem. Soc.* **114**, 7698–7703 (1992).

203. Pieters, G., Cazzolaro, A., Bonomi, R. & Prins, L. J. Self-assembly and selective exchange of oligoanions on the surface of monolayer protected Au nanoparticles in water. *Chem. Commun.* **48**, 1916–1918 (2012).

204. Collini, E., Ferrante, C. & Bozio, R. Influence of excitonic interactions on the transient absorption and two-photon absorption spectra of porphyrin J-asgregates in the NIR region. *J. Phys. Chem. C* **111**, 18636–18645 (2007).

205. Jain, P. K., Qian, W. & El-Sayed, M. A. Ultrafast electron relaxation dynamics in coupled metal nanoparticles in aggregates. *J. Phys. Chem. B* **110**, 136–142 (2006).

206. Auguié, B. & Le Ru, E. C. Optical Absorption of Dye Molecules in a Spherical Shell Geometry. *J. Phys. Chem. C* **122**, 19110–19115 (2018).

207. Shabaninezhad, M. *et al.* Ultrafast Electron Dynamics in Thiolate-Protected Plasmonic Gold Clusters : Size and Ligand E ff ect. *J. Phys. Chem. C* **123**, 13344–13353 (2019).

208. Kumar, M., Dey, J., Verma, M. S. & Chandra, M. Nanoscale plasmon-exciton interaction: The role of radiation damping and mode-volume in determining coupling strength. *Nanoscale* **12**, 11612–11618 (2020).

209. Hendel, T., Krivenkov, V., Sánchez-Iglesias, A., Grzelczak, M. & Rakovich, Y. P. Strongly coupled exciton-plasmon nanohybrids reveal extraordinary resistance to harsh environmental stressors:

References

Temperature, pH and irradiation. *Nanoscale* **12**, 16875–16883 (2020).

210. Das, K., Dey, J., Verma, M. S., Kumar, M. & Chandra, M. Probing the role of oscillator strength and charge of exciton forming molecular J-aggregates in controlling nanoscale plasmon-exciton interactions. *Phys. Chem. Chem. Phys.* **22**, 20499–20506 (2020).

211. Yoshida, A., Yonezawa, Y. & Kometani, N. Tuning of the spectroscopic properties of composite nanoparticles by the insertion of a spacer layer: Effect of exciton-plasmon coupling. *Langmuir* **25**, 6683–6689 (2009).

212. Cao, E., Lin, W., Sun, M., Liang, W. & Song, Y. Exciton-plasmon coupling interactions: From principle to applications. *Nanophotonics* **7**, 145–167 (2018).

213. Kolaric, B., Maes, B., Clays, K., Durt, T. & Caudano, Y. Strong Light–Matter Coupling as a New Tool for Molecular and Material Engineering: Quantum Approach. *Adv. Quantum Technol.* **1**, 1800001 (2018).

214. Balci, F. M., Sarisozen, S., Polat, N. & Balci, S. Colloidal nanodisk shaped plexcitonic nanoparticles with large rabi splitting energies. *J. Phys. Chem. C* **123**, 26571–26576 (2019).

215. Melnikau, D., Savateeva, D., Susha, A., Rogach, A. L. & Rakovich, Y. P. Plasmon-exciton strong coupling in a hybrid system of gold nanostars and J-aggregates. *Nanoscale Res. Lett.* **8**, 2–7 (2013).

216. Melnikau, D. *et al.* Strong Magneto-Optical Response of Nonmagnetic Organic Materials Coupled to Plasmonic Nanostructures. *Nano Lett.* **17**, 1808–1813 (2017).

217. Balci, S. Ultrastrong plasmon–exciton coupling in metal nanoprisms with J-aggregates. *Opt. Lett.* **38**, 4498 (2013).

218. Ni, W., Yang, Z., Chen, H., Li, L. & Wang, J. Coupling between molecular and plasmonic resonances in freestanding dye-gold nanorod hybrid nanostructures. *J. Am. Chem. Soc.* **130**, 6692–6693 (2008).

219. Ni, W. *et al.* Effects of dyes, gold nanocrystals, pH, and metal ions on plasmonic and molecular resonance coupling. *J. Am. Chem. Soc.* **132**, 4806–4814 (2010).

220. Meera Mohankumar, Mahima Unnikrishnan, Gopal Narmada Naidu & Sanoop Mambully Somasundaran, Mavilakizhakke Puthiyaveetil Ajaykumar, Rotti Srinivasamurthy Swathi, and K. G. T. Finding the Needle in a Haystack: Capturing Veiled Plexcitonic Coupling through Di ff erential Spectroscopy. *J. Phys. Chem. C* **124**, 26387–26395 (2020).

221. Senthil Kumar, P., Pastoriza-Santos, I., Rodríguez-González, B., Javier García De Abajo, F. & Liz-Marzán, L. M. High-yield synthesis and optical response of gold nanostars. *Nanotechnology* **19**, (2008).

222. Krivenkov, V., Samokhvalov, P., Nabiev, I. & Rakovich, Y. P. pH-Sensing Platform Based on Light-Matter Coupling in Colloidal Complexes of Silver Nanoplates and J-Aggregates. *J. Phys. Chem. C* **3**, 1972–1979 (2021).

223. Yordanova, S., Petkov, I. & Stoyanov, S. Solvatochromism of homodimeric styryl pyridinium salts. *J. Chem. Technol. Metall.* **49**, 601–609 (2014).

224. Kirstein, S. & Daehne, S. J-aggregates of amphiphilic cyanine dyes: Self-organization of artificial light harvesting complexes. *Int. J. Photoenergy* **2006**, 1–21 (2006).

225. Kobayashi, T. *J-Aggregates. Volume 2.* (2012).

226. DeLacy, B. G. *et al.* Coherent Plasmon-Exciton Coupling in Silver Platelet-J-aggregate Nanocomposites. *Nano Lett.* **15**, 2588–2593 (2015).

227. Fales, A. M., Norton, S. J., Crawford, B. M., DeLacy, B. G. & Vo-Dinh, T. Fano resonance in a gold nanosphere with a J-aggregate coating. *Phys. Chem. Chem. Phys.* **17**, 24931–24936 (2015).

References

228. Nasr, C. & Hotchandani, S. Excited-state behavior of Nile Blue H-aggregates bound to SiO2 and SnO2 colloids. *Chem. Mater.* **12**, 1529–1535 (2000).

229. Patlolla, P. R., Mallajosyula, S. S. & Datta, B. Template-Free Self-Assembly of Dimeric Dicarbocyanine Dyes. *ChemistrySelect* **2**, 10709–10717 (2017).

230. Rodarte, A. L. & Tao, A. R. Plasmon-Exciton Coupling between Metallic Nanoparticles and Dye Monomers. *J. Phys. Chem. C* **121**, 3496–3502 (2017).

231. Xu, D. *et al.* Quantum plasmonics: new opportunity in fundamental and applied photonics. *Adv. Opt. photonics* **10**, 703–756 (2018).

232. Trügler, A. & Hohenester, U. Strong coupling between a metallic nanoparticle and a single molecule. *Phys. Rev. B - Condens. Matter Mater. Phys.* **77**, (2008).

233. Van Burgel, M., Wiersma, D. A. & Duppen, K. The dynamics of one-dimensional excitons in liquids. *J. Chem. Phys.* **102**, 20–33 (1995).

234. Lüer, L. *et al.* Lévy Defects in Matrix-Immobilized J-aggregates: Tracing Intra-and Intersegmental Exciton Relaxation. *J. Phys. Chem. Lett.* **8**, 547–552 (2017).

235. Lee, J. H., Min, C. K. & Joo, T. Ultrafast optical dynamics of excitons in J-aggregates. *J. Chem. Phys.* **114**, 377–381 (2001).

236. Minoshima, K., Taiji, M., Misawa, K. & Kobayashi, T. Femtosecond nonlinear optical dynamics of excitons in J-aggregates. *Chem. Phys. Lett.* **218**, 67–72 (1994).

237. Moll, J., Daehne, S., Durrant, J. R. & Wiersma, D. A. Optical dynamics of excitons in J-aggregates of a carbocyanine dye. *J. Chem. Phys.* **102**, 6362–6370 (1995).

238. Del Fatti, N., Arbouet, A. & Vallée, F. Femtosecond optical investigation of electron-lattice interactions in an ensemble and a single metal nanoparticle. *Appl. Phys. B Lasers Opt.* **84**, 175–181 (2006).

239. Jeffries, W. R., Park, K., Vaia, R. A. & Knappenberger, K. L. Resolving Electron-Electron Scattering in Plasmonic Nanorod Ensembles Using Two-Dimensional Electronic Spectroscopy. *Nano Lett.* **20**, 7722–7727 (2020).

240. Lietard, A., Hsieh, C. S., Rhee, H. & Cho, M. Electron heating and thermal relaxation of gold nanorods revealed by two-dimensional electronic spectroscopy. *Nat. Commun.* **9**, (2018).

241. Moody, G. & Cundiff, S. T. Advances in multi-dimensional coherent spectroscopy of semiconductor nanostructures. *Adv. Phys. X* **2**, 641–674 (2017).

242. Shacklette, J. M. & Cundiff, S. T. Role of excitation-induced shift in the coherent optical response of semiconductors. *Phys. Rev. B - Condens. Matter Mater. Phys.* **66**, 1–6 (2002).

243. Wang, W. *et al.* Interplay between strong coupling and radiative damping of excitons and surface plasmon polaritons in hybrid nanostructures. *ACS Nano* **8**, 1056–1064 (2014).

244. Collini, E. 2D Electronic Spectroscopies Towards Quantum Technology Applications. *J Phys Chem C* **accepted f**, (2021).

245. Kobayashi, T., Nishimura, K. & Tokunaga, E. Real-time spectroscopy of pseudoisocyanine J-aggregates with sub-5 fs lasers. *J. Mol. Struct.* **735**–**736**, 179–187 (2005).

246. Juhász, I. B. & Csurgay, Á. I. Impact of undamped and damped intramolecular vibrations on the efficiency of photosynthetic exciton energy transfer. *AIP Adv.* **8**, (2018).

247. Butkus, V., Valkunas, L. & Abramavicius, D. Vibronic phenomena and exciton-vibrational interference in two-dimensional spectra of molecular aggregates. *J. Chem. Phys.* **140**, (2014).

248. Guo, C., Aydin, M., Zhu, H. R. & Akins, D. L. Density functional theory used in structure determinations and Raman band assignments for pseudoisocyanine and its aggregate. *J. Phys.*

References

Chem. B **106**, 5447–5454 (2002).

249. Akins, D. L., Zhuang, Y. H., Zhu, H. R. & Liu, J. Q. Raman excitation spectra of exciton-phonon modes of aggregated 2,2-cyanine using an internal Raman standard. *J. Phys. Chem.* **98**, 1068–1072 (1994).

250. Wiederrecht, G. P., Hall, J. E. & Bouhelier, A. Control of molecular energy redistribution pathways via surface plasmon gating. *Phys. Rev. Lett.* **98**, 1–4 (2007).

251. Wurtz, G. A., Hranisavljevic, J. & Wiederrecht, G. P. Photo-initiated energy transfer in nanostructured complexes observed by near-field optical microscopy. *J. Microsc.* **210**, 340–343 (2003).

252. Guvenc, C. M., Balci, F. M., Sarisozen, S., Polat, N. & Balci, S. Colloidal Bimetallic Nanorings for Strong Plasmon Exciton Coupling. *J. Phys. Chem. C* **124**, 8334–8340 (2020).

253. Yoshida, A. & Kometani, N. Effect of the interaction between molecular exciton and localized surface plasmon on the spectroscopic properties of silver nanoparticles coated with cyanine dye J-aggregates. *J. Phys. Chem. C* **114**, 2867–2872 (2010).

254. Juluri, B. K., Lu, M., Zheng, Y. B., Huang, T. J. & Jensen, L. Coupling between molecular and plasmonic resonances: Effect of molecular absorbance. *J. Phys. Chem. C* **113**, 18499–18503 (2009).

255. Djoumessi Lekeufack, D. *et al.* Core-shell gold J-aggregate nanoparticles for highly efficient strong coupling applications. *Appl. Phys. Lett.* **96**, 1–3 (2010).

256. Hao, Y. W. *et al.* Hybrid-state dynamics of gold nanorods/dye J-aggregates under strong coupling. *Angew. Chemie - Int. Ed.* **50**, 7824–7828 (2011).

257. Liu, R. *et al.* Strong Light-Matter Interactions in Single Open Plasmonic Nanocavities at the Quantum Optics Limit. *Phys. Rev. Lett.* **118**, 1–6 (2017).

258. Kirschner, M. S. *et al.* Phonon-Driven Oscillatory Plasmonic Excitonic Nanomaterials. *Nano Lett.* **18**, 442–448 (2018).

259. Song, T. *et al.* Compounding plasmon-exciton strong coupling system with gold nanofilm to boost rabi splitting. *Nanomaterials* **9**, 1–10 (2019).

260. Kirschner, M. S. *et al.* Phonon-induced plasmon-exciton coupling changes probed via oscillation-associated spectra. *Appl. Phys. Lett.* **115**, (2019).

261. Kirschner, M. S., Lin, X. M., Chen, L. X. & Schaller, R. D. Phase control of coherent acoustic phonons in gold bipyramids for optical memory and manipulating plasmon-exciton coupling. *Appl. Phys. Lett.* **116**, (2020).

262. Stete, F., Bargheer, M. & Koopman, W. Optical non-linearities in plasmon-exciton core-shell particles: The role of heat. *arXiv* 1–7 (2020).

263. Itoh, T., Hashimoto, K., Ikehata, A. & Ozaki, Y. Direct demonstration for changes in surface plasmon resonance induced by surface-enhanced Raman scattering quenching of dye molecules adsorbed on single Ag nanoparticles. *Appl. Phys. Lett.* **83**, 5557–5559 (2003).

264. Uwada, T., Toyota, R., Masuhara, H. & Asahi, T. Single particle spectroscopic investigation on the interaction between exciton transition of cyanine dye J-aggregates and localized surface plasmon polarization of gold nanoparticles. *J. Phys. Chem. C* **111**, 1549–1552 (2007).

265. Ni, W., Ambjörnsson, T., Apell, S. P., Chen, H. & Wang, J. Observing plasmonic-molecular resonance coupling on single gold nanorods. *Nano Lett.* **10**, 77–84 (2010).

266. Zengin, G. *et al.* Approaching the strong coupling limit in single plasmonic nanorods interacting with J-aggregates. *Sci. Rep.* **3**, 1–8 (2013).

267. Itoh, T. *et al.* Single-molecular surface-enhanced resonance Raman scattering as a quantitative

References

probe of local electromagnetic field: The case of strong coupling between plasmonic and excitonic resonance. *Phys. Rev. B - Condens. Matter Mater. Phys.* **89**, 1–8 (2014).

268. Zengin, G. *et al.* Realizing strong light-matter interactions between single-nanoparticle plasmons and molecular excitons at ambient conditions. *Phys. Rev. Lett.* **114**, 1–6 (2015).

269. Roller, E. M., Argyropoulos, C., Högele, A., Liedl, T. & Pilo-Pais, M. Plasmon-Exciton Coupling Using DNA Templates. *Nano Lett.* **16**, 5962–5966 (2016).

270. Stete, F., Schoßau, P., Bargheer, M. & Koopman, W. Size-Dependent Coupling of Hybrid Core-Shell Nanorods: Toward Single-Emitter Strong-Coupling. *J. Phys. Chem. C* **122**, 17976–17982 (2018).

271. Daniel, M. C. & Astruc, D. Gold Nanoparticles: Assembly, Supramolecular Chemistry, Quantum-Size-Related Properties, and Applications Toward Biology, Catalysis, and Nanotechnology. *Chem. Rev.* **104**, 293–346 (2004).

272. Gómez-Graña, S. *et al.* Surfactant (Bi) layers on gold nanorods. *Langmuir* **28**, 1453–1459 (2012).

273. Dovzhenko, D. S., Ryabchuk, S. V., Rakovich, Y. P. & Nabiev, I. R. Light-matter interaction in the strong coupling regime: Configurations, conditions, and applications. *Nanoscale* **10**, 3589–3605 (2018).

Appendixes

Appendixes

A. Additional experimental results

i. Calculation of the H_2TPPS^{2-} configuration on BNSs surface
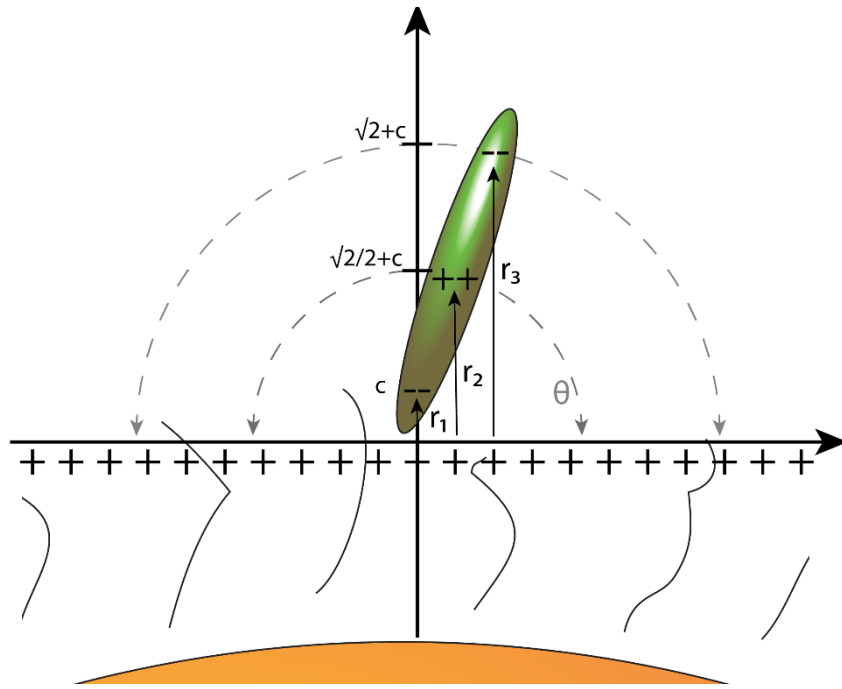
Figure A1. 2D representation of a H_2TPPS^{2-} molecule on a BNS surface. The y and x axes indicate the distance expressed in nm to the point of contact between the two nanoobjects.

H_2-$TPPS^{2-}$ geometry can be approximated as a square with side of √2 nm, bearing four negative charges at the corner and two positive charges in the centre.[191] Since the SNSs and BNSs diameters are at least twice the H_2-$TPPS^{2-}$ length, their interaction with H_2-$TPPS^{2-}$ can be approximated as the interaction of a plane with a homogeneous charge density (figure A1). Considering a H_2-$TPPS^{2-}$ grafted to the BNS surface with two negatively charged sulphate groups, simply trigonometrical considerations allow to calculate the distances between the surface and the charges as:

$$r_1 = c \tag{A1}$$

$$r_2 = \frac{\sqrt{2}}{2}\operatorname{sen}(\theta) + c \tag{A2}$$

$$r_3 = \sqrt{2}\operatorname{sen}(\theta) + c \tag{A3}$$

with c the distance between the TMAOt cationic layer and the sulfonate groups, which is sum of their van der Waals radii. Let us define V as the electric potential of a plane with a homogeneous charge density proportional to the opposite of the distance from it. The general formula for the electric potential energy is:

$$U_e = \frac{1}{2}qV; \qquad \text{(A4)}$$

with q the value of the electric charge. Thus, U_e can be calculated as:

$$U_e \propto \frac{1}{2}\left(-2qr_1 + 2qr_2\right). \qquad \text{(A5)}$$

The first term between brackets is the contribution of the protonated pyrrolic groups, while the second term is the contribution of the sulfonate groups. Substituting equations (A1) and (A2) in equation (A5), it follows that:

$$U_e \propto sen(\theta). \qquad \text{(A6)}$$

From these considerations it follows that the minimum of H_2-TPPS^{2-} potential energy is reached when the porphyrin is parallel to NSs surface, while its maximum corresponds to the perpendicular orientation.

ii.   Fitting results of the TA experiments performed on NS-TPPS nanohybrids and NSA

Table A1. $\tau_{e\text{-}e}$, $\tau_{e\text{-}ph}$ and $\tau_{ph\text{-}env}$ retrieved by RDD fitting model in the analysis of NSA, NS-TPPS_100 (reported in the table as "100") and NS-TPPS_1040 (reported in the table as "1040") for different pump fluences and probe wavelengths. For each time constant, the first column reports the wavelength of the probe in nm. Then, for each sample, the time costant value and the error retrieved by the global fitting of three different dynamics at close wavelengths are reported in ps. NSA fluences are slightly different (165 and 470 µJ/cm^2), but comparable with the one used for the nanohybrids. To ease the comparison, we reported the NSA data at the same fluences of NS-TPPS_100 and NS-TPPS_1040.

Pump fluence 734 uJ/cm^2												
Probe λ	$\tau_{e\text{-}e}$					$\tau_{e\text{-}ph}$					$\tau_{ph\text{-}env}$			
	NSA	**100**		**1040**		**NSA**	**100**		**1040**		**NSA**	**100**		**1040**	
520		0.220	0.007	0.290	0.010		2.87	0.04	2.70	0.04		116	10		
530		0.22	0.01	0.240	0.007		2.66	0.03	2.57	0.03		168	16	87	15
540		0.213	0.006	0.223	0.006		2.44	0.02	2.40	0.02		258	27	154	21
550		0.211	0.006	0.176	0.006		2.19	0.02	2.22	0.02		427	49	273	43
560		0.159	0.006				1.96	0.02				605	141	248	69
570															
580															
590															

Pump fluence 530 uJ/cm^2

Probe λ	$\tau_{e\text{-}e}$ NSA		$\tau_{e\text{-}e}$ 100		$\tau_{e\text{-}e}$ 1040		$\tau_{e\text{-}ph}$ NSA		$\tau_{e\text{-}ph}$ 100		$\tau_{e\text{-}ph}$ 1040		$\tau_{ph\text{-}env}$ NSA		$\tau_{ph\text{-}env}$ 100		$\tau_{ph\text{-}env}$ 1040	
520			0.283	0.008					2.27	0.03					73	5		
530			0.269	0.006	0.312	0.009			2.21	0.02	2.24	0.03			145	14	86	11
540			0.217	0.005	0.266	0.006			2.08	0.02	2.13	0.02			297	28	162	17
550			0.200	0.006	0.202	0.006			1.89	0.02	2.01	0.02			491	66	219	27
560			0.183	0.006	0.202	0.006			1.63	0.02	1.83	0.02			844	208	270	43
570																		
580																		
590																		

Pump fluence 414 uJ/cm^2

Probe λ	$\tau_{e\text{-}e}$ NSA		$\tau_{e\text{-}e}$ 100		$\tau_{e\text{-}e}$ 1040		$\tau_{e\text{-}ph}$ NSA		$\tau_{e\text{-}ph}$ 100		$\tau_{e\text{-}ph}$ 1040		$\tau_{ph\text{-}env}$ NSA		$\tau_{ph\text{-}env}$ 100		$\tau_{ph\text{-}env}$ 1040	
520	0.181	0.008	0.337	0.014			3.20	0.08	2.02	0.04			77	5	68	6		
530	0.180	0.005	0.301	0.009			3.72	0.05	1.93	0.03			128	15	110	10		
540	0.203	0.006	0.240	0.008	0.290	0.007	3.56	0.05	1.86	0.02	1.89	0.02	181	28	190	23	107	13
550	0.195	0.007	0.247	0.009	0.226	0.006	3.26	0.04	1.68	0.03	1.78	0.02	410	166	286	40	99	16
560	0.197	0.009	0.239	0.012	0.199	0.005	3.00	0.04	1.47	0.03	1.63	0.02			505	96	689	158
570	0.226	0.011					2.72	0.05										
580	0.18	0.02					2.22	0.05										
590	0.19	0.03					1.65	0.07										

Pump fluence 330 uJ/cm^2

Probe λ	$\tau_{e\text{-}e}$ NSA		$\tau_{e\text{-}e}$ 100		$\tau_{e\text{-}e}$ 1040		$\tau_{e\text{-}ph}$ NSA		$\tau_{e\text{-}ph}$ 100		$\tau_{e\text{-}ph}$ 1040		$\tau_{ph\text{-}env}$ NSA		$\tau_{ph\text{-}env}$ 100		$\tau_{ph\text{-}env}$ 1040	
520			0.365	0.015					1.88	0.04					68	6		
530			0.299	0.008	0.343	0.012			1.83	0.02	1.70	0.03			94	9	51	8
540			0.236	0.008	0.294	0.008			1.77	0.02	1.62	0.02			203	26	75	9
550			0.252	0.009	0.214	0.006			1.57	0.02	1.59	0.02			271	37	179	24
560			0.168	0.009	0.223	0.007			1.43	0.02	1.43	0.02			685	151	203	40
570																		
580																		
590																		

Probe λ	τ_{e-e} NSA		τ_{e-e} 100		τ_{e-e} 1040		τ_{e-ph} NSA		τ_{e-ph} 100		τ_{e-ph} 1040		τ_{ph-env} NSA		τ_{ph-env} 100		τ_{ph-env} 1040	
520	0.278	0.015	0.49	0.03			2.66	0.07	1.24	0.04			156	23	56	6		
530	0.289	0.010	0.35	0.02	0.47	0.03	2.59	0.04	1.26	0.03	1.21	0.03	143	20	73	9	66	14
540	0.248	0.009	0.257	0.014	0.307	0.013	2.50	0.03	1.25	0.03	1.24	0.02	314	93	115	23	331	48
550	0.249	0.008	0.167	0.014	0.248	0.013	2.22	0.03	1.217	0.034	1.17	0.02			164	51	177	33
560	0.179	0.011	0.15	0.02	0.156	0.013	2.14	0.03	1.05	0.04	1.08	0.03			382	307	42	16
570	0.21	0.02					1.73	0.04										
580	0.17	0.03					1.31	0.07										
590																		

Appendixes

Table A2. τ_{e-e}, τ_{e-ph}, $\tau_{plex,1}$ and $\tau_{plex,2}$ retrieved by RD+D fitting model in the analysis of NS-TPPS_1040 at different pump fluences in the region of UR_B. For each time constant, the first column reports the fluence in $\mu J/cm^2$. Then, for each sample, the time constant value and the error retrieved by the global fitting of five different dynamics at close wavelengths are reported in ps.

UR_B							
Fluence	τ_{e-e}	τ_{e-ph}		$\tau_{plex,1}$		$\tau_{plex,2}$	
734	0.5	2.35	0.08	28	5	534	52
530	0.6	1.69	0.02	25	4	353	15
414	0.5	2.06	0.08	18	6	142	23
173	0.3	1.42	0.08	15	8	149	17

Table A3. τ_{e-e}, τ_{e-ph}, τ_{plex} retrieved by RD+D fitting model in the analysis of NS-TPPS_100 and NS-TPPS_1040 at different pump fluences in the region of LR_Q. For each time constant, the first column reports the fluence in $\mu J/cm^2$. Then, for each sample, the time constant value and the error retrieved by the global fitting of five different dynamics at close wavelengths are reported in ps.

LR_Q												
Fluence	τ_{e-e}				τ_{e-ph}				τ_{plex}			
	NS-TPPS_100		NS-TPPS_1040		NS-TPPS_100		NS-TPPS_1040		NS-TPPS_100		NS-TPPS_1040	
734	0.34	0.03	0.30	0.07	2.94	0.10	2.8	0.2	507	56	712	29
530	0.29	0.02	0.32	0.07	2.43	0.09	1.97	0.14	524	67	715	34
414	0.20	0.03			2.07	0.09	1.97	0.14	388	35	493	19
330	0.64	0.20			1.7	0.2	1.47	0.14	131	64	322	19
173	0.77	0.52			1.2	0.3	1.6	0.2	151	21	363	32

iii.   Further 2DES analysis

Figure A2. 2DES rephasing maps of a) TDBC-Jaggregates, b) NUs, c) nanohybrid **1**, d) nanohybrid **2** at selected values of t_2, indicated at the bottom right of each panel.

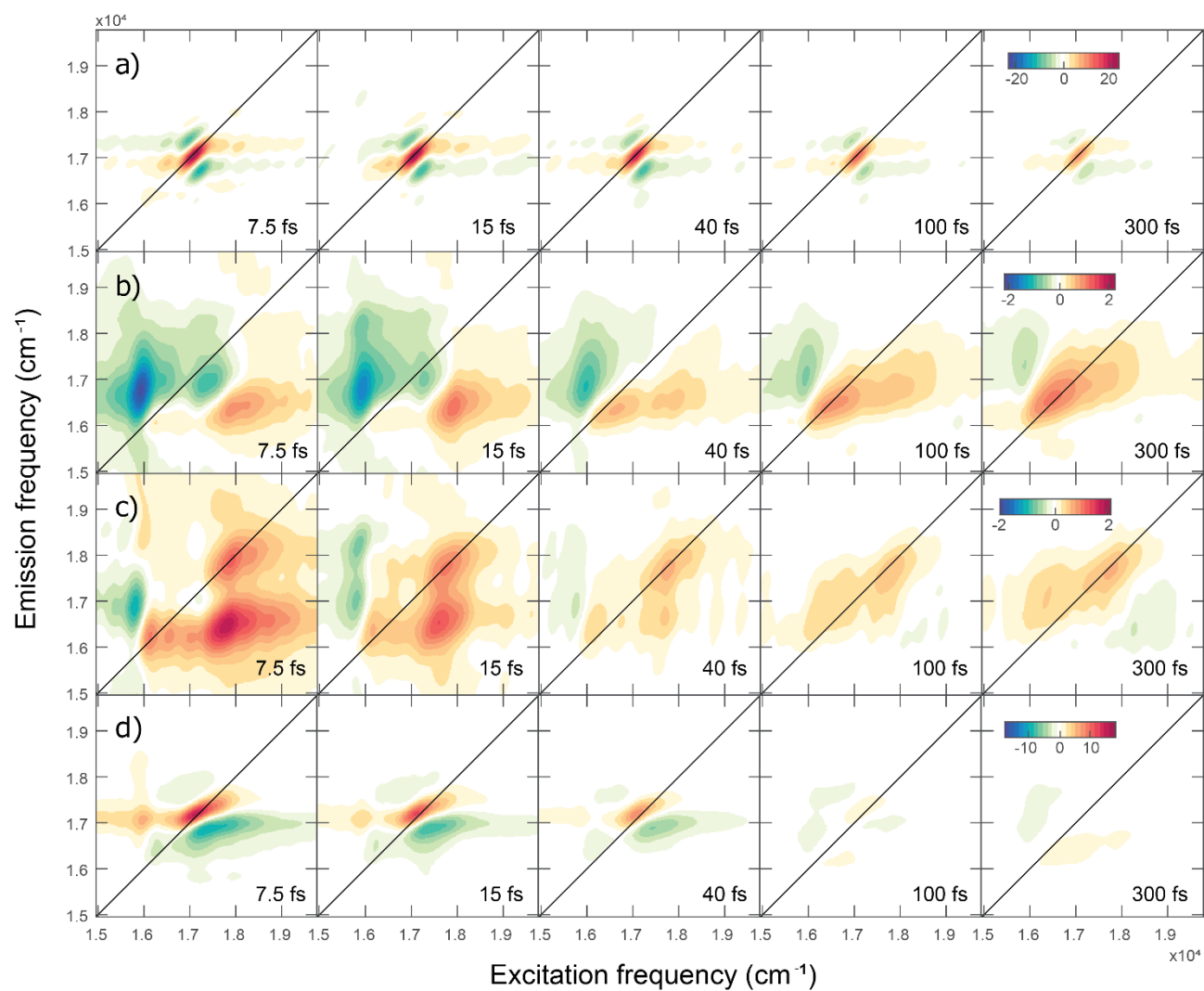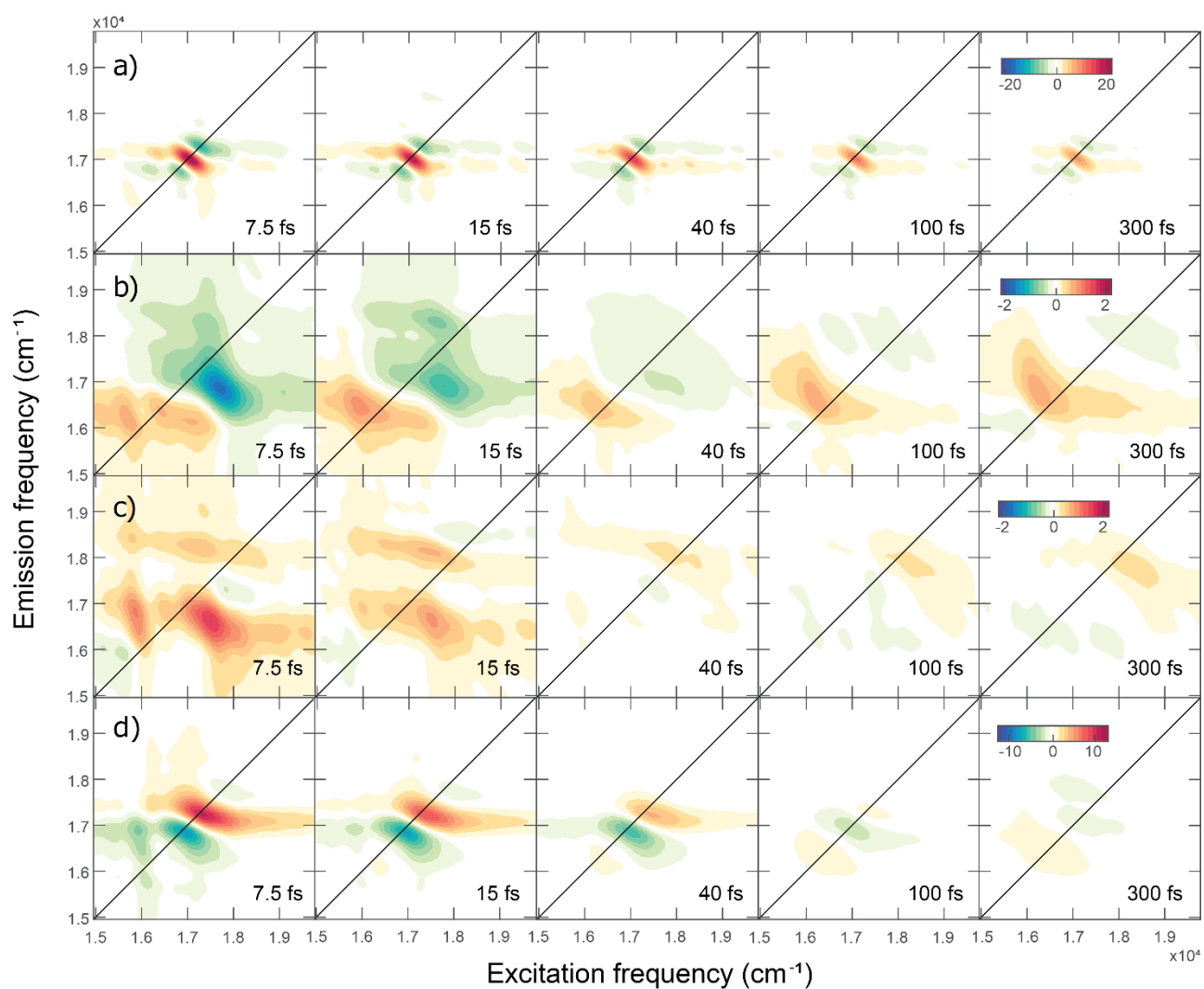Figure A3. 2DES non rephasing maps of a) TDBC-J-aggregates, b) NUs, c) nanohybrid **1**, d) nanohybrid **2** at selected values of t$_2$, indicated at the bottom right of each panel.

Figure A4. FROG measurement obtained at the sample position in a 1mm cuvette filled with dimethyl sulfoxide performed with the exciting laser profile of figure 15.1c. The laser pulse duration is estimated to be 10 fs.
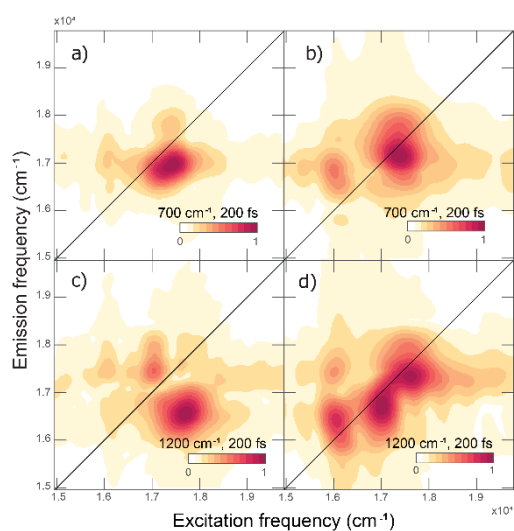
Figure A5. CAS associated with the vibrational mode at a)-b) 700 cm^{-1} and c)-d) 1200 cm^{-1}. Rephasing CAS are reported on the left, non rephasing CAS on the right.
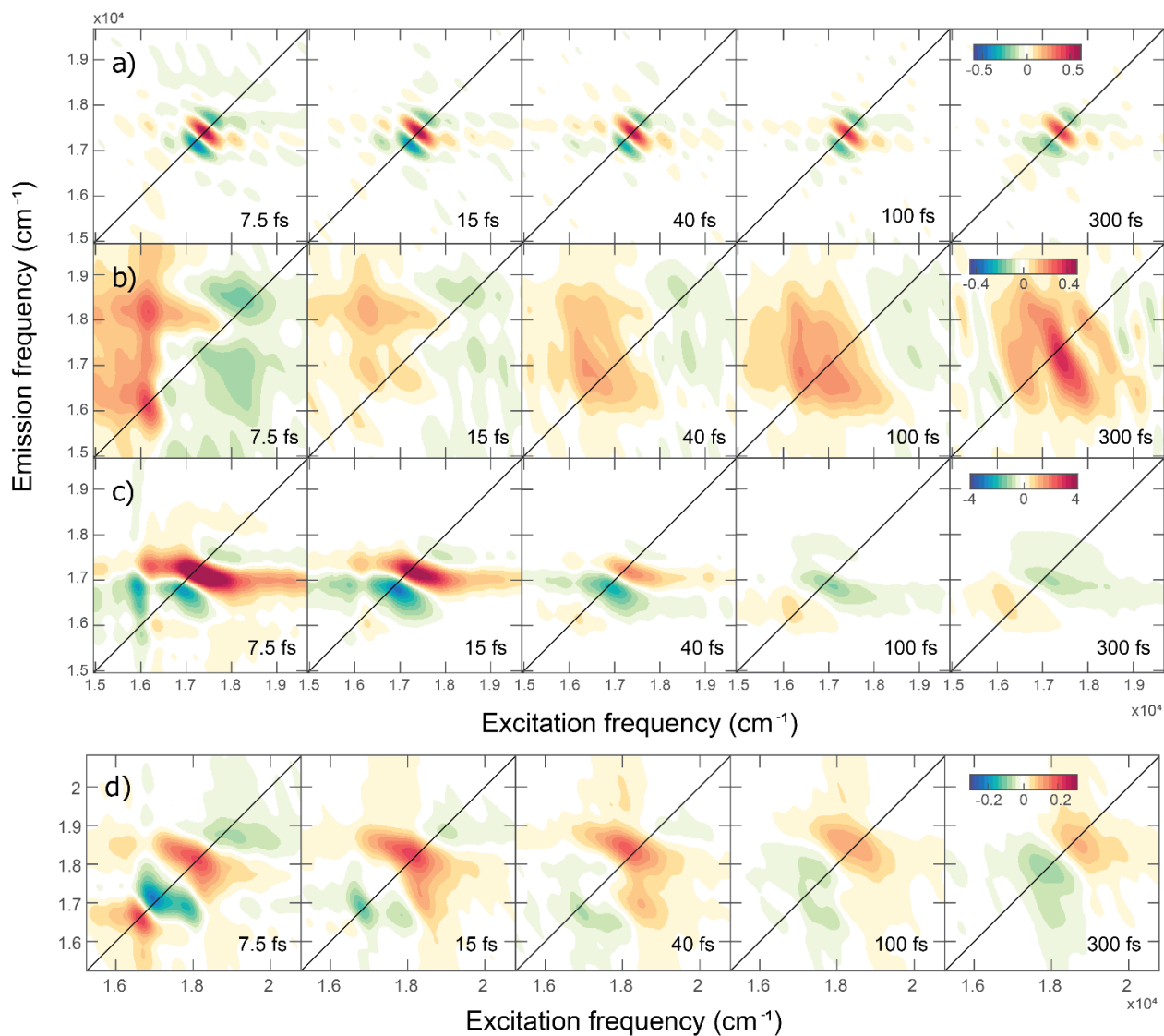
Figure A6. 2DES non rephasing maps of a) PIC-J, b) NUs, c) the nanohybrid, d) the PIC molecules non aggregated at selected values of t$_2$, indicated at the bottom right of each panel.

Figure A7. 2DESpure absorptive maps of a) PIC-J, b) NUs, c) the nanohybrid, d) the PIC molecules non aggregated at selected values of t_2, indicated at the bottom right of each panel.
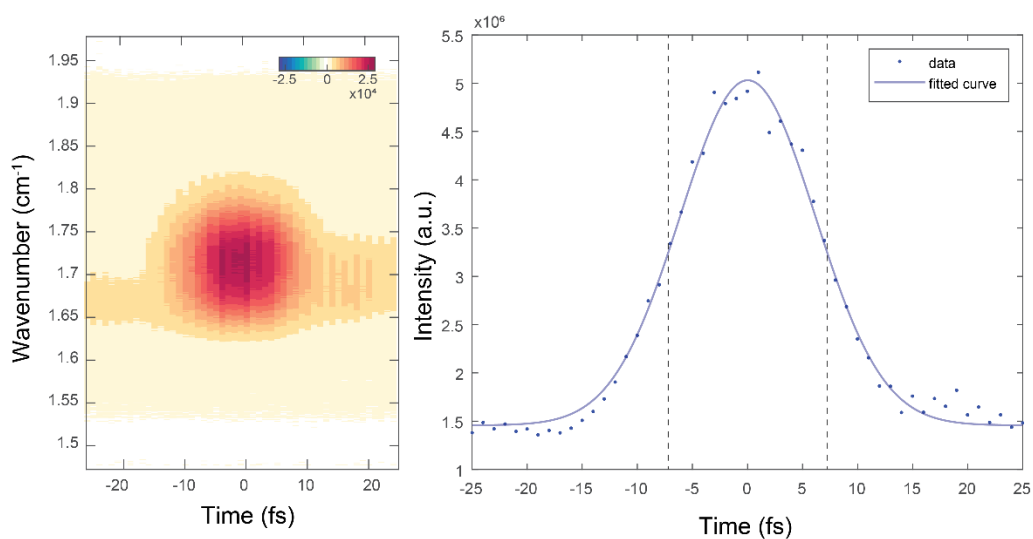
Figure A8. FROG measurement obtained at the sample position in a 1mm cuvette filled with dimethyl sulfoxide performed with the exciting laser profile of figure 16.1c and figure 16.1d. The laser pulse duration is estimated to be 10 fs and 13.4 fs, respectively.
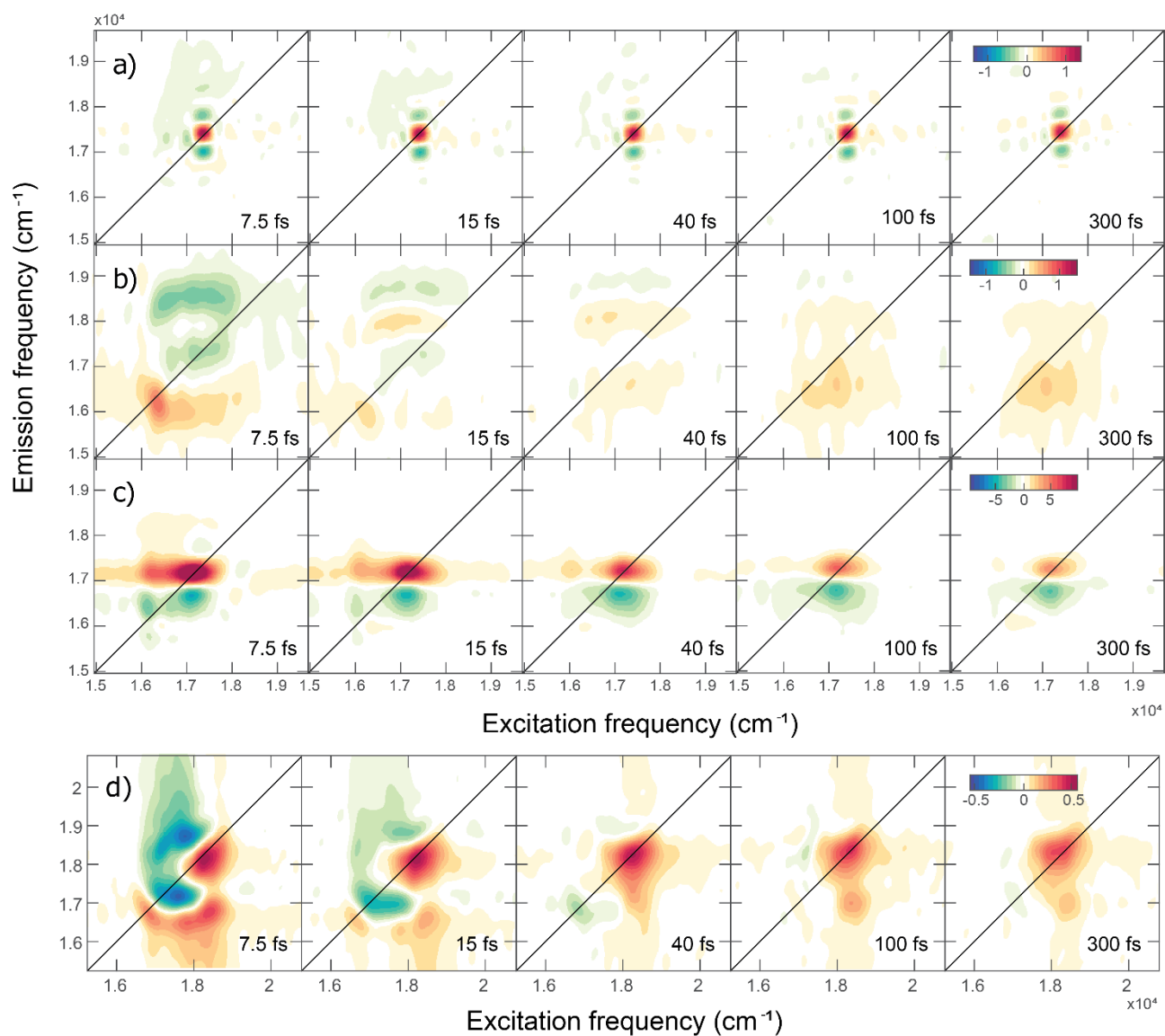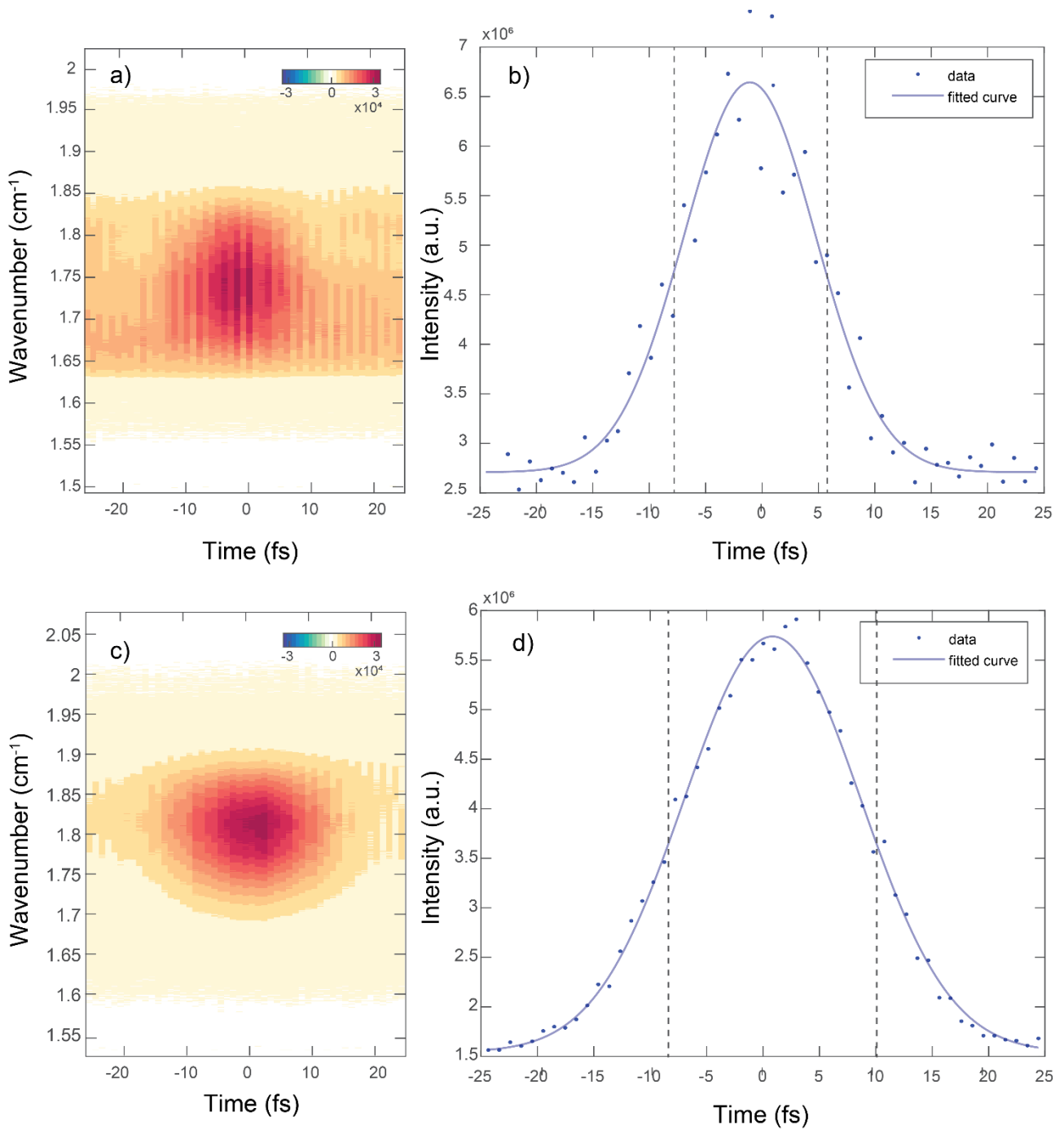
B. Additional information on the contents of part IV

Table B.1: List of all the QEs with their full names.

QEs acronym	QEs full name
TC	3,3'-Disulfopropyl-5,5'-dichlorothiacyanine sodium salt
AF488	Alexa Fluor 488 tetrafluorophenyl
Cc	Citocrome C
CV	Cresyl Violet 640
Cy	3,3'-diethylthiacyanine iodide
Cy5	1,3,3-trimethyl-2- [5-(1, 3, 3-trimethyl-1,3-dihydro-indol-2-ylidene)-penta-1,3- dienyl]-3H-indolium chloride
Cy75	5-Chloro-2-[3-[5-chloro-3-(4-sulfobutyl)-3H-benzothiazol-2-ylidene]-propenyl]-3-(4-sulfobutyl)-benzothiazol-3-ium hydroxide
DBTC	2,2'-dimethyl-8-phenyl-5,6,5',6'-dibenzothiacarbocyaninechloride
DOTCI	3,3' -diethyloxatricarbocyanine iodide
Em	Emoglobine
FITC	fluorescein isothiocyanate
HITC	1,1',3,3,3',3'-hexamethylindotricarbocyanine perchlorate
IR806	2-[2-[2-chloro-3-[2-[1,3-dihydro-3,3-dimethyl-1-(4-sulfobutyl)-2H-indol-2-ylidene]-ethylidene]-1-cyclopenten-1-yl]-ethenyl]-3,3-dimethyl-1-(4-sulfobutyl)-3H-indolium hydroxide, inner salt sodium salt
JC1	5,50,6,60-tetrachloro-1,10,3,30-tetraethyl-imidacarbocyanine iodide
MB	Methylene Blue
MG	Malachite green
O720	Oxazine 720
O725	Oxazine 725
OC	3,3'-disulfopropyl-5,5'- dichlorooxacyanine triethylammonium salt
PIC	1,1'-diethyl-2,2'-cyanine
R640	Rhodamine 640
R6G	Rhodamine 6G
S2165	2-[3-[1,1-dimethyl-3-(4- sulfobutyl)-1,3-dihydro-benzo[e]indol-2-ylidene]-propenyl]-1, 1-dimethyl-3-(4-sulfobutyl)-1H-benzo[e]indolium hydroxide
S9	2-([3-(2-[4-(Dimethylamino)phenyl]ethenyl)-5,5-dimethyl-2-cyclohexen-1-ylidene]methyl)-3-methylbenzothiazolium perchlorate, 2-[[3-[2-[4-(Dimethylamino)phenyl]ethenyl]-5,5-dimethyl-2-cyclohexen-1-ylidene]methyl]-3-methylbenzothiazolium perchlorate
SO-PIC	1,1'-sulphonatedipropyl-2,2'-cyanine
SQ	2,4-bis[(1-ethyl-3,3-dimethyl-2,3-dihydroindol-2-ylidene)- methyl]squaraine dye
TC(Et)	5,5'-dichloro-3,3'-disulfopropyl-9- ethylthiacarbocyanine triethylamine
TC(Et)'	5-Phenyl-2-[2-[[5-phenyl-3-(4- sulfobutyl)-3H-benzoxazol-2-ylidene]-methyl]-but-1-enyl]-3-(4-sulfobutyl)- benzoxazolium hydroxide
TC(Ph)	3,3'-disulfopropyl-5,5'-dichloro-9-phenylthiacarbocyanine triethylammonium salt
TDBC	5,5',6,6'-tetrachloro-1-1'-diethyl-3,3'-di(4-sulfobutyl)-benzimidazolocarbocyanine
TPPS	Tetraphenyl porphyrin sulphonate

Table B.2: List of all the CL molecules with their full names.

CL molecules acronym	CL molecules full name
BH₄⁺	
THCP	Tetrakis(hydroxymethyl)phosphonium chloride
3-mercaptopropionic acid	
AHDT	16-amino-1- hexadecanethiol hydrochloride
APT	6-amino-1-hexanethiol hydrochloride
AUT	11-amino- 1-undecanethiol hydrochloride
Cisteine	
Citrate	
Cl⁻	
CPC	hexadecylpyridinium chloride monohydrate
CTAB	Hexadecyl trimethyl ammonium bromide
CTAC	Hexadecyl trimethyl ammonium chloride
DBAC	Benzyldimethylhexadecylammonium chloride
DNA origami	
Mercaptoetansulphonate	
MUA	11-mercaptoundecanoic acid
PAH	Poly allylamine hydrochloride
PEG-S	Polyethilenglicole sulphur
PEI	Polyethileneimine
PSS	Sodium 4-styrenesulfonate
PVP	Polyvinilpirrolidone
PVSA	Polyvinylsulfonic acid
SOt	1-sulphonate octyl thiol
Thiocoline	
TMAOt	1-trimethyl ammonium octyl thiol
TMAUt	1-trimethyl ammonium undecyl thiol

Table B.3: Numbers and percentages quantifying the data about plexcitonic samples.

NPs material				
	CPM-s	%	CPM-d	%
Au	46	67	12	40
Ag	10	14	14	47
Au-Ag	13	19	4	13
Sum	69	100	30	100

NPs shape				
	CPM-s	%	CPM-d	%
Spheres	17	25	0	0
Shells	3	4	15	50
Rods	26	38	6	20
Prisms	1	1	4	13
Stars	7	10	4	13
Platelets	2	3	1	3
Cubes	3	4	0	0
Rings	7	10	0	0
Disks	2	3	0	0
Bipiramids	1	1	0	0
Sum	69	100	30	100

CL classes				
	CPM-s	%	CPM-d	%
Weak CL	16	24	10	36
Thiols	15	22	9	32
Polymers	21	31	3	11
Molecules	15	22	6	21
Sum	67	100	28	100

CL native or exchanged				
	CPM-s	%	CPM-d	%
Native	33	47.83	15	50
Exchanged	36	52.17	15	50
Sum	69	100	30	100

CL interactions				
	CPM-s	%	CPM-d	%
(i)	17	25	15	50
(ii)	0	0	6	20
(iii)	39	57	9	30
(iv)	6	9	0	0
(iii)+(iv)	7	10	0	0
Sum	69	100	30	100

QEs				
CPM-s	**%**		**CPM-d**	**%**
TC	6	8	TC	3	10
TC(Et)	3	4	HITC	1	3
DBTC	5	7	Cc	2	7
HITC	2	3	R6G	2	7
TDBC	13	18	TDBC	13	43
JC1	8	11	Em	1	3
S2165	2	3	AF488	4	13
PIC	10	14	PIC	4	13
TPPS	2	3		
Others	20	28		
Sum	71	100		30	100

QEs families				
CPM-s	**%**		**CPM-d**	**%**
Cyanine	53	77	20	67
Carbocyanine	5	7	1	3
Protein	1	1	2	7
Rhodamine	2	3	2	7
Nile blue-like	4	6	0	0
Triarylmethanes	1	1	0	0
Squaraine	1	1	0	0
Porphyrin	2	3	1	3
Alexafluor488			4	13
Sum	69	100	30	100

QEs aggregation state				
CPM-s	**%**		**CPM-d**	**%**
J-aggregates	51	75	20	67
Monomeric dyes	17	25	10	33
Sum	68	100	30	100

Table B.4: Average Rabi splitting energies ($\hbar\Omega_R$) and coupling strength energies ($\hbar g$) and their standard error (σ_{Ω_R} and σ_g, respectively). All the values are reported in meV.

NPs material			
$\hbar\overline{\Omega_R}$	σ_{Ω_R}	$\overline{\hbar g}$	σ_g
Ag	298	114	178	71
Au	189	93	123	50
Au-Ag	204	44	124	23

NPs shape			
$\hbar\overline{\Omega_R}$	σ_{Ω_R}	$\overline{\hbar g}$	σ_g
Cubes	189	77	120	36
Prism	318	102	184	50
Rings	212	53	134	25
Rods	204	74	118	44
Sphere	222	115	145	72

CL Macro areas			
$\overline{\hbar\Omega_R}$	σ_{Ω_R}	$\overline{\hbar g}$	σ_g
Weak CL	260	125	156	57
Thiol	214	130	133	60
Molecule	198	55	116	27
Polymer	194	42	127	26

CL native or exchanged			
$\hbar\overline{\Omega_R}$	σ_{Ω_R}	$\hbar\bar{g}$	σ_g
Native	217	90	134	52
Exchanged	219	116	143	65

Interaction			
$\hbar\overline{\Omega_R}$	σ_{Ω_R}	$\overline{\hbar g}$	σ_g
Strong	256	137	153	65
Weak	200	81	125	46
Covalent	383	198	202	92
Dye-metal	236	118	144	58
Electrostatic	202	87	127	50
Segregation	196	58	113	28

QEs molecules			
$\overline{\hbar\Omega_R}$	σ_{Ω_R}	$\hbar\bar{g}$	σ_g
JC1	207	58	113	28
PIC	171	48	119	28
TDBC	224	90	138	53
All others J agg	167	92	123	52

QEs Aggregation form				
	$\hbar\overline{\Omega_R}$	σ_{Ω_R}	$\hbar\bar{g}$	σ_g
Monomeric Dye	308	156	165	79
J-aggregate	206	90	132	51

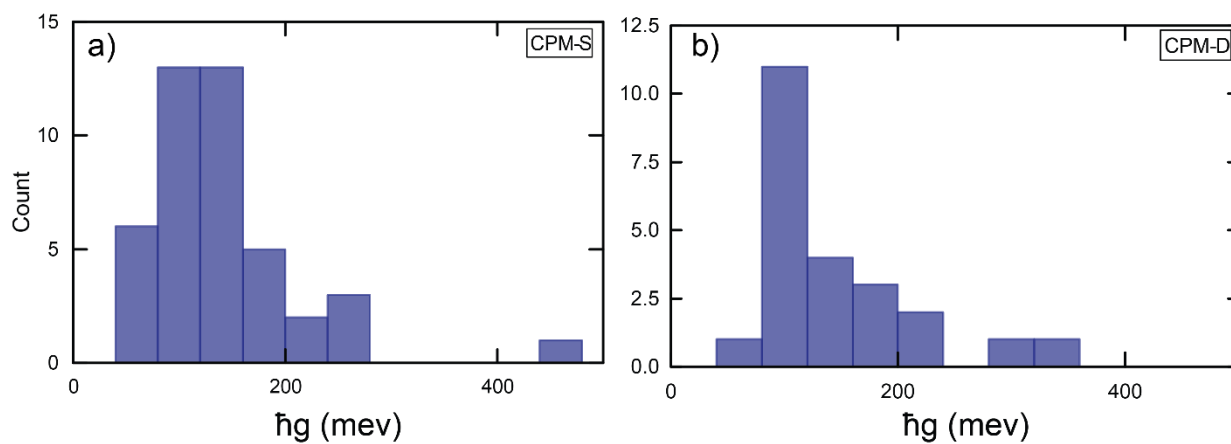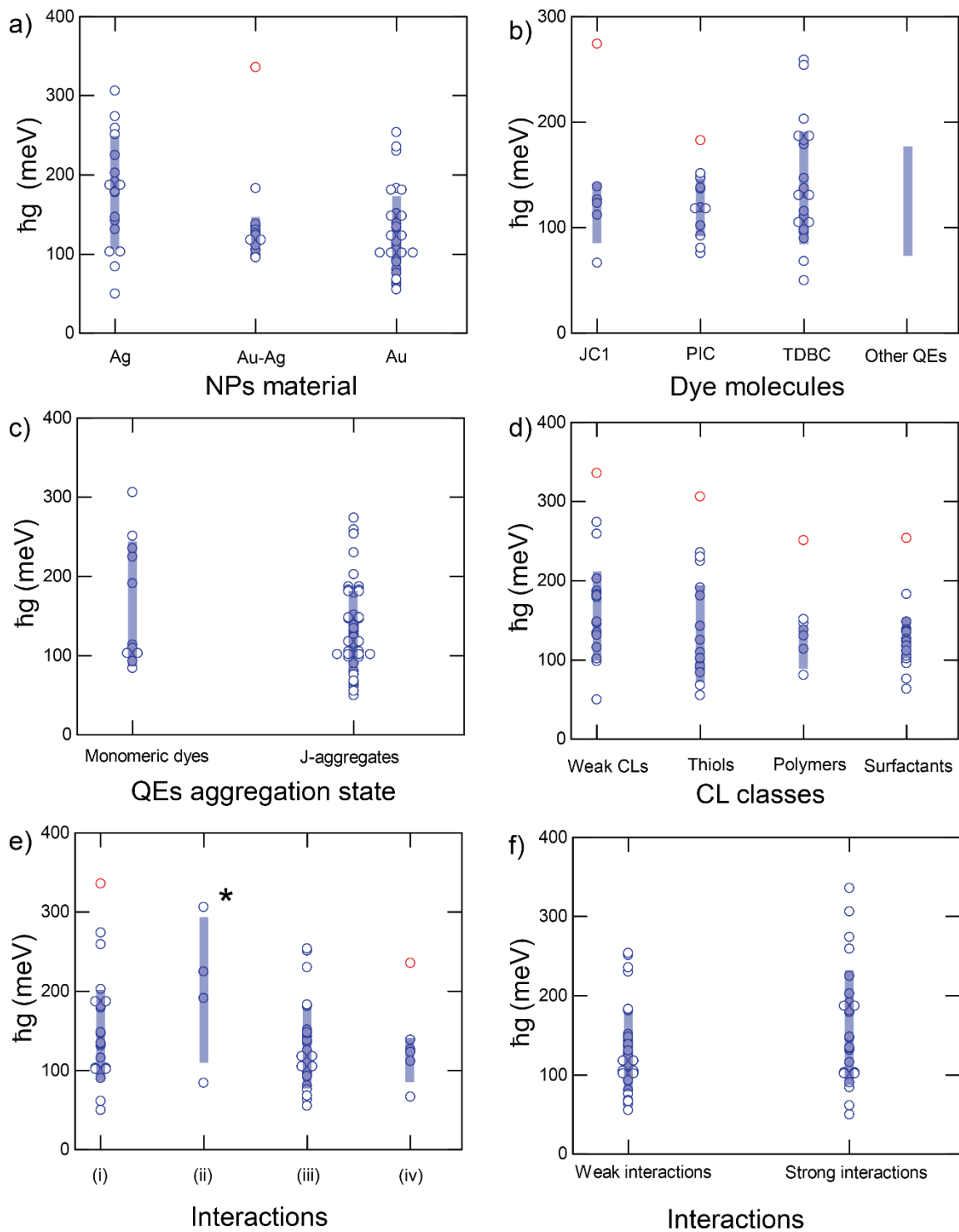
Figure B.1: (a) and (b) histograms of the $\hbar g$ values for CPM-s and CPM-d, respectively.

Figure B.2. Distribution plots correlating ℏg with different classes of CPMs: a) NPs materials, b) dye molecules, c) QEs aggregation state, d) CL classes, e) and f) nature of the interactions. The blue areas represent $\overline{ℏg} \pm \sigma_g$ intervals, while dots are the values for the single CPMs. Red dots were considered outlier and excluded from the calculation of the average values. In panel e), the covalent interaction is labelled with a star to underline its low statistic.

Appendixes

Ringraziamenti

Durante questo dottorato, ho analizzato come materia e luce interagiscano attraverso due prospettive completamente diverse e, probabilmente, complementari. Scritto nero su bianco, mi accorgo di quanto questo abbia dato un contributo significativo alla mia crescita personale, oltre che a quella professionale. Ringrazio quindi i miei relatori, che hanno *in primis* concepito questo percorso.

Ringrazio in particolare la professoressa Elisabetta Collini, per aver voluto investire in un progetto completamente nuovo, e di averlo affidato a me. In questi tre anni mi sono sentito libero nella ricerca, ma contemporaneamente guidato e seguito.

Grazie, inoltre, al professor Fabrizio Mancin, per la sua creatività e la sua capacità di saper far dialogare argomenti di discipline scientifiche apparentemente così diverse.

Ringrazio il professor Stefano Corni, Gabriel e Giovanni, per le fruttuose collaborazioni scientifiche alle quali ho avuto il piacere di partecipare.

Ringrazio la professoressa Camilla Ferrante per aver dato la disponibilità all'utilizzo di alcuni suoi laboratori, il dottor Caicci e il dottor Boldrin per l'aiuto datomi con le misure TEM, il professor Danilo Pedron per avermi ospitato in alcuni suoi laboratori, e il dottor Massimo Pavan per l'assistenza tecnica.

Ringrazio tutti i membri del gruppo MUOS, passati e presenti: Caterina, Edoardo, Elisa, Francesco, Giampaolo, Martijn e Matteo. È stato bello, stimolante e piacevole lavorare con ciascuno di voi, scambiare opinioni scientifiche, condividere la fatica, suggerire e ricevere consigli. Vi ringrazio per il clima che si è creato, che mi riempie di entusiasmo e spesso mi dà nuovi spunti di riflessione. Assieme a voi ringrazio tanti altri colleghi e amici: Carlo, Ilaria, Maria Vittoria, Matteo, Riccardo, Roman, Susanna, Veronica. Grazie a tutti per i pranzi, gli spritz, i dolci e tutto quello che abbiamo condiviso assieme.

Vorrei ringraziare anche la vecchia guardia del gruppo MUOS, la quale, sebbene vista di sfuggita, mi ha lasciato delle conoscenze che si sono rivelate utilissime per tutta la durata della mia tesi: grazie ad Andrea, Elena e Luca.

Ho passato parte del mio dottorato nei laboratori di Fabrizio, a chimica organica. Qui ho incontrato Daniele, Giordano, Luca e Lucia, che vorrei ringraziare per il loro aiuto, i loro consigli

e la loro amicizia: mi hanno aiutato notevolmente ad affrontare le giornate di sintesi più faticose e difficili.

Inoltre, una parte considerevole di questa tesi è stata scritta in quarantena, mentre i miei coinquilini alleggerivano le mie giornate facendomi da mangiare i piatti più buoni di sempre. Per questo, come per le numerose occasioni di svago e di confronto, vi sono grato.

Ringrazio tutte le relazioni e le amicizie che mi sono state vicine in questi anni: Alessandro, Arianna, Beatrice, Elisa, Linda, Marco e Stefano. Grazie al gruppo IMPACT tutto, che per alcuni versi assomiglia più ad una famiglia che ad un gruppo, per i pranzi in allegria, le partite di Keyforge, i discorsi (semi)seri e i Go-kart.

Un grazie in particolare ad Enrico: in te ho trovato un grande amico.

Ringrazio la mia famiglia, che mi ha supportato e spronato sempre a dare il meglio, anche nei momenti più faticosi.

Infine, grazie a Chiara. Nella vita che in questi tre anni abbiamo condiviso, nei momenti difficili mi hai mostrato delle soluzioni che mai mi sarei immaginato, e nei momenti felici eravamo lì, a festeggiarli assieme.

Rileggo queste pagine e mi accorgo di quanto siano piene di nomi, persone, momenti ed esperienze. "J'ai des amis à découvrir et beaucoup de choses à connaître" (Ho degli amici da conoscere e molte cose da scoprire) scriveva Saint-Exupery ne *Il Piccolo Principe*, e in questa frase trovo ben descritte la mia crescita, la mia realizzazione e la mia gratitudine lungo questi tre anni.